GEMS & GEMOLOGY

FALL 2017
VOLUME LIII

THE QUARTERLY JOURNAL OF THE GEMOLOGICAL INSTITUTE OF AMERICA

Review of HPHT Synthetic Diamonds

Radiocarbon Dating of Columbian-Era Saltwater Pearls

PL Spectroscopy and Emerald Origin

Colombian Emerald Field Report

Editorial Staff

Editor-in-Chief
Duncan Pay
dpay@gia.edu

Managing Editor
Stuart D. Overlin
soverlin@gia.edu

Editor
Jennifer-Lynn Archuleta
jennifer.archuleta@gia.edu

Technical Editors
Tao Z. Hsu
tao.hsu@gia.edu
Jennifer Stone-Sundberg
jstone@gia.edu

Editors, Lab Notes
Thomas M. Moses
Shane F. McClure

Editors, Micro-World
Nathan Renfro
Elise A. Skalwold
John I. Koivula

Editors, Gem News
Emmanuel Fritsch
Gagan Choudhary
Christopher M. Breeding

Editorial Assistants
Brooke Goedert
Erin Hogarth

Contributing Editors
James E. Shigley
Andy Lucas
Donna Beaton

Editor-in-Chief Emeritus
Alice S. Keller

Customer Service
Martha Erickson
(760) 603-4502
gandg@gia.edu

Production Staff

Creative Director
Faizah Bhatti

Production Specialist
Juan Zanahuria

Multimedia Specialist
Lynn Nguyen

Photographer
Robert Weldon

Image Specialist
Kevin Schumacher

Video Production
Larry Lavitt
Pedro Padua
Nancy Powers
Albert Salvato
Betsy Winans

Editorial Review Board

Ahmadjan Abduriyim, Tokyo, Japan
Timothy Adams, San Diego, California
Edward W. Boehm, Chattanooga, Tennessee
James E. Butler, Washington, DC
Alan T. Collins, London, UK
John L. Emmett, Brush Prairie, Washington
Emmanuel Fritsch, Nantes, France
Eloïse Gaillou, Paris, France
Gaston Giuliani, Nancy, France
Jaroslav Hyršl, Prague, Czech Republic
A.J.A. (Bram) Janse, Perth, Australia
E. Alan Jobbins, Caterham, UK
Mary L. Johnson, San Diego, California
Anthony R. Kampf, Los Angeles, California
Robert E. Kane, Helena, Montana
Stefanos Karampelas, Basel, Switzerland
Lore Kiefert, Lucerne, Switzerland
Ren Lu, Wuhan, China
Thomas M. Moses, New York, New York
Aaron Palke, Carlsbad, California
Nathan Renfro, Carlsbad, California
Benjamin Rondeau, Nantes, France
George R. Rossman, Pasadena, California
Andy Shen, Wuhan, China
Guanghai Shi, Beijing, China
James E. Shigley, Carlsbad, California
Elisabeth Strack, Hamburg, Germany
Fanus Viljoen, Johannesburg, South Africa
Wuyi Wang, New York, New York
Christopher M. Welbourn, Reading, UK

GEMS & GEMOLOGY

gia.edu/gems-gemology

Subscriptions
Copies of the current issue may be purchased for $29.95 plus shipping. Subscriptions are $79.99 for one year (4 issues) in the U.S. and $99.99 elsewhere. Canadian subscribers should add GST. Discounts are available for group subscriptions, GIA alumni, and current GIA students. To purchase print subscriptions, visit store.gia.edu or contact Customer Service. For institutional rates, contact Customer Service.

Database Coverage
G&G is abstracted in Thomson Reuters products (Current Contents: Physical, Chemical & Earth Sciences and Science Citation Index—Expanded, including the Web of Knowledge) and other databases. For a complete list of sources abstracting *G&G*, go to gia.edu/gems-gemology, and click on "Publication Information."

Manuscript Submissions
Gems & Gemology, a peer-reviewed journal, welcomes the submission of articles on all aspects of the field. Please see the Author Guidelines at gia.edu/gems-gemology or contact the Managing Editor. Letters on articles published in *G&G* are also welcome. Please note that Field Reports, Lab Notes, Gem News International, Micro-World, and Charts are not peer-reviewed sections but do undergo technical and editorial review.

Copyright and Reprint Permission
Abstracting is permitted with credit to the source. Libraries are permitted to photocopy beyond the limits of U.S. copyright law for private use of patrons. Instructors are permitted to reproduce isolated articles and photographs/images owned by *G&G* for noncommercial classroom use without fee. Use of photographs/images under copyright by external parties is prohibited without the express permission of the photographer or owner of the image, as listed in the credits. For other copying, reprint, or republication permission, please contact the Managing Editor.

Gems & Gemology is published quarterly by the Gemological Institute of America, a nonprofit educational organization for the gem and jewelry industry.

Postmaster: Return undeliverable copies of *Gems & Gemology* to GIA, The Robert Mouawad Campus, 5345 Armada Drive, Carlsbad, CA 92008.

Our Canadian goods and service registration number is 126142892RT.

Any opinions expressed in signed articles are understood to be opinions of the authors and not of the publisher.

About the Cover

While the size and color of synthetic diamonds grown by the high-pressure, high-temperature (HPHT) method have changed considerably in the past decade, a combination of gemological characteristics, spectroscopic features, and UV fluorescence reactions provides reliable indication of synthetic origin. Our lead article surveys the HPHT-grown diamonds seen in GIA labs since 2007. The HPHT synthetics on the cover, part of the GIA collection and ranging in weight from 0.31 to 1.94 ct, demonstrate the colors now seen in this lab-grown material. Photo by Kevin Schumacher.

Printing is by L+L Printers, Carlsbad, CA.
GIA World Headquarters The Robert Mouawad Campus 5345 Armada Drive Carlsbad, CA 92008 USA

© 2017 Gemological Institute of America All rights reserved.

ISSN 0016-626X

FSC www.fsc.org MIX Paper from responsible sources FSC® C006300

GEMS & GEMOLOGY

Fall 2017
VOLUME 53, No. 3

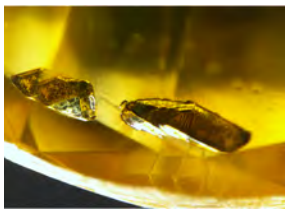
pg. 272


pg. 290


pg. 314


pg. 332


pg. 371

A Review of **HPHT Synthetic Diamonds Grown for Jewelry Use**

Our Fall issue serves up a wealth of topics, including HPHT synthetic diamonds, historical saltwater pearls from the New World, the photoluminescence (PL) spectra of emeralds, synthetic star corundum, and the Colombian emerald mine-to-market industry.

In our lead article, Drs. Sally Eaton-Magaña, James Shigley, and Christopher M. Breeding present a comprehensive study of several thousand HPHT-grown synthetic diamonds using data gathered by GIA between 2007 and 2016. Their study charts a transition from predominately orange-yellow goods to today's more diverse products, where fashioned blue and colorless synthetics exceeding 10 carats and mass-produced HPHT melee grown exclusively for jewelry use are now a marketplace reality. We trust that this survey—which includes a review of current identification criteria for HPHT-grown synthetics—will prove immensely valuable for industry professionals.

"HPHT synthetic diamonds—including blue and colorless gems exceeding 10 carats along with mass-produced melee—are now a marketplace reality."

The second paper is a collaboration between researchers at GIA and the Gübelin Gem Lab. Lead author Chunhui Zhou and his team detail 85 natural saltwater pearls reportedly recovered from Caribbean waters between the fifteenth and seventeenth centuries. The team's analyses verified these fascinating pearls' natural saltwater origin, and ^{14}C isotope radiocarbon dating supports their attested age.

In the first of this issue's two emerald papers, researchers led by Dr. D. Brian Thompson of the University of North Alabama investigate the PL spectra of 48 samples from Colombia, Afghanistan, and Zambia. Their research strongly indicates that variations in trace element concentration within emeralds from these localities correlate with differences in the strength and position of peaks detected in their PL spectra, which could be very promising for determining geographic source.

In our fourth paper, Dr. Karl Schmetzer, Prof. H. Albert Gilg, and Dr. Heinz-Jürgen Bernhardt delve into the characteristics of synthetic star corundum produced in Germany up to the 1970s by Wiede's Carbidwerk. Grown by a variation of the Verneuil method followed by controlled annealing to exsolve the rutile needles, these synthetic gems are visually—and gemologically—distinct from the production of other manufacturers.

Next, Tomasz Powolny and Dr. Magdalena Dumańska-Słowik reexamine spotted "dalmatian jasper," a popular decorative gem material. Based on their analysis of its composition and gemological characteristics, which do not meet the definition of jasper, the authors recommend use of the term "dalmatian stone."

In our final article, Darwin Fortaleché, chief gemologist at Centro de Desarrollo Tecnológico de la Esmeralda Colombiana (CDTEC), and his GIA coauthors provide a comprehensive field report on current mining and the state of the Colombian emerald industry. They cite increased investment by multinational companies, the country's largely untapped emerald reserves, and the initiation of chain-of-custody systems as hopeful signs for the future.

Our Lab Notes section features an entry on a large, high-quality diamond from Brazilian kimberlite. Topics in our Micro-World section include hematite roses and a "flower-in-the-rain" inclusion within a Sri Lankan sapphire, while our Gem News International section spotlights blue-green pyrope-spessartine with high vanadium content and two potential new sources of Nigerian sapphire.

Please enjoy the Fall *G&G*!

Duncan Pay | Editor-in-Chief | dpay@gia.edu

Observations on HPHT-Grown Synthetic Diamonds: A Review

Sally Eaton-Magaña, James E. Shigley, and Christopher M. Breeding

This article presents statistical data and distinctive features for several thousand HPHT-grown synthetic diamonds examined by GIA from 2007 through 2016. This study, the first comprehensive summary published on such a large number and wide variety of samples, describes the reliable means of identifying them, with a focus on material currently marketed for jewelry use. The color of HPHT synthetic diamonds analyzed by GIA has shifted noticeably during this time—in the early years, orange-yellow, yellow, and yellow-orange samples comprised the overwhelming majority, while colorless and blue samples are much more prevalent today. HPHT synthetics are making inroads into the large diamond market, with cut stones larger than 10 carats, as well as the colorless melee market, where small HPHT synthetics are being mass-produced in China. HPHT synthetics can be identified by their distinctive fluorescence patterns using the DiamondView luminescence imaging instrument, the lack of "strain" (anomalous birefringence) when viewed through crossed polarizers, and to a lesser extent by the detection of various features in photoluminescence (PL) spectroscopy. This material may also display magnetism and a short-wave fluorescence and phosphorescence reaction that are inconsistent with similarly colored natural diamonds.

Synthetic gem diamonds grown by the high-pressure, high-temperature (HPHT) process have been commercially available since the mid-1990s. This article presents statistical information and distinctive identification features based on a review of data gathered by GIA, principally at the New York and Carlsbad laboratories, for several thousand HPHT-grown synthetic diamonds. This study includes all HPHT synthetic diamonds submitted to GIA between 2007 (the year GIA started issuing Synthetic Diamond Grading Reports) and 2016. No summary has been published on such a large number of HPHT synthetic samples. We describe here the diagnostic means of identification, with an emphasis on the goods currently being sold for jewelry use. Box A details some of the most important identification criteria that may be used by gemologists.

Of this sample set, 12% were colorless to near-colorless (D–J), 12% blue, 13% yellow, 4% pink to red, and 54% yellowish orange to orangy yellow (e.g., figure 1). The remaining 5% showed other colors, including green-yellow and brown-orange. This set represents both as-grown and treated colors. While some samples were purchased by GIA on the market or from manufacturers, or were loaned or donated to us by manufacturers for study purposes, most were submitted to GIA in polished form for identification or grading reports. To the best of our knowledge, this sample set is representative of the gem-quality HPHT synthetic material available in the trade.

In Brief

- Colors, sizes, and other properties of HPHT synthetic diamonds submitted to GIA's laboratory have changed over the past decade.
- Advances in growth techniques have led to more very large (>2 ct) and very small (<0.05 ct) colorless synthetic diamonds in the trade.
- Identification methods for HPHT synthetics have remained consistent and reliable.
- HPHT synthetic diamonds have become more prevalent, and their market share will likely continue to expand.

See end of article for About the Authors.

Gems & Gemology, Vol. 53, No. 3, pp. 262–284,
http://dx.doi.org/10.5741/GEMS.53.3.262

© 2017 Gemological Institute of America

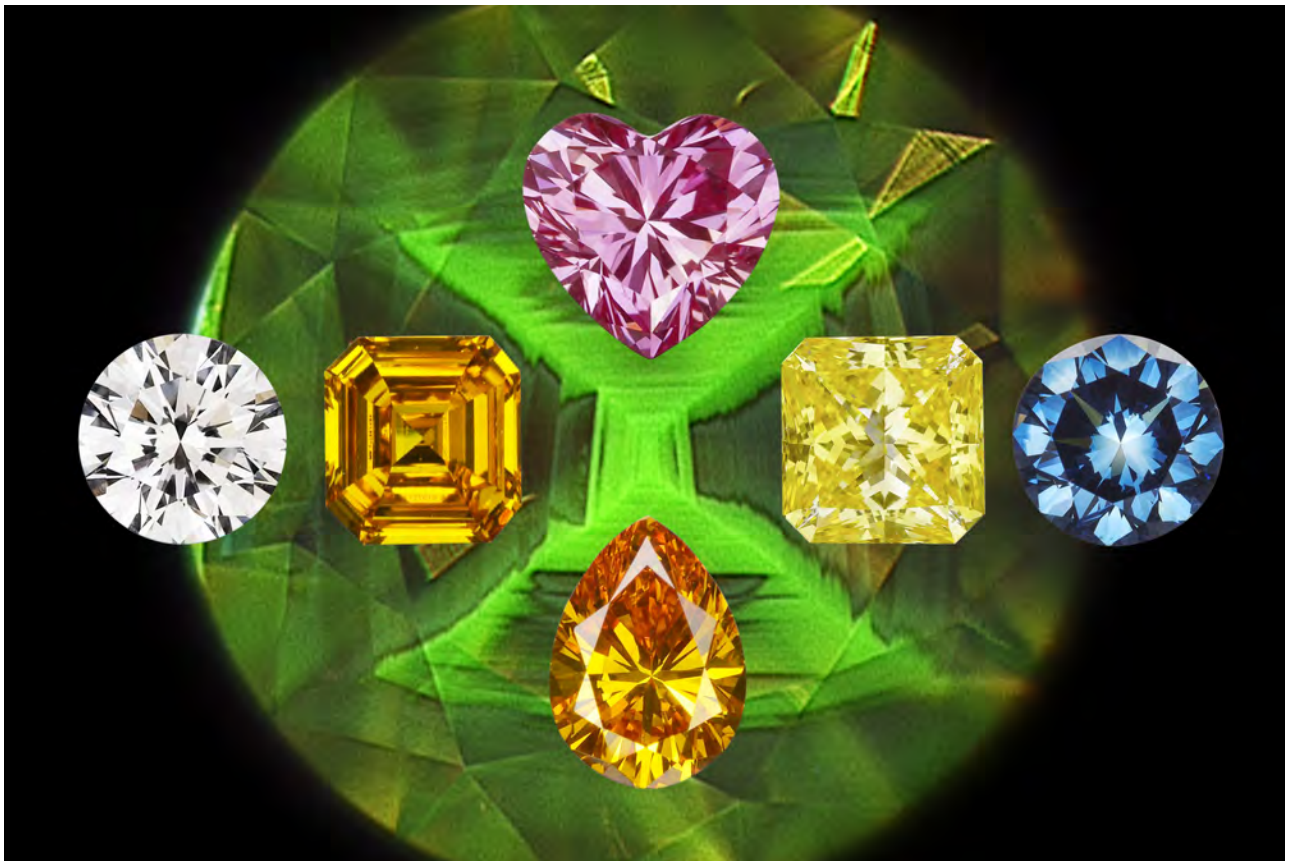

Figure 1. This collection of HPHT synthetics shows the major color products. The background is a DiamondView image with a cross-shaped fluorescence pattern, a well-known diagnostic feature of HPHT synthetics.

The evolution of HPHT synthetics has been detailed in previous *G&G* articles (Shigley et al., 2002, 2004; D'Haenens-Johannsson et al., 2014, 2015) and Lab Notes entries (e.g., Ardon and Batin, 2017; Johnson et al., 2017) that include diamonds within this dataset. Whereas earlier studies examined small batches of material from specific manufacturers (which were likely grown using a similar recipe or HPHT pressure equipment), the goal of the present study is to investigate trends in the distinctive features seen among HPHT synthetic diamonds from multiple sources over the past ten years.

During the decade covered in this review, the colors of HPHT synthetics have shifted from predominantly yellow and orange to colorless and blue. The early years (2007–2008) likely represent the colors manufactured during the prior decade. The high number of submissions in those early years represents material that had already been available in the trade—for example, synthetics in the yellow, green, pink, and blue color ranges discussed by Shigley et al. (2004). There has also been a dramatic expansion in the size ranges. This includes polished gems greater than 10 carats (although production is still limited), as well as a significant increase in the output of HPHT synthetic melee, whose volume and small stone size present particular identification problems for the jewelry trade.

HPHT SYNTHETIC DIAMOND GROWTH

High-pressure, high-temperature diamond growth was first announced by the General Electric Company (GE) in 1955, and today most HPHT synthesis has its origins in the temperature gradient method first developed in 1959 (Bovenkerk et al., 1959). Yet it was only during the 1990s that these products attained sufficient size and gem quality to present significant concerns to the jewelry industry (Shigley et al., 1997). High-pressure reactor chamber design and control of diamond growth parameters have advanced considerably in recent years. The consistent production of larger as well as colorless HPHT synthetics is now possible, and several HPHT synthetic crystals can be grown simultaneously within the

BOX A: IDENTIFICATION CRITERIA FOR THE GEMOLOGIST

While HPHT synthetic diamonds can show several distinctive visual features that aid a gemologist in identification, few features will unambiguously confirm that a diamond is not an HPHT-grown synthetic. Therefore, a negative result does not exclude HPHT synthetic origin. For example, while magnetism is a strong indicator of HPHT growth, a lack of magnetism does not exclude the possibility. Reliable conclusions regarding natural or synthetic origin should be made from a combination of gemological and spectroscopic data, and the origin is probably best determined by a gemological laboratory. The features mentioned below have all been described and illustrated in the published literature.

Strain. The *lack* of observable strain (anomalous birefringence) when a diamond is viewed with polarized light does provide a strong indication of HPHT growth (figure A-1). Natural diamonds are typically subjected to varying stresses during their long growth and transport history. In contrast, HPHT synthetic diamonds are grown in a uniform high-pressure field. Yet the presence of birefringence does not eliminate synthetic origin, as CVD-grown diamonds commonly show strain and HPHT-grown diamonds rarely do (Ardon and Batin, 2017).

Magnetism and Metallic Inclusions. HPHT synthetics span the clarity scale, but those examined by GIA trend toward higher clarity grades (see "Analysis of Quality Grading Factors," figure 6). Due to the flux-metal chemistry necessary for HPHT growth, any observable features, such as metallic inclusions (see figure 8), are usually evidence of a distinctive growth environment. Such metallic inclusions are rarely observed in natural diamonds (Smith et al., 2016). Occasionally, metallic inclusions are present in sufficient concentration in a synthetic diamond to produce a detectable magnetic reaction. The absence of these metallic inclusions, or the absence of a magnetic response, does not exclude HPHT synthetic origin, as research has shown that the magnetic attraction was consistently detected only in the SI–I clarity range (D'Haenens-Johansson et al., 2014). A diamond dealer once related to us the prac-

Figure A-1. Viewed in crossed polarizers, natural diamonds (left) and CVD synthetics (middle) display higher-order interference colors than those generally seen in HPHT synthetics, which tend to display uniform, featureless birefringence (right). Shown in these photos are a 3.49 ct D-color natural diamond (left), a 2.51 ct H-color CVD synthetic (middle), and a 0.46 ct D-color HPHT synthetic (right).

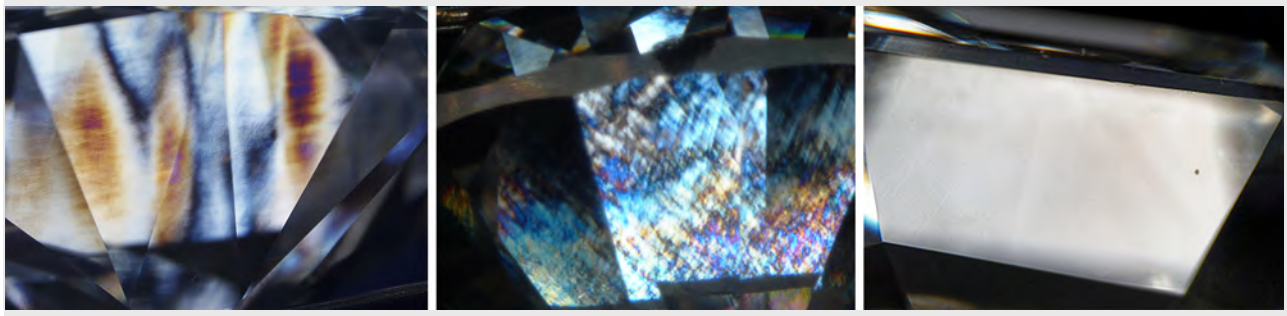

press (D'Haenens-Johansson et al., 2015). In general, HPHT growth proceeds at temperatures and pressures designed to approximate the conditions of natural diamond growth. Within the earth, diamonds generally form at pressures of 5.5–8.0 GPa (55,000–80,000 atmospheres) and temperatures of 1000–1400°C, corresponding to depths of 140–240 km (Shirey and Shigley, 2013).

In HPHT growth, a carbon source such as graphite or diamond powder is placed in the reactor chamber along with other ingredients to facilitate diamond growth atop a diamond seed. A molten metal catalyst (usually containing a mixture of Fe, Ni, Co, or other elements) allows growth to proceed at a lower temperature. This also reduces the technological complexity and some of the expense required to grow diamond under HPHT conditions. HPHT growth occurs at pressures of 5–6 GPa (roughly equivalent to the pressure exerted by a commercial jet airplane if balanced on the tip of a person's finger) and at temperatures of 1300–1600°C. As with CVD diamond growth, HPHT growth proceeds by creating a temperature gradient in which the carbon source is at a slightly higher temperature than the diamond growth seed. This causes the carbon atoms to diffuse through the molten flux toward the slightly colder section of the chamber to form a syn-

tice of sweeping a magnet over a parcel of diamonds as a method for detecting synthetics. While this might have been considered adequate in prior decades, it is no longer a reliable test.

Color Zoning. Due to their growth methods, fancy-color HPHT-grown synthetics often have color zoning related to the arrangement of internal growth sectors, and the concentration of color-causing impurities like nitrogen or boron in some select sectors. The presence of such growth zoning patterns, particularly in diamonds with yellow, yellow-orange, or blue coloration, would strongly suggest an HPHT origin. Geometric patterns of color zoning are rarely seen in natural diamonds. Some natural diamonds with dark-colored zones are due to high concentration of graphitic inclusions (Hainschwang et al., 2014; Eaton-Magaña et al., 2016) rather than the variable incorporation of color centers as seen in HPHT synthetics.

Fluorescence. HPHT synthetic diamonds generally show a stronger fluorescence reaction to short-wave UV than to long-wave UV. This trend is observed for both fancy-color (Shigley et al., 2002, 2004) and colorless material (D'Haenens-Johansson et al., 2015). Interestingly, this observation appears to correlate with type Ib diamond, as King et al. (2005) reported that among the very few natural diamonds that show a similar reaction, almost all were type Ib. The predominant fluorescence colors are green to yellow to orange. Additionally, the vast majority of HPHT synthetics in the "colorless" range exhibit no detectable fluorescence to long-wave UV.

Phosphorescence. As phosphorescence is often quite weak, the reaction is best observed in a darkened room. The observed duration can persist from less than a second to a few tens of seconds. Blue and colorless HPHT-grown synthetics often show light blue phosphorescence, with the luminescence spectral band centered at 500 nm. In this color range, orange phosphorescence at 575 nm is occasionally observed in HPHT synthetics but is thought to be exclusive to this material (Watanabe et al., 1997; Eaton-Magaña and Lu, 2011). The 500 nm phosphorescence band due, in part, to the presence of boron is commonly observed in both type IIb natural diamonds and CVD synthetics, but the phosphorescence is generally less intense.

Diamond Type. Colorless samples that are UV transparent or show no detectable nitrogen in their FTIR absorption spectra—meaning they are type II—should always be sent to a gemological laboratory for testing, as these might have been subjected to HPHT processing or could be CVD or HPHT synthetic diamonds.

Inscription. Major HPHT synthetic manufacturers often inscribe the origin on the girdle (e.g., "Lab Grown" or other wording). However, the lack of an inscription does not necessarily indicate a natural stone, as diamonds can be recut or a manufacturer might not inscribe the synthetic origin.

Advanced Testing. Gem testing laboratories should maintain a full complement of gemological, imaging, and spectroscopic instrumentation, including a DiamondView imaging microscope, an FTIR absorption spectrometer, and a photoluminescence (PL) spectrometer equipped with several lasers. Additionally, these laboratories must have access to HPHT synthetics that are representative of products available in the trade and maintain a database of their properties. They must be constantly vigilant for emerging trends that deviate from standard detection criteria for natural, treated, or synthetic diamonds. Gem labs must also operate under the assumption that today's reliable criteria may not be applicable in the future, which would require alternative methods to ensure that identification keeps pace with the manufacturers' growth technology.

thetic diamond crystal on the seed. Most early gem-quality HPHT synthetics were fancy color, since color-causing impurities, such as nitrogen (yellow) or boron (blue), were often prevalent within the growth system. Recent progress in growth technology has allowed for better control of impurity contents, resulting in the creation of colorless crystals (e.g., figure 2).

ANALYSIS OF EXISTING DATA

We will summarize quality factors, basic gemological properties, ultraviolet fluorescence reactions, and key spectral features based on information gathered when these several thousand HPHT-grown samples were examined by GIA between 2007 and 2016. In some instances, GIA did not collect all data types on a particular HPHT synthetic sample for various reasons: time constraints, the lack of certain instrument capabilities at the time of examination, or the need to limit the analysis to the grading service requirements requested by the submitting client. In the following discussion, therefore, we will indicate the percentage of total submissions for which that data was collected. Nonetheless, the information reported here represents the most substantial database of observations published to date on gem-quality HPHT synthetic diamonds.

Figure 2. This selection of colorless HPHT synthetic crystals (0.50–0.69 ct) was grown by Jinan Zhongwu New Materials Company Ltd. of Shandong, China.

We noted no significant differences in characteristics between the HPHT synthetic samples sourced directly from the manufacturers and those submitted by GIA laboratory clients. The information presented here is strictly limited to HPHT synthetics examined by GIA, which might not represent all of the goods available within the gem trade and certainly not those crystals grown for technological or industrial applications.

ANALYSIS OF QUALITY GRADING FACTORS

Color. Since 2007, there has been a pronounced shift in the color of the HPHT synthetics submitted for grading. In the early years of GIA's Synthetic Diamond Grading Report, the overwhelming majority were orangy yellow to yellowish orange (in this article, this color range is shortened to "yellow-orange"; e.g., figure 3). The proportion of HPHT synthetics with pink coloration has remained generally constant at around 3–8%. During the early years, blue samples were not submitted in large numbers. Since then, the blue and yellow hues have shown some fluctuations in annual percentage but exhibited no distinct trends. Colorless to near-colorless synthetics have shown a dramatic increase, now reaching 43% of the HPHT synthetics submitted to GIA in 2016. While the proportion of yellow-orange HPHT synthetics that have been submitted (and likely manufactured) has decreased in recent years, they still comprise a clear majority of the HPHT synthetics submitted to GIA from 2007 through 2016 (figure 3, right).

Among the colorless to light yellow (D–Z) HPHT synthetics, the vast majority (72%) were in the colorless (D–F) range, while 26% were in the near-colorless (G–J) range, and the remainder had lower color grades. In contrast, most D–Z CVD synthetics examined by GIA were in the near-colorless range: 21% D–F, 67% G–J, and 10% K–N (Eaton-Magaña and Shigley, 2016).

Figure 3. Left: The color distribution of HPHT synthetic diamonds analyzed by GIA, separated by year. Right: The overall distribution of HPHT synthetics submitted to GIA by bodycolor. Yellow-orange HPHT synthetics represented the vast majority of submissions during the early years and constitute a majority of all HPHT synthetics seen at GIA since 2007. In recent years, client submissions of yellow-orange HPHT synthetics have been eclipsed by blue and colorless samples. The percentage shown in red represents the portion of samples submitted for which data are available.

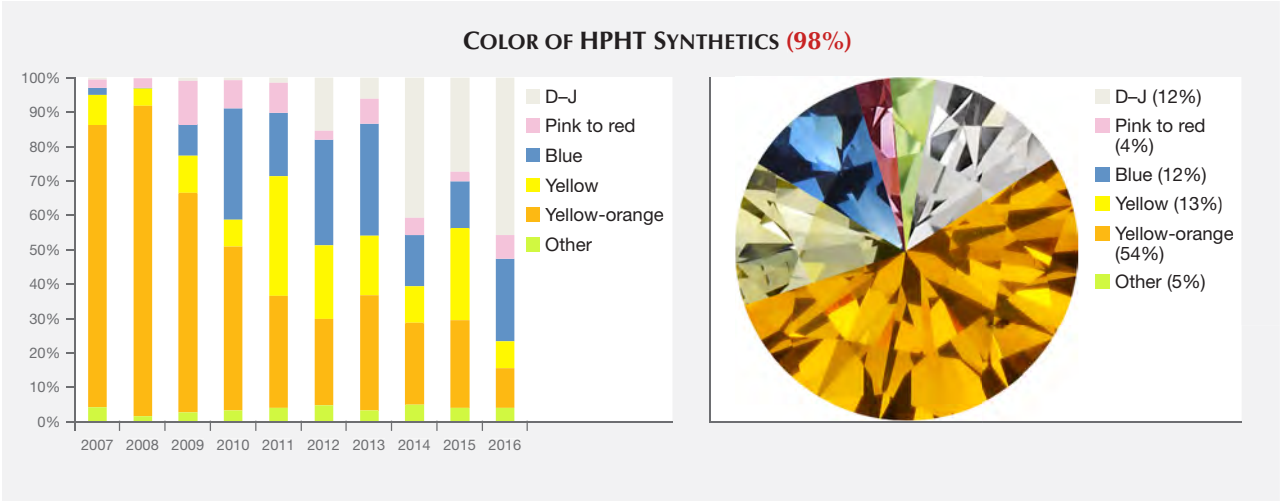

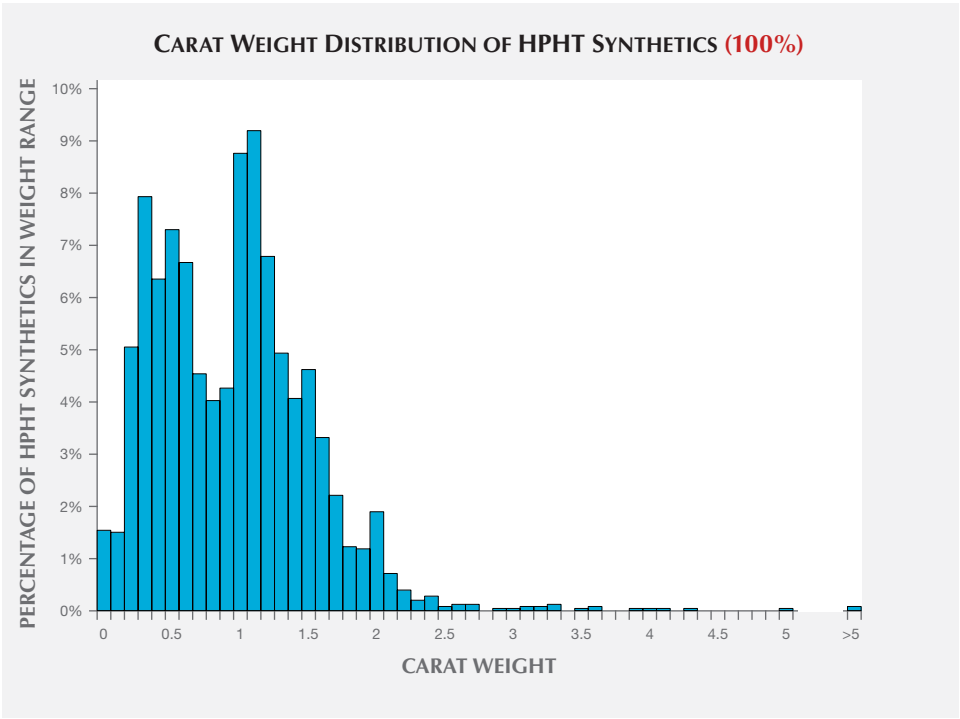

Figure 4. From 2007 through 2016, most of the HPHT synthetic diamonds analyzed by GIA were in the 0.2–0.5 and 1.0–1.5 ct range. The data here are divided into 0.1 ct increments. The percentage shown in red represents the portion of samples for which data are available.

Most colors of HPHT synthetics are believed to be as-grown (i.e., due to impurities) rather than the product of post-growth treatment processing. In contrast, CVD synthetics are often subjected to post-growth treatment. Most near-colorless CVD synthetics are subsequently HPHT treated (to remove any brown coloration), while the pink samples (the other major CVD product) undergo irradiation and annealing (Eaton-Magaña and Shigley, 2016).

The colors of "yellow-orange" and yellow HPHT synthetics are due to the presence of isolated nitrogen incorporated during the growth process (Shigley et al., 2002); however, the additional use of "nitrogen-getters" such as aluminum in the growth system can reduce the incorporation of nitrogen (Sumiya and Satoh, 1996). Almost all "orange" HPHT synthetics included a yellow component, while some contained a brown or pink modifier; very few were pure orange.

"Pink" HPHT synthetics (including purple-pink, red, and brown-red) owe their color to post-growth treatment by irradiation and low-temperature annealing. This procedure creates nitrogen-vacancy (NV) optical centers, which are also the source of color in treated pink diamonds, treated CVD synthetics, and the rare natural and untreated Golconda pinks.

Blue HPHT synthetics result from the presence of boron within the growth chamber. Colorless HPHT synthetics are reportedly sold as-grown without post-growth color modification (D'Haenens-Johansson et al., 2014), and they often contain small amounts of boron, which does not alter their color (but does impart luminescence).

Other less common colors include yellow-green to green samples. Green coloration has a number of origins in HPHT synthetics, including the presence of yellow zones (due to nitrogen) and blue zones (due to boron) that visually combine to give a greenish appearance (Shigley et al., 2004); laboratory irradiation after growth (Shigley et al., 2004); and high quantities of nickel impurities (Johnson et al., 2017).

Carat Weight. Faceted HPHT synthetics in the 1.00–1.50 ct range were the most common, representing 34% of those examined by GIA (figure 4). While HPHT synthetics larger than four carats have been newsworthy during the last few years, relatively few have been submitted, presumably due to very limited production. Additionally, the carat range distribution has not varied considerably from 2007 to 2016. Production of colorless melee has increased greatly in recent years (W. Wang, pers. comm., 2016), but so far no fancy-color synthetics of any size have been submitted to GIA in large numbers. With the announcement in late 2016 of a colorless melee sorting service, GIA has seen more of these very small synthetic diamonds; for more on HPHT synthetic melee, see box B.

Box B: HPHT Synthetic Diamond Melee

The market for near-colorless melee diamond (i.e., less than 0.05 ct) has traditionally been dominated by natural stones. However, dramatic improvements in HPHT growth technology and techniques in the past two or three years have had a profound effect on how jewelers must examine their stocks of melee-sized diamonds. HPHT synthetic diamond melee growth is quickly becoming a large industry in China (figure B-1, left). Factories full of HPHT presses can be found in the Chinese city of Zhengzhou, where companies can each produce more than 1,000 carats of near-colorless synthetic diamonds per day (W. Wang, pers. comm., 2016). After faceting, most of the synthetic melee weighs between 0.005 and 0.03 ct, with colors ranging from D to N and widely variable clarities (figure B-1, right).

The melee is grown as tiny, near-colorless individual crystals using even smaller yellow HPHT synthetic diamond seed crystals. Most of the rough is sold with the seed crystals still attached (figure B-2). Larger HPHT synthetic diamonds are grown upward from the {100} cubic face of the seed crystal and have the cuboctahedral crystal form we have come to expect from HPHT-grown diamonds. While most of the HPHT synthetic melee crystals are also grown from a {100} oriented seed, it is notable that several were grown from both {111} octahedral and {110} dodecahedral seed crystal faces as well (figure B-2). The crystals grown from {111} and {110} oriented seeds show a different form and external characteristics that might not be immediately associated with HPHT synthetics.

Near-colorless HPHT-grown melee share most of the key characteristics used to identify larger HPHT-grown synthetics, but their very small size often obscures visual features and makes spectroscopy difficult. All of the near-colorless synthetic melee known today are type II diamonds with no measurable nitrogen impurities. Some are type IIa, but in many cases trace boron impurities can be detected with FTIR analysis, classifying them as type IIb. The type IIa samples may also contain traces of boron that are below the detection level of most FTIR instruments. Although their fluorescence reaction to long-wave UV is usually very weak orange or not visible at all, the presence of boron gives rise to a very useful phosphorescence. When exposed to very high-energy short-wave UV, such as that of the DiamondView, all HPHT-grown melee diamonds will show some phosphorescence (usually blue) after the UV source has been turned off (figure B-3). Many of these synthetic melee contain metallic inclusions that are difficult to observe under the microscope in such small diamonds. In some cases, however, they are readily attracted to a magnet. Additionally, photoluminescence (PL) analysis reveals high concentrations of nickel-related defects in most HPHT synthetic melee and variable amounts of silicon-related defects in some of them (D'Haenens-Johansson et al., 2014). These PL features rarely occur in natural diamond melee. Finally, DiamondView imaging reveals the individual growth zones typical of HPHT-grown synthetic diamonds, though the extremely small size of the melee often makes it difficult to clearly discern the pat-

Figure B-1. Left: This assortment of 10 carats of near-colorless, HPHT-grown synthetic melee diamond crystals is typical of the material now being produced in China. Right: Most of the melee crystals are faceted into tiny round brilliants such as these, weighing about 0.01 ct each. Photos by Wuyi Wang.

Since 2015, many of the previous records for carat weights of polished synthetic diamonds have been shattered (Deljanin et al., 2015; Wang and Poon, 2016). The Russian company New Diamond Technology has provided several colorless to near-colorless diamonds to GIA greater than five carats, along with several blue samples. This advancement has generated excitement as well as concern in the jewelry trade.

Cut. The majority of the faceted HPHT synthetics analyzed were round brilliants (51%). Other common styles included square (19%) and rectangle (18%), with and without cut corners (figure 5, top).

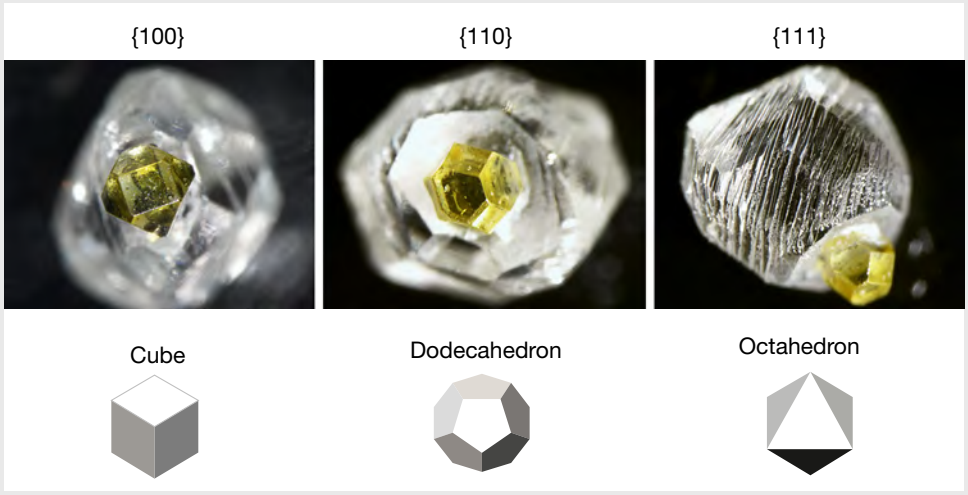

Figure B-2. Although most often grown from the {100} cubic face of the seed crystal (left), some of the synthetic melee were grown from {110} dodecahedral (center) and {111} octahedral (right) seed faces, giving rise to crystal forms and growth striations not typically associated with synthetic diamonds. Photos by Ulrika D'Haenens-Johansson.

terns. In many cases, the patterns are slightly atypical, likely representing the growth using different faces of the seed crystal as described previously (figure B-4).

With the ever-expanding production of near-colorless, melee-sized HPHT-grown synthetic diamonds, the industry must be more vigilant than ever in understanding these tiny goods that are used to adorn jewelry. While we have also examined some CVD-grown melee, most synthetic melee appears to be grown by HPHT methods. Many gemological laboratories now offer low-cost melee testing services to help with identification.

Figure B-3. Following exposure to a high-energy short-wave UV source, HPHT-grown synthetic melee diamonds tend to phosphoresce blue when the UV light is turned off. This effect is due to trace concentrations of boron impurities. Photo by Wuyi Wang.

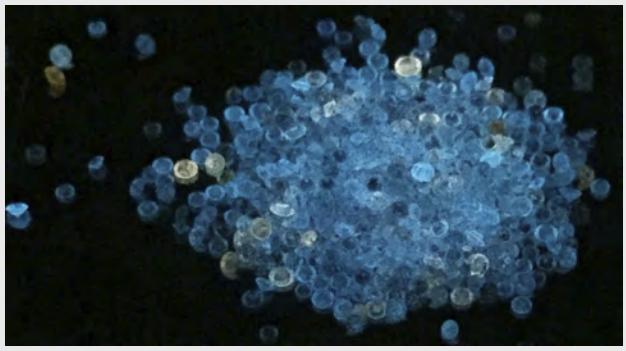

Figure B-4. Left: DiamondView fluorescence images reveal normal cuboctahedral growth patterns in most of the melee, though they are often difficult to observe in such small sizes. Right: Some of the melee show different patterns that may result from growth from atypical seed crystal faces. Photos by Christopher M. Breeding.

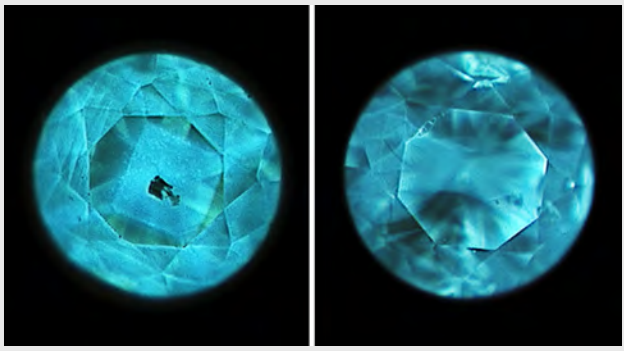

Manufacturers appear to have chosen the round brilliant cut because of the popularity of this style, even though a "fancy" shape would have retained slightly more weight from the original crystal.

Since GIA only assigns cut grades for D–Z color round brilliants, only a small percentage of the HPHT synthetics were eligible for such an assessment. Among these, 44% received a Very Good cut grade, with 30% Excellent and 24% Good (figure 5, bottom).

Clarity. The HPHT synthetics span nearly the entire clarity scale, but most received grades in the VS_1/VS_2 range (figure 6). This is slightly lower than the clarity

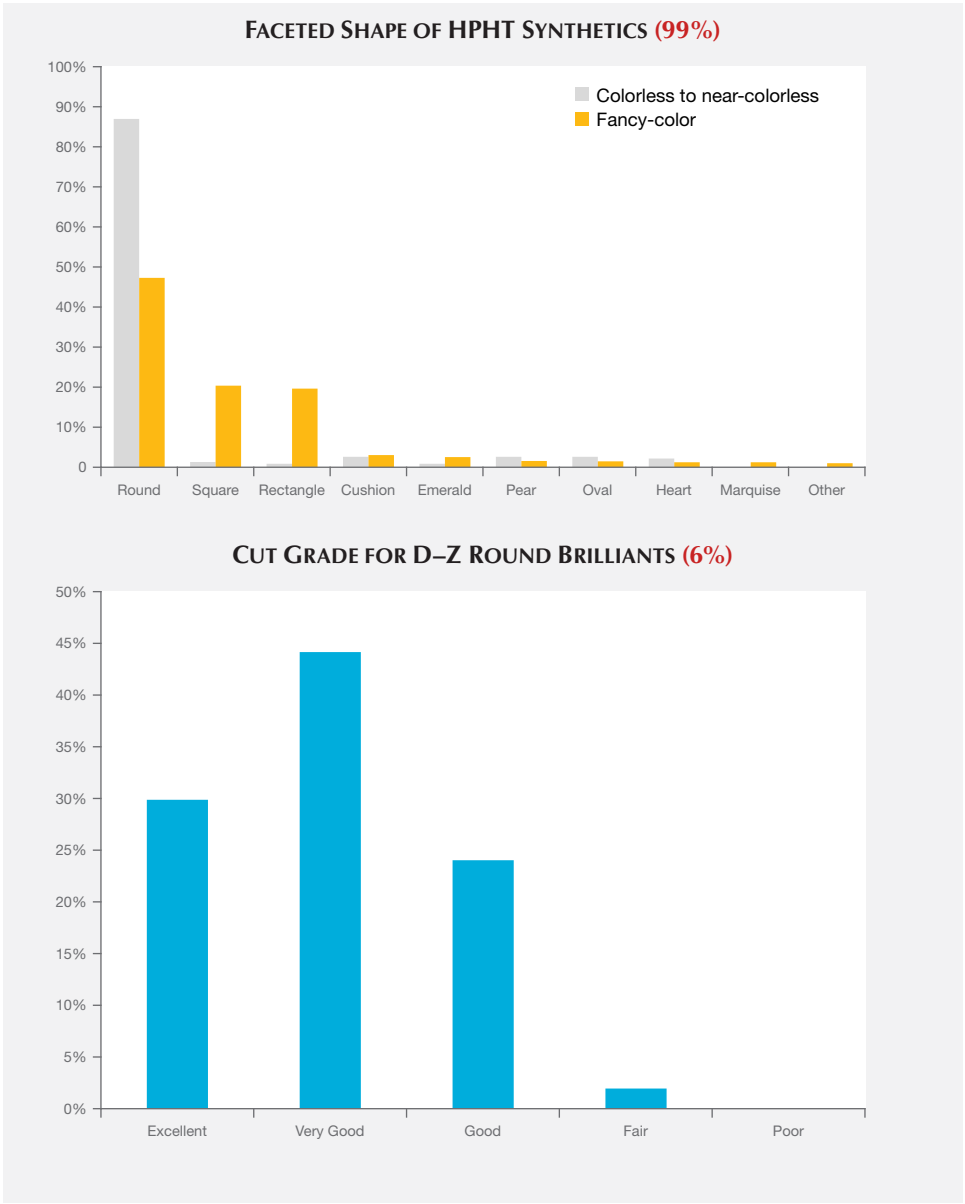

Figure 5. Top: The majority of HPHT synthetics were cut as round brilliants. Bottom: For D–Z round-brilliant HPHT synthetics, a plurality had a Very Good cut grade. The percentages shown in red represent the portion of samples for which data are available.

range observed for CVD synthetics, most of which were in the VVS_2/VS_1 range, and slightly higher than the VS_2/SI_1 range observed for colorless to near-colorless natural diamonds (Eaton-Magaña and Shigley, 2016). As GIA generally examines only the material that has been released by HPHT manufacturers as worthy of cutting, the samples likely represent what is available within the trade but might not account for the entire manufacturing output.

The clarity distribution is shifted toward higher grades among colorless synthetic diamonds than among fancy-color samples. This may be due to the different chemistry in the HPHT presses that create colorless material, or more likely the fact that most colorless goods date from recent years (figure 3, left) and represent improvements in the control of diamond crystallization.

Clarity grading of diamonds often involves the determination of the "grade-setting" clarity feature. This is the visual characteristic seen at 10× magnification that determines the clarity grade. For example, a diamond might have a large feather and a few sparse pinpoints. While both would be listed as inclusions, the feather would be considered the "grade setter." A number of different grade-setting clarity characteristics were found in these HPHT synthetics (figure 7).

The most common grade-setting inclusions for HPHT synthetic diamonds were identified by labora-

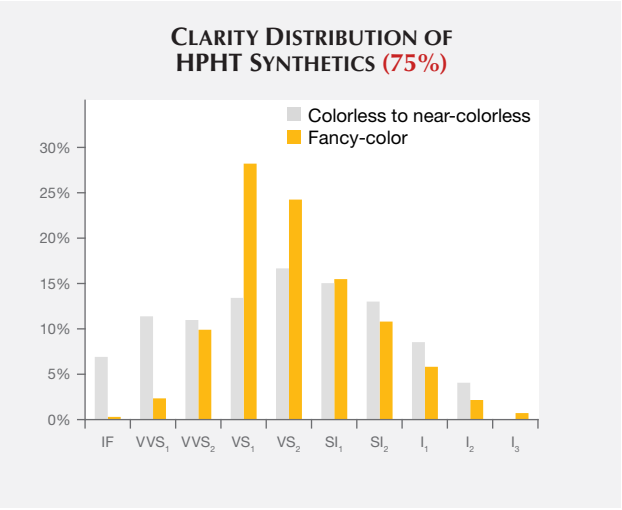

Figure 6. The clarity grade distributions are shown for colorless to near-colorless (D–J) HPHT synthetics (a plurality with VS_2 clarity) and those within the fancy color range (a plurality with VS_1 clarity). The percentage shown in red represents the portion of samples for which data are available.

tory graders as "crystals."[1] The other most common features were feathers, pinpoints, and clouds. These inclusions were mentioned in previous articles (Shigley et al., 2002, 2004; D'Haenens-Johansson et al., 2014, 2015). Many of these features also contained radial fractures surrounding larger inclusions; fractures that reached the surface are plotted as feathers.

ANALYSIS OF OTHER GEMOLOGICAL PROPERTIES

Long-Wave and Short-Wave Fluorescence. While it should not be considered conclusive evidence, the observation of ultraviolet fluorescence with a standard long-wave/short-wave UV unit has been an important and practical means of distinguishing natural diamonds from HPHT-grown synthetics. The determination is based on differences in fluorescence colors, intensities, and patterns (and in some cases the occurrence of persistent phosphorescence). If a fluorescence reaction is observed in an HPHT synthetic, the reaction to short-wave UV radiation is often stronger than to long-wave UV radiation (or the reaction to long-wave is altogether absent). For HPHT synthetics in our dataset that had both long- and short-wave fluorescence reactions, 11% showed a stronger long-wave UV reaction, 32% had equal-intensity fluorescence reactions, and 58% had a stronger short-wave reaction.

The bar graphs in figure 9 (top) illustrate the intensity of fluorescence reactions to long-wave and short-wave ultraviolet radiation from a standard gemological UV lamp. Most HPHT synthetics displayed no fluorescence reaction to long-wave UV

[1]Actually metal flux, as shown in figure 8, and noted as flux (or more recently as "growth remnants") on grading reports, but plotted in similar fashion as natural crystals.

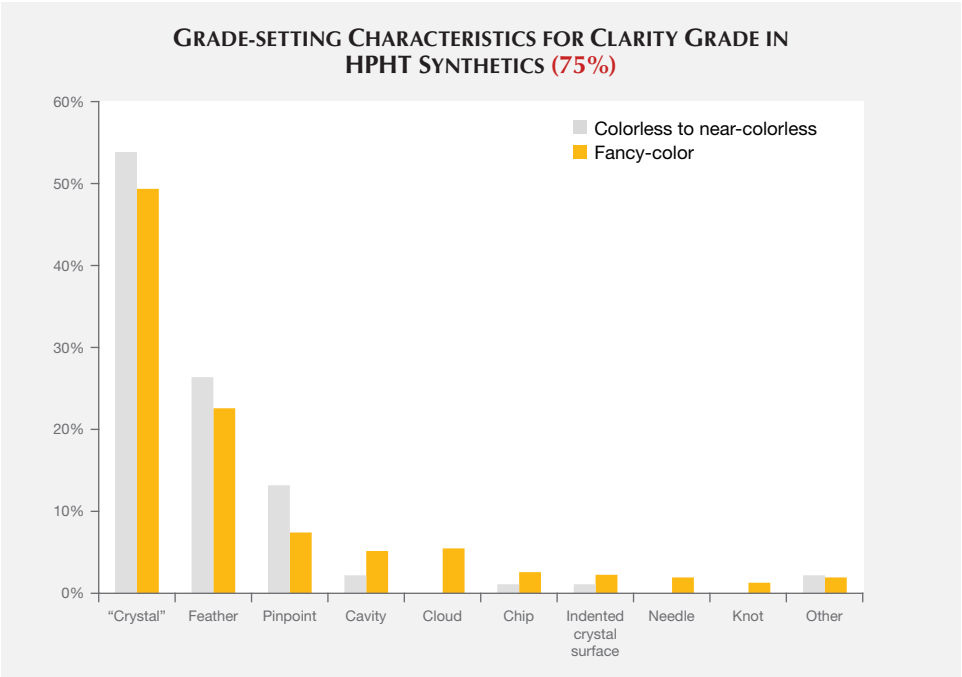

Figure 7. The distribution of grade-setting clarity characteristics is shown for HPHT synthetic diamonds. A "crystal" is defined as solid material, larger than a pinpoint, contained within the diamond. A feather is an internal fracture visible at 10× magnification. A cloud is a cluster of pinpoints (tiny crystals that appear as specks at 10× magnification). A needle is a thin crystal observed with 10× magnification. On grading reports, these characteristics generally are plotted according to these designations, but referred collectively as "growth remnants."

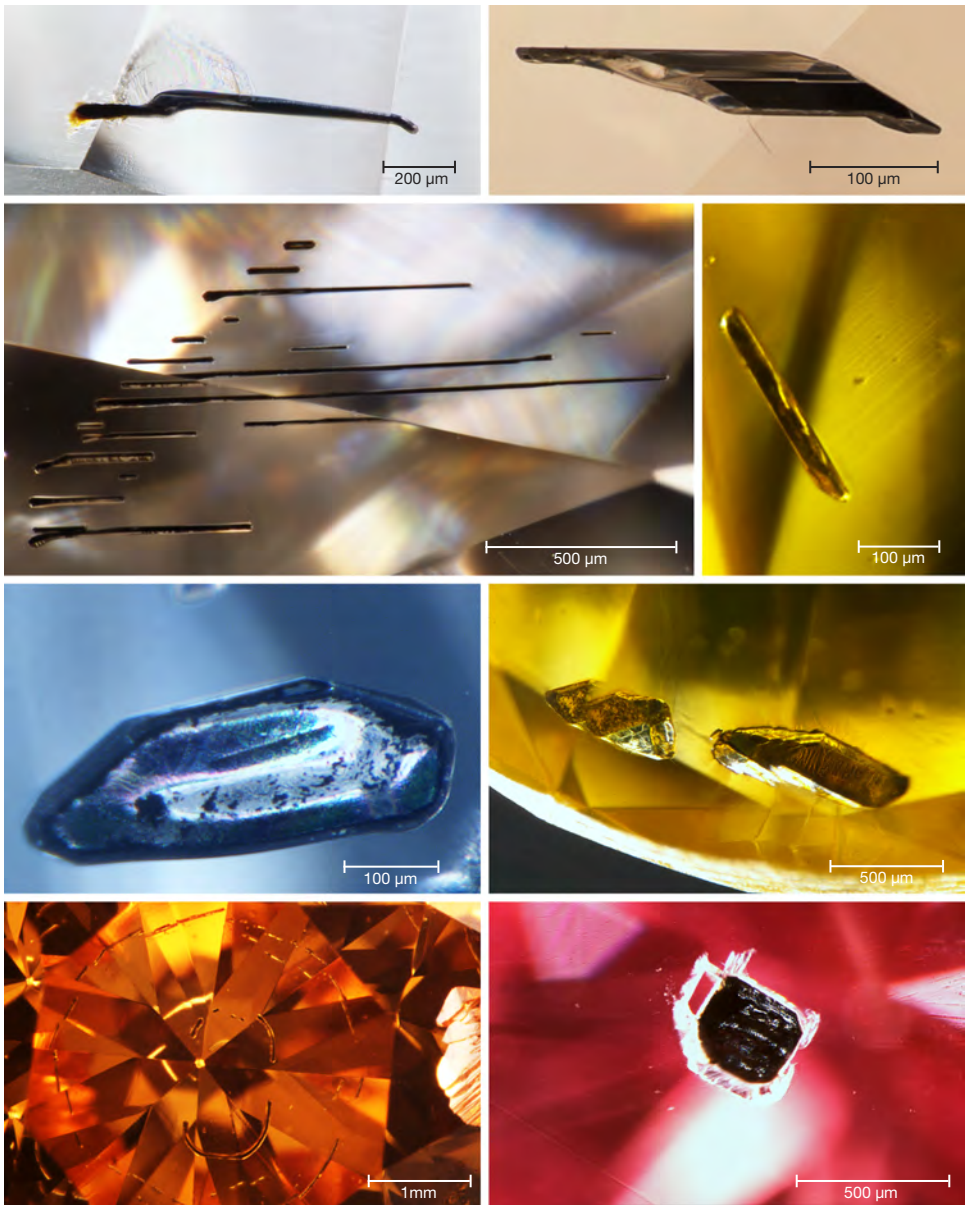

Figure 8. While some HPHT synthetic inclusions appear transparent, most appear to be pieces of dark solidified metal flux. A variety of shapes are possible, including thin rods and irregular shapes, and some are associated with feathers. These metallic inclusions can create a magnetic attraction. Photos by Sally Eaton-Magaña and Troy Ardon.

(across all colors, 74%), while a significantly lower percentage (38%) had no reaction to short-wave UV. While the observed fluorescence intensity was generally greater in response to short-wave rather than long-wave UV, the distribution of fluorescence color was quite similar (figure 9, bottom).

Fancy-Color Material. Among pink to red HPHT synthetics, where the color origin and the fluorescence color are due to the presence of the NV defect centers acquired during post-growth treatment, the majority showed moderate to strong fluorescence, typically with orange or red colors. Only 15% had no reaction to long-wave UV, and all pink HPHT synthetics exhibited an observable reaction to short-wave UV. In comparison, 16% of the natural pink diamonds had no reaction to long-wave UV, and 31% had no reaction to short-wave UV (King et al., 2002). Among those natural diamonds with observed fluorescence, the vast majority gave a blue reaction, while the remainder showed yellow or rarely orange fluorescence. Only a very small percentage (<1%) of natural pink diamonds derive their color from NV centers, and it is this small percentage that showed orange rather than blue fluorescence.

Among yellow to yellow-orange material, the percentage of HPHT synthetics showing a fluorescence reaction to long-wave UV was lower than for short-

Figure 9. Fancy-color and colorless HPHT synthetics had distinctly different fluorescence reactions to long-wave and short-wave UV. Most of the HPHT synthetics showed no reaction to long-wave UV, while a majority showed an observable reaction to short-wave UV. The percentages shown in red represent the portion of samples for which data are available. The plots of fluorescence color only include those samples that had a reaction.

wave. The observed fluorescence colors were typically green to orange. This color range was distinctly different from those observed in natural diamonds, in which the most common color of long-wave fluorescence was blue (92%; King et al., 2005).

Colorless Material. Only 2% of colorless HPHT synthetics showed a fluorescence reaction to long-wave UV. This is a far lower percentage than observed among natural diamonds. Moses et al. (1997) reported that 35% of natural diamonds in the same color

range had detectable long-wave fluorescence, and that 99% of the fluorescence reactions were blue due to the N3 optical defect combined with "band A" luminescence (Zaitsev, 2003). By contrast, the small percentage of HPHT synthetic diamonds with detectable long-wave fluorescence emitted orange and yellow colors.

Meanwhile, a much higher percentage (88%) of colorless HPHT synthetics showed a fluorescence reaction to short-wave UV (figure 9). This reaction is consistent with fancy-color HPHT synthetics (Shigley et al., 2004) and prior observations of colorless HPHT synthetics (D'Haenens-Johansson et al., 2014), and opposite the expected reaction for natural diamonds (Shigley et al., 1993).

Short-Wave UV Phosphorescence. HPHT synthetics in the blue and colorless color ranges often show observable light blue phosphorescence (e.g., D'Haenens-Johansson et al., 2014, 2015) due to boron impurities (Watanabe et al., 1997). Treated and natural blue type IIb diamonds often showed blue phosphorescence as well, though typically weaker (natural type IIb diamonds can also show red phosphorescence; Eaton-Magaña and Lu, 2011). Among the other HPHT synthetic diamond colors, the majority did not exhibit observable phosphorescence. For example, only one of the yellow-orange samples showed phosphorescence (weak orange).

DiamondView Imaging. For the past two decades, the DiamondView fluorescence imaging instrument has been an important diamond identification tool for major gemological laboratories. The design of the sample holder allows diamonds to be positioned and examined in various orientations, and the fluorescence reactions can be observed in real time. The very short wavelength (~225 nm) and high intensity of the UV excitation source creates fluorescence just beneath facet surfaces, producing a distinct reaction. Although most HPHT synthetics show no reaction to a standard long-wave UV light source and many are inert to short-wave UV, *all* diamonds—including all HPHT synthetics—show some observable reaction to the high-intensity, high-energy UV source.

Differences in UV fluorescence colors and patterns provide the basis for DiamondView analysis (Welbourn et al., 1996). Because of their unique growth environment, HPHT synthetics exhibit distinctive fluorescence reactions under the DiamondView.

Growth Features. The growth features of HPHT synthetics are created largely by the prevailing growth chemistry and process conditions that have existed for several decades. In order to lower the temperature and pressure necessary for HPHT growth, as well as the associated expense, manufacturers use a metal catalyst (see "HPHT Synthetic Diamond Growth" above). At these lower temperatures, octahedral growth (as seen in natural diamond crystals) is not observed (Welbourn et al., 1996). Instead, cuboctahedral growth predominates (at even lower temperatures, cube growth would occur). The vast majority of distinctive growth features seen in HPHT synthetics are due to this cuboctahedral arrangement of internal growth sectors, as well as accompanying variations that can occur with different metal catalysts (Welbourn et al., 1996).

The two as-grown HPHT synthetic crystals in figure 10 demonstrate the characteristic external crystal morphology. Their corresponding DiamondView fluorescence images show the different fluorescence reactions along these growth faces. The impurities and defects created in HPHT synthetics can vary greatly depending on the growth face, and these variations

Figure 10. As-grown HPHT crystals show a cuboctahedral growth morphology that is quite distinct from both natural and CVD-grown diamonds. These higher-order growth faces, such as (113), incorporate defects at different concentrations, leading to distinctive fluorescence colors and patterning that arise from the arrangement of internal growth sectors. The distinctive fluorescence reactions in the DiamondView images on the right remain after polishing, proof of HPHT growth. Photos and images by Sally Eaton-Magaña (top row) and GIA staff (bottom row).

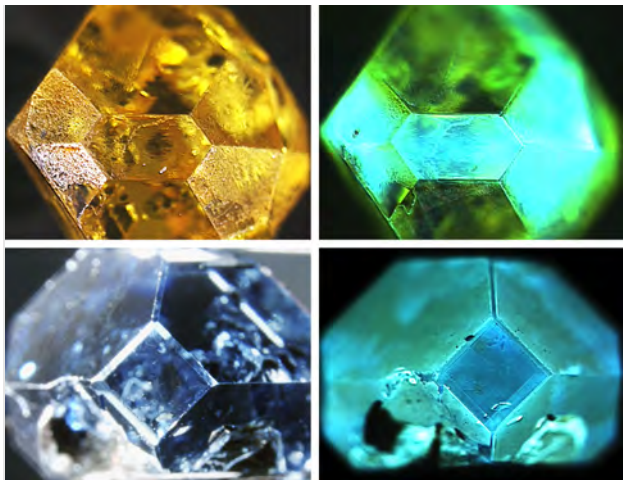

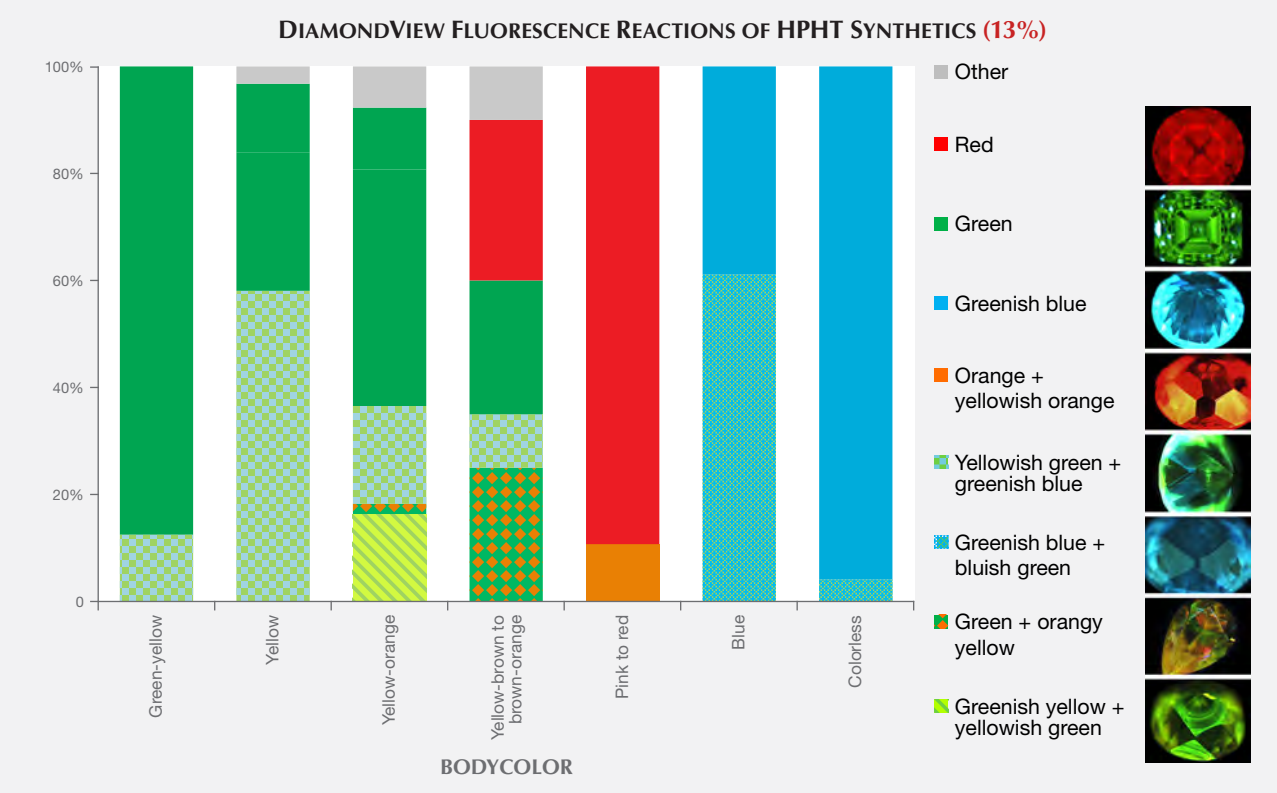

Figure 11. Due to the variety of growth conditions and optical defects among the various colors of HPHT synthetic diamonds—grown with low accidental amounts or deliberately high amounts of nitrogen and/or boron—these samples exhibit a wide variety of DiamondView fluorescence reactions. The distinct internal growth structure seen with the DiamondView is generally diagnostic of HPHT synthesis. Most colorless HPHT synthetics have low but detectable amounts of boron, and DiamondView imaging shows similar colors and phosphorescence properties as blue HPHT synthetics. The percentage shown in red represents the portion of samples for which data are available.

are revealed by the different fluorescence colors. Once an HPHT synthetic is polished, the as-grown morphology can no longer be easily observed unless there is noticeable color zoning. However, the differences in defect chemistry within these growth faces are preserved even in colorless material, with the fluorescence reaction and pattern revealed quite clearly by DiamondView imaging.

Fluorescence Color. With the DiamondView, a wide variety of fluorescence colors can be observed in HPHT synthetics. HPHT synthetics often exhibit more than one fluorescence color (e.g., green and greenish blue in figure 10, top); examples of the fluorescence colors are shown in figure 11.

Fancy-color diamonds generally show a contrast in fluorescence color between the various growth planes. Often the planes reveal two distinct fluorescence colors, or a combination of regions with and without fluorescence. The green fluorescence is ascribed to H3 defects, while the orange to red fluorescence originates from NV centers. The origins of the other fluorescence colors are less understood by scientists. A comparison of these fluorescence colors against other known spectral features did not indicate any compelling correlations.

With colorless HPHT synthetics, the contrast in fluorescence color between growth sectors is much more subtle (D'Haenens-Johansson et al., 2014) and can be difficult for a gemologist to detect even while rotating the sample in the DiamondView. For colorless diamonds in particular, the gemologist must be especially vigilant when looking for growth features in the DiamondView. This reduction in color contrast is due to fewer defects and color-causing impurities in colorless as compared to fancy-color HPHT synthetics. Therefore, the concentration differences of defects between the growth sectors that create the fluorescence will not be as apparent.

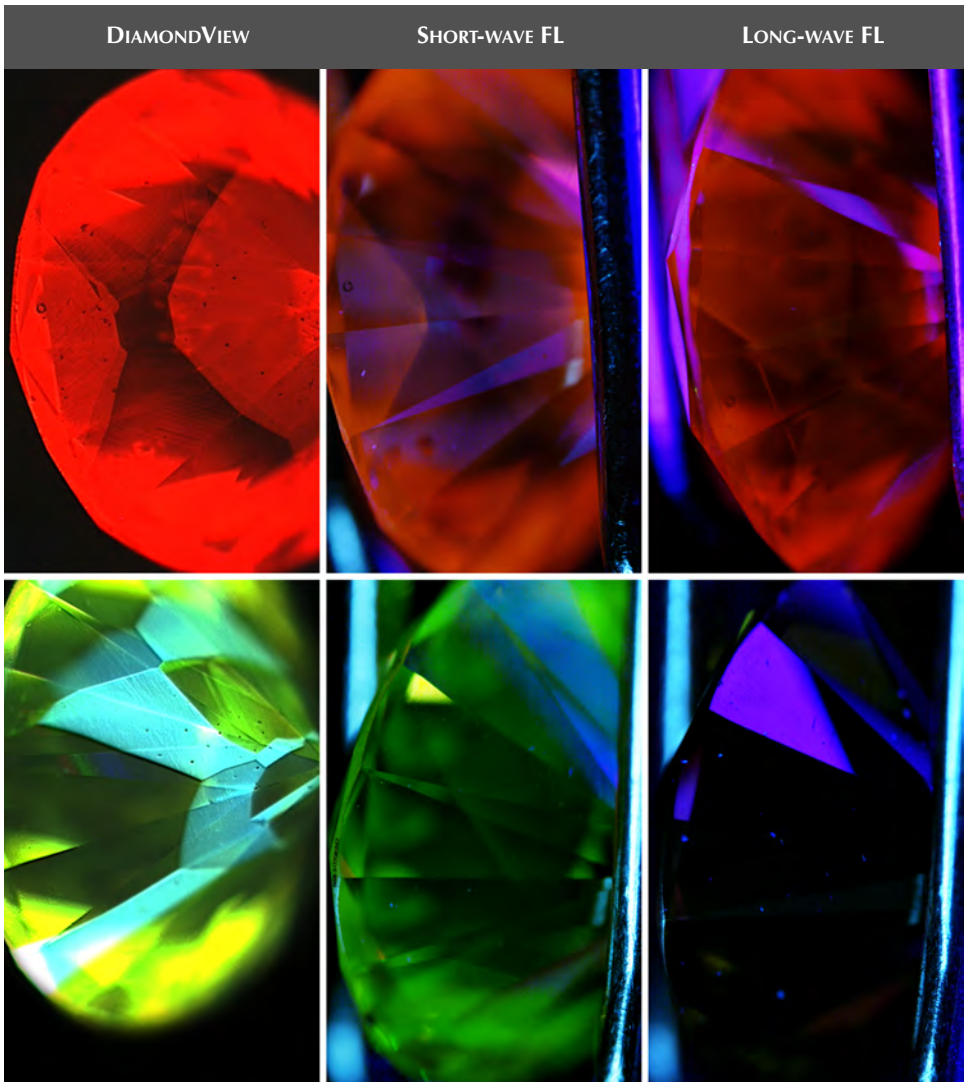

Figure 12. These images show the differences in detail and color contrast when two HPHT synthetics are illuminated by the DiamondView instrument (deep ultraviolet illumination at ~225 nm), short-wave UV (254 nm), and long-wave UV (365 nm). The top series, of a 0.32 ct Fancy Deep pink, shows the ideal case in which HPHT synthetic features are observable with short-wave UV. The bottom series, of a 0.59 ct Fancy Vivid orangy yellow, represents a far more common observation. Besides a difference in fluorescence (FL) intensity between short-wave and long-wave UV, there is no evidence of HPHT growth patterns. For the short-wave and long-wave UV images, purple reflections of the UV source are observed in addition to the diamonds' fluorescence.

DiamondView Reaction Compared with Short-Wave and Long-Wave UV Fluorescence. Figure 12 shows the fluorescence reaction observed for two fancy-color HPHT synthetics. The series in figure 12 (top) clearly indicates the hourglass growth zoning indicative of HPHT synthetic growth when illuminated by the deep ultraviolet (~225 nm) illumination of the DiamondView. Using short-wave UV, the hourglass pattern is still visible, but not as distinct. While the HPHT synthetic exhibits some reaction to long-wave UV, there is no observable pattern.

Far more common among HPHT synthetics is the sample in figure 12 (bottom), in which the DiamondView shows a reaction that is distinctive of HPHT synthetics while the short-wave and long-wave UV fluorescence pattern are not at all diagnostic of HPHT growth. The superior detail and pattern contrast of DiamondView imaging has made the instrument indispensable in gemological laboratories, as the quality of data cannot be matched using short-wave or long-wave UV lamps. Published reports on synthetic diamonds often include fluorescence reactions observed with the DiamondView, so the gemologist should understand that such reactions are less intense and less obvious using a standard long-wave/short-wave UV lamp.

SPECTROSCOPIC PROPERTIES

While HPHT samples have more diagnostic gemological properties than CVD samples (such as color zoning, lack of strain, and magnetism; see box A), the absence of these properties does not conclusively identify a diamond as natural. Spectroscopic techniques are essential to verify the growth origin of *all* diamonds. Among the samples identified as potential HPHT synthetics, a combination of features in

Fourier-transform infrared absorption (FTIR), visible/near-infrared (Vis-NIR) absorption, and photoluminescence (PL) spectroscopy will confirm the determination. Therefore, positive detection of HPHT synthetics is best accomplished by a major gemological laboratory that maintains a database of known natural, treated, and synthetic diamonds and sees a sufficient quantity of goods to spot emerging trends.

Infrared (IR) Absorption Spectroscopy. In colorless diamonds, IR absorption spectroscopy is most useful in separating type Ia, which represents the vast majority of natural diamonds, from diamonds that do not contain aggregated nitrogen (Breeding and Shigley, 2009). This is the basis of GIA's DiamondCheck instrument. This distinction is important in colorless diamonds, as only those without detectable aggregated nitrogen are identified as potentially treated or synthetic.

Among fancy-color HPHT synthetics, either with as-grown yellow-to-green or treated pink colors, IR absorption spectra display the 1344 cm^{-1} peak. This feature indicates the presence of single substitutional nitrogen (i.e., type Ib diamond) and shows that the diamond is potentially quite young in geologic terms. While some natural diamonds can also be type Ib, this peak is a good indicator of potential HPHT synthetic origin, as young diamonds contain only isolated nitrogen. In natural stones, over the millions of years that diamonds reside at higher temperatures in the earth, these isolated nitrogen atoms randomly migrate within the diamond lattice (figure 13) and inevitably find another nitrogen defect to form what are called nitrogen aggregates. The A aggregate (a pair of substitutional nitrogen atoms in adjacent lattice sites) can also combine to form the B aggregate (four nitrogen atoms surrounding a vacant atom position in the lattice). While this aggregation process can be duplicated to some extent in the laboratory using high temperature instead of millions of years, there are differences. For example, the isolated nitrogen indicated by the 1344 cm^{-1} peak will never be completely eliminated using high-temperature treatment, and this feature will still be detected by IR spectroscopy (Dobrinets et al., 2013). Among natural diamonds, the aggregation process over long periods of geologic time removes nearly all isolated nitrogen so that the distinct infrared spectral feature cannot be detected in most natural diamonds.

Many of our HPHT synthetic samples showed, based on their infrared spectra, a pure type Ib character (i.e., only isolated nitrogen), while others exhibited a combination of type IaA (due to heating, which created some aggregated nitrogen) and type Ib (figure 14). Whether the manufacturers are creating A aggregates by maintaining the chamber at high temperature during the growth process or by subjecting the diamonds to post-growth treatment to enhance nitrogen aggregation is not entirely clear.

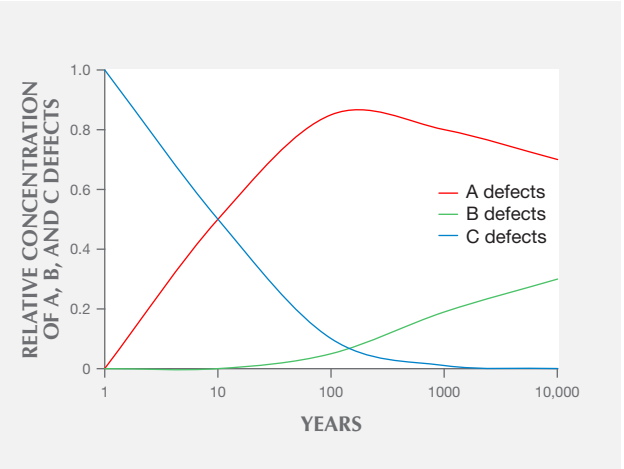

Figure 13. Isolated nitrogen (C defects) decrease as they are converted into aggregated nitrogen (A and B centers) while at temperatures of 800–1400°C within the earth. After Dobrinets et al. (2013), figure 9.2, p. 235. In contrast, young diamonds such as HPHT synthetics have very low nitrogen aggregation.

Blue HPHT synthetics (along with a majority of colorless HPHT samples) were type IIb, indicating either intentional doping or accidental contamination with boron in the growth chamber. Figure 15 shows the distribution of diamond types among HPHT synthetics based on bodycolor. Those with yellow color were predominantly type Ib or a combination of type Ib and type IaA. The blue synthetics were exclusively type IIb. Colorless HPHT synthetics were type IIa or, more commonly, type IIb (where the amount of boron was insufficient to produce any blue coloration). The post-growth treated pinks were type IIa or type Ib, but with very low nitrogen concentrations.

As mentioned previously when discussing color differences in the DiamondView imaging and with color zoning, defect incorporation among the various internal growth sectors of HPHT synthetics can be quite variable. Therefore, boron and isolated nitrogen concentrations are not uniformly distributed throughout. IR absorption spectroscopy on faceted stones generally samples most of the volume of the crystal or cut stone, and the resulting spectra reflect

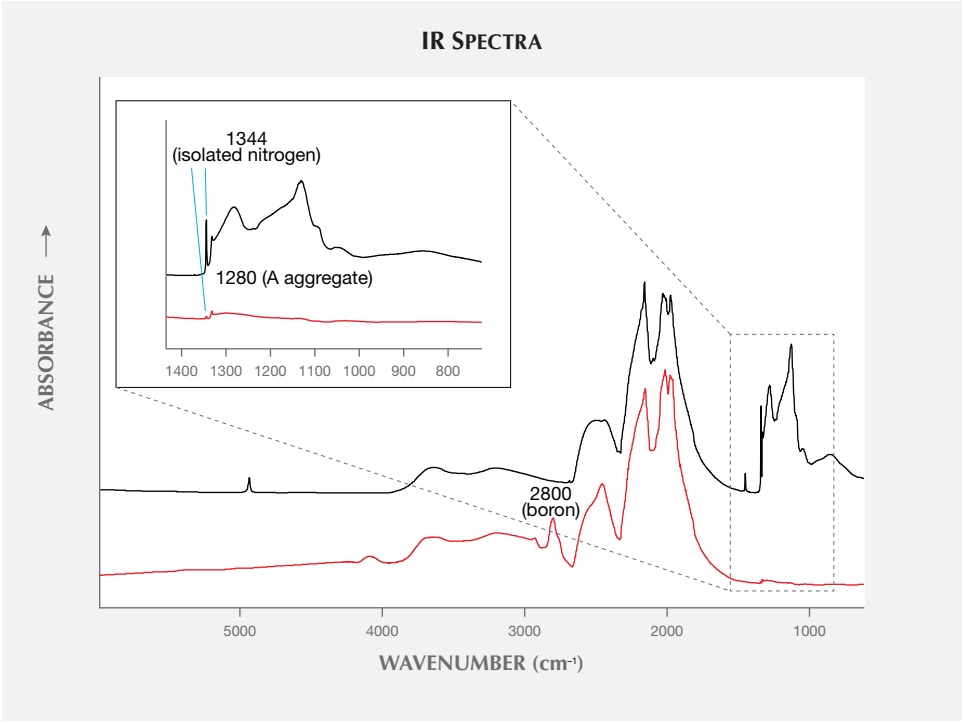

Figure 14. Infrared spectra for two HPHT synthetics. The black trace is the IR spectrum of an HPHT synthetic with type IaA (1280 cm^{-1}) + type Ib components (1344 cm^{-1}). It is a 0.34 ct Fancy brown-red with 220 ppma of isolated nitrogen and 60 ppma of nitrogen A aggregates. The red trace is an IR spectrum of a Fancy light greenish yellow HPHT synthetic with type IIb (95 ppb uncompensated boron; 2800 cm^{-1}) + type Ib (2 ppm isolated nitrogen; 1344 cm^{-1}) components. These spectra show the range in diamond types and nitrogen concentration in HPHT synthetics. The absorption feature between 2700 and 1550 cm^{-1} is principally intrinsic to diamond.

an average concentration across the bulk of the diamond. With that caveat in mind, the electrically uncompensated boron concentration detected by IR absorption (B^0) and the isolated nitrogen concentration (Ns) were calculated from 160 randomly chosen type IIb HPHT synthetics and 180 type Ib (or type IaA + type Ib) HPHT synthetics. The concentration for B^0 was calculated from a method after Collins and Williams (1971) and Fisher et al. (2009), or alternatively Collins (2010). Ns was calculated from a procedure described by Kiflawi (1994). These concentration values are shown in figure 16.

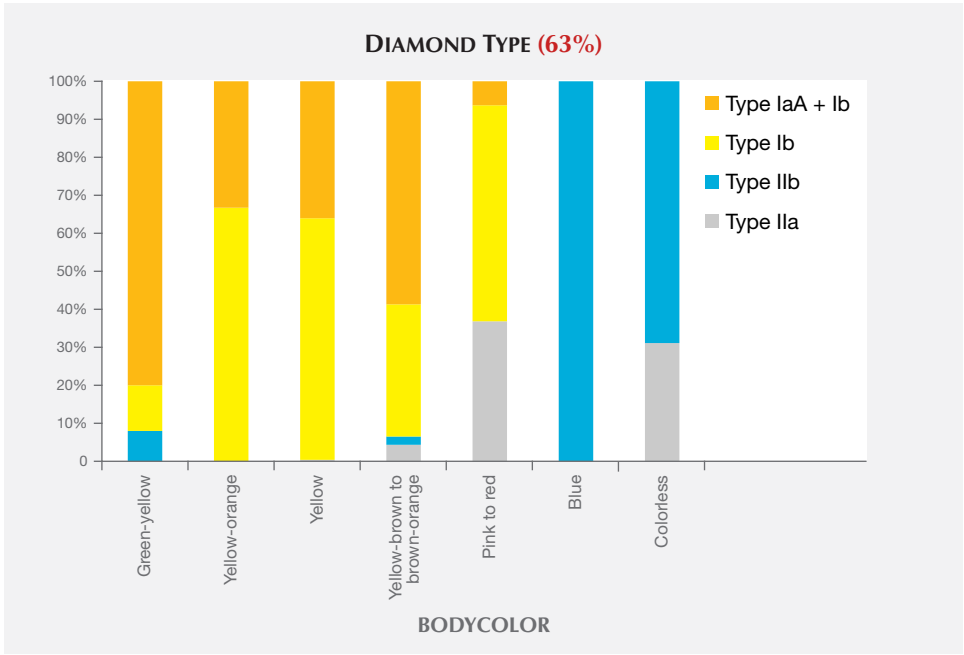

Figure 15. HPHT synthetics span four diamond type combinations: type IIa, type IIb, type Ib, and mixed type IaA + Ib. Those with yellow coloration were predominantly type Ib or mixed type IaA + Ib. Colorless diamonds were either type IIa or had a comparatively low boron concentration and were type IIb. All blue diamonds were type IIb. Pink to red synthetics get their color from post-growth treatment; while most were type Ib, the nitrogen concentration was low (see figure 16, right). The percentage shown in red represents the portion of samples for which data were used.

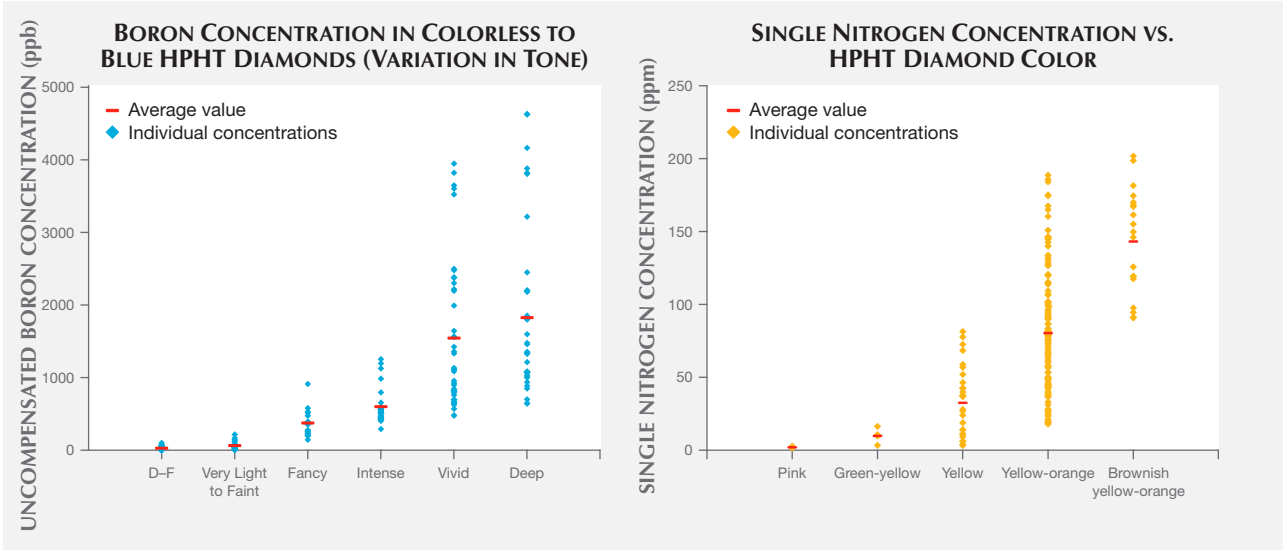

Figure 16. Absolute concentrations for uncompensated boron concentration in type IIb synthetics (left; provided as ppb, parts per billion) and isolated nitrogen concentration in type Ib synthetics (right; provided as ppm, parts per million) were calculated. Increasing the boron concentration in type IIb synthetics predictably increased the depth of color, with Fancy Deep blue synthetics having the highest values. Among the type Ib diamonds, the depth of yellow to orange color increased with nitrogen concentration.

The measured boron concentrations spanned a wide range of values. Figure 16 (left) shows the calculated values for the uncompensated boron concentration, B^0, in colorless HPHT synthetics and in fancy-color blues as the tone increases left to right, from Very Light up to Fancy Deep. In several cases for the Fancy Vivid and Fancy Deep samples, the boron-related feature at 2800 cm^{-1} in the IR spectrum was saturated (i.e., the peak height was beyond the vertical scale of the graph) and could not be calculated with this method and an alternate correlation was performed using the feature at 1290 cm^{-1} (Collins, 2010). The D–F colorless HPHT synthetics had the lowest boron concentrations, with the Very Light to Fancy Light blue samples encompassing a slightly higher range. The highest measured concentration was 4627 ppb, which is comparable to a value calculated for a natural type IIb diamond with very high boron (Johnson and Wang, 2015).

Figure 16 (right) shows the spread of values for the isolated nitrogen concentration for type Ib HPHT synthetics of various colors. The pinks and green-yellows had the lowest nitrogen concentrations, followed by yellow, yellow-orange, and brownish yellow-orange samples. In the early years of production in the 1980s and 1990s, most HPHT synthetics were yellow-orange, likely due to a high nitrogen concentration, which growers were not able to reduce or eliminate as effectively at the time. As the incorporation of isolated nitrogen became better controlled over the years, the orange coloration was reduced. Therefore, the manufacturers could more consistently produce HPHT synthetics with lower quantities of nitrogen, allowing a wider variety of colors and the production of more saleable stones. For example, the pink synthetics look more appealing when starting with an HPHT synthetic that has low, rather than high, concentrations of nitrogen (Shigley et al., 2004).

Vis-NIR Spectroscopy. For many of the fancy-color HPHT synthetics, the broadband absorptions observed in the visible/near-infrared spectra resemble those of their natural diamond counterparts. This similarity illustrates the need for multiple spectroscopic techniques and gemological observations to confirm an identification result. Spectra for blue and most yellow to yellow-orange HPHT samples are indistinguishable from natural diamond spectra. The Vis-NIR spectra of pink to red diamonds indicate the treatment history of irradiation and annealing that created the pink color rather than the synthetic origin (figure 17). For most colors of HPHT synthetics, a small percentage of the samples showed spectral peaks associated with the metal catalyst, mostly nickel (figure 17; Zaitsev, 2003).

Yellow-orange HPHT synthetics comprise a majority of the samples examined by GIA to date. These

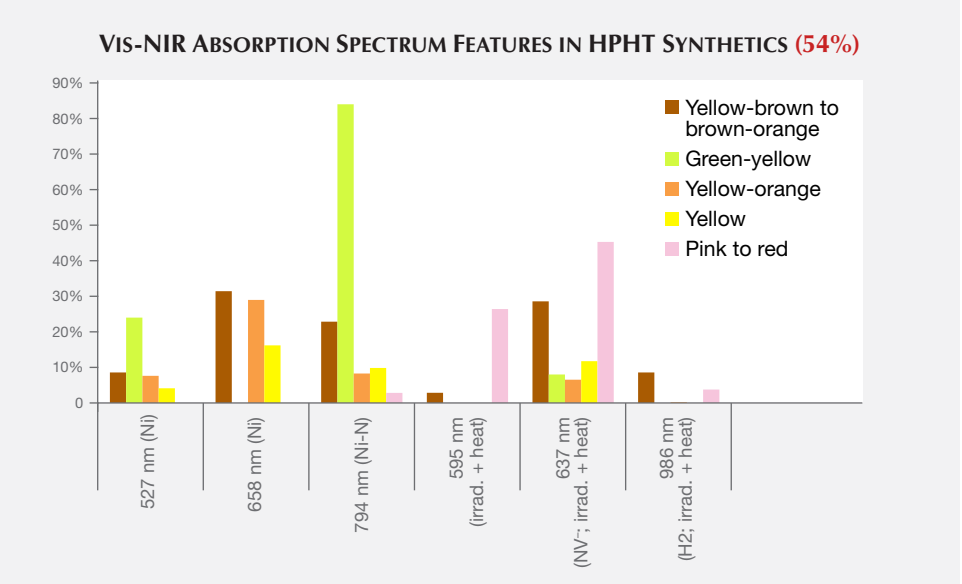

Figure 17. The major features seen in the Vis-NIR absorption spectra are shown for HPHT synthetics, grouped by color. These peaks were ascribed to nickel incorporation from the catalyst, nitrogen-related defects due to a high concentration of nitrogen, or post-growth treatment that increased these specific nitrogen defect complexes (Zaitsev, 2003). The percentage value shown in red represents the portion of samples for which data were used.

include samples with color grades in order of increasing orange contribution: orangy yellow, orange-yellow, yellow-orange, and yellowish orange. To examine whether the differences in color grade between these "yellow-orange" HPHT synthetics and the pure yellow samples could be detected in the Vis-NIR spectra, we plotted 25 randomly selected yellow HPHT synthetics and 25 yellowish orange HPHT synthetics (figure 18). In these spectra, there was little difference in the absorption between the yellow and the yellowish orange synthetics at wavelengths greater than 600 nm. Below 600 nm, however, the onset of increased absorption occurs at longer wavelengths in yellowish orange synthetics. In other words, the portion of the graph showing increased absorption is shifted toward longer wavelength values for the yellowish orange samples, pushing the transmission window closer to the orange region. This absorption increase at longer wavelengths among the yellowish orange samples is due to greater nitrogen absorption within the UV range and consistent with IR calculations for the isolated nitrogen shown in figure 16 (up to 100 ppm N in yellow samples, and up to 200 ppm N in yellow-orange samples). As the HPHT synthetic process improved and less nitrogen was incorporated, the nitrogen-related absorption decreased as well.

Photoluminescence (PL) Spectroscopy. PL spectroscopy is a very sensitive analytical technique that can detect light emission from optical defects at much lower concentrations than absorption spectroscopy. The PL method, where spectral features are excited by incident laser light of specific wavelengths, is therefore capable of detecting optical centers in diamond when Vis-NIR and IR absorption cannot. PL spectroscopy is a vital technique for gemological laboratories in determining diamond origin and color origin, and HPHT synthetics are no exception.

PL spectra features for HPHT synthetics were predominantly nitrogen (H3, NV^0, NV^-, and H2) and nickel defect-related (658, 696, 794, and 883/884 nm; Zaitsev, 2003; figure 19). While nickel was present in

Figure 18. The Vis-NIR spectra of 25 yellow and 25 yellowish orange synthetics are compared to show a shift in the nitrogen-related absorption edge at ~520 nm, the cause of their color differences. This shift to higher wavelengths is caused by a higher isolated nitrogen concentration in the yellowish orange HPHT synthetics.

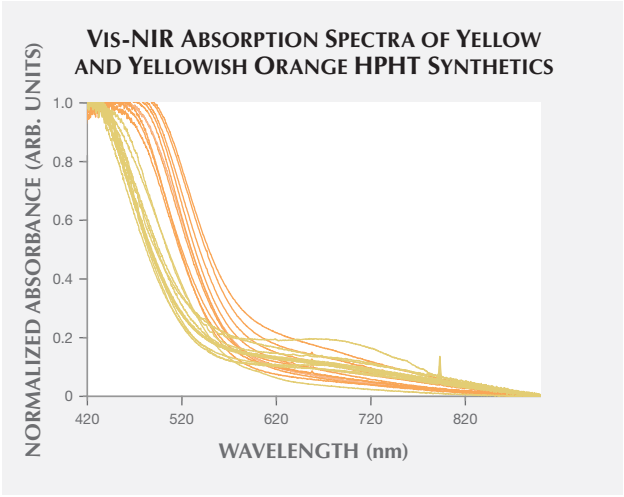

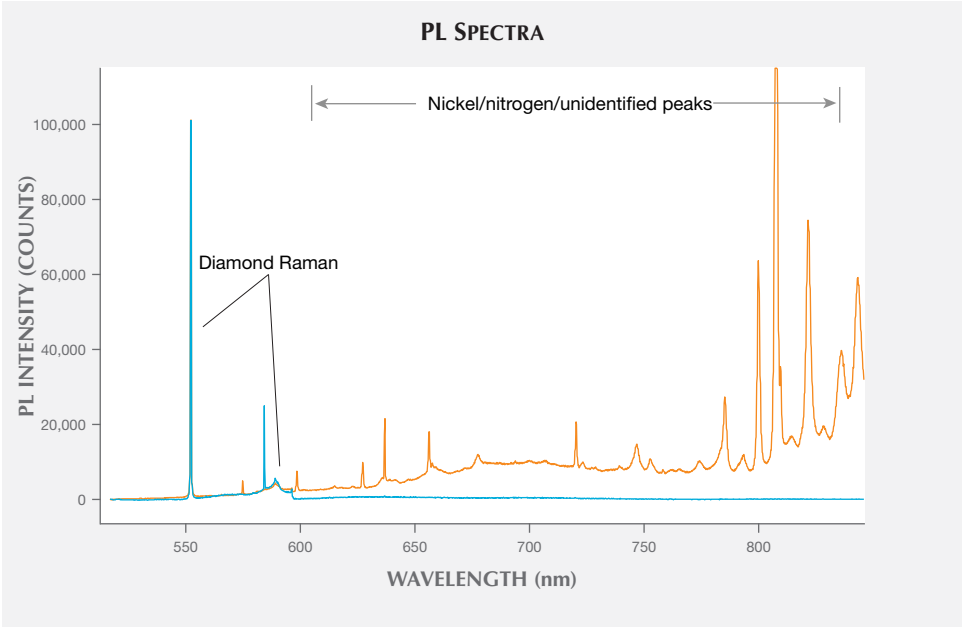

Figure 19. These PL spectra were recorded using 514 nm excitation with the first-order Raman intensities in each spectrum scaled to be equal. The blue trace is for a 0.71 ct type IIb Fancy blue HPHT synthetic; it did not contain any peaks besides intrinsic diamond-related peaks in the PL spectra using 488, 514, and 830 nm excitation. The orange trace represents a 0.45 ct Fancy Deep brownish orangy yellow diamond showing a variety of peaks, including nitrogen- and nickel-related defects.

a notable percentage of the synthetics—the 794 nm peak was detected in 83% of the tested yellow-orange HPHT synthetics, while the 883/884 nm doublet was present in 30% of the colorless and 8% of the blues—it was not found in all synthetics and is not a reliable indicator (figure 20). It is occasionally observed in the luminescence spectra of natural diamonds (Lang et al., 2004; Eaton-Magaña et al., 2016). Not surprisingly, the

Figure 20. The major features seen in the PL spectra of HPHT synthetics, grouped by color. These peaks were either ascribed to nickel incorporation due to the catalyst, nitrogen-related defects due to a high concentration of nitrogen, or post-growth treatment that increased these specific nitrogen complexes. A sizeable portion of the blue and colorless synthetics were featureless, besides their intrinsic diamond peaks, using 488, 514, or 830 nm laser excitation. The percentage value shown in red represents the portion of samples for which data were used.

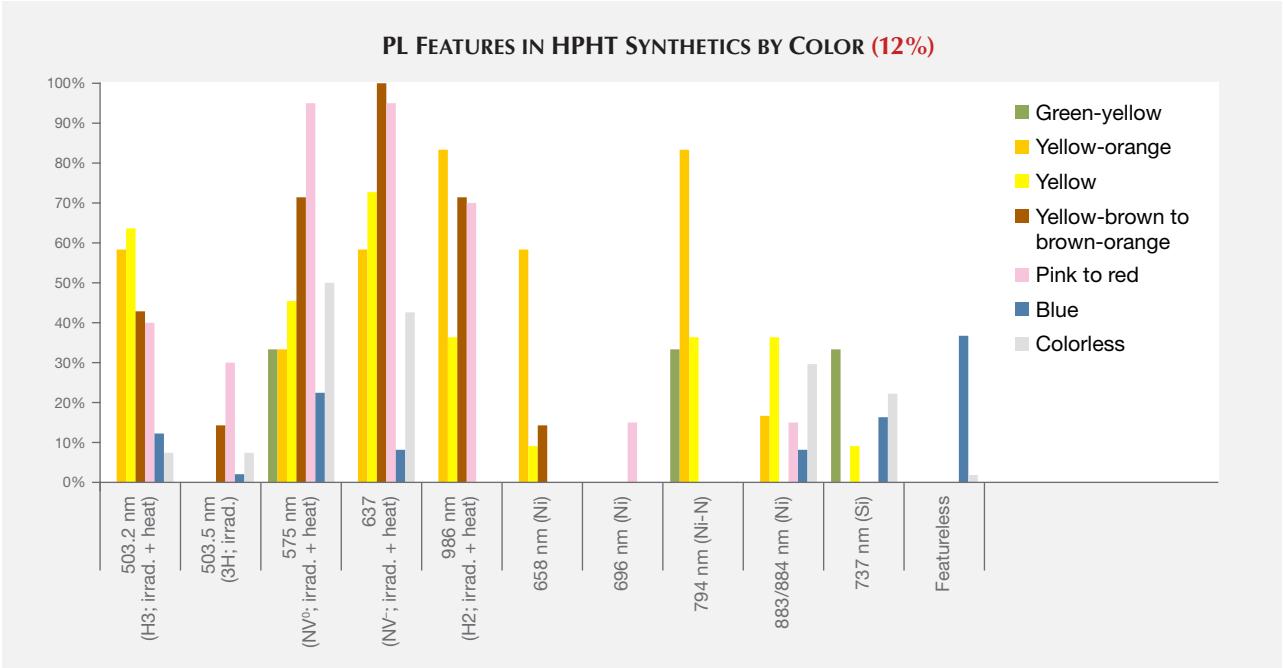

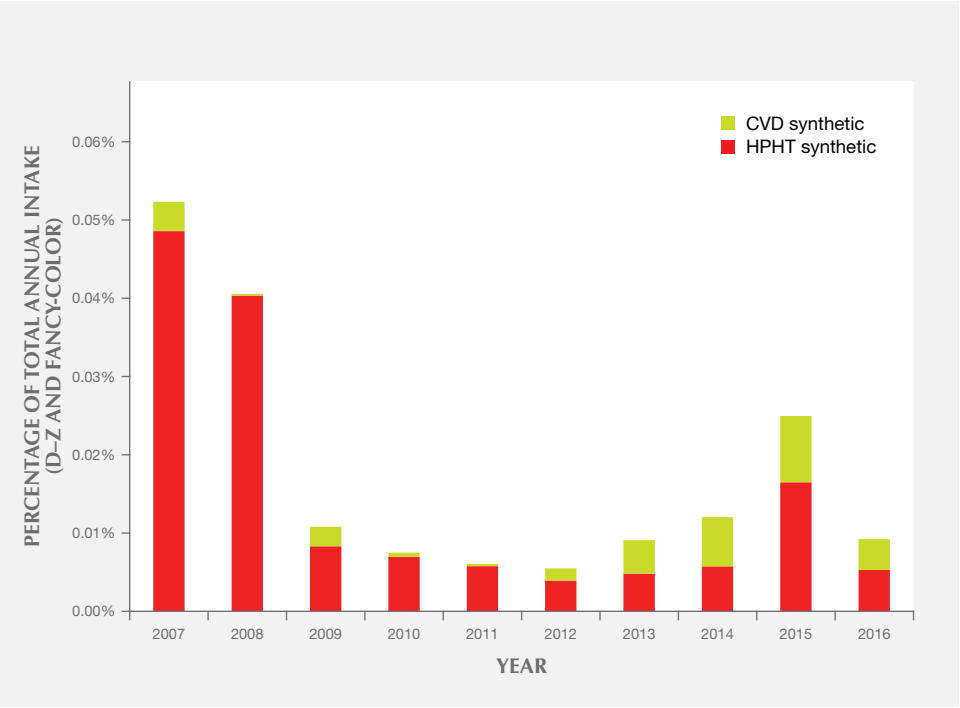

Figure 21. This plot shows the distribution of CVD and HPHT synthetics among all diamonds submitted to GIA for grading. Compared to natural diamonds, the percentage of synthetic diamonds overall is very small. The higher percentages in 2007–2008 are due to the introduction of the GIA Synthetic Diamond Grading Report in early 2007. During this period, GIA received submissions of synthetic diamonds that had been manufactured over the course of many years.

HPHT synthetics with yellow coloration (including yellow, yellow-orange, and yellow-brown) had high percentages of nitrogen-related defects. Pink synthetics, while generally having a lower nitrogen concentration than the yellow synthetics, undergo post-growth coloration treatment that increases the concentration of these nitrogen-related PL defects.

There were also some spectral peaks we were unable to identify (e.g., 536, 707, 712, 912, and 953 nm; not shown), which could also correspond to nitrogen or nickel-related defects or be related to other metal catalysts or other impurities within the source materials. Also present in samples of various colors was the silicon-related defect, SiV^- (737 nm; D'Haenens-Johansson et al., 2011). A significant portion of the type IIb diamonds (37%) were entirely featureless by PL spectroscopy (figure 20). Several PL features, such as 3H and peaks at 648.2 and 776.4 nm, are regularly detected in natural type IIb diamonds, yet these peaks are not observed in type IIb HPHT synthetics due to the features' low thermal stability (Eaton-Magaña and Ardon, 2016).

FUTURE

Figure 21 shows the percentages of CVD and HPHT synthetics out of the total annual intake of D–Z and fancy-color diamonds submitted to GIA's laboratory. The overall percentages are quite small—around 0.01% in most years. The volume of synthetics was highest in 2007–2008, the first two years after the introduction of GIA's Synthetic Diamond Grading Report, as many years of prior synthetic production were submitted. As mentioned in the Eaton-Magaña and Shigley (2016) survey of CVD synthetics, we expect that the number of HPHT synthetic diamonds submitted will continue to increase, especially at the extreme ends of the weight scale—both melee-sized and greater than 4 carats. Improvements in growth processes are making it easier to grow a large quantity of colorless melee synthetics, or to maintain growth over a long enough period to produce larger crystals.

We predict that in the coming years most HPHT synthetics will be blue or colorless, with fancy pink and fancy yellow colors available but to a lesser extent. Yellow-orange will still be submitted to GIA but in small numbers. There is already an abundance of yellow-orange HPHT synthetics, and these will be an important part of the market for many years. Other interesting products have recently been seen in GIA laboratories, such as an attractive Fancy Deep green HPHT synthetic colored by massive amounts of nickel impurities (Johnson et al., 2017). Quality factors such as carat weight, cut grade of round brilliants, and clarity will likely continue to improve over the coming years.

CONCLUSION

Today the HPHT growth process is used to produce colorless or fancy-color synthetic diamonds with high clarity. In recent years, extremes in carat weight—both melee (again, see box B) and larger sizes greater than four carats—have attracted the most attention and made the greatest strides. As growth processes continue to improve, clarity will likely improve, color zoning within fancy-color diamonds will become less noticeable, and the resulting synthetics will likely be visually less distinguishable from polished natural diamonds. Nevertheless, these HPHT synthetics display ultraviolet fluorescence reactions and inclusion features that are unusual in natural diamonds. The results described in this article illustrate how these samples all exhibit spectroscopy features that are quite different from those found in comparable natural diamonds. Based on the use of analytical instruments and access to our large database of gemological information, the synthetic diamonds examined to date by GIA can be readily identified.

ABOUT THE AUTHORS

Dr. Eaton-Magaña and Dr. Breeding are senior research scientists, and Dr. Shigley is a distinguished research fellow, at GIA in Carlsbad, California.

REFERENCES

Ardon T., Batin R. (2016) Lab Notes: HPHT-grown synthetic with strain. *G&G*, Vol. 52, No. 4, pp. 417–418.

Bovenkerk H.P., Bundy F.P., Hall H.T., Strong H.M., Wentorf R.H. (1959) Preparation of diamond. *Nature*, Vol. 194, No. 4693, pp. 1094–1098, http://dx.doi.org/10.1038/1841094a0

Boyd S.R., Kiflawi I., Woods G.S. (1994) The relationship between infrared absorption and the A defect concentration in diamond. *Philosophical Magazine Part B*, Vol. 69, No. 6, pp. 1149–1153, http://dx.doi.org/10.1080/01418639408240185

——— (1995) Infrared absorption by the B nitrogen aggregate in diamond. *Philosophical Magazine Part B*, Vol. 72, No. 3, pp. 351–361, http://dx.doi.org/10.1080/13642819508239089

Breeding C.M., Shigley J.E. (2009) The "type" classification system of diamonds and its importance in gemology. *G&G*, Vol. 45, No. 2, pp. 96–111, http://dx.doi.org/10.5741/GEMS.45.2.96

Collins A.T. (2010) Determination of the boron concentration in diamond using optical spectroscopy. *Proceedings of the 61st Diamond Conference*, Warwick, UK.

Collins A.T., Williams A.W.S. (1971) The nature of the acceptor centre in semiconducting diamond. *Journal of Physics C: Solid State Physics*, Vol. 4, No. 13, pp. 1789–1800, http://dx.doi.org/10.1088/0022-3719/4/13/030

Deljanin B., Alessandri M., Peretti A., Åström M. (2015) NDT breaking the 10 carat barrier: World record faceted and gem-quality synthetic diamonds investigated. *Contributions to Gemology*, No. 15, pp. 1–7.

D'Haenens-Johansson U.F.S., Edmonds A.M., Green B.L., Newton M.E., Davies G., Martineau P.M., Khan R.U.A., Twitchen D.J. (2011) Optical properties of the silicon split-vacancy center in diamond. *Physical Review B*, Vol. 84 No. 24, pp. 245208-1–245208-14, http://dx.doi.org/10.1103/PhysRevB.84.245208

D'Haenens-Johansson U.F.S., Moe K.S., Johnson P., Wong S.Y., Lu R., Wang W. (2014) Near-colorless HPHT synthetic diamonds from AOTC Group. *G&G*, Vol. 50, No. 1, pp. 30–45, http://dx.doi.org/10.5741/GEMS.50.1.30

D'Haenens-Johansson U.F.S., Katrusha A., Moe K.S., Johnson P., Wang W. (2015) Large colorless HPHT-grown synthetic gem diamonds from New Diamond Technology, Russia. *G&G*, Vol. 51, No. 3, pp. 260–279, http://dx.doi.org/10.5741/GEMS.51.3.260

Dobrinets I.A., Vins V.G., Zaitsev A.M. (2013) *HPHT-Treated Diamonds: Diamonds Forever*. Springer, Heidelberg, Germany.

Eaton-Magaña S., Lu R. (2011) Phosphorescence in type IIb diamonds. *Diamond and Related Materials*, Vol. 20, No. 7, pp. 983–989, http://dx.doi.org/10.1016/j.diamond.2011.05.007

Eaton-Magaña S., Ardon T. (2016) Temperature effects on luminescence centers in natural type IIb diamonds. *Diamond and Related Materials*, Vol. 69, pp. 86–95, http://dx.doi.org/10.1016/j.diamond.2016.07.002

Eaton-Magaña S., Shigley J. (2016) Observations on CVD-grown synthetic diamonds: A review. *G&G*, Vol. 52, No. 3, pp. 222–245, http://dx.doi.org/10.5741/GEMS.52.3.222

Eaton-Magaña S., Ardon T., Zaitsev A.M. (2017) Inclusion and point defect characteristics of Marange graphite-bearing diamonds after high temperature annealing. *Diamond and Related Materials*, Vol. 71, pp. 20–29, http://dx.doi.org/10.1016/j.diamond.2016.11.011

Fisher D., Sibley S.J., Kelly C.J. (2009) Brown colour in natural diamond and interaction between the brown related and other colour-inducing defects. *Journal of Physics: Condensed Matter*, Vol. 21, No. 36, Article 364213, 10 pp., http://dx.doi.org/10.1088/0953-8984/21/36/364213

Gaillou E., Post J.E., Rost D., Butler J.E. (2012) Boron in natural type IIb blue diamonds: Chemical and spectroscopic measurements. *American Mineralogist*, Vol. 97, No. 1, pp. 1–18, http://dx.doi.org/10.2138/am.2012.3925

Hainschwang T., Notari, F., Vadaski E. (2014) The Rhodesian Star: An exceptional asteriated diamond. *Journal of Gemmology*, Vol. 34, No. 4, pp. 306–315.

Johnson P., Myagkaya E. (2017) Lab Notes: HPHT synthetic diamond with intense green color. *G&G*, Vol. 53, No. 1, pp. 96–98.

Johnson P., Wang W. (2015) Lab Notes: Intense blue diamond with very high boron concentration. *G&G*, Vol. 51, No. 2, pp. 176–177.

Kiflawi I., Mayer A.E., Spear P.M., van Wyk J.A., Woods G.S. (1994) Infrared absorption by the single nitrogen and A defect centres in diamond. *Philosophical Magazine Part B*, Vol. 69, No. 6, pp.

1141–1147, http://dx.doi.org/10.1080/01418639408240184
King J.M., Shigley J.E., Guhin S.S., Gelb T.H., Hall M. (2002) Characterization and grading of natural-color pink diamonds. *G&G*, Vol. 38, No. 2, pp. 128–147, http://dx.doi.org/10.5741/GEMS.38.2.128
King J.M., Shigley J.E., Gelb T.H., Guhin S.S., Hall M., Wang W. (2005) Characterization and grading of natural-color yellow diamonds. *G&G*, Vol. 41, No. 2, pp. 88–115, http://dx.doi.org/10.5741/GEMS.41.2.88
Kitawaki H., Abduriyim A., Okano M. (2008) Identification of melee-size synthetic yellow diamonds in jewelry. *G&G*, Vol. 44, No. 3, pp. 202–213, http://dx.doi.org/10.5741/GEMS.44.3.202
Klein P.B., Crossfield M.D., Freitas J.A., Collins A.T. (1995) Donor-acceptor pair recombination in synthetic type-IIb semiconducting diamond. *Physical Review B*, Vol. 51, No. 15, pp. 9634–9642, http://dx.doi.org/10.1103/PhysRevB.51.9634
Lang A.R., Yelisseyev A.P., Pokhilenko N.P., Steeds J.W., Wotherspoon A. (2004) Is dispersed nickel in natural diamonds associated with cuboid growth sectors in diamonds that exhibit a history of mixed-habit growth? *Journal of Crystal Growth*, Vol. 263, No. 1–4, pp. 575–589, http://dx.doi.org/10.1016/j.jcrysgro.2003.11.116
Moses T.M., Reinitz I.M., Johnson M.L., King J.M., Shigley J.E. (1997) A contribution to understanding the effect of blue fluorescence on the appearance of diamonds. *G&G*, Vol. 33, No. 4, pp. 244–259, http://dx.doi.org/10.5741/GEMS.33.4.244
Shigley J.E. (2008) A review of current challenges for the identification of gemstones. *Geologija*, Vol. 50, No. 4, pp. 227–236.
Shigley J.E., Fritsch E., Koivula J.I., Sobolev N.V., Malinovsky I.Y., Pal'yanov Y.N. (1993) The gemological properties of Russian gem-quality synthetic diamonds. *G&G*, Vol. 29, No. 4, pp. 228–248, http://dx.doi.org/10.5741/GEMS.29.4.228
Shigley J.E., Moses T.M., Reinitz I., Elen S., McClure S.F., Fritsch E. (1997) Gemological properties of near-colorless synthetic diamonds. *G&G*, Vol. 33, No. 1, pp. 42–53, http://dx.doi.org/10.5741/GEMS.33.1.42
Shigley J.E., Abbaschian R., Clarke C. (2002) Gemesis laboratory-created diamonds. *G&G*, Vol. 38, No. 4, pp. 301–309, http://dx.doi.org/10.5741/GEMS.38.4.301
Shigley J.E., McClure S.F., Breeding C.M., Shen A.H.-T., Muhlmeister S.M. (2004) Lab-grown colored diamonds from Chatham Created Gems. *G&G*, Vol. 40, No. 2, pp. 128–145, http://dx.doi.org/10.5741/GEMS.40.2.128
Shirey S.B., Shigley J.E. (2013) Recent advances in understanding the geology of diamonds. *G&G*, Vol. 49, No. 4, pp. 188–222, http://dx.doi.org/10.5741/GEMS.49.4.188
Smith E.M., Shirey S.B., Nestola F., Bullock E.S., Wang J., Richardson S.H., Wang W. (2016) Large gem diamonds from metallic liquid in Earth's deep mantle. *Science*, Vol. 354, No. 6318, pp. 1403–1405, http://dx.doi.org/10.1126/science.aal1303
Soonthorntantikul W., Siritheerakul P. (2015) Lab Notes: Near-colorless melee-sized HPHT synthetic diamonds identified in GIA laboratory. *G&G*, Vol. 51, No. 2, pp. 183–184.
Sumiya H., Satoh S. (1996) High-pressure synthesis of high-purity diamond crystal. *Diamond and Related Materials*, Vol. 5, No. 11, pp. 1359–1365, http://dx.doi.org/10.1016/0925-9635(96)00559-6
Wang W., Poon T. (2016) Lab Notes: Large blue and colorless HPHT synthetic diamonds. *G&G*, Vol. 52, No. 2, pp. 195–196.
Watanabe K., Lawson S.C., Isoya J., Kanda H., Sato Y. (1997) Phosphorescence in high-pressure synthetic diamond. *Diamond and Related Materials*, Vol. 6, No. 1, pp. 99–106, http://dx.doi.org/10.1016/S0925-9635(96)00764-9
Welbourn C.M., Cooper M., Spear P.M. (1996) De Beers natural versus synthetic diamond verification instruments. *G&G*, Vol. 32, No. 3, pp. 156–169, http://dx.doi.org/10.5741/GEMS.32.3.156
Yelisseyev A., Babich Y., Nadolinny V., Fisher D., Feigelson B. (2002) Spectroscopic study of HPHT synthetic diamonds, as grown at 1500°C. *Diamond and Related Materials*, Vol. 11, No. 1, pp. 22–37, http://doi.org/10.1016/S0925-9635(01)00526-X
Yelisseyev A., Steeds J.W., Babich Y., Feigelson B. (2006) A new approach to investigation of nickel defect transformation in the HPHT synthetic diamonds using local optical spectroscopy. *Diamond and Related Materials*, Vol. 15, No. 11/12, pp. 1886–1890, http://dx. doi.org/10.1016/j.diamond.2006.07.027
Zaitsev A.M. (2003) *Optical Properties of Diamond: A Data Handbook*. Springer-Verlag, Berlin.

GEMS & GEMOLOGY 2017

CONGRATULATIONS

This year, hundreds of readers participated in the 2017 *Gems & Gemology* Challenge. Entries arrived from around the world as readers tested their gemological knowledge by answering questions listed in the Spring 2017 issue. Those who earned a score of 75% or better received a GIA Certificate of Completion recognizing their achievement. The participants who scored a perfect 100% are listed below.

G&G Challenge Winners

Canada
Diane Gauthier
Janusz Meier

Czech Republic
Jaroslav Jiránek
Krystyna Samek

France
Jurga Lenktaityte

Malaysia
Arnold Cheong

Spain
Patricia Muñoz Soriano

United Kingdom
Francesca Lawley

United States
Robert Campbell
Kenneth Fogelberg
Thaïs Anne Lumpp-Lamkie
Lisa A. Marsh-Vetter
Tim Richardson
Geraldine M. Vest
Ryan Waddell
Colleen Walsh
Flora Walters
Thomas Wendt

Answers

See pages 110–111 of the Spring 2017 issue for the questions.

1 (d), 2 (a), 3 (c), 4 (b), 5 (d), 6 (a), 7 (d), 8 (c), 9 (d), 10 (b), 11 (b), 12 (b), 13 (b), 14 (c), 15 (a), 16 (a), 17 (b), 18 (c), 19 (d), 20 (a), 21 (b), 22 (*), 23 (d), 24 (c), 25 (c)

* Question withdrawn

Saltwater Pearls from the Pre- to Early Columbian Era: A Gemological and Radiocarbon Dating Study

Chunhui Zhou, Gregory Hodgins, Todd Lange, Kazuko Saruwatari, Nicholas Sturman, Lore Kiefert, and Klaus Schollenbruch

Natural pearls were recovered and treasured by the indigenous peoples of the Americas long before Columbus's voyages reached the New World. The once-abundant oyster beds of the Caribbean islands off the coast of Venezuela were heavily exploited during Spanish colonization, as pearls were harvested and shipped back to the Old World. A total of 85 saltwater natural pearls reportedly from the pre- to early Columbian era (late fifteenth to early seventeenth century) and found in Central and South America were examined for this study. Gemological and advanced analyses confirmed they were natural saltwater specimens, most likely originating from a *Pinctada* species. In addition, ^{14}C isotope radiocarbon dating of material from the samples supported the claimed age of these pearls.

Pearls were treasured by the indigenous peoples of the Americas for millennia (Donkin, 1998). These beautiful gems were commonly associated with spiritual power, social rank, and feminine fertility (Saunders, 1999). Pearls were found in the palaces of Montezuma and were prized by the later inhabitants of Mexico and Peru (Kunz and Stevenson, 1908). The discovery of the New World by Christopher Columbus in 1492 and subsequent Spanish colonization radically changed the lives of the natives. Many were enslaved by colonists in pursuit of gems such as pearls, one of the most sought-after commercial products of the period.

The New World's most productive sources of pearls in the early 1500s were the oyster beds near the Venezuelan islands of Margarita, Cubagua, and Coche, and to a lesser extent in the waters off the Colombian coast and the Gulf of California in Mexico (Mackenzie et al., 2003; Southgate and Lucas, 2011; see figure 1). Within a few decades of the New World's discovery, the production of natural pearls peaked as a consequence of heavy demand in the Old World. These treasures were shipped to Spain and used in jewelry and ornamentation for the nobility and the Church. During the Renaissance period, pearls and pearl jewelry became extremely popular in Europe due to the influx of significant quantities of saltwater pearls from the newly discovered Americas (Dirlam et al., 1985). Even today, famous historical pearls such as La Peregrina or the Hanoverian pearls owned by Queen Elizabeth I are still in fine condition. Archival records and auction house sales prove that "old pearls" have survived through the centuries. Yet the Spanish failed to understand the importance of conservation and sustainable harvest-

In Brief

- Large amounts of natural pearls were harvested off the coast of Venezuela during the early 16th century and shipped back to the Old World, causing depletion of the oyster beds.
- The gemological properties of the pearls reportedly from this region and era were studied by GIA and the Gübelin Gem Lab. These pearls were confirmed to have natural saltwater origin.
- ^{14}C isotope radiocarbon dating of material from the samples using accelerator mass spectrometry supported the claimed age of these pearls.

See end of article for About the Authors and Acknowledgments.
Gems & Gemology, Vol. 53, No. 3, pp. 286–295,
http://dx.doi.org/10.5741/GEMS.53.3.286
© 2017 Gemological Institute of America

ing (Romero, 2003). Production fell sharply by the mid-1500s due to the scarcity of oysters and as a result of indigenous rebellions (Romero et al., 1999).

There were attempts to revive pearl harvesting in the 1600s, and a few intermittent fishing activities also took place in the eighteenth and nineteenth centuries, but on a much smaller scale. One can still see the pearling traditions reflected in the coat of arms for Nueva Esparta, the Venezuelan state that comprises the islands of Margarita, Coche, and Cubagua. Shown in figure 2, the emblem depicts a strand of natural pearls. Such pearls are seen in numerous jewelry pieces from this period, as well as in paintings depicting women of all classes wearing multi-strand pearl and coral bracelets, necklaces, and earrings (Pierce and Frick, 2015).

Establishing the ages of such historical pearls requires advanced analytical techniques in addition to routine gemological testing. Radiocarbon (^{14}C) dating is a method for determining the age of an object containing organic material. Three isotopes of carbon occur naturally: ^{12}C and ^{13}C (both stable) and ^{14}C (unstable or radioactive). These isotopes exist in equilibrium and enter into plants and animals through biological food chains until their death. The amount of ^{14}C will then slowly decay with a half-life of 5,568 years (the Libby standard). The remaining concentrations of ^{14}C may be detected using accelerator mass spectrometry (AMS), making it possible to calculate the sample's age. However, there is a difference between radiocarbon dating of a terrestrial sample and a sample from a marine environment due to the delay in exchange rates between atmospheric CO_2 and ocean bicarbonates, and the dilution effect caused by the mixing of surface waters with the very old upwelled deep waters. A global marine reservoir correction using the IntCal Marine13 calibration data set is commonly applied for marine samples. In addition, local marine reservoir corrections (delta R) can be applied if the samples are of known geographic origin. Radiocarbon dating has been widely used in many fields, including history, oceanography, geology, archaeology, and materials science (Taylor et al., 2013), so its importance in determining the approximate age of samples is well established.

The present study focuses on a group of pearls reportedly from the pre- to early Columbian era. They were purportedly collected in Central or South America, most likely off the island of Cubagua, although their history and exact origin are not clear. The pearls appeared to be old, judging from their external form and the worn condition of their nacreous surfaces (figure 3). Gemological examination at GIA and age dating at the University of Arizona and the

Figure 1. Heavy exploitation of pearls occurred during Spanish colonization near the Venezuelan islands of Margarita, Cubagua, and Coche.

Figure 2. The history of pearl harvesting in the Venezuelan state of Nueva Esparta (which comprises Margarita, Coche, and Cubagua) is reflected in its coat of arms.

Figure 3. These natural pearls, reportedly from the pre- to early Columbian era, represent some of the 85 samples examined in the study. They were discovered already drilled but were only recently strung as a necklace. The center blister pearl (31.41 × 16.86 × 10.25 mm) consists of multiple small pearls that formed as an aggregate. Photo by Sood Oil (Judy) Chia.

University of Tokyo confirmed that these were saltwater natural pearls from the pre- to early Columbian era. Meanwhile, the Gübelin Gem Lab conducted an independent study on pearls from the same supplier that were said to be from the same geographic source. Their results are included in this joint study in order to identify the nature and origin of these intriguing gems.

MATERIALS AND METHODS

A total of 75 baroque to semi-baroque pearls ranging from 3.46 × 2.80 × 2.17 mm to 31.41 × 16.86 × 10.25 mm were examined in the study conducted by GIA. According to the supplier, these are part of a large collection of natural specimens reportedly from Central or South America, most likely the waters off Cubagua. It is presumed that they were later found buried underground, although the exact origins were not clear to the supplier. Shell powder taken from one blister pearl in this group was used in ^{14}C radiocarbon dating experiments (figure 4). One small pearl weighing 0.74 ct was also sacrificed for an additional ^{14}C radiocarbon dating experiment.

The pearls were examined with a standard gemological microscope, and photomicrographs were obtained using a Nikon SMZ1500 stereomicroscope. Internal structures were examined using a MatriX-FocalSpot Verifier HR FSX-090 2D real-time X-ray microradiography (RTX) unit (45 kV and 0.18 mA excitation). XRF reactions were observed using a MatriX-FocalSpot Verifier PF-100 X-ray fluorescence unit (100 kV and 3.2 mA excitation) equipped with a Canon EOS REBEL T4i DSLR camera (5-second exposure, F5.0, ISO 12800). The chemical composition of 11 loose samples was obtained with a Thermo Scientific ARL Quant'x energy-dispersive X-ray fluorescence (EDXRF) spectrometer. Conditions varied depending on the element of interest: low Za—8 kV voltage, no filter, 50 sec live time; low Zc—12 kV voltage, aluminum filter, 200 sec live time; mid Zc—28 kV voltage, Pd thick filter, 100 sec live time; high Zb—50 KV voltage, Cu thick filter, 50 sec live time.

Radiocarbon dating experiments were carried out at the University of Arizona's Accelerator Mass Spectrometry Laboratory in Tucson. Shell powder (40 mg) from one blister pearl was ultrasonically cleaned for one hour in several changes of type 1 deionized water (>18 MΩ). Carbon was isolated by acid hydrolysis using 85% phosphoric acid under vacuum. The carbon dioxide was cryogenically purified and quantified manometrically in a known volume. Stable isotope measurements ($\delta^{13}C$) were made offline on an aliquot of sample gas using a VG Isotech dual-inlet stable-isotope mass spectrometer. The carbon stable isotope value was measured against an internal laboratory standard referenced to VPDB, to a precision of ±0.1‰. Graphitization was carried out using Zn and Fe by the

Figure 4. Some of the pearl samples studied by GIA. Powders taken from the shell attached to a blister pearl on the far left were used in carbon dating experiments. Photo by Chunhui Zhou.

method reported by Slota et al. (1987), and AMS measurements were carried out using an NEC 2.5 MeV Pelletron accelerator mass spectrometer. The measurement standards were NIST SRM 4990B and 4990C. The measurements were background-subtracted and corrected for isotope fractionation. The radiocarbon measurements were calibrated to calendar age ranges using the Marine13 database and OxCal 4.2.4 software, with a local marine reservoir correction (delta R). The local marine reservoir correction was estimated by assuming that the true origin of the shell was off the coast of Cubagua Island. A marine reservoir correction database (http://calib.org/calib) was queried, and a local marine reservoir value was calculated as the mean delta R from the five nearest reference samples.

Additional radiocarbon dating experiments were performed at the University of Tokyo's University Museum on the shell powders from the same blister pearl sample (67.8 mg) and the sawn half of a small natural pearl sample (54.5 mg; see figure 5). Both samples were pretreated with weak hydrochloric acid (0.1 M) to clean their surfaces. After the acid pretreatment, they were pulverized using an agate mortar for carbon purification and graphitization. Each pulverized sample was encapsulated in vacuum vessels with anhydrous phosphoric acid (100%) and reacted at 70°C (Wachter and Hayes, 1985). CO_2 gas reaction products were purified using a vacuum line and transferred into the reaction tube containing pure Fe powder. After filling the reaction tube with hydrogen gas (2.2 times an equivalent molar amount of carbon), the reaction tubes were heated to 650°C for six hours (Kitagawa et al., 1993). In order to calculate the conventional ^{14}C age (before present, or BP), the $\delta^{13}C$ value for the correction of isotope fractionation was measured simultaneously (Stuiver and Polach, 1977).

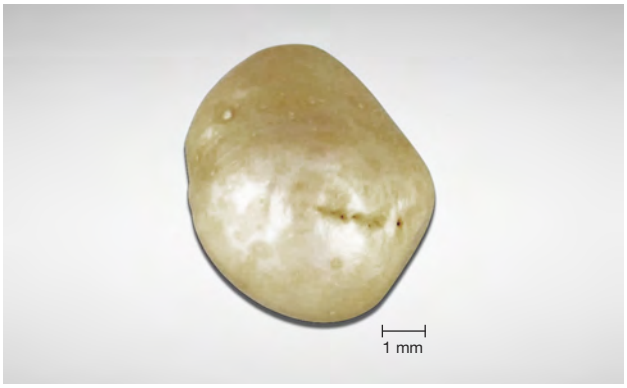

Figure 5. A small natural pearl used in an AMS experiment for this study. Photo by Masumi Saito.

Ten additional pearls, reportedly from the same supplier, were tested independently by the Gübelin Gem Lab in Lucerne, Switzerland. The Gübelin lab used RTX to examine the growth structures and EDXRF chemical analysis to determine the saltwater or freshwater origin. Furthermore, five of these samples were radiocarbon dated at an independent institute in Switzerland.

RESULTS

General Observations. Although the pearl samples were of various shapes and sizes, their external appearances were similar (figures 3–6). Fifty-three of them were drilled and strung as a strand necklace, and the rest were undrilled. The drilled pearls were reportedly drilled before their discovery and only recently strung. The drill hole outlines did appear "handmade," with primitive jagged edges as opposed to the even and round drill holes created by modern drilling machines. Most of the pearls showed white or off-white (cream) bodycolors, while reddish or brownish stains could be found on the surfaces of a few. Microscopic examination revealed overlapping

Figure 6. Ten of the undrilled natural pearls examined by GIA. These samples range in size from 6.65 × 6.50 × 5.10 mm to 8.20 × 7.84 × 5.92 mm. Photo by Sood Oil (Judy) Chia.

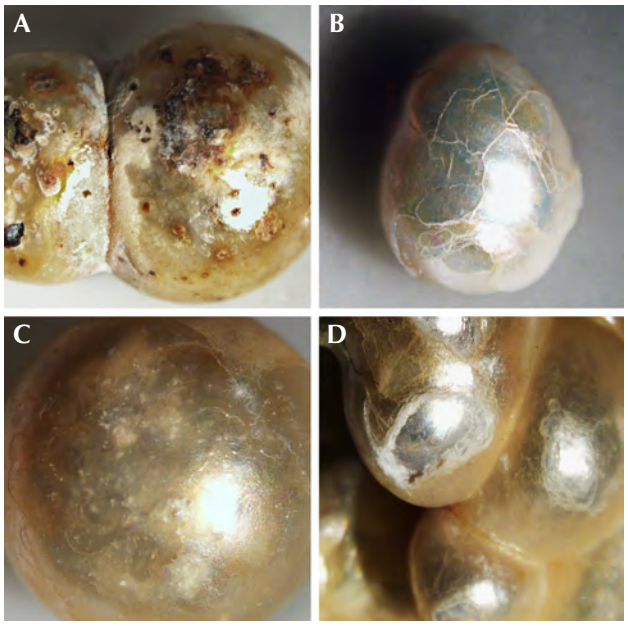

Figure 7. Some of the pearls displayed various signs of aging, including (A) reddish and brownish surface stains, (B) surface to subsurface cracks, (C) worn nacre, and (D) damaged and peeled nacre. Photos by Chunhui Zhou.

aragonite platelets typically seen in nacreous pearls, as well as evidence of aging, including delicate chalky outer surfaces, worn and peeled layers, and surface cracks in some cases (figure 7). However, many of the samples still displayed good surface conditions, a high luster, and a strong orient from underlying nacreous layers, reflecting their once-fine quality (figure 8). Additionally, one of the undrilled pearls and the large center pearl in the strand were found to be blister pearls, consisting of multiple small pearls that formed into an aggregate with a cut shell base (again, see figures 3 and 4). These strongly resembled pearls believed to be from the Venezuelan islands that were recovered from a colonial-era Spanish shipwreck off the coast of Florida (Koivula et al., 1992).

Internal Structures. The pearls in this study exhibited various natural internal structures revealed by RTX, in keeping with many other natural samples tested by GIA. Some had a relatively tight internal structure with only a few faint growth arcs. Twin pearls or pearls with three or more segments were also common in this group, with either natural concentric growth rings or tight structure in each segment separated by boundary or fold features. Other structures observed included natural concentric growth rings and/or dark organic-rich centers with natural growth arcs (figure 9). The central blister pearl in the strand had a very interesting appearance and structure. It was an aggregation of many smaller pearls, and its base was flat, likely the result of being cut from a host shell. Its internal structure correlated with its external appearance, with numerous small growth centers separated by boundary/fold lines. The centers of these small growth units usually contained conchiolin-rich materials that displayed dark areas observed via microradiography (figure 10, left). Similar multiple growth structures were observed in the loose blister pearl from which powder was taken for carbon dating (figure 10, right). On the whole, the internal structures proved these were natural pearls that formed without human interference (CIBJO, 2016).

Figure 8. Additional natural pearls from the same supplier showing relatively good surface condition and quality. These samples were not tested for this study. Photo courtesy of Peter Balogh.

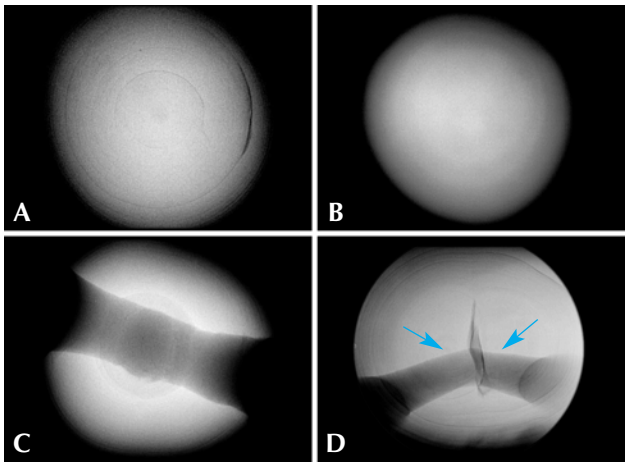

Figure 9. Various natural internal growth structures were observed in the group of pearls studied by GIA. Representative RTX images of structures are shown. A: A clear natural concentric structure with a dark core. B: A tight structure showing minimal features. C: A dark "collapsed" core with an organic-rich area around it. D: A twin pearl showing a clear dark boundary between the two segments of the specimen.

X-ray Luminescence and EDXRF Spectrometry. X-ray luminescence is used to separate saltwater from freshwater pearls owing to the latter's higher concentrations of manganese (Mn; Hänni et al., 2005, Kessrapong et al., 2017). Freshwater pearls may show obvious greenish yellow fluorescence under X-ray excitation, while saltwater natural pearls are usually inert. Even the freshwater nuclei used in saltwater bead-cultured pearls may be detected, depending on the thickness of their nacre. All the samples tested in this study lacked luminescence under X-ray exposure, indicating that they formed in a saltwater environment. EDXRF qualitative analysis detected only calcium (Ca) as the major element and strontium (Sr) as a trace element in the majority of samples. Very low quantities of Mn were detected, further confirming a saltwater origin. The results are consistent with earlier studies on Mn and Sr concentrations of saltwater pearls from bivalve mollusks (Gutmannsbauer and Hänni, 1994), and the Sr/Mn concentration ratios are generally very high compared to typical freshwater counterparts, similar to previous studies (Karampelas and Kiefert, 2012). However, pearls discolored by reddish and brownish stains were found to possess high levels of iron (Fe) on their surfaces. These stains may have been due to the various storage and environmental conditions the pearls were exposed to throughout their long history, where rust (iron oxide) or other forms of oxidizing contamination found their way onto, and partially into, the surfaces.

Figure 10. Left: A large natural blister pearl consisting of numerous smaller "seed" pearl aggregates. Virtually every "seed" pearl reveals its own organic-rich nucleus/core. Right: Internal structure of another loose blister pearl showing similar multiple nuclei growth.

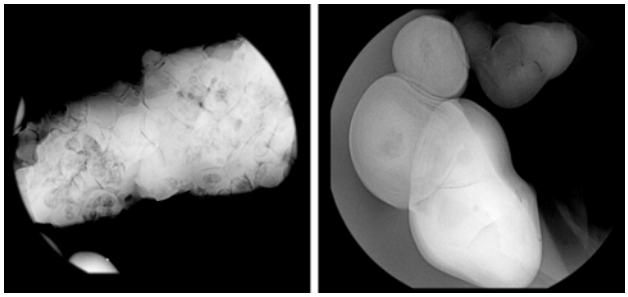

^{14}C Radiocarbon Dating. The radiocarbon dating result of the shell powders from a blister pearl sample tested at the University of Arizona is shown in figure 11. The uncalibrated ^{14}C age was measured to be 776 years (+/– 25 years) BP. Using the Marine13 database and OxCal 4.2.4 software with a local marine reservoir correction (delta R), the calibrated calendar age ranges were measured to be between the years 1472 to 1537 (68% probability) and 1455 to 1615 (95% probability).

Additional experiments were conducted at the University of Tokyo on a sample of the same shell powder from the blister pearl and one additional pearl sample. The uncalibrated age of the shell powder was 713 years (+/– 16 years) BP, and the uncalibrated age of the pearl sample was measured to be 719 years (+/– 14 years) BP. Using the same database and software as the University of Arizona, the University of Tokyo measured calibrated calendar ages ranging from 1519 to 1616 (68% probability) and 1491 to 1648 (95% probability) for the shell powder (figure 12), and from 1508 to 1615 (68% probability) and 1487 to 1644 (95% probability) for the pearl sample (figure 13). One thing to point out is that due to discontinuous regions of the calibration curve, not all dates in the radiocarbon age range are equally likely. A better probabilistic method is to take the original normal distribution of radiocarbon age ranges and use it to generate a histogram showing the relative probabilities for calendar ages. Local marine reservoir correction for the Caribbean Sea (Wagner et al., 2009) was also included in the University of

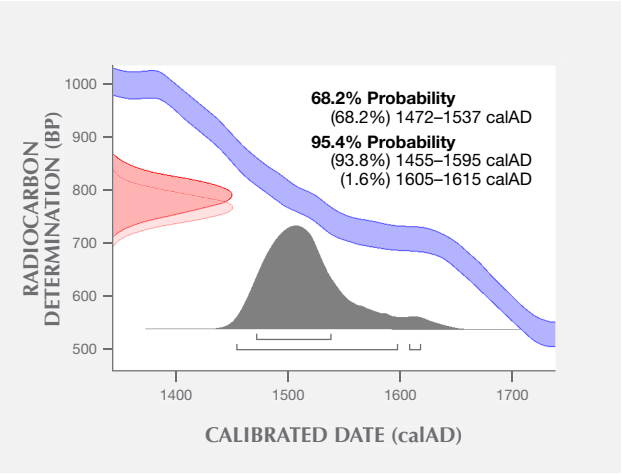

Figure 11. Radiocarbon dating results (both uncalibrated and calibrated ^{14}C age) of the shell powder from a blister pearl sample tested by the University of Arizona. The blue band is the calibration curve, while the peaks in red represent the uncalibrated ^{14}C age and the peak in gray the calendar age range distributions.

Tokyo measurements. Whenever possible, it is important to know the geographic location of samples under investigation, as the final data may be affected (from a few years to a few hundred years) by the lack of such valuable information. In summary, the radiocarbon dating results from both laboratories suggested that these samples were from the pre-Columbian or, more likely, early Columbian era, when natural pearl resources in Central and South America were heavily exploited by Spain.

Figure 12. The University of Tokyo's radiocarbon dating results (both uncalibrated and calibrated ^{14}C age) of the shell powder from the same blister pearl sample.

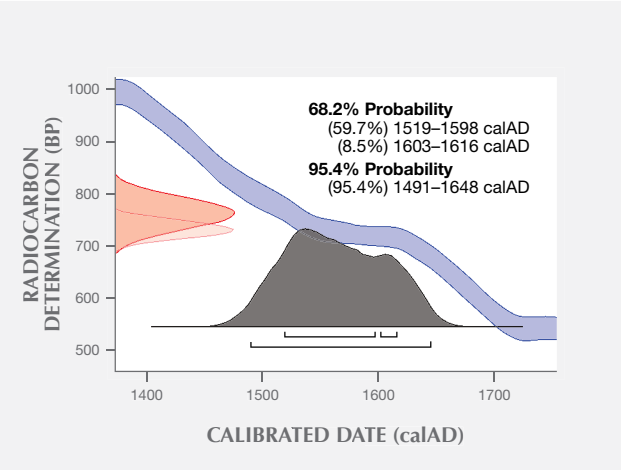

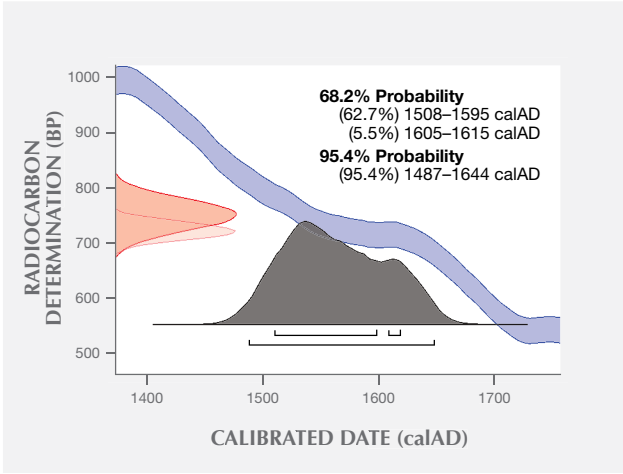

Figure 13. Radiocarbon dating results (both uncalibrated and calibrated ^{14}C age) of an additional pearl sample tested by the University of Tokyo.

Additional Results Obtained by the Gübelin Gem Lab. Independent testing at the Gübelin Gem Lab of 10 loose pearls, reportedly from the same supplier, supported these results. X-ray microradiography revealed natural growth structures, and EDXRF chemical analysis confirmed the saltwater origin (figure 14). Some of these pearls exhibited a ceramic or clay-like residual layer on their surface. This material may have originated from the vessel in which the pearls were stored for several centuries, perhaps a clay jar or clay pot (figure 15). Furthermore, five of the samples were radiocarbon dated at an independent institute in Switzerland, and their results revealed various date ranges (figure 16), with local marine reservoir adjusted for waters off the coast of Venezuela:

(1) 1504 to 1587 (68% probability) and 1490 to 1635 (95% probability)
(2) 1468 to 1513 (68%) and 1451 to 1539 (95%)
(3) 1591 to 1667 (68%) and 1547 to 1677 (95%)
(4) 1534 to 1618 (68%) and 1508 to 1648 (95%)
(5) 1543 to 1626 (68%) and 1517 to 1654 (95%)

The results confirmed that these pearls were from the pre- to early Columbian era.

DISCUSSION

The radiocarbon dating of pearls that formed between the mid-nineteenth century and very recently has been reported previously. The results were found to be useful in providing additional valuable information on the age, provenance, and/or identification of those pearls (Krzemnicki and Hajdas, 2013). Test-

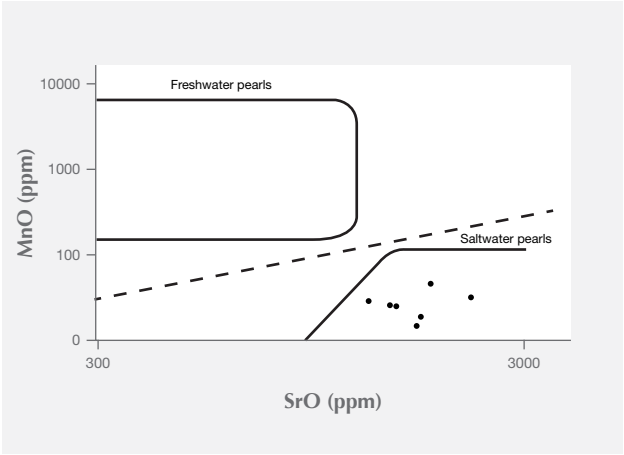

Figure 14. In most cases, the chemical analysis of pearls can easily distinguish between freshwater and saltwater origin. This is achieved by determining the ratio of the trace elements Mn and Sr, which are present within saltwater and freshwater pearls to varying degrees. EDXRF chemical analysis performed by the Gübelin Gem Lab concurred with the results obtained by GIA and confirmed a saltwater origin. Three of the 10 samples had Mn concentrations below 10 ppm and are not shown in this graph.

Figure 15. Ceramic or claylike material was found on the surface of some samples tested by the Gübelin Gem Lab. This material may have come from the vessel in which the pearls were stored for centuries. Photo by Klaus Schollenbruch.

ing in this study at different AMS facilities confirmed that the samples were from the pre- to early Columbian era. Local marine reservoir corrections were applied to the results obtained from each institution with the assumption that the pearls originated from the waters of the Caribbean Sea, as claimed by the supplier. Results from the different laboratories determined the approximate ages within fairly consistent time frames.

It is interesting to note that radiocarbon dating results indicate that the pearls appear to be of various ages, with some possibly preceding 1541. That was the year a hurricane and a possible tsunami destroyed the town of Nueva Cádiz on Cubagua (O'Loughlin and Lander, 2003), suggesting that the pearls may have been hidden in Cubagua, if the client's claims are true, after the hurricane struck. Finally, it is worth mentioning that the variation in the results obtained from the different laboratories is common in radiocarbon dating experiments, as was shown in the famous case involving the Shroud of Turin (Damon et al., 1989). The slight differences between

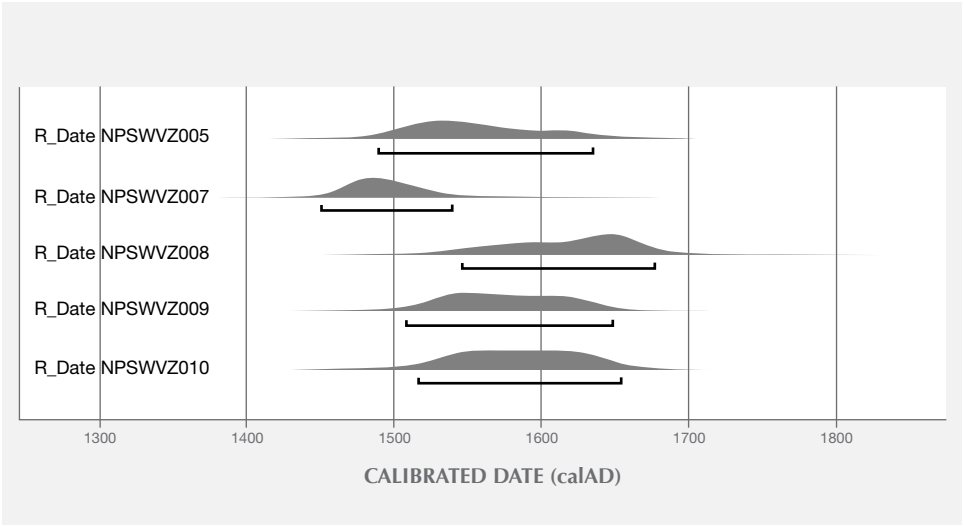

Figure 16. Radiocarbon dating results of five pearls chosen for examination by the Gübelin Gem Lab show various pre- to early Columbian-era age ranges. Bracketed calendar ranges represent a 95% probability of the pearls' ages.

AMS laboratories may arise at several points, likely stemming from differences in cleaning protocols.

To summarize, both gemological and advanced chemical analyses confirmed that these were natural saltwater pearls, probably from a *Pinctada* species mollusk—e.g., *Pinctada imbricata*, which were harvested en masse during the Spanish colonization—if the reported geographic origin of the pearls is accurate.

CONCLUSION

This joint study has demonstrated that radiocarbon dating may play a pivotal role in determining the age of pearls—and possibly supporting the provenance determination—and distinguishing between natural and cultured pearls. This technique requires a small amount of sample powder (as low as 5 mg) to be extracted and analyzed and may have limitations with pearls of unknown geographic origin. Freshwater pearls may pose additional challenges due to the underlying geology of the watershed (limestone, for example). Pearls formed after 1955 also have atomic bomb–derived radiocarbon levels that make obtaining accurate results even more challenging.

The pearls and shell powders from which the samples in this study were taken were reportedly found off the Caribbean islands near Venezuela and were believed to be from the pre- to early Columbian era. Routine gemological studies confirmed they were natural saltwater pearls that probably formed in a *Pinctada* mollusk genus. Radiocarbon dating experiments conducted by three different institutions were in agreement with the claimed ages of the samples (within acceptable tolerances) and indicated that the pearls originated from a period when European colonists had just discovered the Americas (the late fifteenth to seventeenth centuries). The fact that these were not shipped back to Europe suggests that they belonged to Native Americans or colonists living in the region. Given their age, it is remarkable how well preserved these pearls are after spending centuries in unknown conditions.

ABOUT THE AUTHORS

Dr. Zhou is a research scientist and manager of pearl identification at GIA in New York. Dr. Hodgins is director and Mr. Lange is a staff scientist at the University of Arizona Accelerator Mass Spectrometry Laboratory in Tucson, Arizona. Dr. Saruwatari is a staff gemologist at GIA in Tokyo. Mr. Sturman is senior manager of global pearl services at GIA in Bangkok. Dr. Kiefert is chief gemologist, and Dr. Schollenbruch is a gemologist, at the Gübelin Gem Lab in Lucerne, Switzerland.

ACKNOWLEDGMENTS

The authors thank Prof. Minoru Yoneda and Dr. Takayuki Omori at the Laboratory of Radiocarbon Dating in the University Museum, University of Tokyo, for the help and guidance on the experiments conducted at their facility. The authors also thank Dr. Shoko Odake at GIA's Tokyo laboratory for her assistance with experiments conducted in Japan. Finally, the authors thank Peter Balogh for supplying the pearl samples in this study, and Antoinette Matlins for establishing the contact between Mr. Balogh and the Gübelin Gem Lab.

REFERENCES

CIBJO (2016) *The Pearl Book*. The World Jewellery Confederation.

Damon P.E., Donahue D.J., Gore B.H., Hatheway A.L., Jull A.J.T., Linick T.W., Sercel P.J., Toolin L.J., Bronk C.R., Hall E.T., Hedges R.E.M., Housley R., Law I.A., Perry C., Bonani G., Trumbore S., Woelfli W., Ambers J.C., Bowman S.G.E., Leese M.N., Tite M.S. (1989) Radiocarbon dating of the Shroud of Turin. *Nature*, Vol. 337, No. 6208, pp. 611–615, http://dx.doi.org/10.1038/337611a0

Dirlam D.M., Misiorowski E.B., Thomas S.A. (1985) Pearl fashion through the ages. *G&G*, Vol. 21, No. 2, pp. 63–78, http://dx.doi.org/10.5741/GEMS.21.2.63

Donkin R.A. (1998) *Beyond Price: Pearls and Pearl-Fishing: Origins to the Age of Discoveries.* American Philosophical Society, Philadelphia.

Gutmannsbauer W., Hänni H.A. (1994) Structural and chemical investigations on shells and pearls of nacre forming salt- and fresh-water bivalve molluscs. *Journal of Gemmology*, Vol. 24, No. 4, pp. 241–252.

Hänni H.A., Kiefert L., Giese P. (2005) X-ray luminescence, a valuable test in pearl identification. *Journal of Gemmology*, Vol. 29, No. 5/6, pp. 325–329.

Karampelas S., Kiefert L. (2012) Gemstones and minerals. In H.G.M. Edwards and P. Vandenabeele, Eds., *Analytical Archaeometry: Selected Topics*. Royal Society of Chemistry, Cambridge, United Kingdom, p. 309.

Kessrapong P., Lawanwong K., Sturman N. (2017) *Pinctada maculata* (pipi) bead-cultured blister pearls attached to their shells.

GIA Research News, April 25, https://www.gia.edu/gia-news-research/pinctada-maculata-bead-cultured-blister-pearls-shells
Kitagawa H., Masuzawa T., Nakamura T., Matsumoto E. (1993) A batch preparation method for graphite targets with low background for AMS ^{14}C measurements. *Radiocarbon*, Vol. 35, No. 2, pp. 295–300, http://dx.doi.org/10.1017/S0033822200064973
Koivula J.I., Kammerling R.C., Fritsch E., Eds. (1992) Gem News: Natural pearls from the New World. *G&G*, Vol. 28, No. 3, p. 202.
Krzemnicki M.S., Hajdas I. (2013) Age determination of pearls: A new approach for pearl testing and identification. *Radiocarbon*, Vol. 55, No. 3, pp. 1801–1809, http://dx.doi.org/10.1017/S0033822200048700
Kunz G.F., Stevenson C.H. (1908) *The Book of the Pearl*. The Century Co., New York, p. 23.
Mackenzie C.L., Troccoli L., Leon S. L.B. (2003) History of the Atlantic pearl-oyster, *Pinctada imbricata*, industry in Venezuela and Colombia, with biological and ecological observations. *Marine Fisheries Review*, Vol. 65, No. 1, pp. 1–20.
O'Loughlin K.F., Lander J.F. (2003) *Caribbean Tsunamis: A 500-Year History from 1498–1998*. Springer-Science+Business Media, LLC, New York, Appendix F.
Pierce D., Frick J.W. (2015) *Glitterati: Portraits & Jewelry from Colonial Latin America at the Denver Art Museum*. Denver Art Museum, p. 22.
Romero A. (2003) Death and taxes: the case of the depletion of pearl oyster beds in sixteenth-century Venezuela. *Conservation Biology*, Vol. 17, No. 4, pp. 1013–1023, http://dx.doi.org/10.1046/j.1523-1739.2003.01406.x
Romero A., Chilbert S., Eisenhart M.G. (1999) Cubagua's pearl-oyster beds: The first depletion of a natural resource caused by Europeans in the American continent. *Journal of Political Ecology*, Vol. 6, pp. 57–78.
Saunders N.J. (1999) Biographies of brilliance: pearls, transformations of matter and being, c. AD 1492. *World Archaeology*, Vol. 31, No. 2, pp. 243–257, http://dx.doi.org/10.1080/00438243.1999.9980444
Slota P.J., Jull A.J.T., Linick T.W., Toolin L.J. (1987) Preparation of small samples for ^{14}C accelerator targets by catalytic reduction of CO. *Radiocarbon*, Vol. 29, No. 2 pp. 303–306, http://dx.doi.org/10.1017/S0033822200056988
Southgate P., Lucas J. (2011) *The Pearl Oyster*. Elsevier Science, Oxford, United Kingdom, p. 34.
Stuiver M., Polach H.A. (1977) Discussion: Reporting of ^{14}C data. *Radiocarbon*, Vol. 19, No. 3, pp. 355–363, http://dx.doi.org/10.1017/S0033822200003672
Taylor E., Long A., Kra R.S. (2013) *Radiocarbon After Four Decades: An Interdisciplinary Perspective*. Springer Science+Business Media, LLC, New York.
Wachter E.A., Hayes J.M. (1985) Exchange of oxygen isotopes in carbon dioxide–phosphoric acid systems. *Chemical Geology*, Vol. 52, No. 3-4, pp. 365–374, http://dx.doi.org/10.1016/0168-9622(85)90046-6
Wagner A.J., Guilderson T.P., Slowey N.C., Cole J.E. (2009) Pre-bomb surface water radiocarbon of the Gulf of Mexico and Caribbean as recorded in hermatypic corals. *Radiocarbon*, Vol. 51, No. 3, pp. 947–954, http://dx.doi.org/10.1017/S0033822200034020

For online access to all issues of GEMS & GEMOLOGY from 1934 to the present, visit:

gia.edu/gems-gemology

Photoluminescence Spectra of Emeralds from Colombia, Afghanistan, and Zambia

D. Brian Thompson, Christian J. Bayens, Matthew B. Morgan, Taylor J. Myrick, and Nealey E. Sims

Laser-excited photoluminescence spectra were collected from 48 emeralds originating from Colombia, Afghanistan, and Zambia. Photoluminescence in emerald arises from trace chromium impurities, and its spectrum displays two narrow *R* lines overlaid upon a broadband signal. In the collected spectra, peak positions of these *R* lines varied across a small range of wavelengths; the origin-dependent nature of these variations may be helpful in identifying the geographic source of unknown samples. Comparisons between *R*-line peak wavelengths and corresponding trace element concentrations of samples revealed strong correlations between peak shifts of the R_1 line and increases in magnesium and sodium concentrations, and between peak shifts of the R_2 line and increases in lithium and sodium concentrations. These correlations suggest that substitution defects of magnesium for aluminum with sodium impurities may be responsible for the R_1 line peak shifts, and similar defects of lithium for beryllium with sodium impurities may be responsible for the R_2 line peak shifts. Finally, a comparison between photoluminescence count rates and chromium and iron concentrations showed that count rates decrease exponentially with increasing iron concentration.

Emerald (figure 1) is a gem variety of beryl ($Be_3Al_2Si_6O_{18}$), whose green color arises from trace impurities of chromium and/or vanadium. While pure beryl is colorless, the trace amounts of Cr and V ions absorb light in the red and blue-violet region of the visible spectrum to produce emerald's green color (Schwarz and Schmetzer, 2002). Emeralds may also contain trace amounts of iron; this chromophore ion, also responsible for colors seen in the heliodor and aquamarine varieties of beryl (Nassau, 1978), may add a yellow or blue tint.

Some of the visible light energy absorbed by emerald's Cr ions can reappear as red photoluminescence (Nassau, 1978). This photoluminescence (PL) is usually not bright enough to be seen under normal lighting conditions. Illuminating an emerald with green monochromatic laser light produces a PL reaction that can be observed when the excitation light is blocked by a color filter (figure 2). Laser-excited PL spectra of emerald (figure 3) contain a broadband structure, peaking at about 715 nm, that results from a Stokes-shifted reversal of the electron transition

Figure 1. Emerald crystals from Colombia (top right), Afghanistan (bottom right), and Zambia (left). Each emerald's hexagonal prismatic crystal habit has been enhanced by polishing flat the two hexagonal end faces (perpendicular to the crystal's c-axis) and two or more prism sides (parallel to the c-axis). Photo by D.B. Thompson.

See end of article for About the Authors and Acknowledgments.
Gems & Gemology, Vol. 53, No. 3, pp. 296–311,
http://dx.doi.org/10.5741/GEMS.53.3.296
© 2017 Gemological Institute of America

Figure 2. With a green laser beam illuminating it from the left, and a color filter positioned in front to remove green light, an emerald crystal (center) is seen to emit red photoluminescence. Photo by D.B. Thompson.

that produces emerald's red absorption band (Lai, 1987). Superimposed upon this structure are two narrow lines that arise from electronic decay of a doublet metastable state, known as *R* lines (Wood, 1965). These *R* lines also appear in emerald absorption spectra, where the longer-wavelength line (denoted R_1) peaks at around 683 nm and the shorter-wavelength line (R_2) peaks at around 680 nm (Wood, 1965).

In Brief

- The *R* lines appearing in PL spectra of emeralds specimens from Colombia, Afghanistan, and Zambia show peak shifts that depend upon geographic source.
- Comparisons between emerald specimens' *R*-line peak wavelengths and their atomic impurity concentrations suggest which trace elements are responsible for the observed peak shifts.
- An emerald's PL emission intensity increases with atomic chromium concentration and decreases exponentially with atomic iron concentration.
- *R*-line peak measurements show promise as an aid in determining the geographic origin of emeralds.

Moroz et al. (2000) collected PL spectra from natural emeralds from nine deposits, as well as from a synthetic emerald. In their PL spectra, the peak positions of the *R* lines of emeralds from schist-host deposits showed moderate shifts in wavelength compared to those lines from emeralds originating from other types of deposits. The authors suggested that these wavelength shifts might be caused by Mg or Fe ions substituting at Al sites, based on the principle that these impurities occur at higher concentrations in schist-origin emeralds.

Recently, Thompson et al. (2014) collected PL spectra of natural emeralds from 11 different localities and synthetic emeralds from four different sources. The results confirmed observations made by Moroz et al. (2000): R_1 lines of synthetic emeralds peak at the shortest wavelengths, while in natural non-schist emeralds this line peaks at the same or longer wavelengths. In schist-origin emeralds the line peaks at an even longer wavelength, with peak positions spread across a range on the order of 1.0 nm. By comparison, the spread of R_2 lines of most emeralds fell within a 0.2 nm range, though some schist-origin emeralds had R_2 lines shifted up to 0.3 nm outside this range toward shorter wavelengths.

Thompson et al. (2014) compared their natural emeralds' R_1-line wavelengths to chemical composition measurements of a different set of emeralds with the same origin, and observed correlation between R_1-line wavelengths and SiO_2 weight concentrations. The authors suggested that R_1 line shifts might arise from impurity substitutions at Si crystal sites in

Figure 3. Photoluminescence (PL) spectra of emerald samples from the selected countries of origin were collected with the polarization axis of the excitation laser light aligned perpendicular to the crystal's c-axis. The black trace is from the Colombian sample shown in figure 1, the red trace from the Afghan sample, and the blue trace from the Zambian sample.

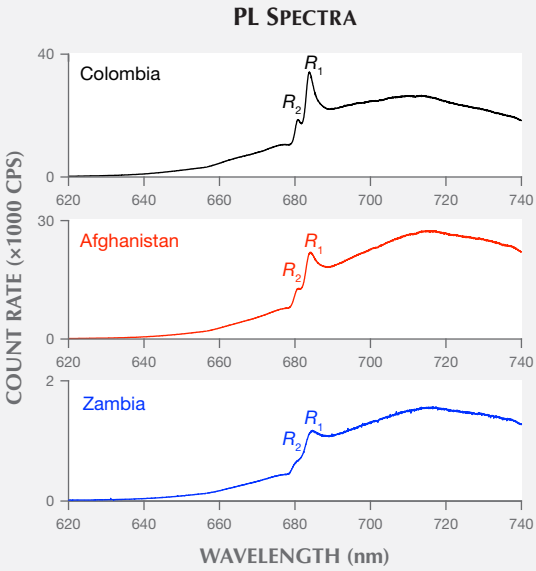

emerald. This speculation was incorrect, as an earlier X-ray diffraction study of beryl (Aurisicchio et al., 1988) found no evidence for substitution defects occurring at Si crystal sites in any type of natural or synthetic beryl. Schmetzer and Bernhardt (1994), and more recently Schmetzer (2015), showed that the minor reductions in Si weight concentrations in emerald could arise from an accrual of substitutions at Al crystal sites.

While Aurisicchio et al. (1988) found no ion substitutions at Si tetrahedral sites in beryl, they examined the other beryl crystal cation sites and did find that two types of substitutions can occur at Al octahedral sites. One is isovalent substitution, where the Al ion is replaced by another trivalent cation. Using Schmetzer's (2015) notation, this substitution can be written as

$$Al^{3+} \leftrightarrow Me^{3+} (Me^{3+} = V, Cr, Mn, Fe, etc.)$$

The other type is an aliovalent substitution, where the Al ion is replaced by a divalent cation. This substitution is accompanied by an alkali ion to provide charge compensation, where the alkali ion occupies an interstitial site within the beryl's open channels parallel to the c-axis (Goldman et al., 1978). This substitution can be written as

$$Al^{3+} \leftrightarrow Me^{2+} + Me^{+} (Me^{2+} = Mg, Mn, Fe, etc., \text{ and } Me^{+} = Li, Na, K, Cs, etc.)$$

Only a single substitution is possible at the tetrahedral site, the aliovalent substitution:

$$Be^{2+} \leftrightarrow Li^{+} + Me^{+} (Me^{+} = Li, Na, K, Cs, etc.)$$

Here the Be ion is replaced by a Li ion, accompanied by another alkali ion occupying an open channel site to provide charge compensation. While Aurisicchio et al. found that this substitution is common in some varieties of beryl, they did not observe significant occurrence of this substitution in emerald.

Saeseaw et al. (2014) performed microscopic, spectroscopic, and trace element analysis of emeralds with three-phase inclusions. Here we examine their samples from Colombia, Afghanistan, and Zambia. These samples are of interest because of the different geologies in which they formed. Colombian emeralds formed through hydrothermal processes in sedimentary shale, whereas Zambian emeralds are found in metamorphic phlogopite schists. The Afghan emeralds are hosted in metamorphic-metasomatic phlogopite schists subjected to strong hydrothermal processes (Groat et al., 2008; Giuliani et al., 2012). In short, Afghan emerald formed in a process similar to that which formed Colombian emeralds, but within host material similar to Zambian emeralds. As a result, the Colombian and Zambian emeralds exhibit distinctly different concentrations of several trace impurities, while impurity concentrations in Afghan emeralds bridge these two extremes (Saeseaw et al., 2014).

This study expands upon the work of Thompson et al. (2014) and presents *R*-line peak wavelength results derived from PL spectra of 48 Colombian, Afghan, and Zambian emerald samples prepared by GIA's laboratory in Bangkok; most of these samples were also used in Saeseaw et al. (2014). The present study demonstrates that the accumulation of *R*-line peak wavelength data from samples of known origin can provide evidence for or against various geographic origins. The peak wavelength data are compared with the samples' trace impurity concentrations to iden-

TABLE 1. Chemical composition of emerald samples (ppma), as measured by LA-ICP-MS.

	Colombia	Afghanistan	Zambia
^{7}Li	90–345 (173)	225–596 (301)	1280–2323 (1704)
^{9}Be	91,359–118,638 (108,826)	96,325–120,710 (107,886)	90,388–122,046 (106,214)
^{23}Na	1037–6730 (3382)	4621–10,646 (8053)	11,482–14,262 (13,365)
^{24}Mg	1021–6076 (3034)	3683–10,070 (7299)	9804–13,946 (11,762)
^{27}Al	57,790–75,526 (66,762)	53,057–70,257 (62,230)	48,171–62,381 (55,249)
Si normalized value	(206,897)	(206,897)	(206,897)
^{39}K	0–13 (3)	63–612 (316)	172–300 (243)
^{45}Sc	2–83 (30)	27–880 (225)	6–41 (19)
^{51}V	116–1731 (618)	93–1264 (488)	30–72 (42)
^{53}Cr	83–677 (295)	79–1432 (651)	357–1427 (924)
^{57}Fe	69–723 (219)	380–3153 (1439)	2252–3834 (3069)
^{133}Cs	1–2 (1)	3–12 (7)	0–207 (149)

Analyses were performed at GIA's Bangkok lab. Data are reported in minimum and maximum values, with average concentration in parentheses, and assume ideal oxygen concentration of 535,782 ppma. Alkali and transition metals with less than 25 ppma for all samples are not included in the table.

tify which trace impurities might be responsible for shifting *R*-line peak wavelengths. The study concludes with a comparison between Cr and Fe concentrations and broadband PL emission intensity to quantify the role each element plays in emerald photoluminescence.

MATERIALS AND METHODS

We collected PL spectra from 48 emerald samples on loan from GIA's Bangkok laboratory. Twenty of the samples were from the Coscuez and Muzo mines in the Boyacá region of Colombia, separated by about 10 km; 16 samples from two mines, Kameer Safeed and Koskanda, in the Khendj area of Afghanistan's Panjsher region, separated by less than 1 km; and 12 samples from the Kagem mine in the Kafubu area of Zambia. Forty-five of these samples were used in the work by Saeseaw et al. (2014), while one Afghan sample and two Zambian samples were used for the first time in this report. As outlined by Saeseaw et al. (2014), GIA altered its emeralds from their original rough form by polishing one or two flat surfaces perpendicular to each crystal's c-axis; some also have flat surfaces polished parallel to the c-axis. A specialized tool designed to locate the c-axis of a specimen (Thomas, 2009) was used to align the samples for polishing these flat surfaces.

As Saeseaw et al. (2014) describe, GIA's Bangkok laboratory determined the chemical composition of each emerald sample using laser ablation–inductively coupled plasma–mass spectrometry (LA-ICP-MS). For quantitative analysis, the spectrometer was

Figure 4. The experimental setup showing laser output (bottom left) and the optical fiber with collimating lens (top left) facing the beam path. The other end of the optical fiber connects to a CCD spectrometer (not shown). An emerald sample sits upon the suction cup of a vacuum pen. The pen itself is held in a rotation mount (upper right), which is attached to an XYZ translation stage (partially visible). With the crystal oriented as shown, the laser beam will cross its polished end face at normal incidence. The inset shows the laser's circular beam spot (in blue) positioned at the edge of the crystal face closest to the collection lens. The beam itself is parallel to the crystal's c-axis, and the beam's polarization axis E is perpendicular to the c-axis. This is the typical orientation used to collect E⊥c photoluminescence spectra. Photo by D.B. Thompson.

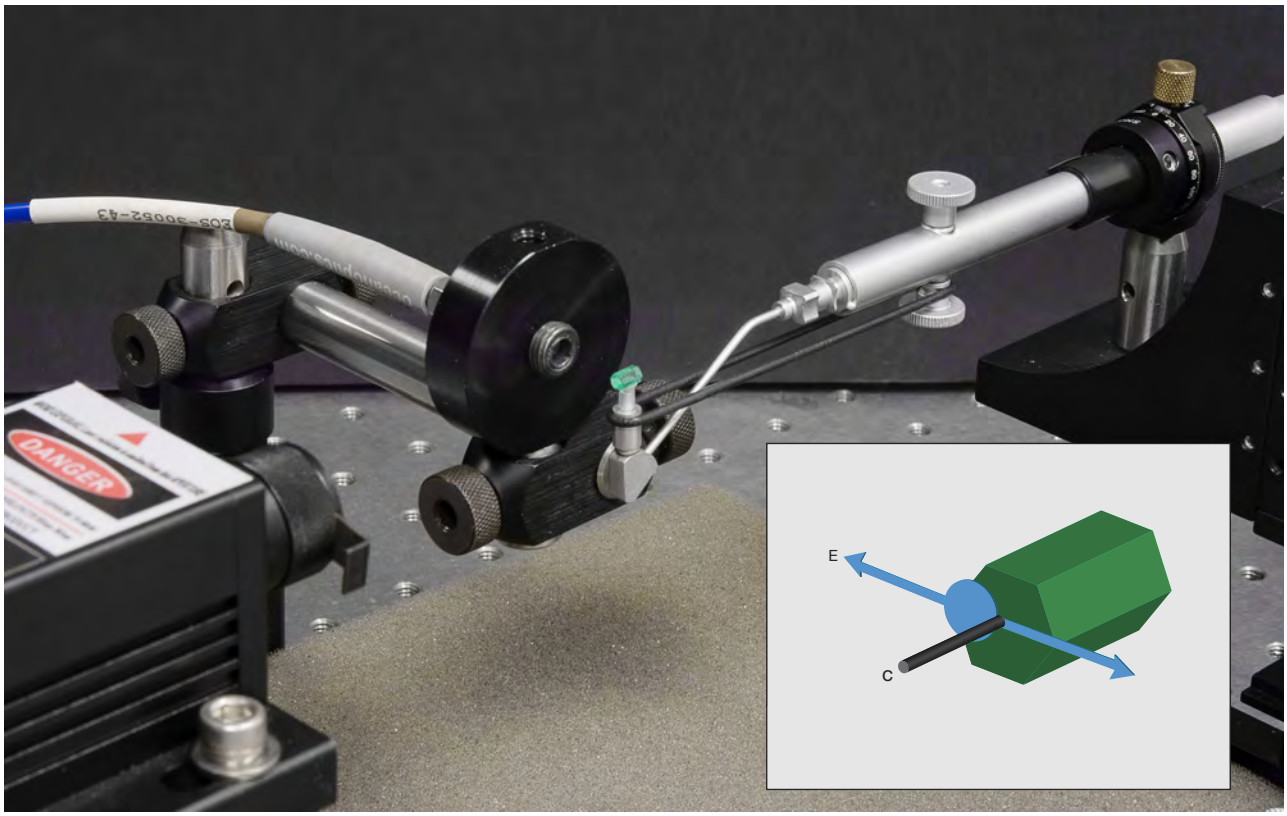

calibrated using NIST 610 and 612 glasses with known concentrations of elements. Along with providing the emerald samples, GIA also supplied their chemical composition measurements (table 1).

The experimental setup for collecting PL spectra (figure 4) has been described previously (Thompson et al., 2014). A continuous-wave diode pumped solid state (DPSS) laser (Laserglow LRS-532-TM-100-10) emits a 100 mW, 532 nm beam with horizontal polarization. Then a 0.5 mm diameter optical fiber with a 25° field-of-view collimating lens, mounted perpendicular to the laser beam, collects PL emission at room temperature from an emerald sample placed within the overlap region between the laser beam and collection lens field of view. The PL emission collected by the fiber enters a charge-coupled device (CCD) spectrometer (Ocean Optics USB4000) with a custom grating that disperses light over the 580–740 nm wavelength range; this spectrometer has full width at half maximum (FWHM) resolution of 0.20 nm, and the average width of each spectrometer channel is 0.045 nm. Discrete line emissions from argon and neon spectral lamps were used to calibrate the spectrometer's wavelength scale.

For this study, one change was made to the previous setup: A vacuum pen (Dazor SPK-100-VPEN) was used to position the emeralds. The pen's pulley system allows complete rotation of the sample about an axis through the stone. The pen itself is held in another rotation mount to allow rotation of the sample about a second, orthogonal axis. In turn, the rotation mount is attached to an XYZ translation stage with at least 13 mm of travel in three orthogonal directions. This assembly provides fine control for positioning a sample so that the laser beam can intersect any point along its surface (not obscured by the pen's vacuum suction cup) at any incident angle.

Emerald is optically uniaxial, and PL emission spectra collected when the excitation laser beam's polarization axis is perpendicular to the crystal's c-axis ($E \perp c$) differ from those collected with the beam's polarization axis parallel to the c-axis ($E \parallel c$). Both R_1 and R_2 peak positions change, as does the R_1/R_2 peak height ratio, as described in box A. Emeralds from different localities show the largest quantitative variations for these peak parameters when the spectra are collected with $E \perp c$ beam-crystal axes orientation. Therefore, the current study only considers spectra collected with $E \perp c$ beam-crystal axes orientation.[1]

To collect a PL spectrum with $E \perp c$ orientation, the sample itself is positioned so that the excitation laser beam enters a flat surface polished perpendicular to the crystal's c-axis at normal incidence. With this orientation, the excitation laser beam's polarization axis is also perpendicular to the crystal's c-axis. The sample is always positioned so that the beam overlaps the emerald edge closest to the optical fiber's collection lens (again, see figure 4). This sampling position was chosen to minimize PL emission traveling through unilluminated emerald before entering the fiber.

To construct each sample's PL spectrum, 100 accumulated scans were averaged; each scan's typical integration time was one second. In a similar manner, with the laser shuttered, a "dark" spectrum was produced. The final PL spectrum was created by subtracting the so-called dark spectrum from the sample spectrum. Doing so reduced counting noise arising from thermal motion of electrons in the spectrometer's CCD.

These emerald PL spectra (e.g., figure 3) exhibit local minima on either side of the *R* lines. To isolate the *R*-line contribution in each PL spectrum, a baseline is subtracted from the data. The line's endpoints at 678.5 and 688.5 nm were selected to coincide with these local minima. The resulting spectra (e.g., figure 5) are referred to as *R*-line spectra.

The *R*-line spectra in figure 5 each show two lines with width and peak separation at least an order of magnitude larger than the spectrometer's resolution. Besides the two peaks, no other fine structure appears in the spectra. After creating an *R*-line spectrum, peak-finding software (O'Haver, 2014) was used to extract R_1 and R_2 peak wavelengths and corresponding count rates, which were used to determine an R_1/R_2 peak height ratio. The R_1 and R_2 peak wavelengths reported here are means of values extracted from four separate spectral measurements. The resulting uncertainty in peak position is ±0.02 nm, as given by the four measurements' standard deviation of the mean.

The first step in analyzing the *R*-line datasets was to examine how *R*-line peak wavelength distributions vary with sample origins. This is done by performing independent sample *t* tests on *R*-line peak

[1] GIA's laboratory in Bangkok prepared the samples used here with c-axes aligned perpendicular to polished crystal faces, so that arranging a crystal for collection of E⊥c PL spectra (e.g., figure 4) was straightforward. An E⊥c PL spectrum can also be collected from a cut emerald even when its c-axis is not aligned perfectly perpendicular to its table facet; the strong variation of R_1/R_2 peak height ratio described in box A can be employed systematically to locate an E⊥c alignment through the table of any cut emerald sample.

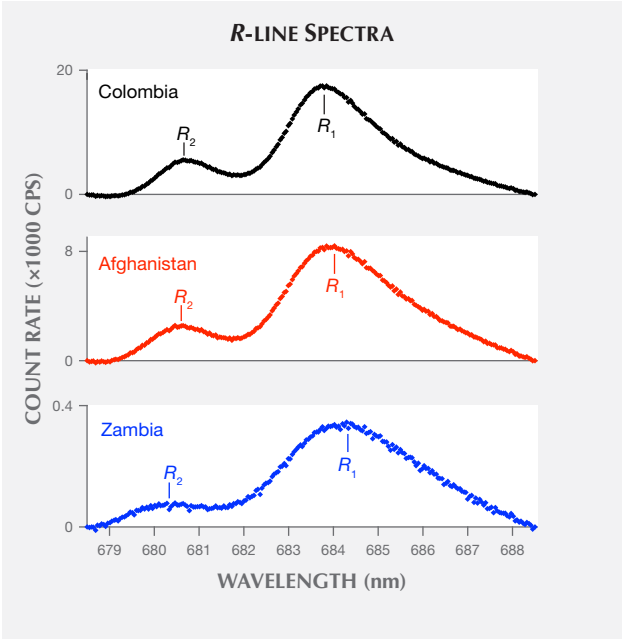

Figure 5. R-*line spectra of emerald samples resulting from the baseline subtraction of PL spectra in figure 3.* R_1 *is defined as the line at the center of the peak at the longer wavelength, and* R_2 *is defined as the line at the center of the peak of the shorter wavelength.*

wavelength values from samples with two different geographic origins (Crow et al., 1960). The Discussion section contains examples of how a random sample's measured *R*-line wavelength can be compared with measured distributions to either support or reject possible origins.

We then determined whether a linear relation exists between *R*-line peak wavelengths and concentrations of a particular trace element by calculating the coefficient of determination r^2 between the two datasets. In linear regression analysis of two variables, the coefficient of determination represents the fraction of variance of one dataset that is predictable from a "best-fit" linear relation with the other dataset (Crow et al., 1960). The coefficient of determination can range between 0 and 1, and two datasets are identified as strongly correlated when the coefficient of determination between them has a value $r^2 \geq 0.64$.

An issue arises from comparing *R*-line peak wavelengths extracted from the PL spectra to the trace element concentrations measured by LA-ICP-MS. In particular, the laser-illuminated volume in a sample that produces PL may not coincide with the surface spots where laser ablation was applied for mass spectrometry. This is a concern because trace element concentrations in natural emerald crystals can, and generally do, vary throughout the samples (Schmetzer, 1994; Schmetzer and Bernhardt, 1994). As a result, the LA-ICP-MS spot measurements of trace element concentrations may not perfectly match average concentrations within the bulk PL emission volume. This can reduce coefficients of determination between *R*-line parameters and trace element concentrations, leading to outliers in the resulting scatterplots.

In this report, scatterplots are presented for the *R*-line peak wavelength vs. trace element concentration datasets that demonstrate the highest coefficients of determination (i.e., strongest correlation). Next, linear regression is used to find each scatterplot's "best-fit" trend line, where the slope of this line corresponds to the pairwise variation of the dataset, and where its intercept identifies the *R*-line's peak wavelength for zero concentration of the trace element.

RESULTS

Examining *R*-line spectra extracted from the emeralds' PL spectra (figure 5), we see that the Colombian sample's R_1 line peaks at the shortest wavelength, the Afghan sample's line at a longer wavelength, and the Zambian sample's line at the longest wavelength. A plot of the mean R_1 peak wavelength of samples from each origin (figure 6) shows that this origin-based peak shift holds true on average. An overlap between Afghan and Colombian samples, seen in figure 6, results from a single anomalous R_1 peak wavelength value in each origin's dataset.

To compare R_1 peak wavelength distributions between Colombian and Afghan samples, we performed an independent sample *t* test. The *t* test uses the following values from each geographic sample's wavelength distribution: number of samples (N), mean wavelength value (M), and the standard deviation (SD) of these values. The *t* test produces a *t* value, t(df), where df represents the degrees of freedom. One then uses the *t* value to determine fractional probability (*p*) that the two populations share the same mean value, and to determine the 95% confidence interval (95% CI) for the difference between their mean values. The results show extremely significant differences in the distributions for the Colombian (N = 20, M = 683.777 nm, SD = 0.060 nm) and Afghan samples (N = 16, M = 684.013 nm, SD = 0.084 nm); t(34) = 9.88, $p < 0.0001$, and 95% CI [0.188 nm, 0.285 nm]. The low *p* value between this pair of sample datasets suggests that the measured difference between their mean peak wavelengths probably does not arise from an accident of sampling.

BOX A: VARIATIONS OF *R*-LINE PARAMETERS WITH THE ORIENTATION ANGLE BETWEEN EMERALD C-AXIS AND LASER BEAM POLARIZATION

Moroz et al. (2000) collected PL spectra from emerald samples with the excitation laser beam's polarization axis parallel to the crystal's c-axis (E ∥ c) and with the beam's polarization axis perpendicular to the c-axis (E ⊥ c). Comparing an emerald's E ∥ c orientation PL spectrum to its E ⊥ c orientation spectrum, the R_1 and R_2 peak positions and relative peak intensities both differ.

Thompson et al. (2014) rotated a rough emerald sample with hexagonal prismatic crystal habit in a laser beam from an E ∥ c orientation to E ⊥ c orientation while collecting PL spectra at 10° intervals. From these spectra, they extracted angular distributions of R_1 and R_2 peak positions and R_1/R_2 peak height ratios. These angular distributions showed that the R_1/R_2 peak height ratios varied smoothly from a minimum value around 1 when E ∥ c to a maximum value around 3 when E ⊥ c. They also showed that the R_1 and R_2 peak positions were relatively constant at angles around the E ⊥ c orientation, but varied rapidly at angles midway between E ⊥ c and E ∥ c orientations.

As noted in the text, we extracted R_1 and R_2 peak positions from E ⊥ c PL spectra of emeralds to compare with their impurity concentrations. To verify the consistency of these peak position values even under slightly imperfect orientation of the sample's c-axis relative to the excitation beam's polarization direction, here we reproduce the procedure outlined by Thompson et al. (2014) for collecting angular distributions of these parameters. The procedure was carried out using a hexagonal prismatic crystal sample from each of the three geographic origins (again, see figure 1). The c-axis of these samples lay parallel to the prism's central axis and perpendicular to the end faces.

Initially, each sample's c-axis was aligned parallel to the laser light's horizontal polarization axis and perpendi-

Figure A-1. Examples of emerald orientations used to collect PL spectra at different angles between the crystal's c-axis and the laser beam's polarization axis. The top row shows the crystal's c-axis oriented parallel with the laser beam's horizontal polarization axis, creating the E ∥ c orientation. With the fiber-optic collection lens located to the left of the sample, the laser illuminates the bottom left edge of the emerald. The middle row shows the crystal's c-axis at a 50° angle from the beam's polarization axis. The same edge region of the crystal is illuminated by laser light. The bottom row shows the crystal's c-axis perpendicular to the beam's polarization axis, creating an E ⊥ c orientation. Once again, the same edge region of the crystal is illuminated. Photos by D.B. Thompson.

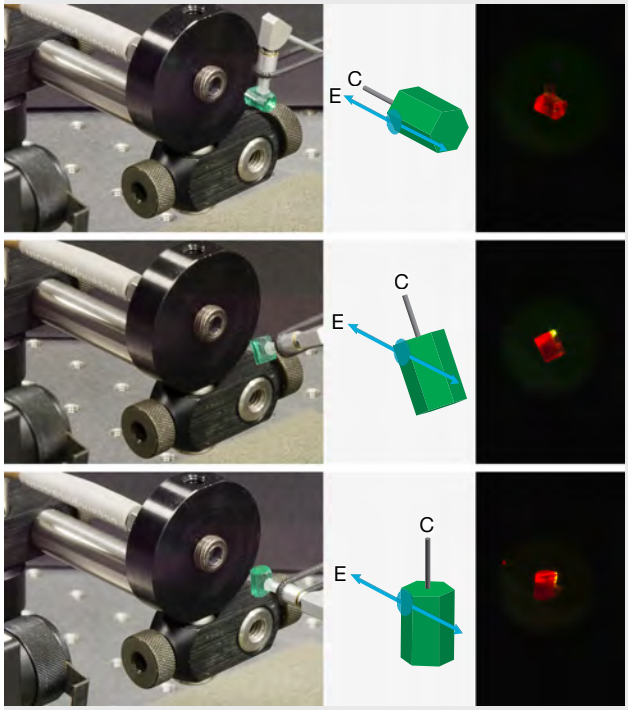

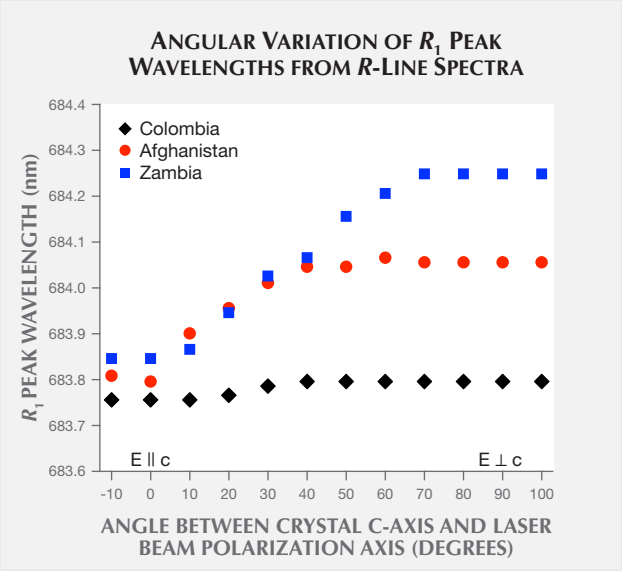

Figure A-2. The angular variation of R_1 *peak wavelengths extracted from* R*-line spectra of emerald crystals from the three geographic origins.*

cular to the laser beam propagation direction itself to create the E ∥ c orientation. Then the sample's c-axis could be rotated to create any angle between it and the laser's polarization axis, including the E ⊥ c orientation (see figure A-1). For each sample, the procedure involves collecting 12 PL spectra at 10° intervals, ranging from 10° below E ∥ c to 10° above the E ⊥ c orientation. As described in the text, we isolated the *R*-line contribution from each spectrum to create an *R*-line spectrum, from which we extracted R_1 and R_2 peak positions and count rates.

Plotting each sample's R_1 peak positions on an angular scale (figure A-2), it is readily apparent that the peak wavelengths of samples from the three different geographic regions exhibit a much wider spread in the E ⊥ c orientation than the E ∥ c orientation. For all three samples, the value of the R_1 peak wavelength is constant for angles between E and c-axes from E ⊥ c to 70°. Below that angular range, the peak wavelength varies continuously through to the E ∥ c orientation.

A plot of each sample's R_2 peak positions on an angular scale (figure A-3) shows that the Colombian and Afghan samples have nearly the same set of peak wavelength values across the angular range, while the Zambian sample's peak positions occur at consistently lower wavelengths. As with the R_1 line, the value of the R_2 peak wavelength for all three samples remains relatively constant up to 20° away from the E ⊥ c orientation.

Figure A-3. The angular variation of R_2 *peak wavelengths extracted from* R*-line spectra of emerald crystals from the three geographic origins.*

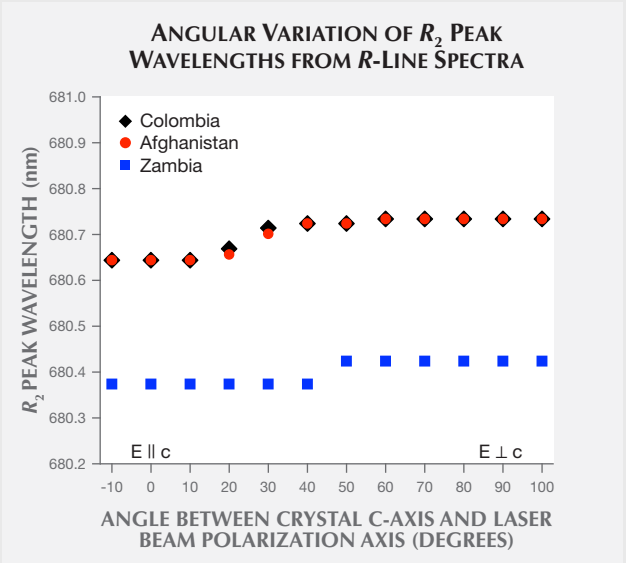

Finally, a plot of each sample's R_1/R_2 peak height ratio on an angular scale (figure A-4) shows that this ratio varies across the entire angular range from E ⊥ c orientation to E ∥ c orientation. For all three samples, the maximum value of this ratio occurs at the E ⊥ c orientation and the minimum value occurs at the E ∥ c orientation.

These comparisons of *R*-line spectral parameters at different angles explain why the present study concentrates on peak wavelengths extracted from E ⊥ c spectra. The primary reason is that the E ⊥ c orientation leads to the widest spread in R_1 peak positions. Nearly as important from a measurement perspective is that a slight misalignment away from this orientation will not alter the values of these peak wavelengths. Similarly, the R_2 peak position measurements at the E ⊥ c orientation are slightly more resistant to small misalignment.

In contrast to *R*-line peak wavelengths, values for the R_1/R_2 peak height ratios are sensitive to the angle between the crystal's c-axis and the excitation beam's polarization. While this sensitivity makes the R_1/R_2 peak height ratio a useful check of angular alignment, here we need not consider this peak parameter any further.

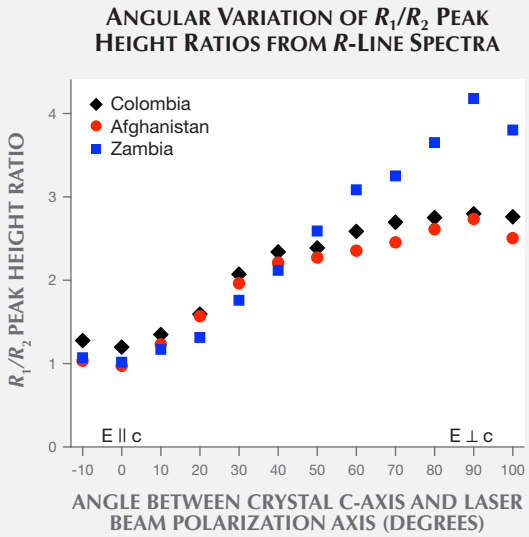

Figure A-4. The angular variation of R_1/R_2 *peak height ratios extracted from* R*-line spectra of emerald crystals from the three geographic origins.*

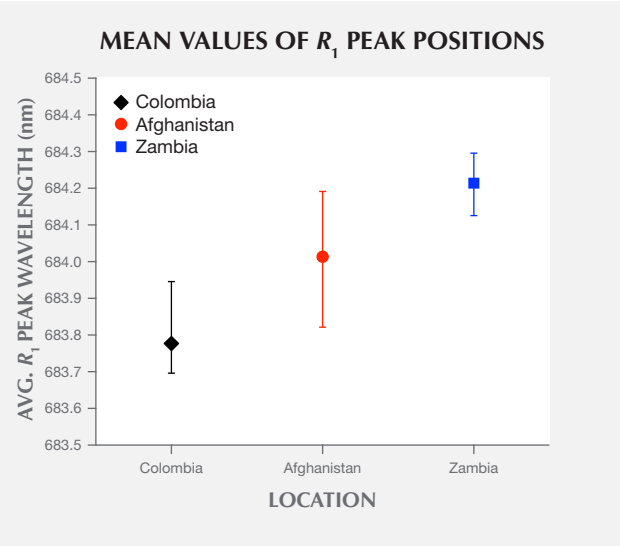

Figure 6. Mean values of R_1 *peak positions extracted from the* R*-line spectra of emerald samples from three regions. The black diamond corresponds to the mean value of 20 Colombian samples, the red circle to the mean value of 16 Afghan samples, and the blue square to the mean value of 12 Zambian samples. The error bars identify maximum and minimum wavelength values recorded for samples from each region.*

An independent sample *t* test was also performed between Afghan and Zambian samples. Similarly, there were extremely significant differences in the distributions for the Afghan (N = 16, M = 684.013 nm, SD = 0.084 nm) and Zambian samples (N = 12, M = 684.214 nm, SD = 0.046 nm); t(26) = 7.46, $p < 0.0001$, 95% CI [0.145 nm, 0.255 nm]. Once again, the low *p* value between this pair of sample datasets indicates that the measured difference between peak wavelengths probably does not arise from an accident of sampling.

Comparing the R_1 peak wavelengths dataset with each trace element concentration dataset (table 1) provided by GIA, the Mg and Na concentration datasets have very strong correlations with the R_1 peak wavelengths dataset. Each concentration dataset has the same coefficient of determination with the wavelengths dataset, namely $r^2 = 0.83$. By contrast, comparisons between the R_1 peak wavelengths dataset and all other trace element concentration datasets yield values for coefficients of determinations below 0.64.

A plot of all samples' R_1 peak wavelength vs. Mg concentration (figure 7) illustrates the first correlation. For this case, the best-fit trend line resulting from linear regression predicts a minimum R_1 peak wavelength (with no Mg concentration) of 683.65 nm and a peak shift of 0.048 nm per 1000 ppma increase in Mg concentration. The scatterplot also outlines the trend line's 95% confidence band, where a new data point collected from a random sample is predicted to fall within this band 19 times out of 20 (Natrella, 2013).

Very similar correlation is seen in a plot of all samples' R_1 peak wavelength vs. Na concentration (figure 8). The trend line here predicts nearly the same minimum R_1 peak wavelength (with no Na concentration) of 683.66 nm and a peak shift of 0.041 nm per 1000 ppma increase in Na concentration. The scatterplot also shows this trend line's 95% confidence band.

Returning to the *R*-line spectra (figure 5), the Colombian and Afghan samples' R_2 lines peak at similar wavelengths, while the Zambian sample's line is shifted to a shorter wavelength. A plot of the mean R_2 peak wavelength of samples from each origin (figure 9) shows that Colombian and Afghan samples' mean peak positions are overlapped by the extreme values in their distributions. In contrast, the mean peak position of Zambian samples is shifted to

Figure 7. A plot of each sample's R_1 *peak wavelength vs. Mg concentration. The coefficient of determination between these two datasets is* $r^2 = 0.83$*. The solid black trend line has a slope of 0.049 nm/1000 ppma and an intercept at 683.65 nm. The two dashed green lines outline the 95% confidence band for predictions using the best-fit trend line.*

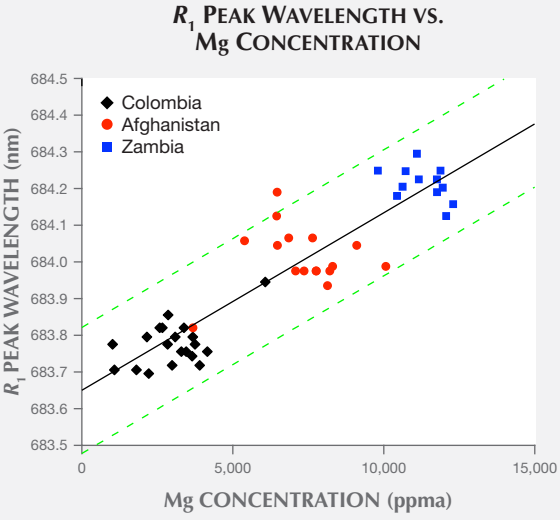

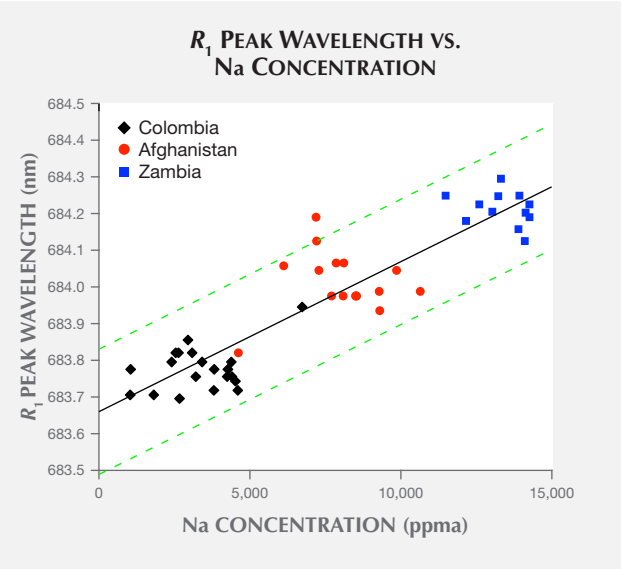

Figure 8. A plot of each sample's R_1 *peak wavelength vs. Na concentration. The coefficient of determination between these two datasets is* $r^2 = 0.83$. *The solid black trend line has a slope of 0.041 nm/1000 ppma and an intercept at 683.66 nm. The two dashed green lines outline the 95% confidence band for predictions using the best-fit trend line.*

a shorter wavelength and is not overlapped by the other samples' distributions.

To compare R_2 peak wavelength distributions between Afghan and Zambian samples, independent sample *t* tests were performed. The results show extremely significant differences in the distributions for the Afghan (N = 16, M = 680.699 nm, SD = 0.042 nm) and Zambian samples (N = 12, M = 680.461 nm, SD = 0.041 nm); t(26) = 15.00, $p < 0.0001$, 95% CI [0.205 nm, 0.270 nm]. Here, the *p* value for the Afghan and Zambian samples indicates little probability that they share the same mean value for R_2 peak wavelength.

An independent sample *t* test was also performed between Colombian and Afghan samples. The results show no significant differences in the distributions for the Colombian (N = 20, M = 680.712 nm, SD = 0.047 nm) and Afghan samples (N = 16, M = 680.699 nm, SD = 0.042 nm); t(34) = 0.87, $p = 0.39$, 95% CI [0.017 nm, 0.044 nm]. This high *p* value for the Colombian and Afghan samples indicates significant probability that they may share the same mean value for R_2 peak wavelength.

When the R_2 peak wavelengths dataset is compared with each trace element concentration dataset, Li ion concentration (table 1) has the strongest correlation, with coefficient of determination $r^2 = 0.79$. The Na ion concentration dataset also shows strong correlation with R_2 peak wavelengths, with coefficient of determination $r^2 = 0.68$. The coefficients of determination between the R_2 peak wavelengths dataset and all other trace element concentration datasets have values well below 0.64. A plot of R_2 peak wavelength vs. Li concentration (figure 10) illustrates their correlation. Here the best-fit trend line predicts a maximum R_2 peak wavelength (with no Li concentration) of 680.74 nm and a peak shift of –0.154 nm per 1000 ppma increase in Li concentration. The scatterplot also shows this trend line's 95% confidence band.

Examining the full set of PL emission spectra (again, see figure 3), it is apparent that even though the narrow *R* lines' structure varies from one location to another, the overall shape of the broadband structure is roughly similar. As the PL emission arises from Cr substituting at Al sites in the beryl crystal, we first consider if the peak count rate of this broadband structure (located at about 715 nm) might be directly proportional to the emerald sample's Cr concentration. A plot of all samples' broadband peak count rates vs. Cr concentration (figure 11) shows no evidence that they are directly propor-

Figure 9. Mean values of R_2 *peak positions extracted from the* R*-line spectra of emerald samples from the selected countries. The black diamond corresponds to the mean value of 20 Colombian samples, the red circle to 16 Afghan samples, and the blue square to 12 Zambian samples. The error bars identify maximum and minimum wavelength values recorded for each region.*

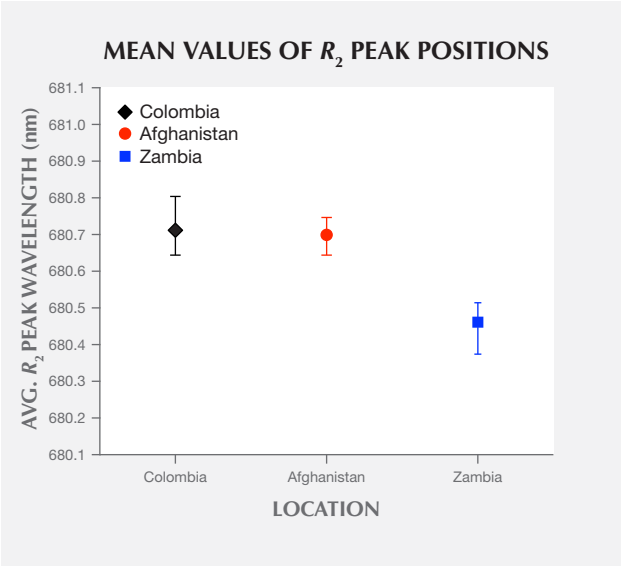

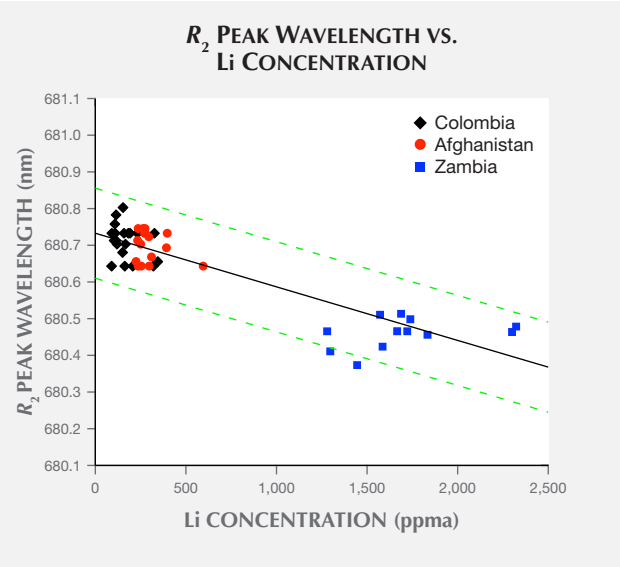

Figure 10. A plot of each sample's R_2 peak wavelength vs. Li concentration. The coefficient of determination between these two datasets is $r^2 = 0.79$. The solid black trend line has a slope of –0.154 nm/1000 ppma and an intercept at 680.74 nm. The two dashed green lines outline the 95% confidence band for predictions using the best-fit trend line.

tional. In this plot, most Colombian samples have low Cr concentrations and high count rates. Then there were Zambian samples that had high Cr concentrations and very low count rates, and Afghan samples appear all over the plot. Granted, the peak count rate does also depend upon the PL collection efficiency of the instrument. But with the luminescence collection volume (defined by the overlap of light beam, emerald, and optical fiber field of view) confined along one edge of the emerald, and with an effort to position the emerald edge to maximize these count rates, we do not expect much variation in collection efficiency.

As mentioned earlier, Fe ions can also substitute at Al cation sites in the beryl crystal, and it is well known that Fe dissipates PL emission by Cr (Nassau, 1978). A plot of all samples' broadband peak count rates vs. Fe concentration (figure 12) shows that count rates drop exponentially with increasing Fe concentration. Thus, the high Fe concentration in Zambian emeralds explains the low values of their observed count rates.

Following these examinations, we attempted to construct an empirical model where peak count rate was proportional to Cr concentration and decayed exponentially with increasing Fe concentration. In testing this model against our data, we found that peak count rate was better predicted when it was proportional to the square root of Cr concentration. The empirical formula we found that best predicts count rate I is

$$I = A\sqrt{[\mathrm{Cr}]} \cdot 10^{-\frac{[\mathrm{Fe}]}{B}} \qquad \text{(equation 1)}$$

where [Cr] and [Fe] are chromium and iron atomic concentrations, respectively (see box B). The empirical parameter B in the exponent is the Fe concentration that reduces Cr photoluminescence count rate by a factor of ten, while the parameter A represents the instrument's collection efficiency. Rewriting equation 1 as a linear function of iron concentration [Fe]

$$\log(I/\sqrt{[Cr]}) = -[Fe]/B + \log(A) \qquad \text{(equation 2)}$$

suggests plotting the common logarithm of each sample's $I/\sqrt{[Cr]}$ ratio vs. iron concentration (figure 13). This pair of datasets has a coefficient of determination $r^2 = 0.85$. Linear regression establishes values for the empirical parameters. The best-fit value for A is 1400, but this parameter is not much use beyond our experiment since it would have to be refitted for a different setup. The best-fit value for B is 2200 ppma Fe. This B parameter is independent of experimental setup, and it quantifies the low count rates observed

Figure 11. A plot of each sample's PL count rate at the 715 nm peak of broadband emission vs. chromium concentration. Colombian samples with low Cr concentrations exhibit high count rates, while Zambian samples with high Cr concentrations exhibit low count rates.

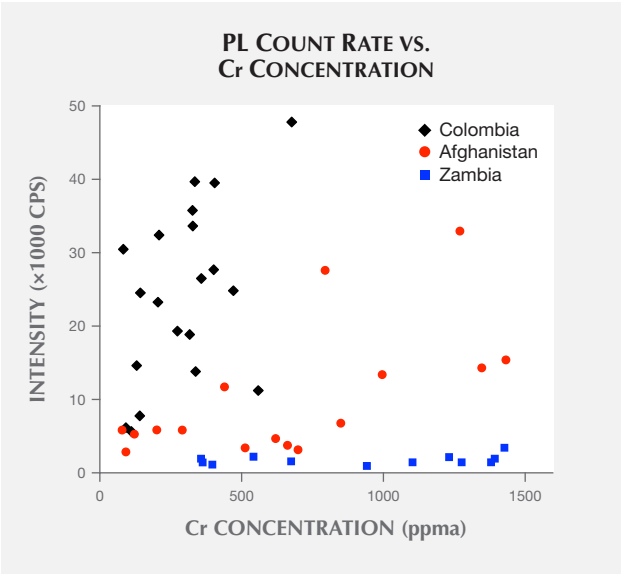

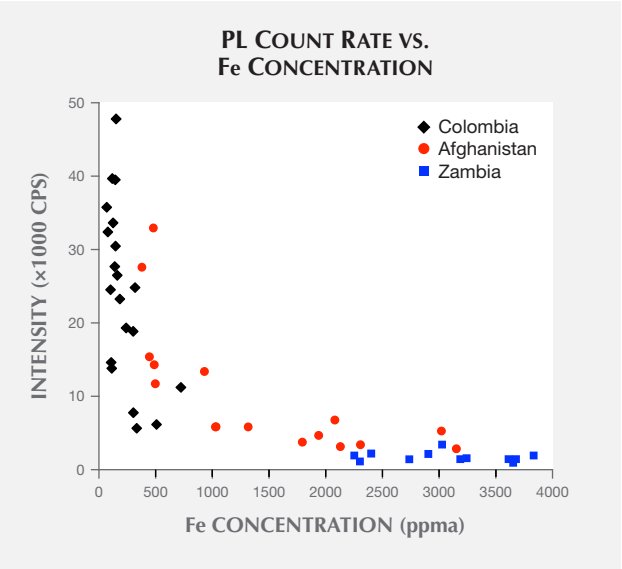

Figure 12. A plot of each sample's PL count rate at the 715 nm peak of broadband emission vs. iron concentration. Colombian samples with low Fe concentrations exhibit high count rates, while Zambian samples with high Fe concentrations exhibit low count rates. The general trend appears to be an exponential decay of count rate as Fe concentration increases.

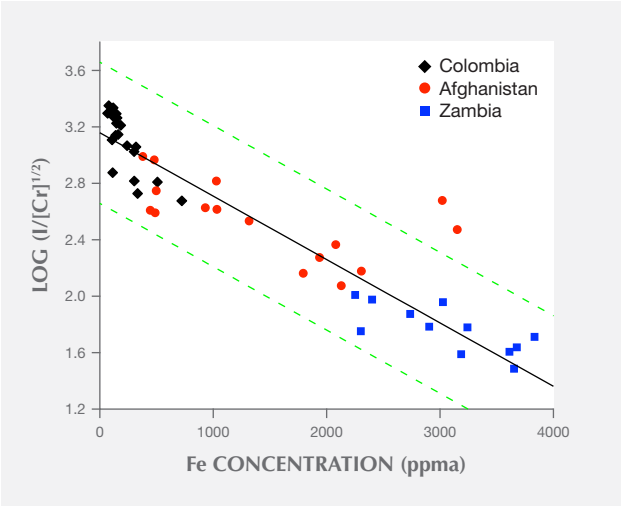

Figure 13. Dividing PL count rates of each sample's broadband peak emission I *by the square root of its chromium concentration [Cr], and taking the common logarithm, with the results plotted versus each sample's iron concentration [Fe]. These datasets have coefficient of determination* $r^2 = 0.85$. *Our model prediction suggests the data should follow a trend line given by equation 2 in the text, which contains empirical parameters* A *and* B. *The solid black trend line is a plot of equation 2 using the best-fit values for these parameters,* A = *1400 and* B = *2200 ppma Fe. The two dashed green lines outline the 95% confidence band for predictions using the best-fit trend line.*

from Zambian samples. In figure 13, all Zambian samples have Fe concentrations above the 2200 ppma concentration, reducing PL emission by a factor of ten; several samples have Fe concentrations above 3300 ppma concentration, reducing emission by a factor of 30. With the empirical parameters determined from regression, the empirical formula predicts count rates in our setup within a factor of two of all samples' observed count rates except for two Afghan samples. The formula underestimates count rates of these two samples by about a factor of six.

DISCUSSION

Using an *R*-line Wavelength Measurement to Reject a Possible Origin. *R*-line peak wavelength values extracted from the PL spectra of emeralds exhibit distributions that tend to be localized according to geographic origin. Here we consider how one might use these distributions as an aid to origin identification. Assuming each origin's measured distribution of *R*-line peak wavelengths represents that population's true normal probability distribution[2], we consider an *R*-line peak wavelength extracted from a random sample's PL spectrum. If the random sample's origin is completely unknown, and its origin might not be any of the three considered here, how can knowledge of the sample's *R*-line peak wavelength be used to reject one or more of these as possible origin assignments?

Answering this question requires setting a significance threshold. If a comparison of the sample's *R*-line measurement with an origin population's distribution has a *p* value that is less than the chosen significance threshold, then that population is rejected as a possible sample origin. Here the *p* value is the probability of measuring an *R*-line peak wavelength from a population's sample that is equal to or more extreme than what was actually measured (Kahn, 2016). Given the uncertainties in the mean values and standard deviations of distributions pre-

[2]One can use the number of measured samples (N) from the population to quantify how far the measured distribution may deviate from the population's true probability distribution by determining uncertainties in the measured distribution's mean and standard deviation (Natrella, 2013). The 95% CI uncertainties in mean values of R_1 peak wavelengths range from ±0.028 nm for Colombian samples to ±0.045 nm for Afghan samples; the same 95% CI uncertainties in standard deviations range from ±0.018 nm for Colombian samples to ±0.034 nm for Afghan samples.

Box B: Testing the Empirical Formula Relating PL Intensity to Cr and Fe Concentrations

To test the empirical formula represented by equations 1 and 2, we extracted broadband peak intensities from PL spectra collected from an additional nine natural emerald samples with different origins. These samples also were provided by GIA's Bangkok laboratory, and they were similarly altered with polished faces perpendicular to their c-axes. The laboratory also provided chemical concentrations of each sample, which were measured using LA-ICP-MS. Three of the samples were from the Chivor mine in Colombia, and another three from the Davdar emerald mines in China; these six samples were used in the report by Saeseaw et al. (2014). The last three samples were collected by GIA from the Swat Valley region of Pakistan but were not used in the Saeseaw report.

The results of this test appear in a scatterplot (figure B-1) showing the common logarithm of each test sample's $I/\sqrt{[Cr]}$ ratio vs. its Fe concentration. The test data shows general agreement with the corresponding trend line plot of equation 2 (using best-fit values of parameters listed in figure 13), with all data points located within the trend line's 95% confidence band. In addition, the empirical formula written as equation 1 predicts count rates for all test samples within a factor of two of their observed count rates.

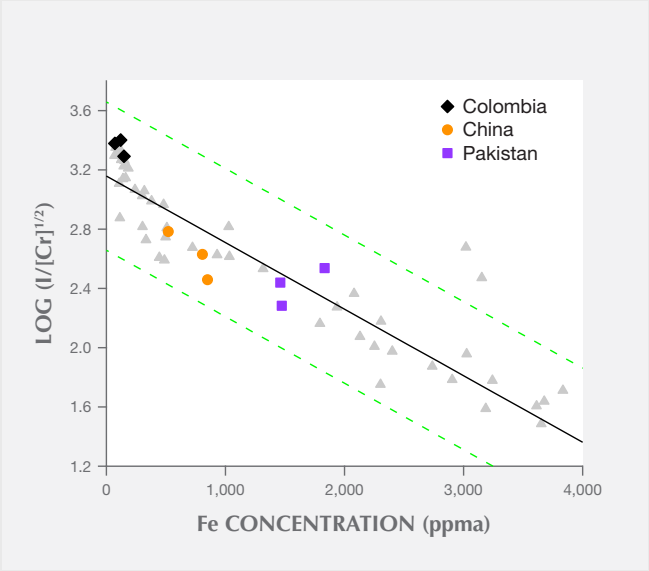

Figure B-1. Dividing PL count rates of each test sample's broadband peak emission I *by the square root of its chromium concentration* [Cr], *and taking the common logarithm, with the results plotted versus each test sample's iron concentration [Fe]. The black diamonds represent data from Colombian samples, the violet squares Pakistani samples, and the orange circles Chinese samples. The gray triangles reproduce the datasets presented in figure 13. The solid black trend line is a plot of the best-fit form of equation 2 to those datasets, and the dashed green lines form the boundaries of the equation's 95% confidence band.*

sented here, one might choose to set the significance threshold at an extreme value of 0.0001.

The rejection criterion can be simplified by using a z score. The z score between a measured value x and a population with mean M and standard deviation SD is given by $z = |x - M|/SD$, and it identifies how many standard deviations away from the mean the value x falls (Natrella, 2013). The range of probability values $p < 0.0001$ corresponds to a z score range of values $z > 3.70$ (Abramowitz and Stegun, 1972). If the z score between a random sample's R-line peak wavelength measurement and an origin population's peak wavelength distribution is greater than 3.70, then that population is rejected as a possible sample origin.

As an example, consider an extreme R_1 peak wavelength value that appeared in our Colombian dataset. The R_1 peak wavelengths of most Colombian samples cluster around the reported mean value M = 683.777 nm with standard deviation SD = 0.060 nm. But as shown in figures 7 and 8, one sample known to be of Colombian origin has an R_1 peak wavelength value x = 683.946 nm. Of the 20 Colombian samples reported here and six other examples reported by Thompson et al. (2014), this value is by far the most extreme recorded for a Colombian sample. The z score between this sample's R_1 peak wavelength and the Colombian distribution is z = 2.817, so it does not meet the threshold for rejection.

However, the z score between that sample's R_1 peak wavelength and the Afghan distribution is only $z = 0.798$, well below the rejection criterion. If the origin of this sample was truly unknown, we could not reject either Colombia or Afghanistan. In contrast, the z score between the sample's R_1 peak wavelength and the Zambian distribution is $z = 5.826$, which exceeds the threshold for rejection. Therefore, Zambia can be rejected as a possible origin.

As another example, could a sample with R_1 peak wavelength equal to $x = 684.000$ nm possibly be from Colombia? The z score between this R_1 peak wavelength and the Colombian distribution is $z = 3.717$, which exceeds the minimum z value for rejection. We therefore would reject Colombia as a possible origin for any sample with R_1 peak value at or above this wavelength.

Identifying a Mechanism Responsible for Shifts in R_1-Line Peak Wavelengths. We propose that the trace element dataset producing the highest coefficient of determination with a particular R-line dataset is most likely the impurity substitution responsible for shifting the R-line's peak wavelength. When two or more trace element datasets produce similar high values of r^2 with the R-line's dataset, we must consider how each may be involved with the R-line's peak shift.

As noted earlier, the shift in R_1 peak wavelength with increasing Mg and Na impurity concentrations shows very strong correlations, with the same coefficient of determination for both concentration datasets, $r^2 = 0.83$. These strong correlations suggest that the R_1 peak shift arises primarily from the aliovalent substitution of Mg at Al octahedral crystal sites, with charge balance provided by Na occupying an open channel site: $Al^{3+} \leftrightarrow Mg^{2+} + Na^{+}$.

Comparing the Mg and Na ion concentration datasets reveals that the presence of one ion correlates very strongly with the presence of the other, with a coefficient of determination $r^2 = 0.99$ between the two datasets. Yet a plot of Mg vs. Na concentration (figure 14) does not exhibit a one-to-one match, where each Mg ion would be accompanied by exactly one Na ion. In fact, the trend line resulting from linear regression reveals a slight excess of Na ions, where 10 Mg ions are matched by 11 Na ions. This 10% difference between Na and Mg ion concentrations may arise from a matrix effect in the LA-ICP-MS measurements (Sylvester, 2008). The efficiency with which different ions are ablated from the NIST glass matrix used for calibration may differ slightly

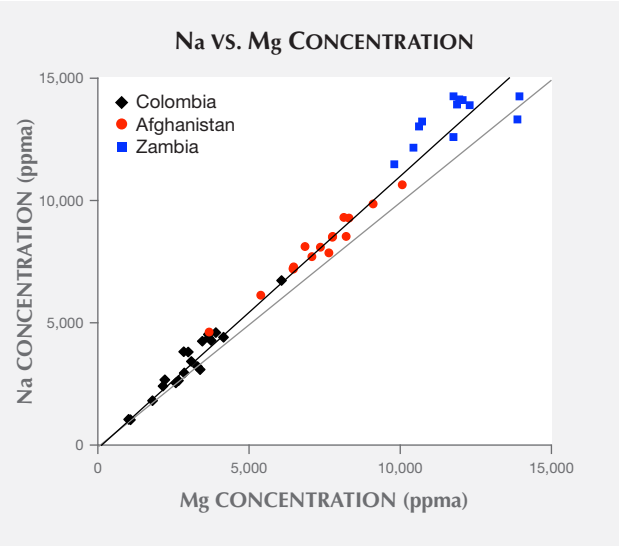

Figure 14. A plot of each sample's sodium vs. magnesium concentration. The coefficient of determination between these two datasets is $r^2 = 0.99$. *The black trend line has a slope of 1114 ppma Na/1000 ppma Mg. For comparison, the gray line has unit slope.*

from the efficiency of ions released by ablation from beryl matrix. If an excess of Na ions does not originate from a matrix effect, however, these ions may contribute to the R_2 peak shift, as described below.

Identifying a Mechanism Responsible for Shifts in R_2-Line Peak Wavelengths. As noted in the Results section, the R_2 peak wavelengths dataset exhibits strong correlation with the Li ion concentration dataset, with coefficient of determination $r^2 = 0.79$. The lack of correlation between R_2 peak positions and divalent and trivalent cation concentrations suggests that substitution at Al crystal sites is not responsible for the R_2 peak shift. Conversely, Li is the only cation that substitutes at the tetrahedral Be crystal site in beryl (Aurisicchio et al., 1988). To maintain charge balance, an accompanying alkali ion also must occupy an interstitial site. Besides Li concentrations, only the Na concentration dataset shows any significant correlation with the R_2 peak wavelengths dataset, with coefficient of determination $r^2 = 0.68$.

As described above, most Na atoms appear to be paired with Mg atoms. In attempting to isolate the "excess Na" concentration (comprised of those Na ions not paired with Mg) by subtracting Mg concentrations from corresponding Na concentrations, the resulting excess Na concentration dataset shows slightly stronger correlation with R_2 peak positions than does the full Na dataset, with coefficient of de-

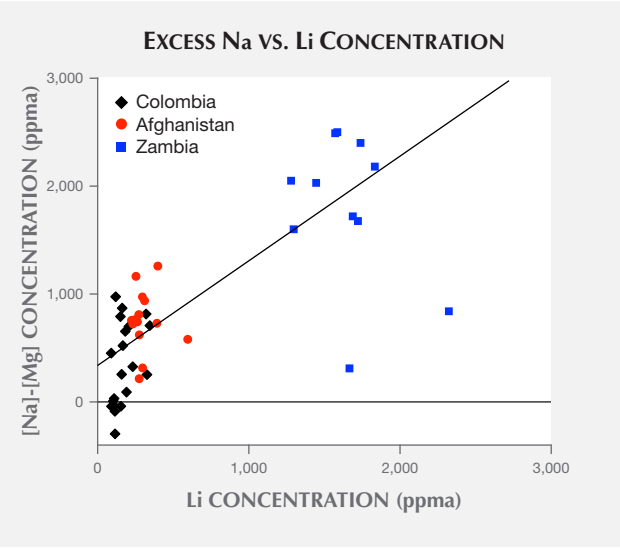

Figure 15. A plot of each sample's "excess Na" (the difference between sodium and magnesium concentrations) vs. lithium concentration. The coefficient of determination between these two datasets is r^2 = *0.66. The black trend line has a slope of 970 ppma Na/1000 ppma Mg and an intercept of 330 ppma excess Na.*

termination $r^2 = 0.72$. Adding the excess Na concentrations to corresponding Li concentrations creates even stronger correlation with R_2 peak positions, with coefficient of determination $r^2 = 0.83$. This coefficient of determination is higher than that achieved using the Li dataset by itself.

Comparing the Li and excess Na ion concentration datasets gives a coefficient of determination $r^2 = 0.66$, just barely exceeding the strong correlation threshold. A scatterplot of Li concentrations vs. excess Na concentration (figure 15), along with a best-fit trend line, demonstrates the correlation. The scatterplot does exhibit many outliers, including examples where subtracting a sample's Mg concentration from the corresponding Na concentration produces a slightly negative value. Overall, there appear to be several instances where there is not enough excess Na to match up with Li.

The strong correlation between samples' R_2 peak wavelengths and Li impurity concentrations suggests that the R_2 peak shift arises primarily from Li ions substituting at the tetragonal Be crystal sites. Interpreting correlations of excess Na impurity concentrations with the R_2 peak shift and with Li concentrations suggests that when Na ions are available, they may provide charge balance for the substitution. When Na ions are not available, we propose that the charge balance may be maintained by an additional Li ion occupying an open channel site: $Be^{2+} \leftrightarrow Li^+ + Na^+, Li^+$.

CONCLUSIONS

We have collected photoluminescence spectra of emerald samples from Colombia, Afghanistan, and Zambia. Extracting peak wavelengths of *R* lines appearing in emerald's E ⊥ c PL spectrum, we observed that values tend to be distributed according to geographic origin. With knowledge of localized distributions from a given origin, an *R*-line measurement of a random sample can provide evidence for or against the possibility of that origin.

Emerald samples from these three different origins were selected because they displayed distinctly different trace element impurity concentrations. Comparing peak positions of their *R* lines with corresponding concentrations of impurity ions, we have identified strong correlations between *R*-line peak shifts and increasing concentrations of specific impurities. In particular, the *R*-line peak wavelengths can also be used to estimate concentrations of three non-chromophore impurities in emerald: magnesium, sodium, and lithium. This assessment can supplement measurements of these impurities using other chemical composition analysis techniques, such as X-ray fluorescence, electron microprobe analysis, and LA-ICP-MS. The correlations also suggest likely mechanisms responsible for the *R*-line peak shifts.

Finally, comparing peak intensities of the broadband structure appearing in PL spectra with corresponding concentrations of chromium and iron impurities led to identification of an empirical formula where photoluminescence count rate increases with the square root of chromium concentration and decreases exponentially with increasing iron concentration. While it has long been known that iron impurities tend to quench chromium photoluminescence in gemstones, here we have quantified this effect.

ABOUT THE AUTHORS

Dr. Thompson is a professor in the department of physics and earth science at the University of North Alabama in Florence. Mr. Bayens worked with Dr. Thompson as an undergraduate researcher and is now a client systems engineer at Epic Systems in Madison, Wisconsin. Mr. Morgan, a former student of Dr. Thompson, is now an electronics engineer for the U.S. Army at Redstone Test Center in Huntsville, Alabama. Mr. Myrick is a student in electrical engineering at the University of Alabama in Tuscaloosa. Ms. Sims, a former student of Dr. Thompson, is a doctoral student in geophysics at the University of Alaska, Fairbanks.

ACKNOWLEDGMENTS

The authors thank Kenneth Scarratt for making emerald samples available for study. We also appreciate Vincent Pardieu for his support in providing samples. We are deeply grateful to Sudarat (Kai) Saeseaw for preparing samples and for providing their chemical concentration measurements. Lastly, we thank H. David Muse for checking the veracity of our statistical inferences.

REFERENCES

Abramowitz M., Stegun I.A. (1972) *Handbook of Mathematical Functions*. NBS Applied Mathematical Series 55, National Bureau of Standards, Washington, DC, Table 26.1, pp. 966–972.

Aurisicchio C., Fioravanti G., Grubessi O., Zanazzi P.F. (1988) Reappraisal of the crystal chemistry of beryl. *American Mineralogist*, Vol. 73, No. 7-8, pp. 826–837.

Crow E.L., Davis F.L., Maxfield M.W. (1960) *Statistics Manual*. Dover Publications, Mineola, New York.

Giuliani G., Ohnenstetter D., Fallick A.E., Groat L.A., Feneyrol J. (2012) Geographic origin of gems linked to their geological history. *InColor*, Vol. 19, pp. 16–27.

Goldman S.D., Rossman G.R., Parkin K.M. (1978) Channel constituents in beryl. *Physics and Chemistry of Minerals,* Vol. 3, No. 3, pp. 225–235, http://dx.doi.org/10.1007/BF00633572

Groat L.A., Giuliani G., Marshall D.D., Turner D. (2008) Emerald deposits and occurrences: A review. *Ore Geology Reviews*, Vol. 34, No. 1, pp. 87–112, http://dx.doi.org/10.1016/j.oregeorev.2007.09.003

Kahn D.S. (2016) *Attacking Probability and Statistics Problems*. Dover Publications, Mineola, New York, pp. 74–82.

Lai S.T. (1987) Highly efficient emerald laser. *Journal of the Optical Society of America B: Optical Physics*, Vol. 4, No. 8, pp. 1286–1290, http://dx.doi.org/10.1364/JOSAB.4.001286

Moroz I., Roth M., Boudeulle M., Panczer G. (2000) Raman microspectroscopy and fluorescence of emeralds from various deposits. *Journal of Raman Spectroscopy*, Vol. 31, No. 6, pp. 485–490, http://dx.doi.org/10.1002/1097-4555(200006)31:6%3C485::AID-JRS561%3E3.0.CO;2-M

Nassau K. (1978) The origins of color in minerals. *American Mineralogist*, Vol. 63, No. 3-4, pp. 219–229.

Natrella M.G. (2013) *Experimental Statistics*. Dover Publications, Mineola, New York.

O'Haver T.C. (2014) Peak finding and measurement [computer software]. *A Pragmatic Introduction to Signal Processing*. College Park, MD, http://terpconnect.umd.edu/~toh/spectrum/PeakFindingandMeasurement.htm

Saeseaw S., Pardieu V., Sangsawong S. (2014) Three-phase inclusions in emerald and their impact on origin determination. *G&G*, Vol. 50, No. 2, pp. 114–132, http://dx.doi.org/10.5741/GEMS.50.2.114

Schmetzer K. (1994) Torrington emerald update. *Australian Gemmologist*, Vol. 18, No. 10, pp. 318–319.

Schmetzer K. (2015) Letters: Photoluminescence of emeralds: Sample orientation procedure and correlation of the R1 peak position with SiO_2 contents. *Journal of Gemmology*, Vol. 34, No. 5, pp. 441–443.

Schmetzer K., Bernhardt H.-J. (1994) Isomorphic replacement of Al and Si in tetrahedral Be and Si sites of beryl from Torrington, NSW, Australia. *Neues Jahrbuch für Mineralogie Monatshefte*, Vol. 3, pp. 121–129.

Schwarz D., Schmetzer K. (2002) The definition of emerald–the green variety of beryl colored by chromium and/or vanadium. In Extralapis: Emeralds of the World, *extraLapis English* No. 2, Lapis International, East Hampton, Connecticut.

Sylvester P.J. (2008) Matrix effects in laser ablation-ICP-MS. In P.J. Sylvester, Ed., *Laser Ablation ICP-MS in the Earth Sciences: Current Practices and Outstanding Issues (Short Course)*. Vol. 40, Mineralogical Association of Canada, pp. 67–78.

Thomas T. (2009) Corundum c-axis device for sample preparation. *GIA Research News*, http://www.gia.edu/gia-news-research-nr6809

Thompson D.B., Kidd J.D., Åström M., Scarani A., Smith C.P. (2014) A comparison of R-line photoluminescence of emeralds from different origins. *Journal of Gemmology*, Vol. 34, No. 4, pp. 334–343.

Wood D.L. (1965) Absorption, fluorescence, and Zeeman effect in emerald. *Journal of Chemical Physics*, Vol. 42, No. 10, pp. 3404–3410, http://dx.doi.org/10.1063/1.1695742

Synthetic Star Sapphires and Rubies Produced by Wiede's Carbidwerk, Freyung, Germany

Karl Schmetzer, H. Albert Gilg, and Heinz-Jürgen Bernhardt

Asteriated synthetic rubies and sapphires were produced by Wiede's Carbidwerk of Freyung, Germany, between the mid-1950s and the end of the 1970s. The rough crystals were grown slowly through a proprietary variant of the Verneuil method, developed in the mid-1950s, in the form of almost spherical to elliptical boules. After crystal growth, rutile needles were exsolved by annealing at temperatures ranging from 1100°C to 1500°C. Notably, such needles were somewhat shorter than those generally produced in asteriated material from other Verneuil manufacturers, particularly Linde in the United States, giving the cabochons a slightly different visual appearance. Furthermore, the production process using oriented seeds and a variable temperature-time protocol resulted in samples consisting of up to three growth zones. Such properties may aid in identifying Wiede's synthetics produced up to the end of the 1970s.

During the 1940s and 1950s, various processes for the production and/or improvement of asterism in corundum were described in patent documents assigned to Linde Air Products Company or to the Linde division of Union Carbide and Carbon Corporation in the United States. The first patent application was filed in August 1947 and published in November 1949 by Burdick and Glenn. In principle, the creation of asteriated synthetic corundum was based on a two-step process comprising (1) the production of titanium-bearing corundum crystals and (2) the formation of rutile precipitates. The precipitates were responsible for scattering and reflecting incident light and thereby forming the three intersecting light bands of a six-rayed star. The first asteriated rubies and sapphires were grown by the Verneuil technique, with the addition of a titanium-bearing compound as a component of the nutrient powder (Burdick and Glenn, 1949). The patent mentioned that the alumina powder from which the crystals were grown should contain at least 0.1% and not more than 0.3% TiO_2. Without further dopants, colorless star sapphires were obtained; by including chromium oxide or iron oxide, rubies or blue sapphires could be produced.

The disadvantage of this basic process was that the resultant needle-like precipitates were confined to the skin of the Verneuil boules, thus restricting the size and number of asteriated cabochons that could be cut. Cabochons cut from the interior of the boules might not exhibit asterism, and blue sapphires could also show colorless zones in growth sectors without titanium. Furthermore, cabochons cut with the titanium-bearing skin in the center of the final cabochon might not display asterism on the sides toward the base (Burdick and Jones, 1954).

To overcome these disadvantages and grow rubies and sapphires with more complete stars—and without colorless zones in blue sapphires—it was necessary to have a more homogeneous distribution of titanium in the corundum crystals. Obtaining such an improved distribution was accomplished by growing the Verneuil boules under fluctuating thermal conditions. In practice, this fluctuation was achieved by alternately increasing and decreasing the rate of oxygen fed to the oxygen-hydrogen flame of the Verneuil burner. The process mentioned was patented in United States by Linde (Burdick and Jones, 1954), and a series of international applications were also filed (e.g., in Germany, Great Britain, France, and Switzerland). As represented schematically in the patent by Burdick and Jones, the sapphire and ruby boules grown under such conditions showed—in the direction of crystal growth—layers with high titanium contents in all

See end of article for About the Authors and Acknowledgments.
Gems & Gemology, Vol. 53, No. 3, pp. 312–324,
http://dx.doi.org/10.5741/GEMS.53.3.312
© 2017 Gemological Institute of America

Figure 1. Synthetic asteriated blue sapphire from the historical production of Wiede's Carbidwerk, Freyung, Germany. The sample weighs 2.63 ct and measures 8.9 × 6.8 mm. Fiber-optic illumination. Photo by K. Schmetzer.

zones, alternating with layers where titanium was restricted to the rim of the boules. Again, the concentration of titanium oxide within the alumina powder used for crystal growth was stated to be in the range of 0.1 to 0.3 wt.% TiO_2.

As a consequence of the protections against possible infringement afforded by the patent filings, other producers who wished to use the Verneuil process for growing gem-quality asteriated rubies and sapphires had to develop techniques different from that described in the Burdick and Jones patent. In particular, German researchers were successful in independently developing such a method. Synthetic asteriated corundum of German production began reaching the market in increasing quantities in the second half of the 1950s, and the material was described as contrasting with the Linde stones in both visual appearance and gemological properties (Breebaart, 1957).

The German synthetic star rubies and sapphires (figure 1) were grown by Wiede's Carbidwerk of Freyung, Bavaria, a family-owned company that had been creating rubies, sapphires, and variously colored spinels since about 1913 (Schmetzer et al., 2015). The technical differences between the German and American production processes were divulged in German patents DE 1 002 300 and DE 1 007 753 by Ancot and Eppler, both filed in February 1955 and then published in August and October 1957, respectively. Descriptions of the new asteriated gem corundum were also provided in gemological publications by Eppler (1957/1958, 1958 a,b). While these mentioned that a slower growth process was used in Germany, the emphasis was on contrasts in the gemological properties and visual appearance of the star rubies and sapphires produced by Linde and at Wiede's. The publications did not refer to the underlying patents or production methods that resulted in such differences between the two companies' materials.

The synthetic star rubies and sapphires produced by Wiede's Carbidwerk have similarly been mentioned in gemological textbooks covering asteriated corundum (e.g., Nassau, 1980; Hughes, 1997, 2017), but, again, details of the technology were neither given nor associated with properties of the samples. The present paper thus focuses on further closing the gap in the gemological literature regarding historical production processes for synthetic gem materials.

TECHNICAL INFORMATION DISCLOSED IN PATENT DOCUMENTS

The methods described by Ancot and Eppler (1957 a,b) in the patents cited above and assigned to Wiede's Carbidwerk were applied for the production of asteriated rubies and sapphires from the mid-1950s to the end of the 1970s. Later production methods for asteriated corundum at Wiede's no longer employed these specific techniques, primarily for economic reasons (H. Schulz, pers. comm., 2014).

In Brief

- In the 1950s, Wiede's Carbidwerk of Freyung, Germany, developed a proprietary, patented variant of the Verneuil method for growing asteriated synthetic corundum.
- Synthetic star rubies and sapphires were produced using this process from the mid-1950s to the late 1970s and were sold commercially, with the United States as one of the primary markets.
- The process employed oriented seeds and applied a variable time-temperature protocol, yielding elliptical to almost spherical boules with several distinct growth zones.
- Samples produced in the 1960s and 1970s have properties that differ slightly from those of asteriated corundum manufactured in the late 1950s and described in earlier research.

Both patent documents indicated that a better distribution of titanium throughout the complete Verneuil-grown corundum crystal was achieved if the TiO_2 content within the Al_2O_3 nutrient powder was increased beyond the 0.1% to 0.3% range described in

Figure 2. Synthetic asteriated corundum produced by Wiede's Carbidwerk. Left: Rough, almost spherical to elliptical boules of synthetic blue star sapphire and synthetic star ruby. The blue sapphire weighs 9.94 ct and measures 10.9 × 10.0 mm; the ruby (one of the samples split at the center and shown from both sides in figure 3) weighs 11.57 ct and measures 14.8 × 12.4 mm. Right: Three synthetic blue star sapphire cabochons and one synthetic star ruby cabochon in direct sunlight. The ruby weighs 8.92 ct and measures 13.2 × 11.0 mm; the sapphire at the bottom left weighs 3.67 ct and measures 9.1 mm in diameter. Photos by K. Schmetzer.

the patents assigned to Linde. Specifically, Ancot and Eppler quoted a percentage of up to 0.52% TiO_2. The titanium oxide was preferably added in the form of anatase. Without other modifications to the growth method, however, the titanium-enriched synthetic material so obtained was highly fragile. To overcome that problem, the melting time for production of the corundum boules was increased by at least a factor of two, or better yet by a factor of six. This, in turn, could be accomplished by decreasing the rate of powder fed per time unit to the growing surface of the crystal in the Verneuil burner.

In the temperature-time protocol applied for crystal growth, the temperature of the Verneuil flame was progressively increased during the initial phase of the production period by altering the oxygen-hydrogen ratio. The mixture of gases started at an O_2:H_2 ratio of 40:100 and was slowly changed to a ratio of 49:100 by the end of this first stage in the growth process. After the maximum O_2:H_2 ratio had been reached, further growth of the ruby or sapphire crystal during a second phase was performed while sustaining the high flame temperature at a constant level.

The resulting rough product did not take the typical form of a cylindrical boule; rather, the product was an almost spherical or elliptical corundum crystal (figure 2, left). The corundum sphere had relatively low internal tension, thus eliminating the normal stress-induced need for splitting cylindrical boules along their longitudinal axis. Rutile precipitates, which were obtained by exsolution in a subsequent heat-treatment step between 1100 and 1500°C using the classical annealing process described in the patents assigned to Linde (see above), were in general equally distributed throughout the ruby or sapphire spheres.

As an example, the production time (melting time) for a spherical corundum crystal of 13 mm in diameter has been quoted at 166 minutes. During the first phase of production, while the mixture of gases was being progressively altered, a spherical boule with a diameter of 10 mm could be obtained in a period of 85 minutes. During the second stage, performed while the high flame temperature was maintained, the diameter could be increased from 10 to 13 mm over a period of 81 minutes. In typical practice, only a single asteriated cabochon would be cut from such a heat-treated, rutile-bearing spherical to elliptical ruby or sapphire crystal (H. Schulz, pers. comm., 2014).

MATERIALS AND METHODS

To prevent any potential confusion with synthetic asteriated gem materials manufactured by Linde or any other producer, the present study started with samples obtained directly from Wiede's Carbidwerk. One synthetic blue sapphire boule, one sapphire cabochon, and one ruby cabochon were furnished by the producer in Freyung. All three samples had unquestionably been manufactured by the general method described in the patents cited above. Four Wiede's synthetic ruby boules from the Mineralogische Staatssammlung (Bavarian State Collection for Mineralogy), Munich, were made available as well. These samples most likely had been donated by Eppler, who also served as a professor teaching mineralogy and gemology at the University of Munich. One additional ruby and three sapphire cabochons

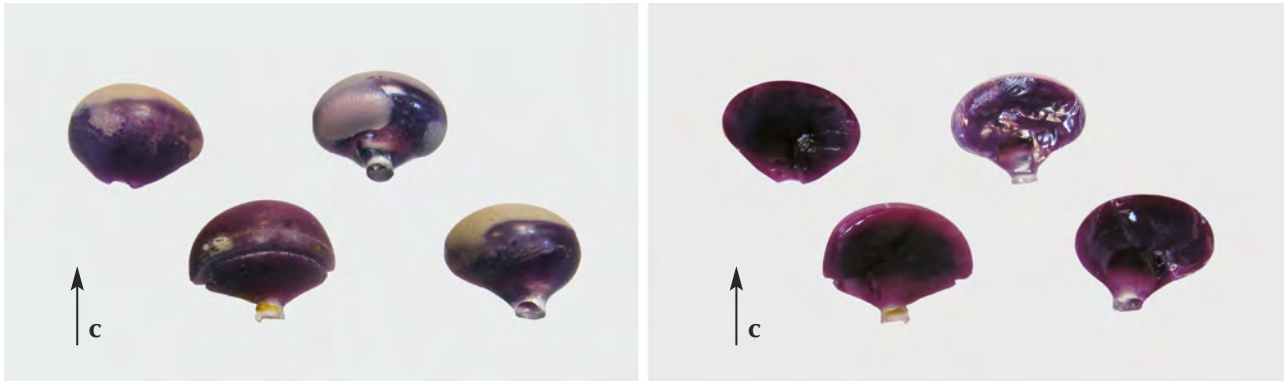

Figure 3. Four boules of synthetic asteriated ruby from Wiede's production. The samples were split at the center to show the internal structure, enabling comparison of the almost spherical outer surface (left) with the central split surface (right). The c-axis of the samples is indicated. The weights of the synthetic rubies range from 10.29 to 12.29 ct; the sample at the lower left measures 14.8 × 12.4 mm. Photos by K. Schmetzer.

with similar properties were provided from two private collections in Germany and Austria. In summary, we were able to examine one sapphire and four ruby boules and four sapphire and two ruby cabochons (figure 2).

All samples were inspected visually and microscopically, especially in immersion. For maximum visibility in evaluating growth zoning and the sizes of rutile needles, one slab was sawn from the base of the blue asteriated cabochon obtained directly from the producer (figure 1) and then polished. To resolve acicular inclusions, this slice and the bases and domes of all six cabochons were also examined at higher magnification (up to 1000×) than normally applied in gemology, in reflected and transmitted light, using a Leitz Ortholux II Pol-BK or a Leica DM LM polarizing microscope. Because the needles observed optically were of different sizes and extremely small in one sample, micro-Raman spectroscopy of four ruby and sapphire cabochons was performed with a focused as well as a defocused primary laser beam using a Horiba XploRA confocal Raman microscope with a 532 nm laser.

VISUAL APPEARANCE AND MICROSCOPIC FEATURES

The external shape of the five rough samples showed that crystal growth had initiated at a small colorless shaft and then gradually widened to larger diameters. The resulting synthetic ruby or sapphire crystals exhibited slightly flattened to slightly elongated (elliptical) or almost spherical forms (figures 3 and 4). As

Figure 4. Details of the outer surface of a synthetic asteriated ruby (left) and a synthetic asteriated blue sapphire (right) from Wiede's. The ruby (10.29 ct, 14.2 × 12.2 mm) is slightly flattened along the c-axis of the crystal, while the blue sapphire (9.94 ct, 10.9 × 10.0 mm) is slightly elongated. Because the ruby crystal has been split at the center, the internal growth zoning with sequential curved growth layers can be seen in detail (center). The c-axis runs north-south in all figures. Photos by K. Schmetzer.

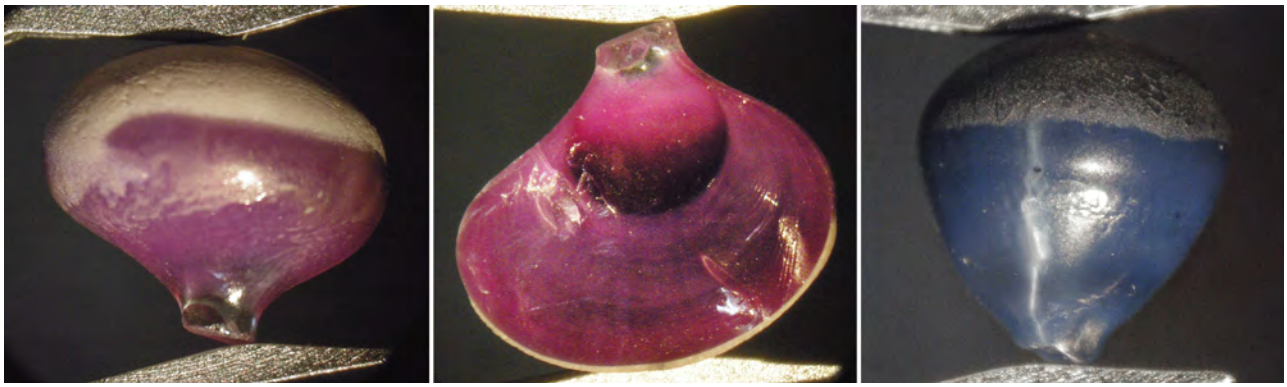

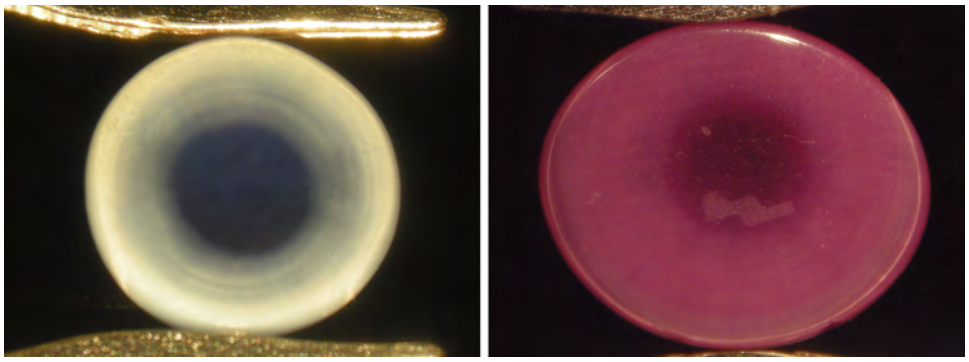

Figure 5. The bases of asteriated synthetic sapphire (left) and ruby (right) cabochons from Wiede's show a clear blue or red center and a somewhat milky bluish or reddish rim. The sapphire measures 7.2 mm in diameter; the ruby measures 13.2 × 11.0 mm. Photos by K. Schmetzer.

proven by the pleochroism of the crystals, the c-axis of the samples was parallel to the direction of crystal growth. Internal growth zoning in the form of sequential curved layers was observed (figure 4, center), especially in some of the ruby crystals that had been split in half (figure 3). These split boules offered a clear visual demonstration of the shell-like internal structure.

With regard to coloration and diaphaneity, three of the four sapphires and both rubies showed a distinct zoning when viewed toward the base of the cabochons, with a clear blue or red center and a somewhat milky bluish or reddish rim (figure 5). Such zoning was apparent when an almost spherical ruby or sapphire boule had been cut at or close to the largest diameter of the crystal (again, see figure 4, left and center). A "W" had been inscribed by sandblasting on the back of one of the cabochons to designate the producer (figure 5, right), a practice used for some of Wiede's asteriated stones (H. Schulz, pers. comm., 2014).

Conversely, any similarly clear central areas, if extant, were obscured in the rough samples. The rough crystals were principally opaque, appearing slightly translucent at best, due to a high concentration of gas bubbles. This was particularly evident throughout the larger, core regions of the crystals, with only the outermost layers of certain ruby samples showing slightly higher transparency than the central portions (again, see figure 3). For cut samples, in contrast to the rough material, three of the four examined sapphire cabo-

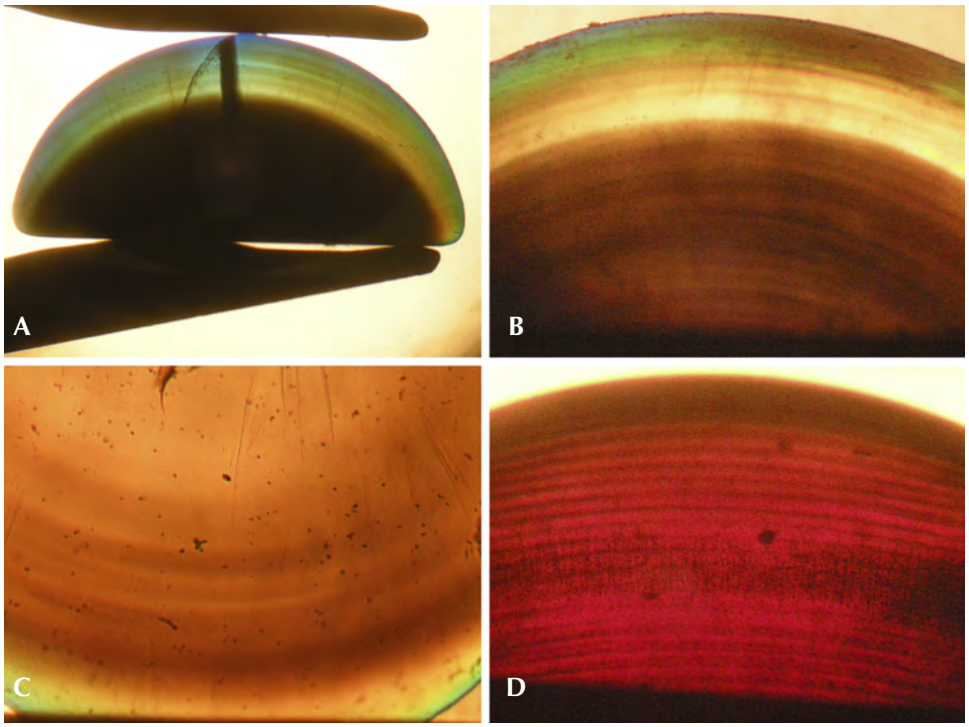

Figure 6. Blue asteriated synthetic sapphires (A–C) and one ruby (D) showing shell-like structures with different concentrations of gas bubbles in the center and at the rim. A: Sapphire cabochon, viewed perpendicular to the c-axis, measuring 8.9 × 4.2 mm; B: Another sapphire cabochon, viewed perpendicular to the c-axis, field of view 3.4 × 2.5 mm; C: A slab sawn from the base of the sapphire cabochon in figure 6A, viewed about 30° to the c-axis, field of view 4.0 × 3.0 mm; D: A ruby cabochon, viewed perpendicular to the c-axis, field of view 3.8 × 2.9 mm. Immersion, transmitted light. Photomicrographs by K. Schmetzer.

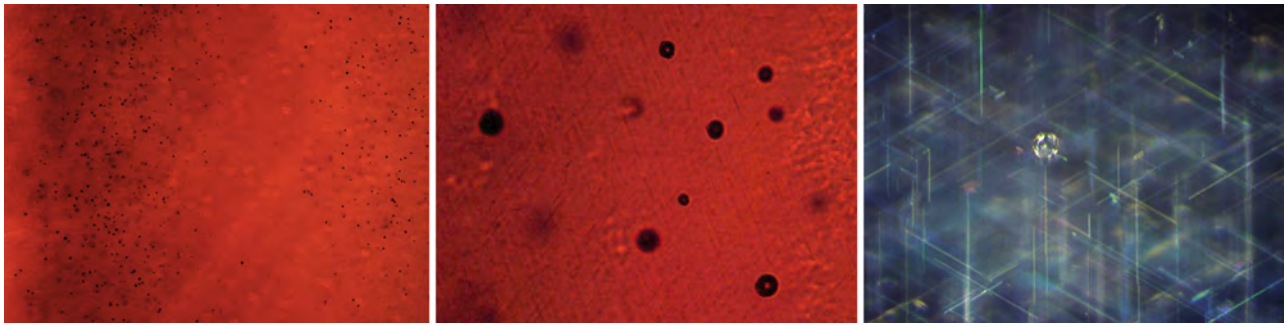

Figure 7. Gas bubbles are concentrated in various layers forming a shell-like structure around the center of the host (left). At higher magnification (center and right), the bubbles appear almost round. Left and center: Transmitted light, field of view 1.0 × 0.75 mm (left) and 100 × 75 µm (center). Right: Reflected light (in which rutile needles are also resolved), field of view 92 × 69 µm. Photomicrographs by H.-J. Bernhardt.

chons and one ruby showed an outermost layer with higher transparency than observed for the main body of the samples. This was best seen in immersion (figure 6, A and B), which clearly revealed a shell-like, layered structure, with different layers containing different concentrations of gas bubbles (figures 6, B–D and 7, left). At higher magnification, the gas bubbles appeared nearly round (figure 7, center and right).

In addition, the samples showed irregularly shaped grain boundaries that crossed the arms of the six-rayed star (figure 8, left). These grain boundaries (also designated as low-angle grain boundaries) could likewise be seen in immersion in transmitted light, together with prismatic glide planes (figure 8, right), the latter of which are referred to as "Plato" striations in the gemological literature. Higher magnification revealed that the grain boundaries (figure 9, left) were related to internal stress (figure 9, center) and that prismatic glide planes were mostly developed at the rim of the sample, forming angles of 120° with each other (figure 9, right). The nature of glide planes is discussed briefly in box A.

RUTILE NEEDLES

In the synthetic blue sapphires and rubies produced by Wiede's Carbidwerk, three series of needle-like

Figure 8. Grain boundaries of the Verneuil-grown synthetic blue star sapphire as observed on the surface in reflected light and fiber-optic illumination (left) and in transmitted light in immersion with crossed polarizers (right). In reflected light, the grain boundaries are seen to cut across the arms of the star; in transmitted light, glide planes (Plato striations) are observed in addition to the grain boundaries, especially at the rim of the sample. Field of view 4.6 × 3.4 mm (left) and 9.2 × 6.9 mm (right). Photomicrographs by K. Schmetzer.

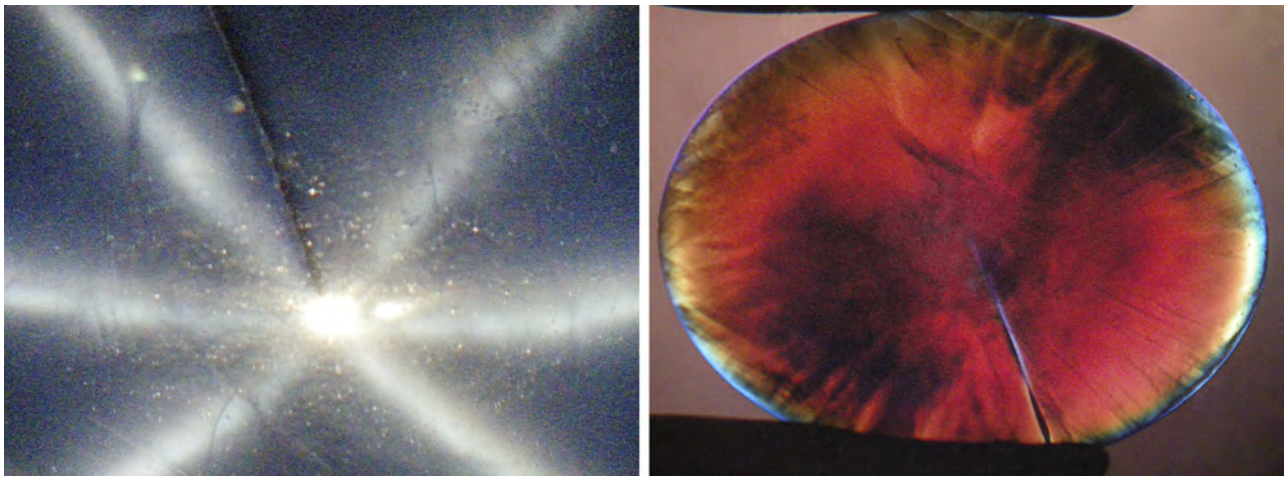

BOX A: ORIENTATION OF RUTILE NEEDLES AND THE NATURE OF PLATO LINES IN SYNTHETIC CORUNDUM

Plato lines are a characteristic feature of Verneuil-grown synthetic corundum. The observed pattern, in most cases consisting of two or even three series of intersecting structural planes, is best seen under crossed polarizers in a direction of view parallel to the optic axis of the ruby or sapphire (Plato, 1952, 1952/1953; Müller, 1952). In gemological textbooks, the description of Plato lines in synthetic corundum is occasionally associated with twinning, repeated twinning, or glide twinning parallel to hexagonal prism faces (Hughes, 1997, 2017). Similarly, Eppler (1964 a,b) identified the pattern as polysynthetic twinning parallel to the first-order hexagonal prism *m* {10$\bar{1}$0}. In doing so, he cited a previous, more detailed publication in *Deutsche Goldschmiede-Zeitung*. Unfortunately, the date of this prior work was given erroneously as 1956 in Eppler (1964a), requiring reference to Eppler (1964b), in German, to ascertain the correct 1959 date.

In that earlier publication, Eppler (1959) recounted investigations of Plato striations in synthetic asteriated Verneuil-grown corundum. He offered details of etching patterns seen in synthetic corundum and described experiments to examine the orientation of rutile precipitates and Plato lines. He observed that the elongation of the exsolved rutile needles was parallel to the planes of the Plato pattern and, further, concluded that the rutile needles and the planes of the Plato pattern were parallel to the first-order hexagonal prism *m* {10$\bar{1}$0}. This conclusion was based on Eppler's awareness of the fact that the second-order hexagonal prism *a* {11$\bar{2}$0} in the crystal class of corundum is parallel to a mirror plane, and thus *a* cannot be considered a twin plane (figure A-1).

In contrast, it is generally known to gemologists that rutile needles in *natural* asteriated and non-asteriated rubies or sapphires are located in planes parallel to the basal pinacoid (0001) and oriented parallel to growth planes representing the second-order hexagonal prism faces *a* {11$\bar{2}$0} of the host (Weibel, 1985; Hughes, 1997, 2017). In cross sections parallel to the basal pinacoid, growth zoning parallel to the second-order hexagonal prism *a* {11$\bar{2}$0} appears visually identical to growth zoning parallel to second-order hexagonal dipyramids—e.g., *n* {22$\bar{4}$3}, *w* {11$\bar{2}$1}, *v* {44$\bar{8}$3}, or *z* {22$\bar{4}$1}. Natural corundum from certain occurrences, such as basaltic sapphires from Australia, Madagascar, or Thailand, show mostly hexagonal dipyramids and no hexagonal prism faces. Consequently, in cross sections perpendicular to the c-axis, rutile needles appear either parallel to traces of the second-order hexagonal prism or parallel to traces of any of the hexagonal dipyramids.

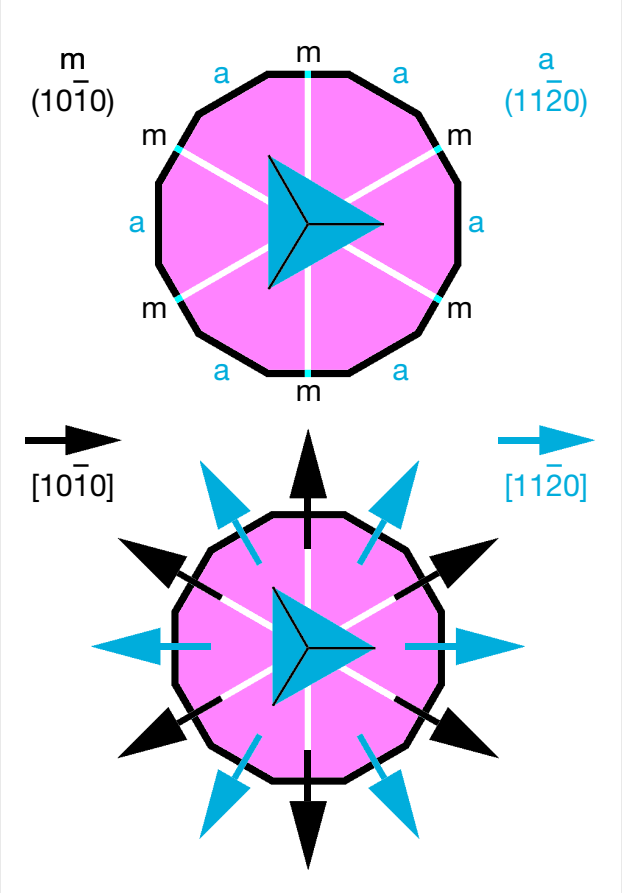

Figure A-1. Schematic representation of crystal faces (top) and crystallographic directions (bottom) in the crystal class of corundum, D_{3d}, with a view parallel to the c-axis. Symmetry elements depicted include the three-fold axis seen in the center and the mirror planes represented by white lines (two-fold axes are not given for simplicity). The first-order hexagonal prism {10$\bar{1}$0} is indicated by the symbol m *and the second-order hexagonal prism {11$\bar{2}$0} by the symbol* a*. The second-order prism faces* a *are parallel to mirror planes and parallel to the <10$\bar{1}$0> directions.*

precipitates, forming angles of 60° with each other, were visible at high magnification (figure 10, A–C). Knee-shaped and V-shaped twins were seen occasionally. Raman spectroscopy of the four Wiede's cabochons examined—which, as noted previously, was performed with both focused and defocused laser

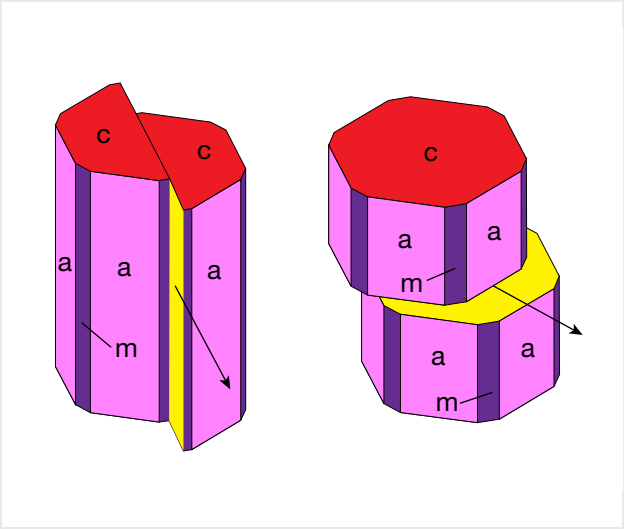

Figure A-2. Schematic representation of prismatic (left) and basal (right) glide planes in corundum. First-order hexagonal prism faces {10$\bar{1}$0} are indicated by the symbol m*, second-order hexagonal prism faces {11$\bar{2}$0} by the symbol* a*, and basal faces (0001) by the symbol* c*. Glide planes (yellow) are parallel to* a *or* c *planes, and the glide directions are shown by arrows.*

The same orientation of inclusions holds true for *synthetic* corundum that contains three series of elongated rutile or TiO_2 particles on planes parallel to the basal face (0001) of the host crystal. The orientation of these needles, which are also frequently twinned, is typically identified (for instance by electron diffraction) as being parallel to the <10$\bar{1}$0> direction of the host, which is parallel to the second-order hexagonal prism *a* {11$\bar{2}$0} (Bratton, 1971; Busovne et al., 1979; Philips et al., 1980; Moon and Philips, 1991; Viti and Ferrari, 2006; He et al., 2011). Relevant orientations of crystal planes and crystallographic directions are depicted in figure A-1.

Although Hughes (1997, pp. 156–158, and 2017, p. 270) would appear to mention one exception to the foregoing well-established orientation scheme for rutile or other TiO_2 precipitates in synthetic corundum, he cited in support Takubo et al. (1980). That study, in turn, characterized the orientation of rutile needles as parallel to the <10$\bar{1}$0> direction of the host. The implication is thus that Hughes (1997, 2017) mistakenly conflated crystallographic directions and crystal faces (again, see figure A-1).

Corundum specimens that were deformed by the application of stress show various slip systems. The main types of plastic deformation are described in the literature as basal and prismatic slip, caused by basal glide planes parallel to the basal pinacoid *c* (0001) and by prismatic glide planes parallel to the second-order hexagonal prism *a* {11$\bar{2}$0} (figure A-2). Occasionally, the presence of a rhombohedral slip system is discussed as well (Scheuplein and Gibbs, 1960; Stephens and Alford, 1964; Klassen-Neklyudova et al., 1970; Gooch and Groves, 1972, 1973; Snow and Heuer, 1973; Bilde-Sørensen et al., 1976, 1996; Kotchik and Tressler, 1980). More specifically, basal and prismatic glide systems are characterized by the glide plane and the glide direction:

basal slip system: glide plane *c* (0001),
glide direction <11$\bar{2}$0>

prismatic slip system: glide plane *a* {11$\bar{2}$0},
glide direction <10$\bar{1}$0>

Basal and rhombohedral glide systems may also be confined to rhombohedral or basal twinning (Heuer, 1966; Wang and Mikkola, 1992; Lagerlöf et al., 1994). However, due to the fact that the second-order hexagonal prism in corundum (crystal class D_{3d}) is parallel to a mirror plane, this glide plane is not considered a twin plane. Conversely, the first-order hexagonal prism *m* {10$\bar{1}$0} is not parallel to a mirror plane. As a consequence, a plane parallel to the first-order hexagonal prism may exist as a twin plane in corundum, as described for flux-grown Chatham synthetic sapphire (Schmetzer, 1987; Kiefert and Schmetzer, 1988).

In summary, we conclude that rutile or other TiO_2 needles in natural or synthetic corundum are located in the basal plane and form three series of oriented particles parallel to the second-order hexagonal prism *a* {11$\bar{2}$0}, which is equivalent to the three <10$\bar{1}$0> directions. The second-order hexagonal prism constitutes one of the principal systems of plastic deformation in corundum but is not considered a twin plane, due to the presence of mirror planes parallel to this face in the applicable crystal class. Plato lines seen in Verneuil-grown synthetic corundum thus represent glide planes resulting from plastic deformation caused by internal stress. Consequently, the term "glide twinning" is erroneous and should not be used.

beams because of the small thickness of some needles—yielded the lines of the corundum host, together with the strongest lines for rutile. Fixing the sample under investigation and observing it at different magnifications, we determined that the elongation of the rutile needles was parallel to the prismatic

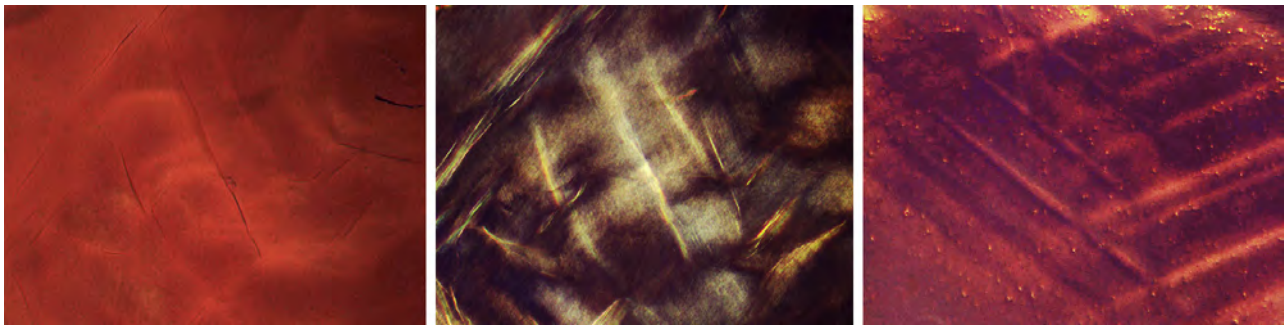

Figure 9. Grain boundaries as observed in transmitted light (left) are related to internal stress, which is best seen under crossed polarizers (center). Glide planes (Plato striations) are visible at the rim of the sample under identical illumination (right). Field of view 1.0 × 0.75 mm (left and center) and 1.5 × 1.1 mm (right). Photomicrographs by H.-J. Bernhardt.

glide planes (Plato striations). This indicated that both the rutile precipitates and the glide planes were oriented parallel to the second-order hexagonal prism (for further details, see again box A).

Rutile needles exsolved in Verneuil-grown synthetic star corundum crystals in the form of cylindrical boules, such as the Linde material and samples from other producers, have been shown to exhibit varying lengths, up to a maximum of about 50 µm (Schmetzer et al., 2015). For the six Wiede's stars studied here, the needle lengths were also variable in each sample, as depicted in figure 10. However, a maximum of approximately 15 µm was reached for one synthetic sapphire (figure 10A; see also figure 1), and maximal lengths between 35 and 45 µm were observed for the other three sapphire cabochons and the two synthetic rubies (figure 10, B and C; see also figure 2, right). The thickness (diameter) of the rutile needles for all six samples was found to be in the range of 0.3 to 0.4 µm. The needle

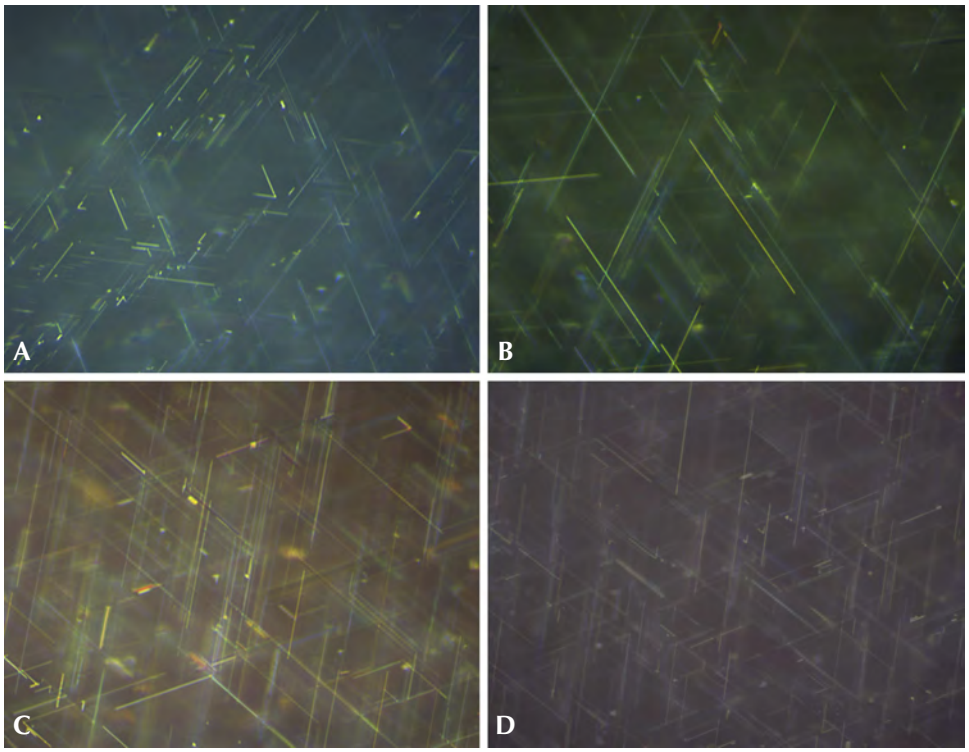

Figure 10. Rutile needles in two asteriated blue sapphires (A and B) and one ruby (C) produced at Wiede's Carbidwerk, and in a Linde synthetic star sapphire (D). In A, the needles' maximum length is about 15 µm, but needles with a maximum length between 35 and 45 µm were exsolved in the other sapphire and ruby samples (B and C). These larger needles are only slightly shorter or even in the range of rutile precipitates often seen in asteriated Linde synthetic sapphires (D). The thickness of the rutile needles is consistent for all samples. Reflected light, oil immersion; field of view (in A–D) 92 × 69 µm. Photomicrographs by H.-J. Bernhardt.

dimensions were always identical at the bases and domes of the cabochons.

At these dimensions, the rutile needles in one blue sapphire were shorter than those observed in any of the other three blue sapphires and the two rubies from Wiede's production. The rutile needles in this one sample were also noticeably shorter than the rutile precipitates observed, in general, in various types of Linde synthetic rubies and sapphires or in similar samples from other producers (figure 10D). For the other five samples from Wiede's production, the rutile needles were only moderately shorter than those in Linde samples, or even occasionally in the same range. In terms of thickness, the needles in the Wiede's cabochons were consistent with those in samples from Linde and other producers.

DISCUSSION AND CONCLUSIONS

The process developed and applied at Wiede's Carbidwerk for the production of synthetic asteriated rubies and sapphires was invented by Ancot and Eppler in the mid-1950s and used at the company until the end of the 1970s. The samples examined for the present paper likely originated from the 1960s and 1970s, thus representing production later than the first generation described by Eppler (1957/1958, 1958 a,b). Nonetheless, the general principles set forth in the two German patents by Ancot and Eppler (1957a,b) remained valid for the later generations, despite continuous incremental refinements in growth techniques throughout the 1960s and 1970s (C. Schulz and H. Schulz, pers. comm., 2016). The present study has revealed additional details regarding the nature of the methods employed for growth of these materials, augmented by insight from the producer, as described below.

Oriented seeds of synthetic sapphire were seen as small colorless shafts in all rough ruby and sapphire crystals grown by Wiede's. As confirmed by the producer, without such oriented seeds, the orientation of the synthetic ruby and sapphire crystals would become unpredictable, and, for preparation of asteriated ruby and sapphire cabochons, the center of the star and cabochon dome would need to be found separately for each crystal.

The use of oriented seeds for growing synthetic corundum was first described in a German patent by R. Thilenius (1941) and later in British and U.S. patent documents by M.H. Barnes (1946, 1953) assigned to Linde Air Products Company or Union Carbide and Carbon Corporation (of which Linde had become a division). These patents explained that a small piece or seed of corundum was embedded in a ceramic foot (figure 11). Next,

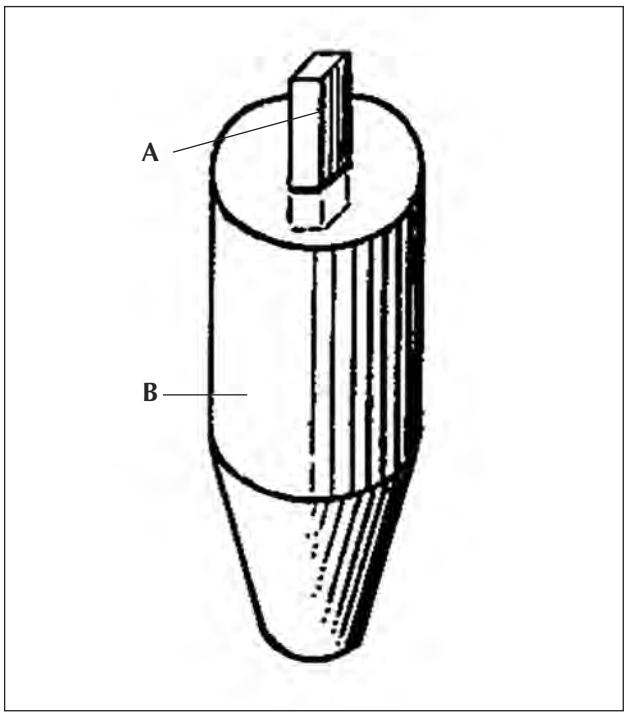

Figure 11. For the production of synthetic asteriated rubies and sapphires by Linde, an oriented seed crystal of synthetic corundum (A) embedded in a ceramic foot (B) was used. After Barnes (1953).

> the top of the seed is then brought to the melting point in the flame and the growing of the crystalline body is begun by admitting powdered gem material to the burner from the container, and accumulating the fused material on the fused top of the starting crystal or seed which thus becomes an integral part of the growing body and forms a single crystal therewith (Barnes, 1946, 1953).

An analogous technique was applied—in general—by Linde for the commercial production of asteriated rubies and sapphires (see the detailed description in the patent by Burdick and Jones, 1954).

The Ancot and Eppler patents dealing with Wiede's methodology stated that crystal growth started at a lower temperature with an O_2:H_2 ratio of 40:100 and was slowly raised during the growth process to a higher temperature and a ratio of 49:100. During the initial stages of crystallization and growth of an oriented corundum single crystal, the flame temperature at the melting point needed to be

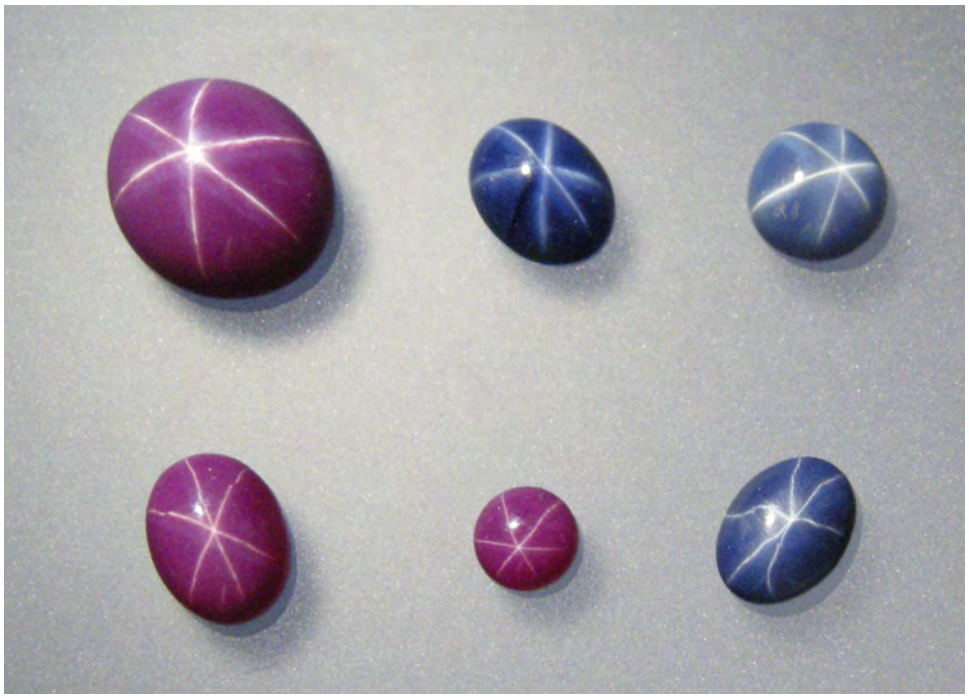

Figure 12. Comparison of asteriated rubies and sapphires produced by Wiede's in the 1960s and 1970s (top row), a synthetic asteriated ruby produced recently by Hrand Djevahirdjian SA (Djeva) in Switzerland (bottom row, left), and two samples grown by Linde in the United States in the 1960s or 1970s (bottom row, center and right). The blue sapphire in the top row, center, contains shorter rutile needles than the other samples. The ruby in the top row, left, weighs 8.92 ct and measures 13.2 × 11.0 mm. Diffused daylight and fiber-optic illumination. Photo by K. Schmetzer.

somewhat lower to avoid melting the seed. For subsequent stages, a higher temperature was required to obtain a homogeneous film of melt over the entire surface of the growing crystal (C. Schulz and H. Schulz, pers. comm., 2016). Such details demonstrate how the general principles described by Ancot and Eppler continued to be used for growing the elliptical or almost spherical corundum crystals, while simultaneously showing that the particular temperature-time protocol given in the Ancot and Eppler patent documents could be modified to a certain degree based upon practical experience. Slightly different temperature-time protocols would also presumably have been applied for growing rubies versus sapphires.

The asteriated ruby and sapphire cabochons examined for the present study reflected the just-described process of seeded growth at varying temperatures. This resulted in up to three discernible growth regions. The clear blue or red area in the center of the cabochons, which was previously noted only by Breebaart (1957), represented the zone of the growing crystal around the oriented seed. In this more transparent area, no exsolved rutile needles were observed microscopically in the current study. Within the two other growth zones (i.e., within the less transparent main body of the crystal and the more transparent outer layer or layers), high concentrations of rutile needles were present. However, it should be mentioned that the outermost, more transparent layer could be thinner or completely absent, again as a consequence of the particular temperature-time protocol used. Fashioning could also lead to variations in the zoned appearance. For example, if only the upper half of the spherical boule were used to produce an asteriated cabochon, any transparent regions below would be removed.

Compared to the rutile needles seen in asteriated corundum manufactured by Linde or other Verneuil producers, those examined in the Wiede's cabochons were generally somewhat shorter in the two rubies and three of the sapphires and distinctly shorter in the fourth sapphire. Eppler (1957/1958, 1958 a,b) had stressed the reduced length of the needles in the Wiede's stones, but perhaps more than would apply to the material considered in the present study. The increased needle thickness he noted in Wiede's synthetics was not observed in the present study. Furthermore, the material examined here contained round gas bubbles, which also contrasted with Eppler's descriptions. Another comment by Eppler that might warrant clarification based on later work is his mention of an absence of Plato striations in the Linde material. Such striations were occasionally found in a recent reexamination of Linde samples (Schmetzer et al., 2015), and hence their presence or absence in a particular stone offers little evidence of the manufacturer. Overall, the difference between Eppler's observations and ours suggests that the ongoing incremental changes in the manufacturing

process used by Wiede's Carbidwerk from the 1950s through the 1970s also caused somewhat varied microscopic properties and visual appearances.

Eppler (1957/1958, 1958 a,b) concluded that the different dimensions of the rutile precipitates within the host corundum cabochons led to moderately broader arms for the six-rayed stars developed in the Wiede's synthetics than those normally observed in Linde samples. In addition, he suggested that the broader, less sharp arms tended to result in a more natural-looking gemstone from Wiede's, as opposed to the typical Linde stars. However, while these observations by Eppler might apply to part of Wiede's early production, there is little contrast between the visual appearance of the Wiede's synthetics from the 1960s or 1970s examined here and samples from Linde or other more recent manufacturers (figure 12).

According to the producer, by using the method invented at Wiede's and patented in the 1950s (or a variant of that process), it is possible to grow stable (non-fragile) ruby and sapphire crystals with even higher titanium concentrations than the upper limit of 0.52 wt.% TiO_2 mentioned above. Such samples, however, are more milky white than the intense blue or red colors preferred, thus rendering them unmarketable (C. Schulz and H. Schulz, pers. comm., 2016).

ABOUT THE AUTHORS

Dr. Schmetzer is an independent researcher living in Petershausen, near Munich, Germany. Prof. Gilg is professor at the Chair of Engineering Geology, Technical University of Munich. Dr. Bernhardt was head of ZEM at the Institute of Geology, Mineralogy and Geophysics, Ruhr University, Bochum. Now retired, he lives in Neckargemünd, near Heidelberg.

ACKNOWLEDGMENTS

Samples for this study were kindly provided by Harald Schulz, director of Wiede's Carbidwerk, Freyung, Germany; by Dr. Rupert Hochleitner, Mineralogische Staatssammlung (Bavarian State Collection for Mineralogy), Munich; and by C. Weise of Munich and L. Rössler of Vienna, from their private collections.

The results of this study were discussed with Christian Schulz and Harald Schulz, the present directors of Wiede's Carbidwerk, who provided helpful information about the growth methods applied. Such information could not have been deduced from examination of the final product but was necessary to understand the properties of the asteriated samples.

REFERENCES

Ancot E., Eppler W.F. (1957a) Verfahren zur Herstellung von synthetischer, Asterismus aufweisender Korunde. DE 1 002 300, issued August 14.

Ancot E., Eppler W.F. (1957b) Verfahren zur Herstellung von synthetischen Sternkorunden. DE 1 007 753, issued October 24.

Barnes M.H. (1946) Improvements in synthetic gem bodies and their manufacture. GB 581,619, issued October 18.

Barnes M.H. (1953) Synthetic gem production. US 2,634,554, issued April 14.

Bilde-Sørensen J.B., Thölen A.R., Gooch D.J., Groves G.W. (1976) Structure of the <01$\bar{1}$0> dislocation in sapphire. *Philosophical Magazine A*, Vol. 33, No. 6, pp. 877–889, http://dx.doi.org/10.1080/14786437608221921

Bilde-Sørensen J.B., Lawlor B.F., Geipel T., Pirouz P., Heuer A.H., Lagerlöf K.P.D. (1996) On basal slip and basal twinning in sapphire (α-Al_2O_3) – I. Basal slip revisited. *Acta Materialia*, Vol. 44, No. 5, pp. 2145–2152, http://dx.doi.org/10.1016/1359-6454(95)00264-2

Bratton R.J. (1971) Precipitation and hardening behavior of Czochralski star sapphire. *Journal of Applied Physics*, Vol. 42, No. 1, pp. 211–216, http://dx.doi.org/10.1063/1.1659569

Breebaart A.J. (1957) Structure & inclusions of synthetic starstones. *Journal of Gemmology*, Vol. 6, No. 2, pp. 72–74, http://dx.doi.org/10.15506/JoG.1957.6.2.72

Burdick J.N., Glenn J.W. Jr. (1949) Synthetic star rubies and star sapphires, and process for producing same. US 2,488,507, issued November 15.

Burdick J.N., Jones R.A. (1954) Synthetic corundum crystals and process for making same. US 2,690,062, issued November 28.

Busovne B.J. Jr., Kotchick D.M., Tressler R.E. (1979) Deformation history effects on the precipitation hardening behavior of Ti^{4+}-doped sapphire. *Philosophical Magazine A*, Vol. 39, No. 3, pp. 265–276, http://dx.doi.org/10.1080/01418617908236900

Eppler Fr. (1957/1958) Synthetischer Sternsaphir und synthetischer Sternrubin. *Zeitschrift der Deutschen Gesellschaft für Edelsteinkunde*, No. 22, pp. 4–7.

Eppler W. (1958a) Synthetische Sternsaphire und synthetische Sternrubine. *Diebeners Goldschmiede Jahrbuch*, Vol. 40, pp. 44–50.

Eppler W.F. (1958b) Notes on asterism in corundum, rose quartz and almandine garnet and chatoyancy in beryl. *Journal of Gemmology*, Vol. 6, No. 5, pp. 195–212, http://dx.doi.org/10.15506/JoG.1958.6.5.195

——— (1959) Die Sandmeier-Plato-Streifung im synthetischen Korund. *Deutsche Goldschmiede-Zeitung*, Vol. 57, No. 2, pp. 62–64.

——— (1964a) Polysynthetic twinning in synthetic corundum. *G&G*, Vol. 11, No. 6, pp. 169–174, 191.

——— (1964b) Polysynthetische Zwillingsstreifen im synthetischen Korund. *Deutsche Goldschmiede-Zeitung*, Vol. 62, No. 1, pp. 22–23.
Gooch D.J., Groves G.W. (1972) Prismatic slip in sapphire. *Journal of the American Ceramic Society*, Vol. 55, No. 2, p. 105, http://dx.doi.org/10.1111/j.1151-2916.1972.tb11220.x
Gooch D.J., Groves G.W. (1973) Non-basal slip in sapphire. *Philosophical Magazine*, Vol. 28, No. 3, pp. 623–637, http://dx.doi.org/10.1080/14786437308221007
He J., Lagerlof K.P.D., Heuer A.H. (2011) Structural evolution of TiO_2 precipitates in Ti-doped sapphire (α-Al_2O_3). *Journal of the American Ceramic Society*, Vol. 94, No. 4, pp. 1272–1280, http://dx.doi.org/10.1111/j.1551-2916.2010.04217.x
Heuer A.H. (1966) Deformation twinning in corundum. *Philosophical Magazine*, Vol. 13, No. 122, pp. 379–393, http://dx.doi.org/10.1080/14786436608212616
Hughes R.W. (1997) *Ruby & Sapphire*. RWH Publishing, Boulder, CO, 511 pp.
Hughes R.W. (2017) *Ruby & Sapphire: A Gemologist's Guide*. RWH Publishing/Lotus Publishing, Bangkok, 732 pp.
Kiefert L., Schmetzer K. (1988) Morphology and twinning in Chatham synthetic blue sapphire. *Journal of Gemmology*, Vol. 21, No. 1, pp. 16–22, http://dx.doi.org/10.15506/JoG.1988.21.1.16
Klassen-Neklyudova M.V., Govorkov V.G., Urusovskaya A.A., Voinova N.N., Kozlovskaya E.P. (1970) Plastic deformation of corundum single crystals. *Physica status solidi (b)*, Vol. 39, No. 2, pp. 679–688, http://dx.doi.org/10.1002/pssb.19700390236
Kotchick D.M., Tressler R.E. (1980) Deformation behavior of sapphire via the prismatic slip system. *Journal of the American Ceramic Society*, Vol. 63, No. 7–8, pp. 429–434, http://dx.doi.org/10.1111/j.1151-2916.1980.tb10206.x
Lagerlöf K.P.D., Heuer A.H., Castaing J., Rivière J.P., Mitchell T.E. (1994) Slip and twinning in sapphire (α-Al_2O_3). *Journal of the American Ceramic Society*, Vol. 77, No. 2, pp. 385–397, http://dx.doi.org/10.1111/j.1151-2916.1994.tb07006.x
Moon A.R., Phillips M.R. (1991) Titania precipitation in sapphire containing iron and titanium. *Physics and Chemistry of Minerals*, Vol. 18, No. 4, pp. 251–258, http://dx.doi.org/10.1007/BF00202577
Müller W.A. (1952) Gerade, winkelige Parallelstreifung in einem synthetischen Saphir. *Deutsche Goldschmiede-Zeitung*, Vol. 50, No. 6, pp. 164–165.
Nassau K. (1980) *Gems Made by Man*. Chilton Book Company, Radnor, PA, 364 pp.
Phillips D.S., Heuer A.H., Mitchell T.E. (1980) Precipitation in star sapphire. I. Identification of the precipitate. *Philosophical Magazine A*, Vol. 42, No. 3, pp. 385–404, http://dx.doi.org/10.1080/01418618008239365
Plato W. (1952) Oriented lines in synthetic corundum. *G&G*, Vol. 7, No. 7, pp. 223–224.
Plato W. (1952/1953) Orientierte Streifung in synthetischen Korunden. *Zeitschrift der Deutschen Gesellschaft für Edelsteinkunde*, No. 2, pp. 10–13.
Scheuplein R., Gibbs P. (1960) Surface structure in corundum: I, etching of dislocations. *Journal of the American Ceramic Society*, Vol. 43, No. 9, pp. 458–472, http://dx.doi.org/10.1111/j.1151-2916.1960.tb13698.x
Schmetzer K. (1987) On twinning in natural and synthetic flux-grown ruby. *Journal of Gemmology*, Vol. 20, No. 5, pp. 294–305, http://dx.doi.org/10.15506/JoG.1987.20.5.294
Schmetzer K., Steinbach M.P., Gilg H.A., Blake A.R. (2015) Dual-color double stars in ruby, sapphire, and quartz: cause and historical account. *G&G*, Vol. 51, No. 2, pp. 112–143, http://dx.doi.org/10.5741/GEMS.51.2.112
Snow J.D., Heuer A.H. (1973) Slip systems in Al_2O_3. *Journal of the American Ceramic Society*, Vol. 56, No. 3, pp. 153–157, http://dx.doi.org/10.1111/j.1151-2916.1973.tb15432.x
Stephens D.L., Alford W.J. (1964) Dislocation structures in single-crystal Al_2O_3. *Journal of the American Ceramic Society*, Vol. 47, No. 2, pp. 81–86, http://dx.doi.org/10.1111/j.1151-2916.1964.tb15660.x
Takubo H., Kitamura Y., Kume Sh., Koizumi M. (1980) Preparation of star-ruby containing large crystals of ruby. Preliminary investigation. In A.V. Sidorenko et al., Eds., *Inhomogeneity of Minerals and Crystal Growth*. Proceedings of the XI General Meeting of IMA, Novosibirsk, 1978, Nauka, Moscow, pp. 305–309.
Thilenius R. (1941) Verfahren zur Herstellung synthetischer Korunde, deren kristallographische Hauptachse und geometrische Achse zusammenfallen. DE 711 293, issued Sept. 29.
Viti C., Ferrari M. (2006) The nature of Ti-rich inclusions responsible for asterism in Verneuil-grown corundums. *European Journal of Mineralogy*, Vol. 18, No. 6, pp. 823–834, http://dx.doi.org/10.1127/0935-1221/2006/0018-0823
Wang Y., Mikkola D.E. (1992) {0001}<$10\bar{1}0$> slip and basal twinning in sapphire single crystals shock-loaded at room temperature. *Journal of the American Ceramic Society*, Vol. 75, No. 12, pp. 3252–3256, http://dx.doi.org/10.1111/j.1151-2916.1992.tb04418.x
Weibel M. (1985) *Edelsteine und ihre Einschlüsse*. ABC Verlag, Zurich, 111 pp.

For online access to all issues of GEMS & GEMOLOGY from 1934 to the present, visit:

gia.edu/gems-gemology

True Colors of "Dalmatian Jasper"

Tomasz Powolny and Magdalena Dumańska-Słowik

"Dalmatian jasper," also known as "dalmatian stone," is a popular decorative gemstone with a unique appearance resembling the spotted coloration of the Dalmatian dog breed. Our research revealed that this gemstone is a peralkaline rock of uncertain provenance. It consists predominantly of feldspars (mesoperthite), quartz, alkali amphiboles, and lesser amounts of hematite and epidote. Black spots found in the examined rock's mass were recognized as arfvedsonite. The authors recommend the use of the term "dalmatian stone" rather than "dalmatian jasper," since the material does not meet the gemological definition of jasper.

Jasper (from the ancient Greek for "spotted stone") has a variety of colors, patterns, and textures that make it a very popular gemstone worn in jewelry and sought after by collectors and geologists. Unfortunately, the term "jasper" has become commercialized and misused by many sellers. In addition, the nomenclature and classification of jaspers are not well coordinated in gemology and petrology (Kostov, 2010). Manutchehr-Danai (2010) considered jasper a dense, translucent to opaque impure variety of chalcedony or chert. Götze (2010) defined it as a mixture of microcrystalline silica with iron oxide and illite, while Kievlenko (1980) classified it as a metamorphic or metasomatic material. Hence, the jasper group is characterized by sedimentary, metamorphic, or igneous rocks. Examples include, respectively, radiolarites such as mookaite jasper (Campos-Venuti, 2012), quartzites such as Sioux Falls jasper (Dietrich, 2009), and rhyolites such as orbicular jasper and picture jasper (Żaba, 2010; Polk, 2012). In general, all jasper types have specific physical, chemical, and aesthetic properties that make them a valuable material for jewelry. Except for silica, most also contain some admixtures such as iron oxides/hydroxides, feldspars, and epidotes (Żaba, 2010).

In some cases, more detailed mineralogical and petrological studies are necessary to determine the particular type of material. "Dalmatian jasper," also known as "dalmatian stone," is a misnomer if we consider the gemological definition of jasper or even other spotted stones mentioned in the literature (some of which were presented in the previous paragraph). Dalmatian stone consists of a white to grayish rock mass devoid of larger phenocrysts, with small crystals of quartz visible to the unaided eye. The rock mass strongly contrasts with the black to greenish spherical assemblages of minerals that are responsible for the unique dalmatian pattern. The diameter of these black spots usually does not exceed 4 mm. The surface of the rock is sometimes covered by red to brown iron oxide/hydroxide minerals.

In Brief

- Dalmatian stone is a magmatic (possibly extrusive) peralkaline rock of uncertain provenance, mostly composed of quartz and feldspars.
- Alkali amphiboles (arfvedsonite), which crystallized at the late stage of magma evolution, are responsible for the spotted appearance of the stone.
- In light of the gemological definition of jasper, the term "dalmatian stone" should be used instead of "dalmatian jasper."

Published information on dalmatian stone and its mineralogical composition is quite meager. Based only on microscopic observations, Bruder (2006) recognized dalmatian stone as an aplite, consisting predominantly of quartz, feldspars (albite and microcline), and Fe-riebeckite. On the other hand, Campos-Venuti (2012) considered it a variety of devitrified rhyolite and classified it as "rhyolitic jasper." In contrast, some informational websites on various gemstones (e.g., www.healing-crystals-for-you.com/dalmatian-jasper.html) indicate that the black spots in dalmatian stone are composed of tourmaline-group minerals. Moreover, the source of

See end of article for About the Authors and Acknowledgments.
Gems & Gemology, Vol. 53, No. 3, pp. 325–331,
http://dx.doi.org/10.5741/GEMS.53.3.325
© 2017 Gemological Institute of America

Figure 1. Dalmatian stone samples examined in this study reveal a spotted appearance connected with the presence of alkali amphiboles disseminated through feldspar-quartz matrices. Left: A rough block-shaped specimen measuring 1.5 × 1.5 × 1 cm. Right: A polished bracelet (1 cm bead diameter) alongside a pendant measuring 3 cm in length. Photos by Tomasz Powolny.

this gemstone has not yet been specified (Dietrich, 2009).

The aim of this work is to determine the detailed mineralogical composition of dalmatian stone, classify it properly, and discuss potential locations of the rock's outcrops proposed by distributors of the material. To accomplish this we applied microscopic observations in transmitted light, scanning electron microscopy, Raman microspectroscopy, and chemical analysis.

MATERIALS AND METHODS

Three samples of dalmatian stone, including a rough sample, bracelet, and pendant from an unknown locality, were purchased during the International Exhibition and Trade Fair of Minerals, Fossils, and Jewellery at the Krakow University of Economics in Poland. All samples were marked by high hardness and could take a polish. They revealed a spotted texture typical of dalmatian stone (black spots within white to grayish rock matrix) and were poorly altered by weathering processes. The raw specimen was block-shaped (1.5 × 1.5 × 1 cm) and had a rugged surface (figure 1, left). The bracelet consisted of polished beads with waxy luster measuring 1 cm in diameter, while the pendant had an oval shape and measured about 3 cm in length (figure 1, right). These samples were analyzed using polarizing microscopy, scanning electron microscopy, Raman microspectroscopy, and chemical analysis via inductively coupled plasma–emission spectrometry (ICP-ES) and inductively coupled plasma–mass spectrometry (ICP-MS).

A thin section of the dalmatian stone rough was examined with an Olympus BX51 polarizing microscope with a magnification range from 40× to 400×. Photos were taken using an Olympus DP12 digital camera with Analysis software. Backscattered electron (BSE) images of the polished section were obtained using an FEI Quanta 200 FEG scanning electron microscope equipped with an energy-dispersive spectroscopy (EDS) detector. The system was operated at 25 kV accelerating voltage in a high-vacuum mode.

Raman spectra of black spots seen with the unaided eye were recorded using a Thermo Scientific DXR Raman microscope equipped with 100×, 50×, and 10× magnification objectives, operated in confocal mode and in a backscatter geometry. The samples were excited with a 532 nm laser. The laser focus diameter was approximately 1–2 µm. Acquisition time was 20 seconds. Almost no sample preparation was performed. The polished section of dalmatian stone was cleaned carefully with distilled water and acetone before measurements were made to ensure that it was not contaminated. The spectra were acquired up to 2500 cm^{-1} using Omnic Specta software. Phase identification was performed by CrystalSleuth software in conjunction with the RRUFF database (http://rruff.info). The assignment of particular Raman-active bands was made using data for alkali amphiboles (especially riebeckite) published by Apopei and Buzgar (2010).

The whole-rock analyses were performed at Bureau Veritas Minerals Laboratories Ltd. in Vancouver,

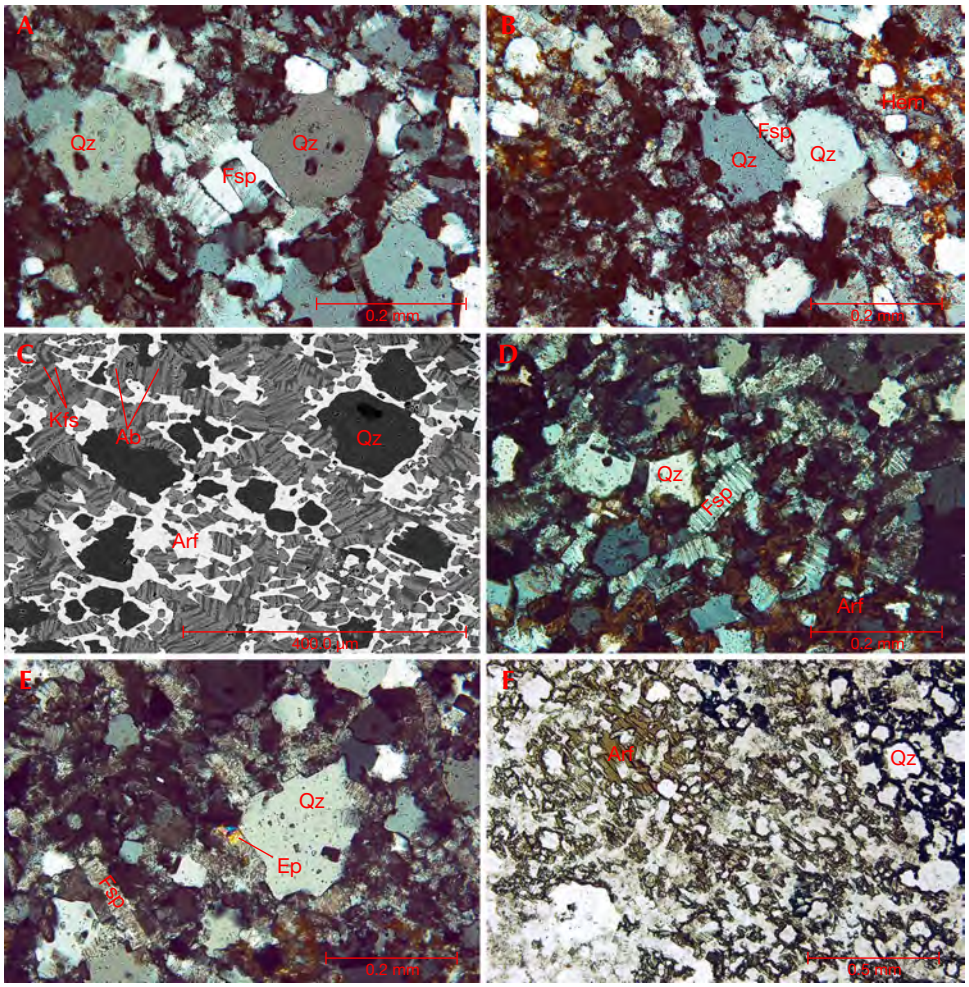

Figure 2. A thin section of dalmatian stone under magnification. A and B: Feldspar partially enclosed in larger quartz crystals, viewed between crossed polarizers. C: Backscattered electron (BSE) image of mesoperthitic feldspar, quartz, and interstitial arfvedsonite. D: Feldspar mesoperthites, viewed between crossed polarizers. E: Epidote-group minerals, viewed between crossed polarizers. F: Interstitial alkali amphiboles in aphyric rock. Photomicrographs by Tomasz Powolny. Note: Arf = arfvedsonite, Qz = quartz, Hem = hematite, Fsp = feldspar, Kfs = K-feldspar (orthoclase), Ab = albite, and Ep = epidote.

Canada. The abundances of major oxides and trace elements were determined using ICP-ES and ICP-MS. The sample was melted and dissolved by lithium borate flux. The results of representative whole-rock analyses are presented in table 1.

RESULTS

Microscopic Characteristics. Dalmatian stone is described as homogeneous, massive, and unfoliated rock. The rock matrix of the sample examined in this study consisted predominantly of quartz, feldspars (mostly mesoperthite), and subordinate alkali amphiboles (arfvedsonite). Epidote-group minerals as well as hematite and goethite formed the secondary phases.

Quartz crystals in the thin section reached sizes up to 0.3 mm (figure 2). These crystals appeared to be sharp-edged because they were often partially overgrown with smaller feldspar crystals. At the contact with alkali amphiboles, some of the quartz crystals exhibited an oval shape.

Feldspars were represented mostly by mesoperthites (intergrowths of K-feldspar with Na-feldspar) up to 0.2 mm in size (figures 2C and 2D). Their crystals were pigmented with hematite and poorly altered. Some were partially enclosed between larger quartz crystals (figures 2A and 2B). Locally, feldspar crystals exhibited Carlsbad twinning and were bent and dislocated, likely resulting from the deformation of magmatic rock components that were not completely solidified.

Alkali amphiboles were represented by anhedral crystals that filled the interstitial spaces between quartz and feldspars (figures 2C and 2F). They usually formed radial-like aggregates. Typical pleochroic colors (X = greenish blue, Y = brownish green, Z = black) identified the alkali amphiboles as arfvedsonite. They were partially altered into iron oxides or hydroxides (hematite and goethite) due to weathering processes.

Minerals from the epidote group formed small crystals or granular aggregates up to 0.05 mm (figure

TABLE 1. Whole-rock major and trace-element analysis of dalmatian stone.

Major element (wt.%)		Trace element (ppmw)					
SiO_2	73.66	Be	16.00	Zr	2072.10	Nd	153.50
TiO_2	0.21	Rb	374.30	Nb	156.50	Sm	30.17
Al_2O_3	10.74	Sr	42.30	Hf	53.40	Eu	0.38
FeO^a_{tot}	4.09	Cs	7.60	Ta	9.40	Gd	28.76
MnO	0.07	Ba	144.00	Th	36.60	Tb	4.90
MgO	0.08	V	17.00	U	14.20	Dy	30.63
CaO	0.48	Co	0.50	Pb	15.60	Ho	5.99
Na_2O	4.40	Ni	2.10	Ga	41.90	Er	19.33
K_2O	4.65	Cu	1.70	La	176.50	Tm	2.88
P_2O_5	0.01	Zn	48.00	Ce	361.40	Yb	18.92
LOI[c]	1.10	Y	163.70	Pr	42.95	Lu	2.88
Total	99.49						
PI[d]	1.14						

[a] *FeO_{tot} = total Fe as Fe_2O_3*
[b] *bdl = below detection limit*
[c] *LOI = loss on ignition*
[d] *PI = peralkaline index ($Na_2O + K_2O/Al_2O_3$)*

2E). They were pale green and exhibited second-order interference colors (blue, yellow, and pink) within a single crystal.

Raman Spectroscopy of Alkali Amphiboles. The Raman spectra of mafic minerals revealed the presence of arfvedsonite and poorly crystalline hematite (figure 3). The most distinct band of arfvedsonite is located at 675 cm^{-1} and may be ascribed to ν_1/ν_s (symmetric stretching vibrations) of the Si-O_b-Si bridges (Apopei and Buzgar, 2010). Arfvedsonite has a relatively complex chemical composition, and concentrations of K, Mg, Mn, or Fe in its structure may have a huge influence on peak location or intensity. Most of the Raman spectra recorded in this study exhibited high fluorescence related to the significant amounts of Fe in the structure of alkali amphiboles. Location and assignment of the bands are listed in table 2.

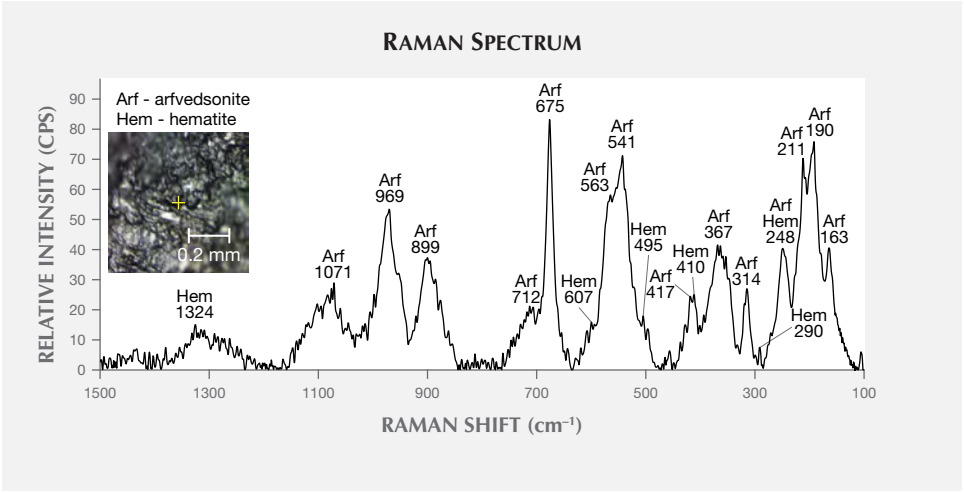

Figure 3. A photomicrograph of the black spot in the dalmatian stone and its Raman spectrum in the 1500–100 cm^{-1} range (excitation point marked by a yellow cross) revealed the presence of arfvedsonite and poorly crystalline hematite.

TABLE 2. Raman band positions (cm^{-1}) and their assignments for arfvedsonite in the 1500–100 cm^{-1} spectral region.

Present study	Lafuente et al. (2015)	Assignment
163	170	Lattice mode
190	199	
211	204	
248	240	
314	317	M-O
367	357	
417	418	
541	533	Deformation modes of Si_4O_{11}
563	558	
675	675	ν_s of Si-O_b-Si (ν_1)
712	721	
899	879	ν_s of O-Si-O
969	981	ν_{as} of O-Si-O
1071	1094	ν_{as} of Si-O_b-Si

ν_s = symmetric stretching
ν_{as} = asymmetric stretching
M-O = vibration modes from the interactions between the cation and oxygen
O_b = bridging oxygen
O = non-bridging oxygen

The broad peak located at 1324 cm^{-1} is diagnostic for disordered hematite and should be assigned to a second-order 2LO mode with $2E_u$ symmetry due to defects in the hematite lattice (Marshall and Marshall, 2013). Hematite bands at 225, 247, 412, 498, and 613 cm^{-1}, which are specific to this mineral according to Legodi and de Waal (2007), overlap with arfvedsonite bands. Consequently, they are hard to distinguish. In addition, the intensity of the arfvedsonite peaks in these spectral regions is quite amplified. The location and assignment of particular bands of hematite are listed in table 3. The presence of this mineral in the measured sample probably originated from the weathering of arfvedsonite.

Geochemistry. The major chemical constituent of the rock in this study was silica (73.66 wt.% SiO_2). The amount of Al_2O_3 was relatively low at almost 11 wt.% (table 1). The rock was slightly enriched in alkalis: Na_2O (4.40 wt.%) and K_2O (4.65 wt.%). In contrast, it was depleted in MgO and CaO; their contents did not exceed 0.5 wt.% (table 1). The analyzed sample was enriched in light rare-earth elements (LREEs): $[La/Sm]_N>1$, $[Sm/Yb]_N>1$, and $[La/Yb]_N=6.69$. It contained relatively high amounts of high-field-strength elements (HFSE) such as zirconium and niobium (2072.1 ppm and 156.5 ppm, respectively). The calculated peralkaline index (Na_2O+K_2O/Al_2O_3 molecular ratio) for this rock was 1.14. The normative composition, calculated using a common algorithm to estimate the standard mineral assemblages for igneous rocks, revealed the presence of quartz (30.26 wt.%), plagioclase (29.67 wt.%; anorthite content 0 wt.%), orthoclase (27.91 wt.%), acmite (6.94 wt.%), diopside (2.11 wt.%), hypersthene (2.07 wt.%), zircon (0.42 wt.%), ilmenite (0.4 wt.%), sodium metasilicate (0.04 wt.%), and apatite (0.02 wt.%).

DISCUSSION AND CONCLUSIONS

Our dalmatian stone sample had a specific mineral assemblage that included quartz, feldspar mesoperthites, and alkali amphiboles (arfvedsonite). It contained acmite in its normative composition and had a peralkaline index higher than 1. As a result, we classify dalmatian stone as a peralkaline rock. Textural features were not distinctive enough to determine whether the rock had an intrusive or extrusive origin. The dalmatian stone specimen examined in our work may represent peralkaline microgranite or aplite as well as peralkaline rhyolite, since the composition of these rocks may be identical. Intrusive origin is supported by the fact that the samples examined in this study do not exhibit the porphyric texture or the glassy or cryptocrystalline groundmass

TABLE 3. Raman band positions and their assignments for poorly crystalline hematite in the 1500–100 cm^{-1} spectral region.

Present study (cm^{-1})	Previous studies[a] (cm^{-1})	Assignment
211	225	A_{1g}
248	247	E_g
290	293	E_g
410	412	E_g
495	498	A_{1g}
607	613	E_g
1324	1320	$2E_u$

[a]*Sources: Legodi and de Waal (2007); Marshall and Marshall (2013)*
E_g = Fe-O symmetric bending
A_{1g} = Fe-O symmetric stretching
$2E_u$ = 2LO mode

that together would indicate a relatively fast cooling. On the other hand, quartz crystals may be treated as phenocrysts because they are slightly larger than other crystals, which could support an extrusive origin. Moreover, interstitial arfvedsonite, in the same form as in our photomicrographs, has been reported in comenditic rhyolite (see www.alexstrekeisen.it/english/vulc/comendite.php).

Peralkaline rocks are generally abundant in continental rift settings (Mbowou et al., 2012; Shao et al., 2015). They are considered end members of the sodic (Atlantic) magma differentiation series (Majerowicz and Wierzchołowski, 1990). The most distinct feature of these rocks is depletion of Al_2O_3 and enrichment in Na_2O and K_2O. The depletion of Al at the late stage of melt crystallization is compensated by Fe. As a result, Fe-bearing alkali amphiboles (e.g., riebeckite and arfvedsonite) could have crystallized at that time. The relatively small amounts of Al in peralkaline rocks probably originate from the "plagioclase effect" that happened with removal of Ca-rich plagioclase ($CaAl_2Si_2O_8$) at an early stage of magma evolution. Such Ca-rich plagioclases have twice as much alumina as alkali feldspars, so their crystallization depletes Al from magma and causes the relative enrichment of Na and K (Mbowou et al., 2012; Shao et al., 2015). The primitive mantle rare-earth element (REE) pattern of dalmatian stone (figure 4) is similar to that reported in peralkaline rocks (e.g., Mbowou et al., 2012) and reveals the strong depletion of europium (also known as a negative europium anomaly). This is due to the fact that plagioclases, which were not found in this study, tend to be enriched in europium.

The microscopic and chemical analyses were used to determine not only the classification of dalmatian stone but also its petrogenesis. Feldspar and quartz probably represent the earliest generations of minerals. The nucleation of alkali amphiboles occurred at the late stage of dalmatian stone's crystallization, forming as anhedral crystals filling the interstitial space between quartz and feldspars. Sodium plagioclases do not occur as individual, discrete crystals but form exsolution lamellae in K-feldspars. Thus, dalmatian stone may be classified as hypersolvus rock, which contains a single feldspar (sometimes with exsolution lamellae) and forms under low H_2O pressures and relatively high temperatures (e.g., Klein and Philpotts, 2013). Epidote-group minerals probably formed during the post-magmatic stage. They also could have crystallized from fluids originating from surrounding rocks (Vlach, 2012).

The provenance of the rock from this study and Dietrich (2009) remains unknown. One possible source of dalmatian stone indicated by gemstone dealers is the Mexican state of Chihuahua. This seems very probable because of the occurrence of Burro Mesa riebeckite rhyolite at Big Bend National Park in the neighboring U.S. state of Texas (reported by Maxwell et al., 1967). These rocks were described as highly siliceous, medium-grained gray rhyolite with quartz phenocrysts in a riebeckite matrix.

Figure 4. A primitive-mantle-normalized rare-earth element (REE) diagram for dalmatian stone. From McDonough and Sun (1995).

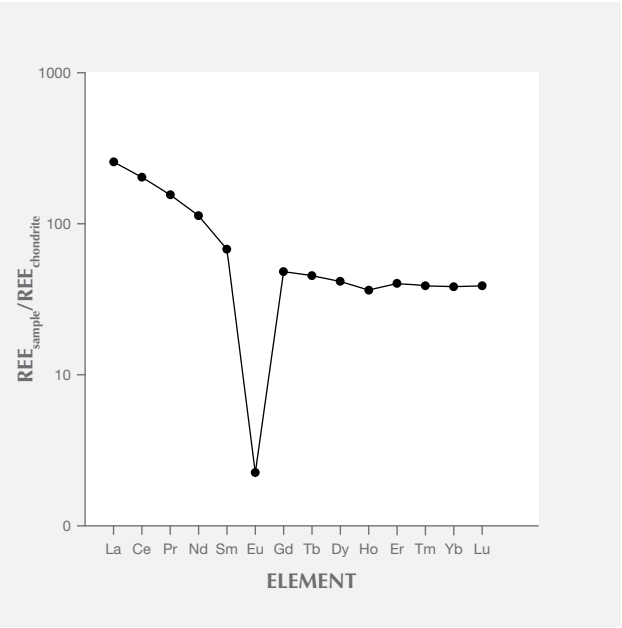

Nevertheless, further investigations are necessary to prove this hypothesis. It should also be mentioned that dalmatian stone may resemble Capo Bianco aplite from the Mediterranean island of Elba. This rock consists of characteristic black tourmaline nodules that contrast strongly with its white groundmass (see Perugini and Poli, 2007).

Dalmatian stone has a unique pattern, but its mineral composition can be identified with advanced and non-destructive methods such as Raman spectroscopy or SEM-EDS. As discussed above, "dalmatian jasper" should be considered a trade name for peralkaline rock (microgranite, aplite, or rhyolite). Eventually, it may be classified—together with such rocks as orbicular jasper or picture jasper—in a group of so-called jasper-like intrusive or effusive rocks with feldspar-quartz composition (see Putolova et al., 1989). To distinguish dalmatian stone from jaspers and jasper-like rocks, it is necessary to make macroscopic observations supported by Raman microspectroscopy.

ABOUT THE AUTHORS

Mr. Powolny is a PhD student, and Dr. Dumańska-Słowik is a mineralogist, in the Department of Mineralogy, Petrology and Geochemistry at the Faculty of Geology, Geophysics and Environmental Protection, AGH University of Science and Technology in Krakow, Poland.

ACKNOWLEDGMENTS

We thank Dr. Jerzy Czerny for his assistance with microscopic observations. The anonymous peer reviewers are gratefully acknowledged for substantial and constructive remarks, which helped to improve the manuscript. This work was financially supported by the AGH University of Science and Technology, research project No. 11.11.140.319.

REFERENCES

Apopei A.I., Buzgar N. (2010) The Raman study of amphiboles. *Analele Stiintifice Ale Universitatii, Al. I. Cuza Iasi Geologie*, Vol. 56, No. 1, pp. 57–83.

Bruder B. (2006) Edelstein-News Nr 1. Dalmatian Stone. http://alfs-mineralien.de.tl/EPI-_-NEWS.htm [in German].

Campos-Venuti M. (2012) *Genesis and Classification of Agates and Jaspers: A New Theory*. Tophgrafia Luciani, Rome, 160 pp.

Dietrich R.V. (2009) Gemrocks: Ornamental & curio stones. http://stoneplus.cst.cmich.edu/Default.htm

Götze J. (2010) Origin, mineralogy, nomenclature and provenance of silica and SiO_2 rocks. *Archeometriai Muhely*, Vol. 3, pp. 163–175.

Kievlenko E. (1980) *Prospecting and Evaluation of Deposits of Gem and Decorative Stones*. Nedra, Moscow, 263 pp. [in Russian].

Klein C., Philpotts A. (2013) *Earth Materials: Introduction to Mineralogy and Petrology*. Cambridge University Press, New York, 533 pp.

Kostov R.I. (2010) Review of the mineralogical systematics of jasper and related rocks. *Geology and Mineral Resources*, Vol. 13, No. 9, pp. 8–12 [in Bulgarian].

Lafuente B., Downs R.T., Yang H., Stone N. (2015) The power of databases: the RRUFF project. In T. Armbruster and R.M. Danisi, Eds., *Highlights in Mineralogical Crystallography*. W. De Gruyter, Berlin, pp. 1–30.

Legodi M.A., de Waal D. (2007) The preparation of magnetite, goethite, hematite and maghemite of pigment quality from mill scale iron waste. *Dyes and Pigments*, Vol. 74, No. 1, pp. 161–168, http://dx.doi.org/10.1016/j.dyepig.2006.01.038

McDonough W.F., Sun S. (1995) The composition of the Earth. *Chemical Geology*, Vol. 120, No. 3-4, pp. 223–253, http://dx.doi.org/10.1016/0009-2541(94)00140-4

Majerowicz A., Wierzchołowski B. (1990) *Petrology of the Igneous Rocks*. Wydawnictwa Geologiczne, Warsaw, 307 pp. [in Polish].

Manutchehr-Danai M. (2010) *Dictionary of Gems and Gemology*. Springer-Verlag, Berlin, p. 565.

Marshall C.P., Marshall A.O. (2013) Raman hyperspectral imaging of microfossils: Potential pitfalls. *Astrobiology*, Vol. 13, No. 10, pp. 920–931, http://dx.doi.org/10.1089/ast.2013.1034

Maxwell R.A., Lonsdale J.T., Hazzard R.T., Wilson J.A. (1967) *Geology of Big Bend National Park, Brewster County, Texas*. The University of Texas Bureau of Economic Geology Publication 6711, 320 pp.

Mbowou G.I.B., Lagmet C., Nomade S., Ngounouno I., Déruelle B., Ohnenstetter D. (2012) Petrology of the Late Cretaceous peralkaline rhyolites (pantellerite and comendite) from Lake Chad, Central Africa. *Journal of Geosciences*, Vol. 57, No. 2, pp. 127–141, http://dx.doi.org/10.3190/jgeosci.118

Perugini D., Poli G. (2007) Tourmaline nodules from Capo Bianco aplite (Elba Island, Italy): an example of diffusion limited aggregation growth in a magmatic system. *Contributions to Mineralogy and Petrology*, Vol. 153, No. 5, pp. 493–508, http://dx.doi.org/10.1007/s00410-006-0167-3

Polk P. (2012) *Collecting Rocks, Gems and Minerals: Identification, Values and Lapidary Uses*. Krause Publications, Iola, WI, 304 pp.

Putolova L.S., Menchinskaya T.I., Baranova T.L., Vdovenko A.P. (1989) *Decorative Varieties of Coloured Stone in the USSR*. Nedra, Moscow, 272 pp. [in Russian].

Shao F., Niu Y., Regelous M., Zhu D.-C. (2015) Petrogenesis of peralkaline rhyolites in an intra-plate setting: Glass House Mountains, southeast Queensland, Australia. *Lithos*, Vol. 216–217, pp. 196–210, http://dx.doi.org/10.1016/j.lithos.2014.12.015

Vlach S.R.F. (2012) Micro-structural and compositional variations of hydrothermal epidote-group minerals from a peralkaline granite, Corupá Pluton, Graciosa Province, South Brazil, and their petrological implications. *Annals of the Brazilian Academy of Sciences*, Vol. 84, No. 2, pp. 407–425, http://dx.doi.org/10.1590/S0001-37652012005000024

Żaba J. (2010) *The Illustrated Encyclopedia of Minerals and Rocks*. Videograf II, Chorzów, Poland, 503 pp. [in Polish].

The Colombian Emerald Industry: Winds of Change

Darwin Fortaleché, Andrew Lucas, Jonathan Muyal, Tao Hsu, and Pedro Padua

Figure 1. Colombian emerald-producing areas such as Muzo have a long tradition of independent mining. The hope of finding the stone that will change their lives is a strong motivator for miners, but bringing them into a formal system is challenging. Photo by Andrew Lucas.

Colombia is synonymous with fine emerald, and production is believed to date back well over a thousand years. Over the centuries the beautiful verdant gemstone, which emerges from areas that are also a lush green, has been linked to violence and human exploitation. Nevertheless, the desire of the Colombian people to mine for this treasure and strike it rich has endured, with enough dreams coming true to drive their passion.

In recent years, industry changes have accelerated, perhaps more profoundly than ever before. While government ownership and regulation, criminal activity, and violence have affected production over the years, the industry's greatest opportunities may still be ahead. Multinational companies are investing heavily in Colombian emerald mining, which has led to modernization. The government's position on emerald mining has also improved dramatically in this period. Calls for transparency and traceability have led to branding and a revamping of the industry's image. The loose system of independent miners (figure 1) is seeing efforts at formalization. These landmark changes are occurring at a time when most of the country's emerald reserves have yet to be mined.

In October 2015, a joint GIA and Colombian team met at the First International Emerald Symposium in Bogotá to interview industry leaders and government officials. Many topics involving industry change were

See end of article for About the Authors and Acknowledgments.
GEMS & GEMOLOGY, Vol. 53, No. 3, pp. 332–358,
http://dx.doi.org/10.5741/GEMS.53.3.332
© 2017 Gemological Institute of America

Figure 2. Colombian emeralds were prized by the Spanish during their colonization of the New World. These stones and jewelry were lost at sea en route to Spain. Photo by Shane F. McClure.

discussed at the symposium. Afterward, the team traveled to Colombia's major mines and visited dealers and cutters in Bogotá to document the current state of the mine-to-market industry. We were also able to collect rough emerald samples for the GIA laboratory's country-of-origin reference collection.

HISTORY

Volumes have been written about the history of Colombian emeralds. Our history section is therefore a brief overview of a fascinating and well-documented topic.

Before the arrival of the Spanish in 1499, emeralds were mined by the indigenous people of what is today Boyacá Province. Archaeologists estimate that natives were mining and trading Colombian emeralds as early as 1000 BC (Sinkankas, 1981). When the Spanish arrived, they quickly took over the mining areas and forced the indigenous people into slavery, extracting emerald for European royalty and aristocrats (figure 2) as well as Mogul rulers in India. The inhumane treatment of the natives led Philip III of Spain (r. 1598–1621) to issue a decree protecting them, but the tribes had already suffered greatly by then (Keller, 1981).

Mines that had been Spanish royal property fell under Colombian government control after independence in 1810. Still, many independent miners—called *guaqueros*—continued to dig for emerald. By 1979

Figure 3. Regional map of the major tectonic domains and structural features of Colombian emerald zones. WC = Western Cordillera, CC = Central Cordillera, EC = Eastern Cordillera. Reproduced from Mora et al. (2008).

two companies, Tecminas in Muzo and Esmeracol S.A. in Coscuez, had begun privatized mining. Relations between the two groups became strained. Elements of the Colombian drug cartels tried to infiltrate the industry in the 1980s, leading to the Green War, in which thousands lost their lives. A peace treaty was signed in 1990, mediated by the Catholic Church. Instrumental in the treaty was the legendary Victor Carranza, known as the "Emerald Czar" and considered the most influential figure in the emerald industry at that time (Angarita and Angarita, 2013).

The last five years have seen more foreign investment and multinational companies entering the Colombian mining industry, stronger efforts at formalization, greater transparency, stricter enforcement of traceability, less violence, and new branding efforts to create a marketable image for today's consumer.

GEOLOGY

As noted by Giuliani et al. (2015), emerald can form in a variety of geological settings but is mainly found in three types of deposits: (1) magmatic-metasomatic, (2) sedimentary-metasomatic, and (3) metamorphic-metasomatic. According to worldwide production data from 2005, about 65% of global production came from magmatic-metasomatic occurrences, while about 28% was from sedimentary-metasomatic deposits and 7% from metamorphic-metasomatic types (Giuliani et al., 2015). Colombia's emerald deposits are the sedimentary-metasomatic type.

Northwestern Colombia is at the intersection of three major tectonic domains: the South American plate in the east and south, the Caribbean plate in the north, and the Cocos and Nazca oceanic plates in the west (figure 3). The Colombian Andes are the most distinguishing surface features resulting from the interactions between the three domains throughout geological history. Since the end of the Cretaceous period about 70 million years ago, the convergence of the Nazca-Cocos oceanic plate with the South American continental plate has played the most important role in shaping the region's topography (Colletta et al., 1990).

From the Tierra del Fuego archipelago to Ecuador, the Andes consist of a single narrow mountain belt, but in Colombia the northernmost Andes split into three branches to form a trident-shaped topographic feature (figure 3). These three mountain ranges are the Western, Central, and Eastern Cordilleras; the last is also referred to as the Cordillera Oriental. The three cordilleras are geologically distinct and came into existence at different times (Irving, 1975). The Western Cordillera consists mainly of Upper Cretaceous ophiolitic rocks, while the Central Cordillera is composed of Precambrian and Paleozoic basement rocks intruded by Mesozoic plutons. The Eastern Cordillera is characterized by a thick folded Mesozoic and Tertiary sedimentary sequence overlying the Precambrian and Paleozoic basements (Colletta et al., 1990). The convergence of the Nazca-Cocos plate with the South American plate has been absorbed partly by the subduction along the Colombian-Equatorian trench and partly by the uplift of the Eastern Cordillera.

All Colombian emerald deposits are located in the Eastern Cordillera. Today, the western zone of the Eastern Cordillera is defined by a series of west-vergent thrusts and the eastern zone by a group of east-vergent thrusts (figure 4). The whole mountain range is bounded by the Magdalena River Valley to the west and the Llanos Basin to the east. During the Middle Miocene (peak at approximately 15 million years ago), the active convergent plate movements generated a great amount of shortening in the Eastern Cordillera region and caused uplift. This scenario is the geologically well-known Andean phase. Worth noting is that the Colombian emeralds formed before the Andean phase.

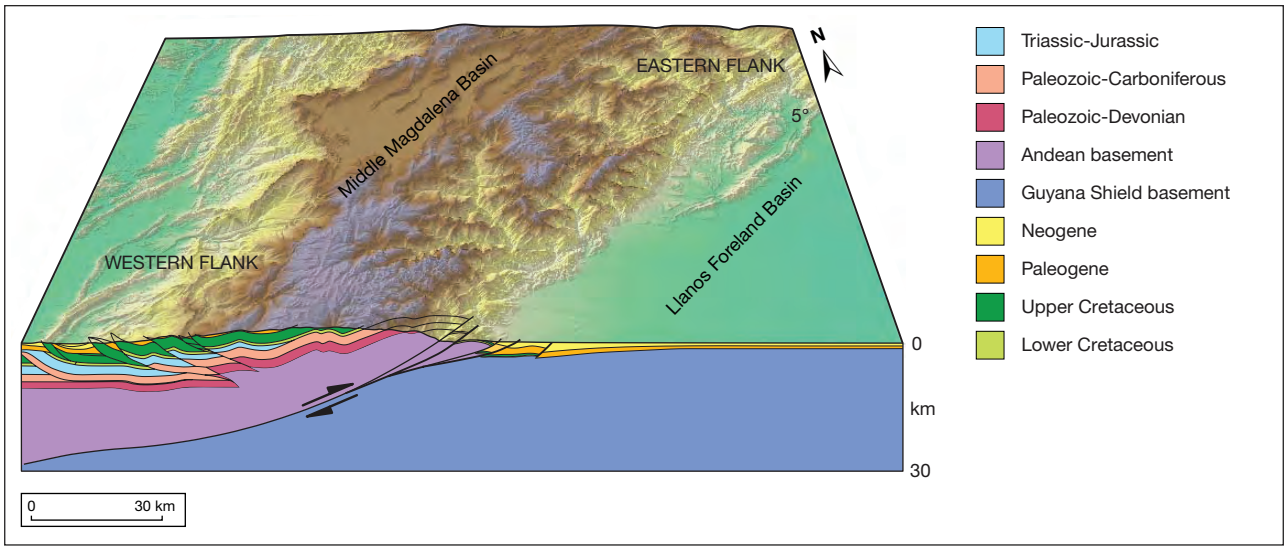

Figure 4. Cross-section of the Eastern Cordillera. The thrust faults along the western and eastern zones together show a typical "flower structure" formed by the east-west shortening. Adapted from Mora et al. (2008).

In Colombia, emeralds are recovered predominantly from Early Cretaceous shales. The shales were some of the topmost infill of a marine foreland basin of the Central Cordillera that began in the Jurassic and matured in the Late Cretaceous. Later, the inversion of this basin before and during the Andean phase generated the relatively high topography of the Eastern Cordillera and some of the local structures for emerald crystallization (Colletta et al., 1990; Branquet et al., 1999).

Previous research and field surveys defined two belts of emerald deposits along the two boundaries of the Eastern Cordillera (figure 5). The western belt includes deposits such as La Glorieta–Yacopi, Muzo, Coscuez, La Pita, and Peñas Blancas; along the eastern belt are Gachalá, Chivor, and Macanal (Branquet et al., 1999). The emerald mineralization is associated with hydrothermal fluid circulation and therefore highly controlled by the structural development within each belt. In both belts, emerald is found

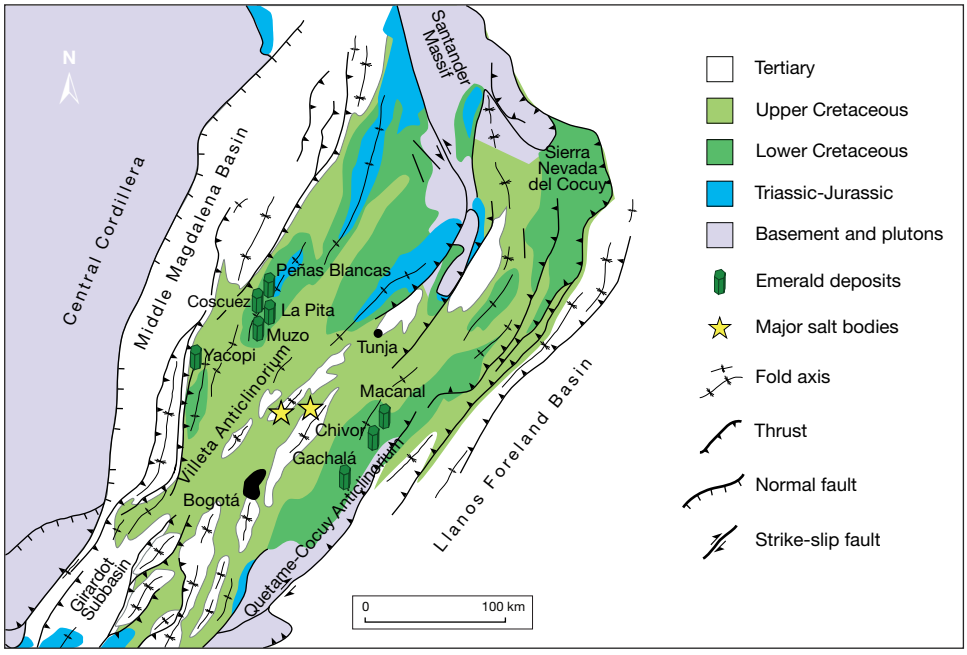

Figure 5. Simplified geological map of Colombia's Eastern Cordillera and the distribution of major emerald deposits along its western and eastern flanks. Notice the major salt bodies exposed northeast of Bogotá. Adapted from Pignatelli et al. (2015) and Giuliani et al. (2015).

within shales of Lower Cretaceous age. Although emerald formed under similar geochemical conditions on both sides, the eastern belt mineralization occurred about 65 million years ago in an extensional environment, while western belt mineralization occurred about 33 million years ago in a compressive environment (Branquet et al., 1999).

In the western belt, emerald mineralization occurred when the hydrothermal brine intruded into the organic-rich black shale. The hot brine formed when heated fluid dissolved the evaporites. The salt domes north of Bogotá are the surface breakouts of the evaporites below the emerald-bearing black shales (figure 5). During the inversion of the basin, some of the lower strata, such as the salt layers, were squeezed out and became exposed on the surface. The hot brine either traveled upward through the faults and other structural weaknesses within the black shale or broke its way through.

Western belt deposits are highly controlled by tear faults perpendicular to the thrust front (Branquet et al., 1999; Giuliani et al., 2015). Tear faults are deeply rooted steep offsets within rocks that have a very strong strike-slip component and often form to accommodate the different migration rates of the thrust fault. The almost vertical tear faults provided ideal conduits for the hydrothermal brine to travel through and intrude the surrounding rock (Branquet et al., 1999). During this process, the brine picked up the necessary components to form emerald from the surrounding shale (Pignatelli et al., 2015). When the temperature decreased and certain chemical components reached the saturation point, emerald began to crystallize within the brine veins, along with other minerals such as calcite, quartz, albite, and pyrite.

The western emerald belt is located at the core of the Villeta anticlinorium (again, see figure 5). Its general stratigraphy includes, from bottom to top, basal décollement (possibly where the evaporites are located), Valanginian-Hauterivian dolomitic limestones, Hauterivian calcareous black shales, Hauterivian siliceous black shales, and Barremian-Aptian mudstone (Branquet et al., 1999). Emeralds formed within either the hydrothermal breccia or the carbonate-pyrite veins in the dolomitic limestones and the calcareous black shales (Branquet et al., 1999). In individual deposits, emeralds are extracted along compressional structures such as thrust faults.

Emeralds formed much earlier in the eastern zone. The present topography and structures are the result of the Andean phase uplift (again, see figure 4). The shortening during the uplift is accommodated by many thrusts and folds, so the structures before the Andean phase are overprinted. Yet the structures within some of the important emerald deposits indicate an extensional environment. Conjugate normal faults, extensional fractures, and rollovers are some of the features that show the local stress field at the time the emeralds crystallized. All of these structures were derived from a main mineralized brecciated level (figure 6), and it appears that the initiation and development of these structures are coeval with hydrothermal fluid circulation and emerald formation (Branquet et al., 1999, 2015). Since the extension occurred under the regional compressional environment and was very limited, the cause is still not clear.

THE EXPEDITION

The 2015 expedition had three main purposes: to present at the International Emerald Symposium in Bogotá; to document the Colombian emerald mine-to-market industry, including the tremendous changes taking place; and to collect rough emerald samples for the GIA laboratory's country-of-origin database reference collection. We also renewed relationships with the Colombian industry and created new ones.

Andrew Lucas led the industry documentation project; Jonathan Muyal headed sample collection; and videographer Pedro Padua filmed the video interviews, industry activities, and the sample collection process. Field guide and Colombian gemologist Darwin Fortaleché handled logistics, provided guidance and insightful commentary, and recorded GPS coordinates of active tunnels, mine camps, and mine markets. Our resourceful driver, Miguel Gonzalez, who was also involved in emerald mining and trading, provided input and helped guide the expedition.

We were able to document all the major mining operations in one trip through the lush green landscape of the Colombian Andes (figure 7). In Bogotá we observed the emerald cutting and trading sectors. More than 44 hours of video and 10,000 photos were captured, including in-depth interviews in the field with miners, cutters, traders, industry leaders, and government officials.

For GIA's reference collection we collected 1,243 rough emeralds weighing a total of 995 carats. Many of these specimens were obtained directly from miners in the field. Authors JM and AL also mined some deposits themselves, digging into the calcite veins

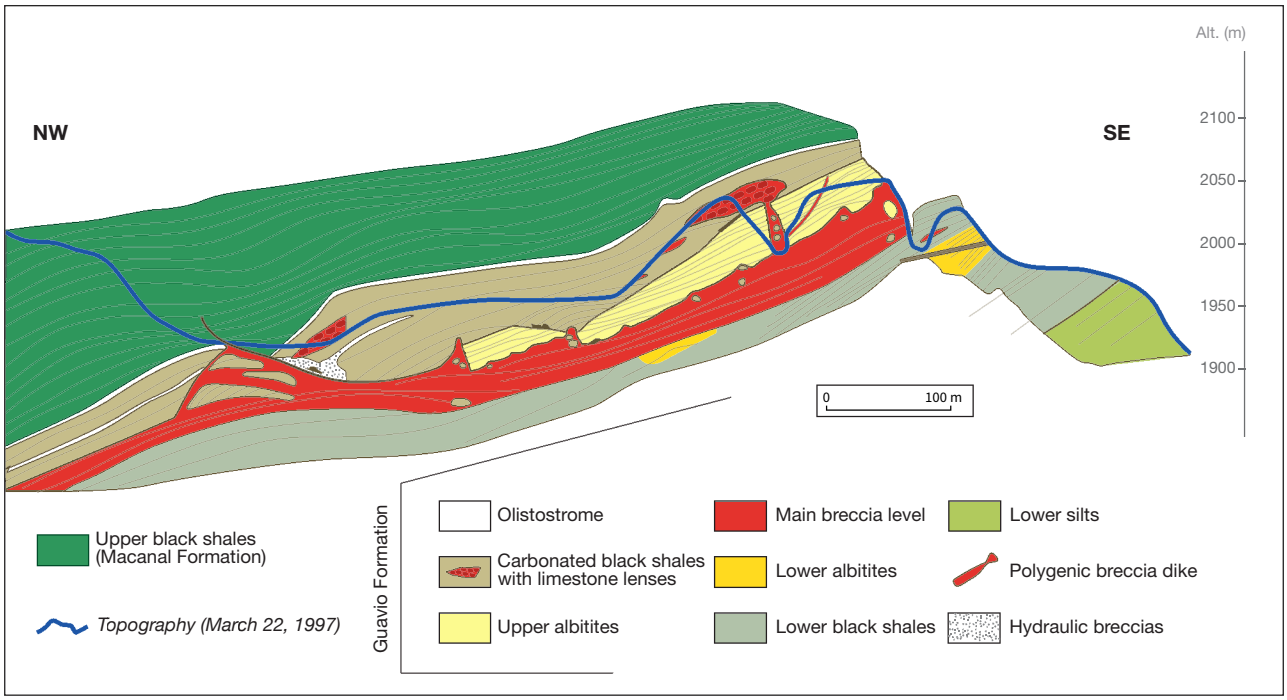

Figure 6. A cross-section of the Chivor mine, located in the eastern zone. The main breccia level is parallel to the sedimentary strata; in this mine, emerald is located in structures extending from this brecciated level. Reproduced from Giuliani et al. (2015).

with jackhammers and hand picks to retrieve the samples (figures 8 and 9).

We arrived in Bogotá on October 12, 2015, to attend the three-day symposium. There the GIA team gave presentations, finalized the expedition plan, and interviewed officials about recent changes. The following two days were spent documenting emerald cutting and trading in Bogotá and meeting with Colombian industry members.

Early on October 18 we left Bogotá for Chivor. Our route took us first to the eastern belt mines of Chivor and Gachalá and then to the western belt mines of the Coscuez, Muzo, and La Pita areas. We stayed at mine camps and at hotels in nearby towns.

Figure 7. En route to mining areas along the Río Minero and Río Itoco in the Colombian Andes was some of the most beautiful terrain the authors had ever seen. Photo by Andrew Lucas.

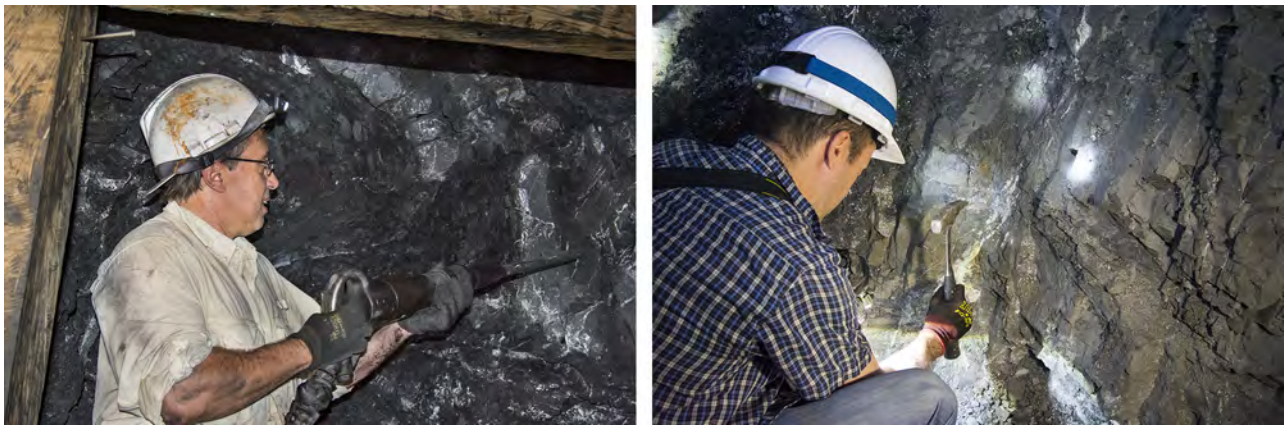

Figure 8. Two of the authors collected emerald directly from the deposits using hydraulic jackhammers to reach the emerald-bearing areas and then hand picks to remove the crystals from the host rock. Photos by Jonathan Muyal (left) and Andrew Lucas (right).

The town of Muzo was used as a base to explore the active mines and markets in the western belt mines. The pace was brisk and usually involved driving at night so we could see the maximum number of mines and markets in our allotted time. By November 1, we were back in Bogotá to prepare the legal export of the emerald rough samples with licensed export brokers and board our return flights. Our expedition was short, given the goal of visiting all the important mining areas in Colombia and documenting cutting and trading, but in the end we were able to cover the entire mine-to-market industry.

EASTERN EMERALD BELT MINES

The production of the eastern belt (table 1) does not match the volume and total value of the western belt, but it still has significant production and can produce high-quality material. These mines are primarily located in the Chivor and Gachalá areas, which are not as developed as those in the Muzo district. The emeralds tend to be more bluish and not quite as saturated as those from the western belt, but they can have higher clarity and are often prized by Chinese buyers looking for the clean, bright material sought after in that market.

Chivor. Upon arrival in the Chivor area, we went to El Manantial, owned by Uvaldo Montenegro. El Manantial had been in continuous production for more than six years. Its name, Spanish for "the spring," refers to the constant flow of water from the mine due to the groundwater in the mountain. The tunnel is pitched at an incline where possible so the

Figure 9. A sampling of the rough emeralds obtained for GIA's country-of-origin reference collection. These samples, ranging from 0.445 to 6.397 ct, came from Coscuez. Photo by Kevin Schumacher.

TABLE 1. Colombian emerald mine locations, eastern belt.

District	Mine	GPS Coordinates	Mine	GPS Coordinates
Gachalá	Bocamina Tesoro	04°42.945' N, 073°26.926' W	Capulina	04°43.274' N, 073°26.583' W
	Bocamina Tesoro 2	04°42.942' N, 073°26.955' W	El Toro 3	04°43.309' N, 073°26.580' W
	Bocamina El Diamante	04°42.899' N, 073°26.888' W	El Toro	04°43.254' N, 073°26.477' W
	El Diamante (mine camp)	04°42.901' N, 073°26.883' W	El Higueron	04°43.613' N, 073°26.404' W
	Bocamina El Diamante 2	04°42.982' N, 073°26.836' W	Matecaña (old)	04°43.609' N, 073°26.341' W
	La Estrella	04°43.026' N, 073°26.805' W	Matecaña	04°43.434' N, 073°26.286' W
	El Toro (mine camp)	04°43.280' N, 073°26.703' W	La Suerte	04°43.749' N, 073°26.216' W
	El Toro 1	04°43.278' N, 073°26.701' W	Bocamina Diamante La Gotera	04°43.614' N, 073°26.098' W
	El Toro 2	04°43.342' N, 073°26.655' W	La Gotera	04°43.615' N, 073°26.098' W
Chivor	El Amarillal	04°51.139' N, 073°23.118' W	San José 1	04°51.128' N, 073°22.900' W
	Acuario Éxito	04°51.181' N, 073°23.123' W	San José 2	04°51.104' N, 073°22.892' W
	San Judas	04°51.188' N, 073°23.123' W	La Catedral	04°51.121' N, 073°22.895' W
	Mirador 1	04°51.177' N, 073°23.094' W	Admin San Pedro (mine camp)	04°51.242' N, 073°22.791' W
	Mirador 2	04°51.212' N, 073°22.995' W	Las Cabañas (mine camp)	04°51.364' N, 073°22.820' W
	San Gregorio	04°51.192' N, 073°22.956' W	Colifror (mine camp)	04°51.083' N, 073°22.655' W
	Milenio 1	04°51.158' N, 073°22.937' W	El Manantial	04°51.242' N, 073°22.463' W
	Milenio 2	04°51.148' N, 073°22.924' W	Dixon	04°51.409' N, 073°22.510' W
	El Porvenir	04°51.138' N, 073°22.913' W		

Note: The term bocamina *refers to the tunnel or shaft opening.*

water can run out. Miners had hit a major pocket just four months earlier and were enjoying a small production when we arrived. The emeralds from this tunnel had a classic Chivor appearance: slightly bluish but often very clean and bright.

The area being worked and producing new material was the Scorpion section. El Manantial's maze-like tunnels are more than 1.7 km long, though some are depleted. One vertical shaft that led to a productive tunnel was nearly filled with water and had to be pumped after every five hours of mining (figure 10), a process that takes two hours. One of El Manantial's tunnels connects to another important Chivor mine, San Gregorio.

We proceeded to a productive zone where they had advanced the tunnel by blasting and removing rock to access an area containing emeralds. Reaching it required walking through the tunnel for nearly two kilometers, with water coming over the tops of our boots, to a divide where the contact zone between the black shale and the calcite vein contained emeralds. The walls of the tunnel were very wet black shale, and the miners chased the white calcite veins to hit emerald production zones. There were also numerous areas of yellowish calcite along with quartz, pyrite, and even some stalactites overhead.

Lighting was furnished primarily by our headlamps and flashlights. Although ventilation tubes extended through the tunnel, the farther in we went,

Figure 10. Flooding is a constant struggle in many of Colombia's mining tunnels. Shafts can rapidly fill with water, and the tunnels often have streams of water running through them. Photo by Andrew Lucas.

Figure 11. A variety of hand tools, including knives, were used at El Manantial to carefully remove emerald crystals from the productive zone. The tool chosen depended on how deeply the crystal was embedded in the rock and whether the miner felt it could be removed without damage. Photo by Andrew Lucas.

the more difficult it was to breathe. After documenting the miners extracting emeralds with hand tools, authors JM and AL took turns extracting emeralds with a rock hammer directly from a calcite vein for GIA's reference collection (figure 11). Next, we witnessed further drilling into the wall face. The miners placed explosives in the drill holes and blasted farther into the calcite vein. During the drilling into the black shale, black dust consumed the area until visibility was down to a few inches.

At the mine camp and dining area, workers offered rough emeralds from El Manantial and other mines in the Chivor area for sale. After buying rough samples for GIA's reference collection, we traveled to Mr. Montenegro's base camp, Las Cabañas. Here we set up our base to explore Chivor and interviewed Mr. Montenegro against the beautiful backdrop of the mountains.

Mr. Montenegro's father, Pedro Pablo, started working in Chivor in 1965, first as a cook and then as a miner. After finding some profitable emeralds, he took his share of the proceeds and began buying stones at the mines and selling to dealers from Bogotá. As his profits and expertise grew, he expanded operations to establish an office in Bogotá and began cutting and selling the finished stones himself. Changes to mining regulations in 1991 paved the way for further privatization of Colombian emerald mining. This led the Montenegros to venture into their own mining concessions in 1993.

To lessen investment burden and risk, most Colombian mining operations involve partnerships. Mr. Montenegro works in five concessions in the Chivor area totaling 140 hectares, with interests in another three concessions being developed. He is currently working 15 tunnels on the five existing concessions—including the San Pedro, San Gregorio, El Manantial, Oriente, Piedra Chulo, Quebra Negra, and Gualí mines—with about 15 miners in each. In all, about 50 tunnels in the Chivor area were in operation, and Mr. Montenegro said there were about 15 concessions with working tunnels.

While Mr. Montenegro works with partners, he owns the concessions or mining licenses. In Colombian emerald mining, an association generally consists of the license owner, who holds 50 percent of the utility, and the partners, who pay for expansion and operations and take 50 percent of the production. This can be deducted from exploration and investigation operations as well as other work, all based on agreement with the investors. Mr. Montenegro owns the mining license at El Manantial and brought in investors to cover operating expenses in some of the productive tunnels. He said he takes 50 percent of the profits, and the rest goes to the investors and miners.

The miners employed by Mr. Montenegro, like many others in Colombian emerald mines, prefer to take a percentage of the profits rather than just a salary. The miners often receive a base salary with social security benefits as well as food and housing, but their main incentive is the profit share and the ability to keep and sell some of the production themselves. In this sense, they have the same incentive as the owners to find emeralds.

On the new concessions, Mr. Montenegro was waiting for environmental assessments before mining and looking for investors. For each of these concessions, he had commissioned an advanced geological study to approach the mine planning in a more modern way. He was also considering more mechanization than is typically found in Colombian tunnel mining, which is closer to artisanal mining. With the geological mapping and mine planning, as well as more modern and larger-scale operations, he predicted that the production currently obtained in a year would be achieved in a month. Since emeralds from Chivor tend to be bright and clean, qualities in high demand in China, he had been traveling there to meet with investors.

Mr. Montenegro said that he is able to stay competitive by mining the stones and taking them through the entire wholesale value chain of treatment, cutting, and sales on the global market. Because the emeralds are not changing hands, he is able to avoid markups. There is also the advantage of being able to provide complete chain of custody. This assures buyers of the legality of their purchase and provides a documented supply chain, including the type of filler used during treatment.

After our first day at El Manantial, we visited numerous operating tunnels and documented the San Gregorio mine, owned by the SOESCOL Company, of which Mr. Montenegro is a controlling shareholder, and the Dixon and Tesoro mines, owned by the San Francisco Company. We also observed small-scale processing outside the tunnel operations in the Chivor area (figure 12).

The Dixon mine has been active for more than 30 years. A Canadian company owned the mine from 1995 to 1998, but for the last 10 years the San Francisco Company and controlling shareholder Hernando Sanchez have operated it. The last major emerald pocket was found in 2001, but since then smaller pockets have been found regularly, keeping the mine profitable (G. Lopez, pers. comm., 2015). At San Gregorio, the situation was similar. In December 2014 and January 2015, pockets were found that produced kilos of emerald rough averaging US$12,000 per carat.

At Dixon and Tesoro, the San Francisco Company employs 14 miners permanently, and another seven are on call for when a pocket is discovered. Miners work from 7 a.m. to 4 p.m. for 20 days straight and then have 10 days off. Dixon mine manager Giovanni Lopez, who has worked there for 22 years, summed up the miners' outlook. While they make a living from the production of small pockets over the years, they are not just looking for a monthly income: They are seeking the big payday. Mr. Lopez said that if he hit a large pocket and became rich, he would invest in other businesses for secure income and continue to mine for another large pocket, for the sheer adrenaline rush of searching for treasure.

In Colombian emerald mining, explosives are a necessity. Water-gel explosives authorized for emerald mining must be purchased from the Colombian military weapons manufacturer Indumil and kept in a secure area according to strict guidelines. The Chivor area has a military presence, and the explosives storage area at each mining operation is guarded by private security. Miners handling the explosives must be certified by the government.

Figure 12. Small-scale processing outside the Chivor tunnels included removing ore from the tunnels and sifting through bags of material in the hope of finding emerald crystals. Photo by Andrew Lucas.

At Tesoro we saw typical Colombian drilling and explosives techniques (figure 13). One of the most difficult assessments was how quickly to advance through the rock to a productive zone without blasting into a pocket and destroying emerald crystals. The drill hole locations also had to be carefully planned to prevent damage to the emeralds.

The miners drilled approximately one-inch-diameter holes into the mine wall, with the hole's length determined by how far they wanted to advance. The detonator was inserted into the explosives, which were loaded into the drill holes with the fuse sticking out of the hole. A separate fuse was used to light them all. We had about a minute to reach a safe area of the tunnel. After the blast, the wall was inspected for signs of an emerald pocket. Once the rubble was cleared away, the process was repeated. The decision of when to blast is a complicated one, as it must balance the need to reach emer-

Figure 13. Hoping to reach an emerald-bearing pocket, the miners stuffed explosives into holes they had drilled and lit a fuse that subsequently lit all the fuses. Photos by Pedro Padua.

ald-bearing pockets with the risk of destroying valuable material.

Gachalá. Upon arriving in Gachalá from Chivor, our first stop was the company Mina La Emilia. We were met at the Diamante mine camp by principal owners Camilo Sanchez, Benito Mendez, and his son Christian Mendez, who is also chief operating officer of Mensal Emeralds. We immediately began examining emerald rough from their tunnels and others in the area. We also met a Chinese buyer, known to author AL, who was buying emerald rough. The buyer was looking for the clean, bright material the Gachalá and Chivor areas are known for.

The next day we had an in-depth look at El Diamante, La Estrella, and El Tesoro, all mined by Mina La Emilia. In Colombia, the name of the concession is often shared by one of its tunnels, in this case the La Emilia tunnel. When dealers refer to the mine an emerald comes from, they might use the concession name or the tunnel name. The La Emilia concession had four active tunnels at the time of our visit.

El Diamante is over 20 years old and begins as a vertical shaft with an elevator that goes down 48 meters to reach a tunnel leading to a second internal vertical shaft. Here we descended by a harness, called *la cincha*, that was lowered with a winch. The second shaft led to subsequent tunnels and other internal vertical shafts. The productive zones were in the tunnels on the first level we reached by elevator.

As we proceeded, we witnessed a common sight in Colombian emerald mine tunnels: the use of wooden braces for structural integrity. The mining areas had an abundance of groundwater, which added weight to the braces and rotted the wood. As we proceeded through El Diamante, we saw numerous wooden braces fracturing. Additional braces had to be built, and in one extreme case the tunnel's entire wooden brace structure system had to be replaced. Often a fractured brace had a new one right next to it.

In following the productive diggings, El Diamante's leadership used a more systematic and thorough exploration methodology. They initially explore through 1,800 meters of a level, following the mineralization, and analyze every 50, 70, or 100 meters, depending on the geology. If they reach 100 meters without indicators of a productive zone, they look for an opposing face. If nothing is found in the opposing face, they make a transverse tunnel, leaving a 25-meter space parallel to the first one, and go back for further exploration. Once they reach the end of the concession area, they stop, move up or down 10 meters, and repeat the process.

The pocket we reached was being worked with a jackhammer to advance along the calcite vein. They had not yet reached an emerald pocket where crystals could be retrieved by hand, but they were close enough that they did not want to blast into the productive zone.

Next we visited La Estrella, a ramp-style tunnel mine that was less than a year old. While El Diamante had a good history of production, La Estrella had not seen significant production by the time of our visit. Nevertheless, there were promising geological indicators that it would be a major producer in the near future. We walked through the tunnels to a zone being worked by the head geologist, who was digging out the calcite vein with hand picks. He thought that they just needed to go deeper into this zone to reach a massive emerald pocket.

While waiting to enter La Estrella, we spoke with the Mendezes. The elder Mendez had been in the emerald business more than 50 years. He was now 82, though one would never know it by the way he moved along the trails and through the mines. He

started out dealing in emeralds at Peñas Blancas, Coscuez, and Muzo and then got into mining. During the 1980s and 1990s, he found that mining and doing business in Gachalá was safer than in the Muzo and Coscuez areas. He also preferred the cooler climate and made the transition to Gachalá over 20 years ago, first in open-pit mining and then tunnel mining.

The family has other concessions elsewhere in Gachalá and in Muzo. All of the production is taken to Bogotá, where the partners hold an auction among themselves. The winning partners may sell the rough to cutters in Bogotá or cut it themselves and sell the stones to global buyers. If the Mendez family wins the auction, they cut and sell the production. They use independent cutters in Bogotá, chosen according to the type of stone and their cutting expertise.

Meanwhile, Christian Mendez is seeking to expand the business on the global market. Their global customers range from retail jewelers to jewelry manufacturers and other wholesale dealers. China is the most important customer, with another strong market in the United Arab Emirates. The U.S. market accepts all qualities from the Mendez family, while the Chinese market prefers fine color and very high clarity and brightness, or very large stones of a more modest quality. The UAE is a diversified market for them, as the wealthy and the royal family want the best and largest stones, while some retail jewelers there seek mid-level commercial goods.

The family wants to move up the value chain and eventually sell finished emerald jewelry to retail customers. Christian Mendez spoke of the industry's future with regard to foreign mining companies. He noted that the country could benefit from mining investment, increased production, job creation, and more tax revenue. At the same time, he sees local Colombian traders and cutters struggling to survive as access to emerald rough has become restricted.

El Tesoro was the third tunnel we visited at La Emilia. It began as a vertical shaft, like El Diamante, but used only a winch-lowered harness system. The harness lowered us to the first level, where a tunnel led to another vertical shaft with wooden ladders to tunnels where the productive zones were.

Our last morning in Gachalá was spent visiting three more tunnel mines—El Toro 1, 2, and 3—for a total of six mines we saw in the district that were either in production or being worked to reach productive zones. Reaching these mines required some hiking through the mountains. El Toro 1 was about a year old and had yet to produce emerald. There were no strong indicators in the tunnel for the miners to follow. El Toro 2 had been worked on and off for about seven months. The area we visited had been worked for four months. The tunnel was 102 meters long, with some indications that emeralds might be found. It had no wooden beam supports and could continue being worked without supports for a time. El Toro 3 had the most activity of the three El Toro mines in Gachalá.

Eastern Belt Mine Markets. The eastern emerald belt did not have the large organized mine markets we would later see in the western emerald belt at Coscuez and Muzo. Miners sold emeralds outside the gate, at the mine camp, and even in the dining areas. Miners and dealers in the town of Chivor sold emerald rough in homes and offices and in the street. More material was available in Chivor, but there was definite interest from buyers in Gachalá. Author JM was able to buy numerous rough samples for the GIA reference collection directly from the miners, including their latest production.

WESTERN EMERALD BELT MINES

Colombia's most productive mines lie in the western emerald belt (table 2). These include the Muzo (figure 14), Coscuez, and Maripí areas, especially along the Río Minero and Río Itoco. We visited numerous tunnels in these areas, from small operations to large commercial enterprises. We also witnessed firsthand the relationship between small independent miners and large-scale operations. The mine markets in this region were also an important source for sample collection. While the landscape still shows the effects from years of large-scale open-pit mining, all the activity today is tunnel mining.

Coscuez. After spending the night in Pauna, we drove to the Coscuez area. We visited the El Chacaro mine market and then the La Paz tunnel, owned by Esmeracol S.A. (Hernando Sanchez, named earlier as a controlling shareholder of the San Francisco Company, is also a controlling shareholder of Esmeracol.) We spent the rest of the day at the La Paz tunnel observing the mining process, including extraction, washing, and trading outside the mine and at the mine camp.

Mine manager Fabian Rodriguez guided our visit through the La Paz tunnel. He comes from a family of emerald miners and has managed operations there for six years. Mr. Rodriguez said that La Paz was founded approximately 25 years ago with the peace agreement that ended the Green War (the tunnel's name means "peace").

TABLE 2. Colombian emerald mine locations, western belt.

District	Mine	GPS Coordinates	Mine	GPS Coordinates
Muzo	La Playa (market)	05°32.000' N, 074°08.542' W	Bocamina Old Mine	05°32.294' N, 074°08.799' W
	Millonarios (mine camp)	05°31.992' N, 074°08.897' W	Oldmine (mine camp)	05°32.304' N, 074°08.771' W
	Bocamina Millonarios	05°32.001' N, 074°08.951' W	Palo Blanco	05°32.337' N, 074°08.965' W
	Fortaleza (mine camp)	05°32.033' N, 074°08.776' W	Catedral	05°32.472' N, 074°08.837' W
	Bocamina Aguardiente Viejo	05°32.134' N, 074°09.042' W	Puerto Arturo	05°32.523' N, 074°08.892' W
	Bocamina El Amarillal	05°32.254' N, 074°08.703' W	Retorno	05°32.560' N, 074°09.069' W
	Bocamina Futuro	05°32.263' N, 074°08.682' W	Tequendama	05°32.667' N, 074°08.864' W
	El Amarillal (mine camp)	05°32.269' N, 074°08.700' W	Morro	05°32.842' N, 074°08.908' W
	Mina Real (mine camp)	05°32.288' N, 074°08.755' W	Pavas Santo Domingo	05°32.925' N, 074°09.834' W
Maripí	Polveros	05°34.981' N, 074°05.595' W	Totumos	05°35.594' N, 074°05.367' W
	Españoles	05°35.191' N, 074°05.507' W	Cunas	05°35.823' N, 074°05.210' W
	Españoles (mine camp)	05°35.198' N, 074°05.507' W	Consorcio	05°36.085' N, 074°05.305' W
	Caselata	05°35.337' N, 074°05.393' W	La Pita	05°36.717' N, 074°05.254' W
	Bonanza	05°35.354' N, 074°35.568' W	Puerto Gringo	05°36.313' N, 074°04.988' W
Coscuez	Abuela Superior	05°37.706' N, 074°08.474' W	Bocamina Tentación	05°37.813' N, 074°09.446' W
	Abuela Inferior	05°37.710' N, 074°08.483' W	Gemacol	05°37.938' N, 074°07.940' W
	Bocamina Millonarios	05°37.706' N, 074°09.443' W	Bocamina Itoco	05°37.846' N, 074°09.345' W
	Bocamina Futuro	05°37.750' N, 074°09.358' W	Bocamina Bonanza	05°37.886' N, 074°09.423' W
	Mina La Abuela (mine camp)	05°37.809' N, 074°08.552' W	Bocamina Morrallero	05°37.912' N, 074°09.432' W
	Bocamina Diamante	05°37.750' N, 074°09.384' W	Muches	05°38.098' N, 074°09.324' W
	Bocamina Matera	05°37.771' N, 074°09.371' W	El Chacaro (market)	05°38.094' N, 074°09.458' W
	Bocamina Fortuna	05°37.772' N, 074°09.475' W	Jerusalén	05°38.140' N, 074°08.938' W
	Esmeracol S.A.	05°37.779' N, 074°09.600' W	Bocamina La Paz	05°38.595' N, 074°09.120' W
	Esmeracol (mine camp)	05°37.781' N, 074°09.599' W	La Paz Coscuez (mine camp)	05°38.600' N, 074°09.064' W

Note: The term bocamina *refers to the tunnel or shaft opening.*

As we entered La Paz, we saw cart after cart being pushed through to the exit. Open carts containing only shale were removed from the tunnel as the miners blasted forward. Closed and locked carts contained emerald-bearing shale. Meanwhile, water constantly flowed out of the tunnel.

We walked 1,650 meters to the first elevator, which went down 48 meters to a second elevator. This took us down another 35 meters to another shaft and elevator, which descended another 48 meters to a tunnel leading to a productive zone. Several tunnels were being worked at the different levels. The material was bagged in white sacks, placed in the carts, and rolled to the elevators to be sent to the top tunnel and wheeled out of the mine. Unloaded empty carts being pushed back to the working areas constantly passed loaded carts, with just enough room for both.

Between La Paz's second and third shafts are two tunnels designed for air circulation and another vertical shaft, referred to as a "chimney," to remove contaminated air. The heat (with temperatures often over 40°C, or 104°F) and 99 percent humidity were draining and often rendered our cameras inoperable. Black shale dust is always in the air, and even masks and respirators do not keep it out of the miners' lungs. Outside the tunnel their faces were covered in the black shale (figure 15), reminiscent of coal miners from a century ago.

Once the carts exited the tunnels, they were pushed to a simple brick shed, where the ore was washed by hand with traditional net-like screens.

Figure 14. The mining area around the town of Muzo is world renowned for its emeralds. Photo by Andrew Lucas.

This method was used at many emerald mines throughout Colombia. One miner would shovel ore into the net while two others held it at opposite ends. A fourth miner would control water flow from a pipe as the two holding the net washed the ore vigorously.

Most of the production was taken to Bogotá, but some was given to miners who would sell it just outside the mine gate (figure 16), at the mine camp dining area, or at the El Chacaro market. At the gate, near the small washing building, locals would wait to receive ore for washing. Allowing locals to wash the tailings is a tradition at Colombian emerald mines.

The miners work eight hours a day, five days a week. At the time of our visit there was some emerald production, but nothing "important" according to Mr. Rodriguez. Even so, 98 miners were working in the La Paz tunnel, and the total staff was 105.

After driving back through the El Chacaro mine market, we spent the night at the small but very lively town of Otanche, which had people in the streets and soccer games in the park. The next day we visited three more active mines in the Coscuez area: Pavimentado, Bonanza, and Terraza, all owned by Esmeracol S.A. We interviewed mine manager Andres Murcia and proceeded to the tunnels, starting with Pavimentado.

After walking through the roughly 1,200-meter tunnel, we had to crawl into a productive zone where the miners were extracting emerald from a wide calcite vein. The heat and humidity reached the point where the camera lens was continuously steamed up and had to be wiped free of condensation just before taking a photo. We were able to see emeralds in the calcite veins being extracted by hammer and chisel. Once all the visible emeralds were removed, the miners drilled holes around the pocket and placed explosives to blast farther into the vein (figure 17).

As in the Tesoro tunnel in the eastern belt, the fuses had to be cut long enough to allow time for everyone to crawl out of the pocket to a safe distance from the blast. After returning to examine the

Figure 15. At La Paz, the miners emerged from the tunnels covered with black shale and drenched in sweat. Photo by Andrew Lucas.

Figure 16. Buyers wait outside the gate at La Paz for miners and locals to bring their share of emerald rough for sale. Photo by Andrew Lucas.

pocket, the miners drilled to remove more calcite, and more emeralds became visible for extraction with hammer and chisel.

Bonanza and Terraza were the hottest and most humid tunnels we visited. Steam poured out of the entrances, and the cameras fogged up immediately. Both were smaller operations than Pavimentado. Afterward, we drove back through the El Chacaro market and then on to Muzo.

Muzo. Upon arriving in Muzo we went to the street market and examined the rough emeralds offered for sale. The first tunnel we visited was El Amarillal, operated by Mina Real Limitada, where we interviewed mining engineer Carlos Diaz. The company has 12 tunnels on the concession. A few years earlier, Mina Real commissioned a geological study to determine the possible productive zones and look for geological faults. When zones with potential are identified, the mine operators focus on those specific zones and determine the exploration method that will not cause damage to the tunnels. Exploration methods are different for each mine, depending on its economic potential. Mines with greater potential are more mechanized and have more workers (C. Diaz, pers. comm., 2015).

El Amarillal had been worked for seven years at the time of our visit. The main tunnel is 1,000 meters long, with numerous vertical shafts in exploration or reaching productive zones. When the miners reach a fault, they find kaolinite and carbonate, minerals associated with emeralds (C. Diaz, pers. comm., 2015). But even then there is no guarantee the zone will be productive. El Amarillal has 400-meter-long segments that have been unproductive, though the miners might pass close to the emeralds while following geological indicators. Emeralds form primarily in the veins but can also be found in the kaolinite that is in contact with the veins, or in a bordering zone. Success is uncertain, so two or three different areas must be explored.

To begin, miners break the hard rock with explosives. Compressed air and jackhammers are used to perforate blast holes between 1.2 and 8.0 meters apart, in which the explosives are placed. The person handling the explosives has completed an army certification course. He activates the detonation, which breaks the rocks, and workers with shovels fill wagons with gravel and take them to trucks for removal.

Another system applies when there is production. A manager from the company (wearing a white helmet) and a partner (wearing a red helmet) take control of the pocket. They put a large quantity of emeralds in a sealed locker and carry it out to a washing location. The emeralds are counted and weighed, then sorted and placed in other sealed containers.

Figure 17. At Pavimentado, miners removed emerald-bearing pieces of calcite veins with hand tools and by drilling into the rock face, before placing explosives in the drill holes to advance the tunnel. Photos by Andrew Lucas.

These stones are set aside and offered for sale at a meeting of partners and investors.

The company has about 60 workers, including controllers, delegates, and mine workers. El Amarillal itself employs about 40 people, half of them mine workers. (In this zone there are also about 200 guaqueros working along the river.) Each work area has a budget for salaries and worker assistance, and the administrative staff is also salaried. Workers receive assistance with their monthly expenses. When production occurs, the workers receive a portion of the rough mined daily or a share of the profits from its sale.

Before tunnel mining began, the company used mechanized surface mining. Although many emerald-bearing veins were unearthed using this method, the environmental impact on the landscape was severe. The area has seen good production at the tunnel mines, not only at El Amarillal but also at the neighboring company's property. Guaqueros have also found valuable emeralds in the river. When it was an open-pit operation there was more independent mining activity, especially at the river. Mr. Diaz acknowledged that the operation would be more efficient with modern equipment, but this requires a substantial investment, typically from a foreign company.

Mina Real is now about a third of the way into a 30-year contract for the concession from the national mining agency, and they are transitioning from the exploration phase to extraction. They expect to see results because they have reached the productive zone with two decades still under contract. The concession was once owned by Victor Carranza, who gave it back to the state before it was purchased by Mina Real Limitada.

The company's emerald sales initially take place among the same 14 partners, consisting of companies or independent merchants who make offers to mine representatives. Among those partners are some emerald exporters. From 2011 to 2015, the mine produced 380,000 carats in emerald rough worth US$700 million.

With lighting and ventilation tubes throughout, El Amarillal's main tunnel was typical of Colombia's better-operated tunnels. It was hundreds of meters long, branching into other tunnels and shafts. There was plenty of activity, with drilling and blasting and emeralds being extracted and wheeled out in carts. We also observed the battle with groundwater as a miner attempted to dig in a shaft that was constantly filling up.

Río Itoco. We had the opportunity to document two very different activities along the Río Itoco, a tributary of the Río Minero: small-scale mining along the riverbank, and the washing of a large-scale mining operation's tailings and ore by thousands of locals.

The small-scale operations were along the river, especially where open-pit operations once existed. The miners used water hoses and picks to break up the soil and would either place the material in wheelbarrows for washing by the river or run it through a makeshift sluice (figure 18). Several hundred independent miners were working the area near the Río Itoco mine market ("La Playa") and El Amarillal. The mining and washing was done in groups, often consisting of family members. At one operation an excavator was used to move material faster. This was the only use of mechanization we saw by these small-scale miners along the river.

We were also present on two mornings when Minería Texas Colombia (MTC) trucks brought tailings and unwashed ore to the riverbanks and dumped them for the locals to wash. It was a captivating sight: a line of trucks coming down the hill from the MTC mining area in regular intervals to drive across the shallow area of the river, slowly raising their hydraulic beds to pour out the tailings without ever coming to a stop. The locals crowded around the passing trucks, and the tailings were spread out to minimize the crush of people.

At first glance, the scene appeared to be a frantic race to scoop up and bag the tailings (figure 19). Upon closer observation, it became clear that there was organization (figure 20). Distinct groups were working together, most likely families and neighbors. The stronger members of the groups would wrestle their way to the tailings and bag the material. They would carry these bags to the river for washing with net-like screens while the rest continued to gather as much of the remaining tailings as they could.

Women were involved in the operation at all stages, from scooping up the tailings to washing them. Virtually everyone was covered in black shale. Meanwhile, numerous buyers waited nearby to make offers. They were easily identified by their clean clothes and the traditional white towel, used to wipe the emerald rough before examination, draped around their necks. If the locals did not immediately receive the price they wanted from the buyers by the river, they would simply walk up the hill to the La Playa market to find a better offer.

Minería Texas Colombia. We spent a full day at the MTC emerald mine, part of Muzo Emerald Colom-

Figure 18. Independent miners on the banks of the Río Itoco use high-pressure water hoses to remove the shale, which will be washed in sluices or taken by wheelbarrow for washing. Photos by Andrew Lucas.

bia. Mine manager Carlos Contreras Cañizo, a native of Mexico, had a background in gold mining using modern methods. He compared the two types of mining.

"With gold you are looking for veins, and you can count on a fairly predictable range of how many grams per ton will be extracted. This can be readily mapped through core sampling and geological studies. With emeralds you follow indicator minerals and find more pockets than a relatively even distribution. So with both gold and emerald, the more earth you mine, the more material you can extract.

"But with emeralds it is far harder to predict the amount per ton, if not impossible, and far harder to predict when you will find them. The other factor is that the gold extracted from a mine has predominantly the same value. However, emeralds extracted can vary tremendously in value, and they cannot predict where the higher-value material is."

Predicting where to find the higher-value emer-

Figure 19. As MTC trucks drove by the Río Itoco just outside the concession and emptied the ore, dozens of people gathered around to secure their share of the tailings. Photo by Andrew Lucas.

Figure 20. The apparent chaos at Río Itoco proved to be an organized system with intense competition for the ore dumped by the trucks. The strongest team members carried bags of ore to the river for the others to wash. Photos by Andrew Lucas.

alds is a challenge even for a large, sophisticated mining operation like MTC. Mr. Cañizo said it was "fifty percent knowledge and hard work, fifty percent luck, and God bless you."

In 2009 MTC was a partner in the Muzo mines, including the famous Puerto Arturo mine. Mr. Cañizo had envisioned creating ramps connecting the different levels to a central ramp for the vehicles, transporting miners via the same shafts used for ore and machinery. At that time MTC was operating Puerto Arturo in a partnership with Coexminas, a Colombian company that had controlled the mine since 1977. One of the three principal partners of Coexminas was Victor Carranza, the "Emerald Czar." Production was split fifty-fifty between the two companies. Part of the deal was a clause stipulating that MTC create 3,200 meters in tunnels or forfeit the arrangement, which limited the mining methodology Mr. Cañizo could pursue. After Mr. Carranza's death in April 2013, MTC acquired the mine and began implementing a ramp and new methodology.

MTC extracts emeralds in a manner similar to that of other Colombian tunnels, using drills and jackhammers to reach the emeralds and then hand picks to extract them. They also use a similar washing process of screens, water, and human muscle. MTC is working six mines or galleries: Palo Blanco, Puerto Arturo, Tequendama, Catedral, Pablo Sanchez, and Matefique (using contractors at the latter two). The main mines in production are Puerto Arturo, Catedral, and Tequendama.

Puerto Arturo is the deepest shaft, currently at 152 meters, while Tequendama is about 85 meters deep and Catedral has two shafts, one 20 meters and the second 60 meters. When Mr. Cañizo took over as mine manager, all the shafts were independent from one other. Now they are connected by tunnels, and the goal is to have a ramp intersect the tunnels currently in production. The La Rampa tunnel is spiral shaped, extending about 400 meters underground to connect all the tunnels. La Rampa is MTC's testing ground for geological research and optimized extraction techniques.

Production from the pockets can be dramatic. In May 2015, MTC recovered 152,000 carats from one area, including large stones weighing up to 1,200 carats. The total yield for 2014 was over 240,000 carats, and by the time of our visit in November 2015 they had produced 384,000 carats for the year (C.C. Cañizo, pers. comm., 2015).

After the ore has been washed, the emeralds are separated into four qualities: precious (large sizes, high quality, intense color), *chispero* (small sizes, high quality, intense color), crystal with tone (good form, light to medium tone), and *morralla* (poor quality). The rough stones are placed in envelopes labeled with the weight, basic quality classification, and tunnel of origin and then picked up for transport to Colombia Texas Transformadora (CTT), a cutting facility in Bogotá's free trade zone.

Muzo Emerald Colombia has invested more than $50 million in modernizing the MTC mine, including ramps to connect the tunnels. The mine employs more than 800 people (figure 21), many of them from the nearby communities. They also support area schools and a health clinic that serves more than 1,000 local people (Burgess, 2015).

Maripí. As with Muzo, mining operations in the Maripí area have changed substantially in recent years. In 2011, two of the authors (DF and AL) visited mines in this area along the Río Minero, including La Pita, Cunas, Totumos, Polveros, Los Españoles, Bonanza, and Consorcio, which was not in operation during this visit.

Figure 21. MTC employs hundreds of men and women from the local communities. Photo by Andrew Lucas.

In the Maripí area we began at Polveros and Los Españoles, documenting mining activities at the latter and interviewing mine manager Fabian Arango. Los Españoles has been worked for about 30 years, but the operation has been more professional in its methodology since 2011. There is usually a workforce of 15 miners at the tunnel. We saw a continuous flow of carts between the mine and a shed where the material was washed with net-like screens (figure 22). The tunnel branched off into others, with the one on our left containing a working productive zone. There was also a 60-meter vertical shaft leading to tunnels with productive zones, but the groundwater seeping in at the lower level had to be pumped out constantly.

The productive zone runs at a 45-degree angle to the vertical shaft and is about 500 meters wide, with the most productive area about 100 meters wide. This productive zone extends to the La Pita, Cunas, and Consorcio mines in Maripí (F. Arango, pers. comm., 2015). This high-potential zone is very expensive to work because of the groundwater filling the tunnels and shaft.

After an important production, mine management will call the partners, who distribute goods to the shareholders. Mine management and the partners seal the emeralds and take them to Bogotá, where they choose the stones to be cut and those to be kept as rough specimens. But first the miners are allowed to go through the rough, and with management they determine what percentage and qualities they will be given to sell on their own. The production percentage they receive is in addition to their salary compensation package, which includes social security and bonuses. The last important yield was in December 2014, from the production zones in the tunnels that extend from the vertical shaft.

La Pita. At La Pita we took a detailed tour and interviewed mine manager Javier Puerto, who had 20 years of emerald geology, prospecting, and mining experience. Operated by Zuliana de Esmeraldas, La Pita opened in 1995. The first significant production came in 1999, when miners found an emerald-bearing pocket. Mr. Puerto began working for the company that same year, when the tunnel was already 1,200 meters long. The concession is about 39 hectares. Mr. Puerto said that since his arrival, the mine had been worked consistently. He pointed out that the deposit is all one mineralized strip extending

Figure 22. At Los Españoles, miners pushed carts of ore through narrow tunnels to an open shed where the ore was washed for emerald. Photos by Andrew Lucas.

from Polveros, Totumo, Cunas, Consorcio, and La Pita up to Puerto Gringo.

We entered the mine through the main tunnel and proceeded 625 meters inside to the first vertical shaft, which was 35 meters deep. At 700 meters we encountered the second shaft, which was 42 meters deep. A hundred meters farther was a 44-meter shaft. Two additional shafts, both much shallower, were filled with water and not being worked at the time. When an area is not being worked, the acidic water corrodes the wooden structure and rusts the metal in just a few months. We went to all the levels, with the fifth level 110 meters below the main tunnel floor. On each level we visited all the productive tunnels and most of those under exploration. The current mine extends from 120 meters below the mine floor to 30 meters above it.

La Pita has several emergency exits in case of flooding, including an exit to the north by Puerto Gringo, and a ventilation chimney. An extractor is used to pump air into the tunnel and down every shaft, up through the working areas, and then out through the chimneys. As a result, the air in the tunnel and shafts is remarkably fresh and free of the gases that can build up in a mine: sulfuric acid, carbon monoxide, carbon dioxide, and even nitrogen oxide, a byproduct of explosives. Pipes bring in electricity from the surface, and an internal control station reduces the energy lost from carrying it over a distance.

The company hires people from the region to ensure as much benefit to the local community as possible. They employ about 120 people per shift, in two groups—from 6 a.m. to 2 p.m. and from 2 p.m. to 10 p.m.

Mr. Puerto noted that emerald deposits are geologically very different from other types of deposits. Most other mineral mining is geometric: Miners advance to find a layer of certain thickness, width, and length, which means constant production can be managed by week, month, and year. With emerald mining, the production zones are variable and output is never constant. Companies might spend two or three years preparing a mine, or they might recover emerald after just 15 days of operations. Every time miners go deeper into a Colombian emerald tunnel, the water level rises and extraction becomes more difficult. Exploration for new veins and pockets through horizontal levels often continues for one or two years until they find the veins. A single vein might be searched for a day, a week, a month, or longer. In many veins, no emeralds are ever found.

According to Zuliana de Esmeraldas's geological surveys, only 8% to 10% of the La Pita deposit has been exploited thus far. They plan to improve the transport system to increase production. For now they use the same carts (figure 23) found throughout Colombian emerald tunnels. They plan to install a mechanized system with inclined automated tracks for transporting the material. To manage the groundwater as they go deeper, they will drill vertically into the shafts and pump out the water (J. Puerto, pers. comm., 2015).

Mr. Puerto pointed out the importance of rock type and structure identification in emerald mining. In the sedimentary-type deposits, structures such as faults are especially important for emerald crystallization. In the western belt, almost all the emeralds were formed within compressional structures such as reverse and tear faults. The faults cross-cut the organic-rich calcareous shale, providing the space while the shale and hydrothermal fluids supplied the necessary ingredients for emerald mineralization. At the tunnel, geologists and miners follow the two major parallel faults of Río Minero and La Pita. The La Pita fault is a reverse fault, a typical structure developed in a compressional environment. Calcareous shale, the major component of the Muzo formation, is the target host rock for miners. After locating the host rock and structures, prospectors look for indicator minerals to trace the emeralds.

Figure 23. The La Pita operation uses elevators to bring up material from lower depths and carts to transport it through the tunnels. Photo by Andrew Lucas.

Zuliana de Esmeraldas has a two-stage distribution protocol. There are about 18 partners, and each visits in person or sends a delegate. The company extracts the emeralds, taking care not to break the crystals, and puts them in bags in the presence of the partners. The bags are sealed and locked in a safe, and a partner or delegate keeps the key. Once enough production has accumulated for the partners to sell, they wash and weigh the emeralds and put them in a security bag. The company's shareholders remove the emeralds in everyone's presence. They check the signatures, make sure all procedures have been followed, and schedule an auction. Outside merchants sometimes come to the auction and deal with people they know or buy the emeralds themselves.

Mr. Puerto pointed out three major production periods for La Pita, starting in the southern sector in 1999. They built shafts, did prospecting and geological exploration, and moved to the northern area, where they had good years in 2001 and 2002. In 2007 and 2008, they had a large production at the floor level, followed by considerable yield in 2010 and 2014. La Pita's production since 1999 is estimated at over $1 billion in rough emerald value.

Cunas. The Cunas mine, owned by Esmeraldas Santa Rosa S.A., has become one of the most important producers along the Río Minero. The Cunas mine camp is located above the tunnel, and the route to the mine was heavily guarded. The tunnel extended several hundred meters to a shaft where a working productive zone was active. It was a typical tunnel-style Colombian emerald mine but very different from La Pita, especially in terms of temperature and air quality. While Cunas also had ventilation tubes and mechanical pumps for circulation, it was much hotter and more humid, reminiscent of the Pavimentado and Bonanza mines at Coscuez. Water rushing through the mine sometimes reached our boot tops, and the air had to be monitored for the buildup of dangerous gases. Ore was carted out of the mine, and emerald-bearing material was identified as it was removed from the rock face, bagged and sealed, and taken to a vault.

Consorcio. The Consorcio mine was closed at the time of our visit. When author AL visited in 2005, it was one of Colombia's most productive mines. Prominas de Zulia, now Zuliana de Esmeraldas and also the owner of La Pita, was Consorcio's first owner when it was discovered in 1999. Initial production was impressive, and by 2001 Victor Carranza was a partner. The company formed subsequently was Consorcio Minero, with 50% belonging to Esmeraldas Santa Rosa (owner of the Cunas mine) and 50% to Zuliana de Esmeraldas. Estimated production value between 2001 and 2008 was about $1 billion (J. Puerto, pers. comm., 2015). A robbery in 2008 led Mr. Carranza to file for bankruptcy, ultimately canceling the agreement between Esmeraldas Santa Rosa and Zuliana de Esmeraldas, and the mine was still closed in 2015 due to ongoing litigation.

Western Belt Mine Markets. As with Chivor, the miners in the western belt usually have rough emeralds for sale at lunchtime or the end of the day. Larger mines often allow locals to wash their tailings and keep the emeralds they find. However, there are some very structured mine markets in the western belt. The largest are the La Playa market on the banks of the Río Itoco, the El Chacaro market at Coscuez, and the La Pita mine market in the Maripí area.

The El Chacaro market was very busy, with miners and dealers offering a wide variety of rough qualities and sizes for sale. When author AL visited in 2005, it was not uncommon to see miners and dealers carrying guns. This time no guns were visible, and there was more trading. The market also offered restaurants, bars, and gambling. When miners and dealers saw a potential buyer, they would put down their drinks or walk away from the gambling table to show their emeralds. There was a bustle of activity in the street, with the mountains and mines as a backdrop. Author JM obtained many emerald samples from miners here.

Also in the Muzo area, we visited the La Playa market, on a hill overlooking the Río Itoco and the Minería Texas Colombia mining area. Here many independent miners and dealers were selling emerald rough. Midmorning activity was brisk, especially after MTC trucks had dumped their tailings by the river and thousands of locals washed through them. After the major trading, miners relaxed at the makeshift bars in the small market (figure 24). One of the most striking scenes was a husband and wife covered in black shale, examining a rough emerald crystal from the MTC tailings.

In addition to the mine markets in the western belt, the town of Muzo is one giant emerald market, with several blocks of activity and miners and dealers offering rough for sale in the streets, shops, and restaurants (figure 25). At peak times, dealers and buyers stood shoulder to shoulder. A local election was also taking place, and many people were out in the streets supporting candidates. No guns were seen in Muzo, either, which was not the case in 2005.

Figure 24. After a hard morning of washing shale for emeralds, miners enjoy a beer at the La Playa market while offering their finds for sale. Photo by Andrew Lucas.

CUTTING AND TRADING IN BOGOTÁ

In 2014, the Colombian emerald industry exported more than two million carats, valued at $147 million, mostly to the U.S. and Asia (Angarita, 2015). For a complete picture of the industry, we returned to Bogotá. Our first stop was the Centro de Desarrollo Tecnológico de la Esmeralda Colombiana (CDTEC), a gemological laboratory and research center. We then visited dealers and cutters in the Emerald Trade Center and street dealers outside the center.

Former general director Dr. Carlos Julio Cedeño gave us a tour of CDTEC, a nonprofit organization established in 2008 that is partly owned by the Colombian government and partly by the major trade associations, among them Fedesmeraldas. CDTEC's mission is to provide research, identification, and certification of gemstones, primarily emeralds. Their laboratory reports identify the material and type of enhancement and certify Colombian origin. They are also involved in testing a natural filler material (developed by the trade associations) that is durable and can be removed and refilled, as well as research on the origin of Colombian emerald through chemical fingerprinting. CDTEC analyzes about 70% of the high-end goods leaving the country (G. Angarita, pers. comm., 2017).

The Emerald Trade Center, built in 1963 and renovated in 1992, is a fourteen-story building that houses about 40 jewelry stores. It also has office space for dealers, cutters, treatment facilities, and services such as money exchanges, brokers, and shipping. We visited the offices of The Best Emeralds, where we saw three cutters faceting and preforming emeralds ranging in weight from 3 to 20 ct. We were fortunate to be there while their master cutter sawed and preformed a 700 ct piece of rough (figure 26) into numerous stones, some weighing over 50 ct after faceting. In Bogotá we also experienced firsthand the legal export process as we prepared our reference sample collection for shipping.

Outside the Emerald Trade Center, the street dealers were very busy on both days we visited. The number of dealers and the trading volume seemed significantly higher than in 2005. Most of the trading was between local dealers looking to fill orders, but there were also some foreign buyers. Cell phones were an integral part of the street business, with dealers constantly on the phone quoting offers to their suppliers or checking interest from potential buyers.

In Bogotá's free trade zone we visited Colombia Texas Transformadora (CTT), owned by Muzo Emer-

Figure 25. Amid the frenzied street market activity in Muzo, author Darwin Fortaleché negotiated our rough emerald purchases. Photos by Andrew Lucas.

Figure 26. At The Best Emeralds, we followed the sawing and cutting of a 700 ct piece of rough and documented the decisions made from start to finish to achieve maximum weight and value. Photos by Andrew Lucas.

ald Colombia, where the rough from the MTC mine in Muzo is sorted and cut. The cutters had years of experience, and the facility was divided into sections for further quality sorting, planning and marking the rough, sawing, and preforming. Details regarding the tunnel of origin and date of mining are transferred to the cut stone. A certification of origin and traceability is provided for each cut stone, documenting the date, place, and time of extraction and its journey through the manufacturing process. The report also comes with photos from each step, the weight from rough to final stone, and a declaration of the filler material (normally cedarwood oil). Since 2011 CTT has received the Quality Systems Management ISO 9001:2008 certification granted by Bureau Veritas, with accreditation from the U.S. ANSI-ASQ National Accreditation Board (ANAB) and the United Kingdom Accreditation Service (UKAS). The Bogotá facility also works with cutting workshops in New York, Hong Kong, and Paris.

A CHANGING INDUSTRY

As we documented the mine operations and interviewed the miners, management, and owners, we saw how the industry has evolved. Most of the changes we witnessed were also discussed during the Bogotá Emerald Symposium.

According to the Ministry of Mines, 63% of all Colombian mining activity is informal (figure 27), and as a result the country does not receive the proper tax revenue (Ulloa, 2015). One of the government's main focuses for mining is organization and formalization. It has adopted five pillars and a "three-door approach" to bring as many guaqueros as possible into the legal mining system.

The five pillars of the mining policy are:

1. Information: Improve the accuracy and trustworthiness of national mining resources through an improved mining census. Increase joint collaboration and communication between agencies such as the Ministry of Mines, the National Mining Agency, the National Hydrocarbons Agency, the Mining and Energy Planning Unit, and the Geological Service. Create reliable traceability through the Unique Register of Mineral Traders (RUCOM) certification to register Colombia's mineral marketers with ANM. RUCOM certification requires detailed information on where and when the minerals were mined. If marketers do not have this certification or cannot document the provenance, the minerals may be seized.
2. Legal security: Legal and technical guidelines for mining depend on the classification of an operation as small, medium, or large. The realities of these different size categories require customized environmental guidelines and technical assistance.
3. Infrastructure: Identify and develop infrastructure needs for the mining community, particularly transportation to and from the mines.
4. Trust: Develop genuine trust between mining communities, mining companies, and the government through improved communication.
5. Competitive conditions: Strengthen partnerships and cooperation with companies in each sector. Promote Organisation for Economic Co-operation and Development (OECD) guidelines for multinational companies to maximize benefits to communities and the country. Provide capital to small- and medium-scale mining companies through a microcredit program from Banco Agrario and the Ministry of Mines (Unninayar, 2015).

The three-door approach provides options for formalizing small-scale independent mining that is not operating legally:

Figure 27. Formalizing mining in a way that balances the needs of independent miners with other factors—large private companies, foreign investment, tax revenue, environmental protection, and transparency—is one of the biggest challenges facing Colombia and many other colored stone producers. Photo by Andrew Lucas.

1. Formalization: The government uses public and private partnerships, regulation, and traceability policies, while providing technical assistance and legitimate financial support through banks to these miners.
2. Reconversion: If informal mining is being carried out in areas where mining is not allowed or not viable, the government works with other organizations to provide alternatives for work in other sectors.
3. Law enforcement and judicial action: If miners carrying out illegal operations do not wish to work in the formal system or be converted to other industries, or if they are involved in criminal activity, the government will vigorously pursue judicial action (Unninayar, 2015).

All exploration and mining concessions are granted by the government through the National Mining Agency. Of Colombia's commercial mining operations—which include gold, platinum, coal, limestone, and other materials—the 359 emerald concessions represent 3.6% of the total number. (Granados, 2015). The emerald concessions cover approximately 88,000 hectares, less than 0.1% of Colombia's total area. About 10% of them are currently in operation. Total mining royalties for 2012 through 2014 were $4.6 million. While the industry's overall size and revenue are small on a national level, the impact on local mining communities is significant (Granados, 2015).

In 2015 there were 178 registered emerald traders under RUCOM, and as of 2017 there are 5,150 (G. Angarita, pers. comm., 2017). The National Mining Agency received 400 new applications for emerald mining concessions from domestic and international companies in 2015. Multinational companies such as MTC are investing or have shown interest in investing in the industry and revitalizing it with modern technology and mining methods. These companies have stressed best business practices and corporate social responsibility as part of their branding campaigns, leading to further dividends in these areas for domestic companies. This has influenced Colombian companies to modernize and formalize to become more competitive. Colombia is one of 52 countries that have implemented the Extractive Industries Transparency Initiative (EITI), an international standard of mining governance and accountability.

When author AL visited the country in 2005, many miners were not paid a salary but were allowed to take some production in an arrangement that was not entirely structured. Miners at different locations, including some of the larger operations, noted that taking too much could be a fatal misstep. At the formal operations we visited during this trip, all of the miners reported that they received a salary, social security, and medical benefits, along with a share of the production. Gone was the sight of dealers and miners armed with guns at the mine markets.

This is not to say that there are no longer issues of grave consequence. Robbery and theft still occur along the supply chain, as they do in most countries that produce colored gemstones. In May 2015, more than 1,000 people took over the MTC mine for over two days and extracted emeralds from a newly discovered pocket. Police eventually gained control, but only after a significant loss. MTC's director believed the raid was conducted by a large, well-armed, and

Box A: The New Generation

Gabriel Angarita (figure A-1) has been president of the Colombian Association of Emerald Exporters (ACODES) since 2009 and also serves on the board of CDTEC, the gemological laboratory in Bogotá. Mr. Angarita, whose father has been in the industry for more than 40 years, has been around emeralds as long as he can remember. The Angarita family is involved in buying rough directly from the mines, dealing the rough domestically, and cutting and selling the stones on the international market through their office in Bogotá. (The Best Emeralds, profiled in the "Cutting and Trading in Bogotá" section, is one of their interests.)

Today, most of Mr. Angarita's time is spent working on behalf of ACODES. His role as president of the association initially took up about two hours per week, but today it is a full-time endeavor. The association, founded in 1979 to improve Colombian emerald exports, now pursues a wide range of objectives.

Mr. Angarita's first major challenge was to bring the Colombian companies together to work in an organized manner. Dealers initially objected to representing Colombia together at trade shows—they thought their customers might be "stolen"—but after a couple of years they found that this type of collaboration actually increased customer interest.

The branding of Colombian emeralds has been another challenge for Mr. Angarita. First he had to convince the industry of the need to create a brand. He has worked to create pavilions at international shows, increase supply chain transparency and integrity of transactions, ensure full disclosure (including treatments), and educate the international trade and consumers about efforts to eliminate violence and crime. By assuring the integrity and "cleanness" of the product, he hopes to create a brand image like the one maintained by Colombian coffee since the 1980s.

ACODES promotes the Colombian emerald brand through efforts such as the "Mother Gems" campaign linking the love of one's mother and Mother Nature with the lush green of the Colombian landscape and its emeralds. Working with CDTEC, the association seeks to assure customers of the consistent use of proper nomenclature, disclosure, and country of origin for Colombian emeralds. ACODES is also collaborating with CDTEC to develop a filler material for clarity enhancement that is completely natural, durable, and removable.

Figure A-1. Gabriel Angarita, president of ACODES, is part of the younger generation that is bringing innovation to the industry and helping create a global brand image for Colombian emeralds. Photo by Andrew Lucas.

Mr. Angarita said the biggest changes he has seen in his career are the dramatic reduction of violence in the mining areas and the increase in transparency. Although violence and criminal influence have hurt the industry in the past, he said this has led to strict regulations and improvements in transparency. The next generation of industry leaders is working to further improve the industry's image and dispel lingering misconceptions. He also wants to see greater benefit to the country, specifically in the mining communities, from the involvement of multinational companies. While he supports the benefits of increased tax revenue, employment, and technology, he also wants to see development in education at the community level.

Mr. Angarita envisions a transfer of knowledge beyond the emerald industry that will better prepare communities and the next generation to compete in the global economy. Ultimately, he says, the richness of Colombia's emerald resources should enrich the minds of the people.

organized criminal group (Burgess, 2015). A facility for military troops was being constructed near the mine during our visit.

The move to larger, well-funded mining companies in Colombia and other countries is an inevitable and beneficial development. The balance that should exist between small-scale miners, local communities, and multinational companies is often difficult to achieve. But this balance is essential to ensure a consistent and transparent supply chain, ethical practices, and a positive image of the industry.

In 2015 Gemfields acquired a 70% interest in Coscuez mining and 20,000 hectares in the Muzo

and Quipama districts for emerald mining (Gilbertson, 2015). Gemfields has since pulled back from operations in Colombia to focus their efforts in Africa.

The Colombian government welcomes and supports foreign investment and participation in the industry (Angel, 2015), which brings formalization, tax revenue, transparency, best business practices, branding, environmental standards, modern methodology and technology, and employment. Many members of the Colombian emerald trade also welcome foreign investment, as they believe it encourages their own development (U. Montenegro, pers. comm., 2015). But others feel that foreign involvement in the Colombian emerald industry should not come at the expense of local businesses, as that would not truly lead to employment and beneficiation. The new generation of Colombian emerald industry leaders look to bring the country into the modern business world while preserving local traditions (see box A).

CONCLUSION

The opportunities for the Colombian emerald industry are strong. Colombian emerald is already the standard that emeralds from all other sources are measured against. National geological studies indicate that only 20% of the country's emerald reserves have been exploited (figure 28). New systems of formalization, tracking, and exporting are being incorporated to ensure greater transparency. Violence has declined, and security at mining locations has improved.

Multinational companies are making an investment that seems to guarantee increased production, even as local mining operations are modernizing. The Colombian emerald industry has already achieved significant beneficiation by developing a cutting industry that handles the majority of domestic production and meets the highest international standards. Indeed, Bogotá's cutters are considered the global experts on cutting Colombian emerald. This cutting industry was built from within, something many African countries hope to achieve. A new generation of industry leaders looks to improve the branding of these emeralds and increase global market share.

These opportunities come with challenges. The image of Colombia as a land of violence and drugs often carries over to emerald and must be overcome. The relationship between new foreign mining and local miners is still delicate at times. The interests and rights of both parties must be protected, and formalization of the mining sector should come with a fair system to include independent miners. None of these challenges is insurmountable, and the industry has the potential to reach unprecedented heights. For Colombian emeralds, the momentum for change seems irreversible.

Figure 28. With an estimated 80% of Colombia's emerald deposits still in the ground, and an industry conscious of foreign investment and opportunity for local communities, the future looks bright. If these efforts succeed, the hard work of emerald mining will lead to greater production and prosperity in the long term. Photo by Andrew Lucas.

ABOUT THE AUTHORS
Mr. Fortaleché is chief gemologist at Centro de Desarrollo Tecnológico de la Esmeralda Colombiana (CDTEC). Mr. Lucas is manager of field gemology for education, Mr. Muyal is a staff gemologist, Dr. Hsu is technical editor of Gems & Gemology, *and Mr. Padua is a video producer, at GIA in Carlsbad, California.*

ACKNOWLEDGMENTS
The authors greatly appreciate the assistance of the individuals and organizations that made this expedition possible: Jean-Claude Michelou, editor-in-chief of InColor*; Luis Gabriel Angarita, president of ACODES; Oscar Baquero, president of Fedesmeraldas; Fabian Arango, mine manager of Los Españoles; and Javier Puerto, mine manager of La Pita. Chivor district: Uvaldo Montenegro, owner of the El Manantial mine; Hernando Sanchez, controlling shareholder of the San Francisco Company. Gachalá district: William Bermudez, manager at Mina La Emilia; Camilo Sanchez, principal owner of Mina La Emilia; and Giovanni Lopez, manager of the Dixon mine. Muzo district: Charles Burgess, director of MTC; Carlos Contreras Cañizo, mine manager at MTC; and Carlos Diaz, mine engineer at El Amarillal. Special thanks to our driver, Miguel Gonzalez.*

REFERENCES

Angarita L.G. (2015) ACODES and industry efforts to brand Colombian emerald. Presentation at the First International Emerald Symposium, Bogotá.

Angarita L.G., Angarita M. (2013) Carranza: The myth and the industry. *InColor*, No. 23, Summer, pp. 20–24.

Angel S. (2015) Colombia's mining outlook. Presentation at the First International Emerald Symposium, Bogotá.

Branquet Y., Laumonier B., Cheilletz A., Giuliani G. (1999) Emeralds in the Eastern Cordillera of Colombia: Two tectonic settings for one mineralization. *Geology*, Vol. 27, No. 7, pp. 597–600, http://dx.doi.org/10.1130/0091-7613(1999)027%3C0597:EITECO%3E2.3.CO;2

Branquet Y., Giuliani G., Cheilletz A., Laumonier B. (2015) Colombian emeralds and evaporites: Tectono-stratigraphic significance of a regional emerald-bearing evaporitic breccia level. *13th SGA Biennial Meeting*, Nancy, France, Proceedings Vol. 4, pp. 1291–1294.

Burgess C. (2015) Minería Texas Colombia's policies on transparency. Presentation at the First International Emerald Symposium, Bogotá.

Colletta B., Hebrard F., Letouzey J., Werner P., Rudkiewicz J.L. (1990) Tectonic style and crustal structure of the Eastern Cordillera (Colombia) from a balanced cross-section. In J. Letouzey, Ed., *Petroleum and Tectonics in Mobile Belts*. Editions Technip, Paris, pp. 81–100.

Gilbertson S. (2015) Gemfields's social responsibility and transparency programs. Presentation at the First International Emerald Symposium, Bogotá.

Giuliani G., Branquet Y., Fallick A.E., Groat L.A., Marshall D. (2015) Emerald deposits around the world, their similarities and differences. *InColor*, Special Issue, pp. 56–69.

Granados J.G. (2015) National Mining Agency and formalization of the emerald industry. Presentation at the First International Emerald Symposium, Bogotá.

Irving E.M. (1975) Structural evolution of the northernmost Andes, Colombia. Geological Survey Professional Paper 846.

Keller P.C. (1981) Emeralds of Colombia. *G&G*, Vol. 17, No. 2, pp. 80–92, http://dx.doi.org/10.5741/GEMS.17.2.80

Mora A., Parra M., Strecker M.R., Sobel E.R., Hooghiemstra H., Torres V., Jaramillo J.V. (2008) Climatic forcing of asymmetric orogenic evolution in the Eastern Cordillera of Colombia. *Geological Society of America Bulletin*, Vol. 120, No. 7-8, pp. 930–949, http://dx.doi.org/10.1130/B26186.1

Pignatelli I., Giuliani G., Ohnenstetter D., Agrosì G., Mathieu S., Morlot C., Branquet Y. (2015) Colombian trapiche emeralds: Recent advances in understanding their formation. *G&G*, Vol. 51, No. 3, pp. 222–259, http://dx.doi.org/10.5741/GEMS.51.3.222

Sinkankas J. (1981) *Emerald and Other Beryls*. Chilton Book Company, Radnor, PA.

Ulloa M.I. (2015) Colombia's ministry of mines and transparency and control of gem commerce. Presentation at the First International Emerald Symposium, Bogotá.

Unninayar C. (2015) Colombia holds the First International Emerald Symposium. *InColor*, Special Issue, pp. 6–15.

For More on Colombian Emeralds

To watch videos of Colombia's emerald mining areas and the cutting and trading industry in Bogotá, go to www.gia.edu/gems-gemology/fall-2017-colombian-emerald-industry or scan the QR code to the right.

Large, High-Quality DIAMOND From Brazilian Kimberlite

Diamonds were first discovered in alluvial secondary deposits of Brazil by gold miners circa 1725. Brazil became the world's premier diamond source for more than a century, until diamonds were located in South Africa. Meanwhile, the search for primary sources continued. More than 1,100 kimberlite pipes have been discovered in Brazil, most of them concentrated near alluvial deposits. So far, only five have been tested using current exploration technology. The Braúna kimberlites in Bahia State were found in the early 1990s, but it was not until 2005 that modern sampling techniques revealed their potential. In 2014, the Lipari Mining Company developed an open-pit mine on one of the Braúna kimberlite pipes, the first primary deposit diamond mine in South America.

Recently, the New York laboratory analyzed a 50.8 ct (10.10 g) near-colorless crystal of high quality submitted by Lipari. The rough was analyzed both before and after faceting as part of GIA's new "Mine to Market" service, which documents a diamond's journey from rough crystal to final faceted gemstone. The rough had a dodecahedral habit, resulting from resorption into mantle fluids post-growth. GIA determined it to be type Ia (bearing nitrogen aggregates). It was relatively clean, with no large mineral inclusions or fractures, indicating that it could be faceted into a high-clarity gem diamond. From this rough crystal, a 20.1 ct round brilliant cut diamond with I color and VS_2 clarity (figure 1) was produced and resubmitted as the second stage of the Mine to Market service. DiamondView images documented the growth structure of this crystal, allowing comparison of the rough to the final faceted gemstone.

Figure 1. Left: A Brazilian kimberlite yielded a 50.8 ct rough type Ia diamond with a dodecahedral habit, the result of resorption. Right: This 20.1 ct round brilliant with I color was cut from the Brazilian rough.

Mid-FTIR spectra taken from both the rough and the faceted stone (figure 2, left) confirmed it to be type Ia, with a moderate concentration of hydrogen; the two spectra overlay each other very closely. Also collected were UV-visible absorption spectra. Typical cape spectra were observed, including the peaks at 415 and 478 nm that are common for a diamond of this color (figure 2, right). Under cross-polarized light, strong "tatami" strain patterns (figure 3) indicated strong plastic deformation during and after growth. These geological processes can limit the ability of such large crystals to survive transport to the earth's surface, adding to the rarity of this impressive diamond.

Although the round brilliant was of high clarity, a small colorless euhedral crystal was observed under the table facet. The morphology of this crystal identified it as a garnet, and Raman analysis using 514 nm laser excitation confirmed it as pyrope garnet (Mg-, Al-rich) (figure 4).

DiamondView images of both the rough crystal and the final faceted gem

Editors' note: All items were written by staff members of GIA laboratories.

Gems & Gemology, Vol. 53, No. 3, pp. 360–368.

© 2017 Gemological Institute of America

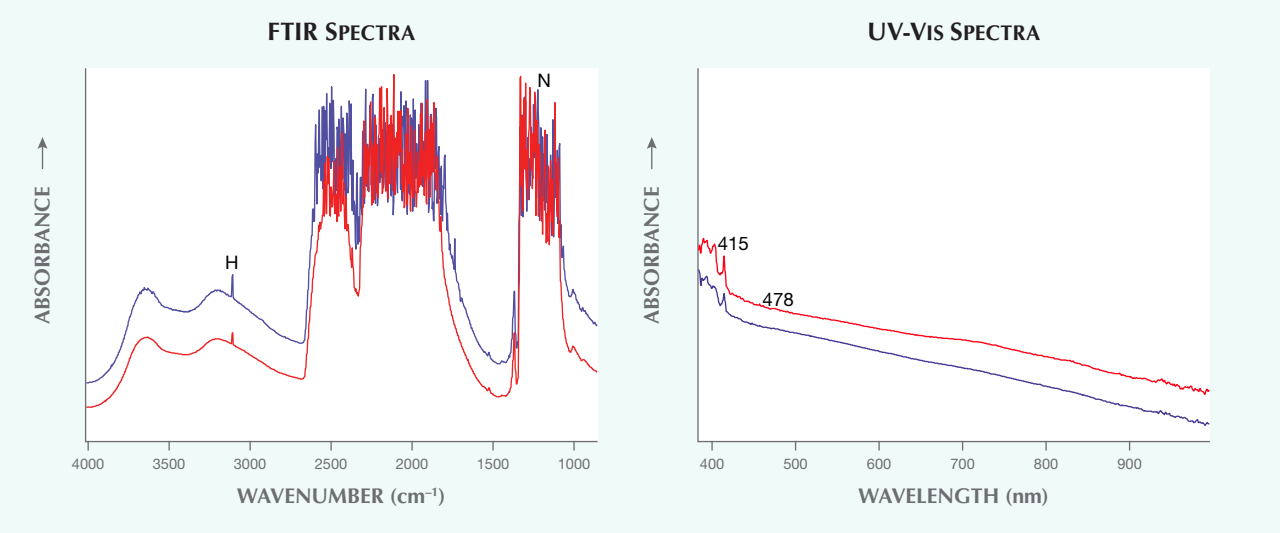

Figure 2. Mid-infrared and UV-visible spectra of the rough diamond crystal (blue trace) and finished round brilliant (red trace) showed that it was a type Ia cape diamond. The spectra are offset for clarity.

revealed similar growth patterns, along with the strong blue fluorescence typical for type Ia diamond (figure 5). These observations further confirmed that the stone was cut from the notable 50.8 ct rough crystal.

Lipari is currently exploring 20 other primary kimberlite sources in Brazil, and similarly impressive diamonds may be forthcoming.

Paul Johnson, Heather Smith, and John King

EMERALD with Mobile Inclusion

Multiphase inclusions are key indicators when identifying emeralds and determining their origin. Gemologists look for the jagged three-phase inclusions in stones of Colombian origin or blocky two-phase inclusions in Brazilian or Zambian emerald. These multiphase inclusions typically require higher magnification and considerable maneuvering of the emerald to get a precise view.

Recently, the Carlsbad laboratory received a 9.02 g rough emerald from Lucas Fassari (Costa Mesa, California). The rough had an eye-visible mobile inclusion (figure 6) consisting of a CO_2 gas bubble and salt crystals suspended in a fluid. The emerald was identified using a handheld spectroscope and op-

Figure 3. Tatami strain patterns, typical for a type Ia diamond, indicate that the crystal experienced plastic deformation during and possibly after growth.

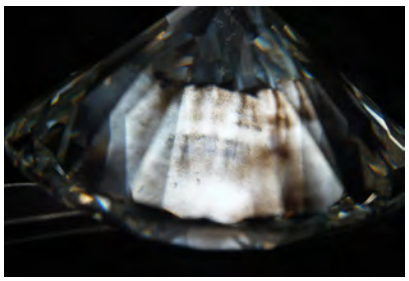

Figure 4. The Raman spectrum obtained from the diamond's crystal inclusion identifies it as a pyrope garnet (Mg-, Al-rich). Inset: The well-formed crystal is approximately 20 microns in diameter.

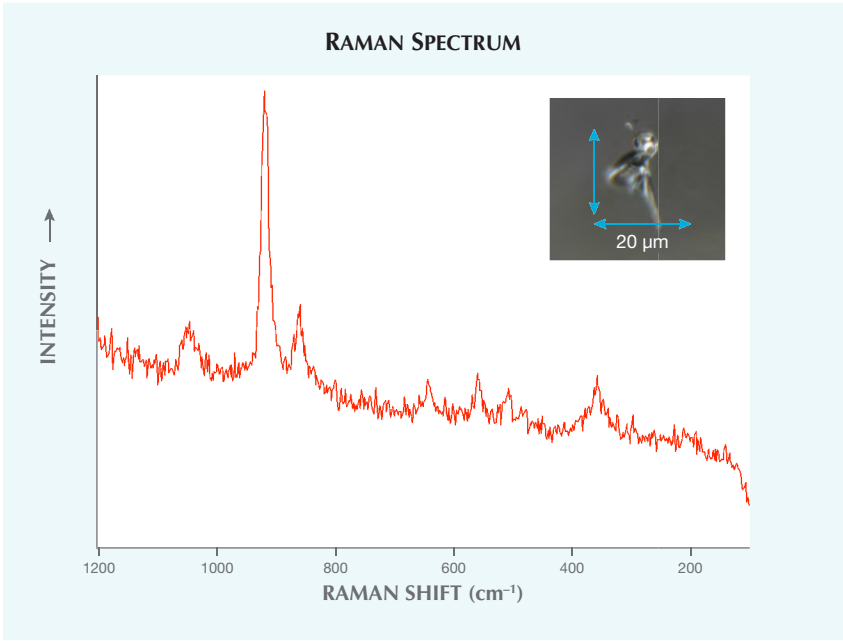

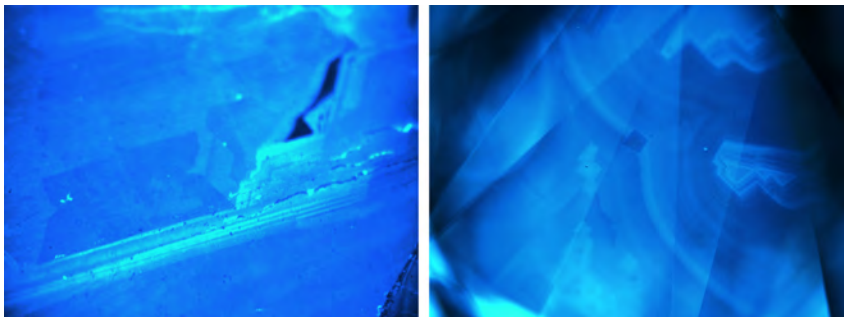

Figure 5. Identical growth structures and fluorescence patterns in DiamondView imaging confirm that the original 50.8 ct rough diamond crystal (left) yielded the finished 20.1 ct diamond (right).

tical properties. It was determined to be of Colombian origin by its jagged three-phase inclusions and crystals that had characteristics of pyrite and calcite. The mobile inclusion was quite large in relation to the rough emerald, which measured 28.76 × 14.82 × 12.83 mm, including its calcite and shale matrix. The CO_2 bubble measured approximately 4 × 3 mm.

Mobile inclusions of this size are captivating to observe, and to see one in an emerald adds more allure to the piece (see video at http://www.gia.edu/gems-gemology/fall-2017-labnotes-emerald-mobile-inclusion). Cutting this specimen into a faceted gemstone would lose what makes this rough emerald unique.

Nicole Ahline

Figure 6. This 9.02 g rough emerald contains a prominent eye-visible mobile inclusion.

Ethiopian Precious OPAL with a Dyed Brown Bodycolor

Brown opal exhibiting play-of-color has been previously reported (M.L. Johnson et al., "Opal from Shewa Province, Ethiopia," Summer 1996 *G&G*, pp. 112–120) and can occasionally be found in the marketplace as "chocolate opal."

Recently, a 17.15 ct semi-transparent oval cabochon with brown bodycolor and strong play-of-color (figure 7, left) was submitted to the Carlsbad laboratory for identification services. Basic gemological observation and properties confirmed that the stone was opal. The spot refractive index was 1.41. The opal displayed hydrophane behavior by absorbing water, which was easily observed during microscopic examination (Fall 2013 Lab Notes, pp. 175–176).

While this specimen's properties were consistent with Ethiopian opal with a natural brown bodycolor, it was necessary to confirm that the color was not the result of dye, since this was hydrophane-type material (N. Renfro and S.F. McClure, "Dyed purple hydrophane opal," Winter 2011 *G&G*, pp. 260–270). Meticulous examination showed that the brown color conformed to the surface, indicating that it was in fact the result of dyeing after the stone had been fashioned. The uneven bodycolor was difficult to detect because of the stone's transparency and strong play-of-color. Careful microscopic examination with strong transmitted and diffused white lighting revealed very subtle color concentrations in pits and uneven blotchy brown patches on the surface (figure 8), which confirmed that the brown color was artificially induced. Interestingly, the back of the stone was almost white in the center and brown along the edge

Figure 7. A 17.15 ct brown dyed precious opal from Ethiopia (left). The back of the stone was almost white, which suggests that it had been re-polished after dyeing (right).

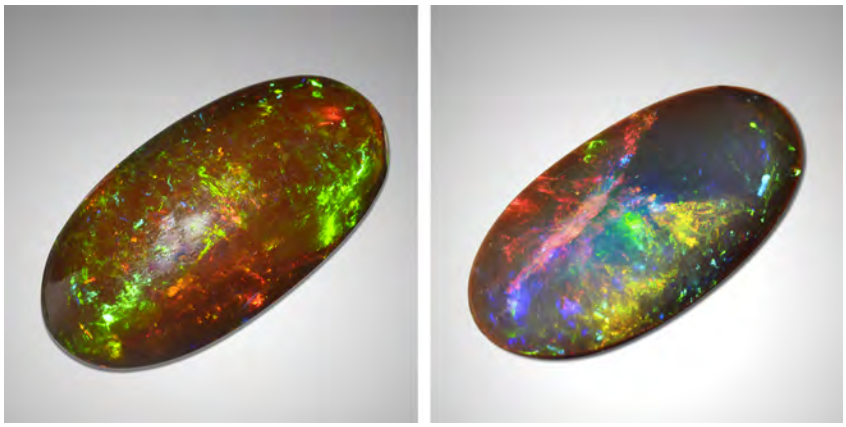

(see figure 7, right), showing clear surface-conformal brown color. This suggests that the back of the stone was repolished after dyeing, which would have removed the dark brown rind in the process.

On the brown side, the opal showed an unusual chalky greenish yellow color when examined under long-wave UV light, possibly due to the dye. Advanced gemological analysis with Raman spectroscopy revealed a natural opal spectrum that was free of any peaks pertaining to foreign substances. Energy-dispersive X-ray fluorescence (EDXRF) did not detect manganese, which is the cause of brown color in Ethiopian opal.

Although dyed opal is often easy to identify, this brown dye looked natural, and the color of the stone did not change after hydrophane testing. While the dye was difficult to detect on the top surface of this stone, its back fortunately appeared to have been repolished, offering additional evidence of dye. When examining opal, it is important to consider carefully whether it could be dyed, especially if it is hydrophane material with a color that occurs naturally.

Jonathan Muyal

Figure 8. Uneven color is observed with the help of strong transmitted and diffused lighting; the blotchy darker brownish area is the result of dyeing. Field of view 3.57 mm.

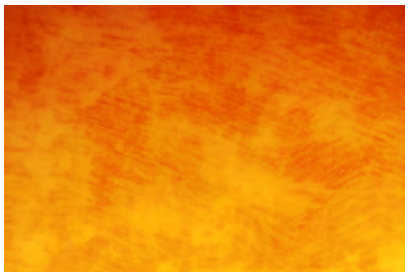

Figure 9. Both of these precious opals show an unusual and attractive bodycolor. The opal on the left is a 6.71 ct transparent pink cushion brilliant. On the right is a 2.37 ct transparent orange round brilliant.

Unusual Bodycolors of Precious Opal

Two faceted loose stones with unusual bodycolors (figure 9) were recently submitted to the Carlsbad laboratory for an identification report. The first, a 2.37 ct transparent round brilliant, showed a weak to moderate play-of-color with irregular color patches and brushstrokes. It exhibited an attractive orange bodycolor (similar to the hue of some *padparadscha* sapphires) and a light degree of haziness. Careful microscopic examination revealed turbid orangy clouds and waves of coarse particles. The larger specimen, a 6.71 ct transparent cushion brilliant, also displayed a weak to moderate play-of-color but more of a pink bodycolor. A similarly hazy appearance from clouds of orangy red particles and tiny black inclusions was also observed (figure 10).

Standard gemological properties were consistent with opal. The orange and pink stones both had a specific gravity of 2.03, with refractive indices of 1.442 and 1.445, respectively. Both were inert to long-wave and short-wave UV light. No indication of clarity enhancement, color treatment, or dye was observed in either. The two stones were therefore identified as natural opal with natural color.

A single drop of water placed on the surface of each stone was observed under direct transmitted light with the microscope in brightfield mode. The opals showed no indication of porosity and did not absorb the water, suggesting they were not hydrophane material (Fall 2013 Lab Notes, pp. 175–176). Crazing was not seen in either opal.

Advanced gemological testing with EDXRF showed properties consistent with natural opal ($SiO_2 \cdot nH_2O$), but also the presence of Fe, most likely from the clouds of particles.

While the exact cause of these pink and orange bodycolors is unknown, the minute inclusions might be influencing the perceived color.

Our gemological observations confirmed the natural origin. However, further study on additional samples would be required to better understand the cause of color in these unique opals. They were reported to be from Mexico, but the author could find no reference consistent with this material.

Jonathan Muyal

Figure 10. The pink opal contained clouds of tiny orangy red particles. Field of view 2.88 mm.

Natural Freshwater "Fish" PEARL

The increased availability of freshwater cultured pearls in the market has brought their natural counterparts to the attention of collectors and the trade. Most natural freshwater pearls have been obtained from European waters and in the United States from rivers in the Mississippi Valley. A natural pearl occurs without human intervention and takes on the characteristic color and surface properties of the mollusk in which it forms. Freshwater pearls, whether cultured or natural, are attractive due to a wide variety of distinctive shapes, hues, and overtones. The New York lab recently examined a unique fish-shaped brownish orange pearl measuring 21.34 × 6.28 × 2.81 mm and weighing 2.12 ct (figure 11).

Figure 11. A 2.12 ct natural freshwater pearl with the form of a fish.

The entire nacreous surface was composed of overlapping platelets. We observed no indications of work, such as polishing, that is sometimes performed to improve a pearl's appearance. One end was wider and more rounded, which bore an uncanny likeness to a fish's head, with an "eye" and "mouth" also discernible. The lustrous orient along the body narrowed to a rounded point, resembling iridescent fish scales on a tail. Natural pearls are often baroque, and American freshwater pearls in particular are often found as elongated "wing" pearls (J.L. Sweaney and J.R. Latendresse, "Freshwater pearls of North America," Fall 1984 *G&G*, pp. 125–140). EDXRF chemical analysis and observation of X-ray fluorescence showed higher levels of manganese, proving that the pearl formed in a freshwater mussel. No indications of treatment such as dyeing or coating were detected under magnification or using advanced analytical procedures. Real-time microradiography and X-ray computed microtomography (μ-CT) analysis revealed clear natural growth structures that conformed to the pearl's shape. 3D rendering of the μ-CT data (figure 12) showed a remarkable likeness to a small fish swimming.

Although this is not the first pearl GIA has examined that bears a resemblance to a living creature (see Fall 2015 Lab Notes, pp. 319–320), it is nonetheless an extraordinary and rare formation that mirrors the form of a fish in surprising detail.

Sally Chan and Emiko Yazawa

Elements in Synthetic Overgrowth On Flux-Heated RUBY and Beryllium-Diffused Sapphire

Heat treatment of rubies and sapphires at high temperatures sometimes leaves redeposition caused by the partial dissolution of the corundum in the crucible; this is referred to as synthetic overgrowth (Fall 2002 GNI, pp. 255–256). GIA's Tokyo laboratory recently had the opportunity to test a red oval mixed cut weighing 2.00 ct and an orange round mixed cut weighing 0.89 ct, both of which showed signs of synthetic overgrowth after testing.

Standard gemological testing and advanced testing including chemical

Figure 12. 3D software rendering of X-ray μ-CT data revealed the pearl's uncanny likeness to a fish.

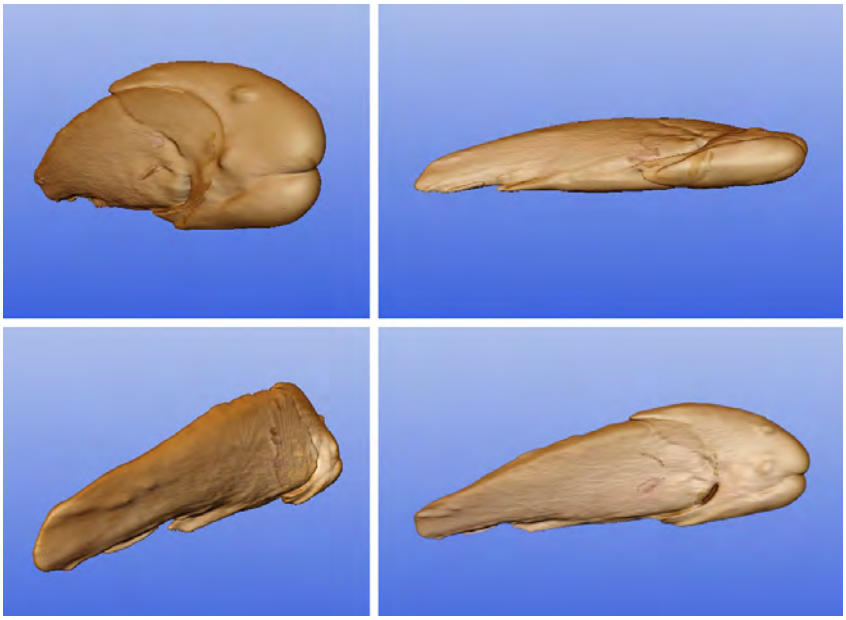

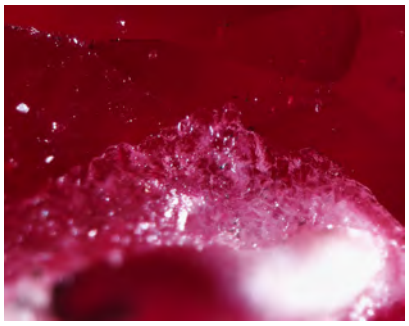

Figure 13. Synthetic overgrowth on the surface of a heated Burmese ruby. Field of view 1.50 mm.

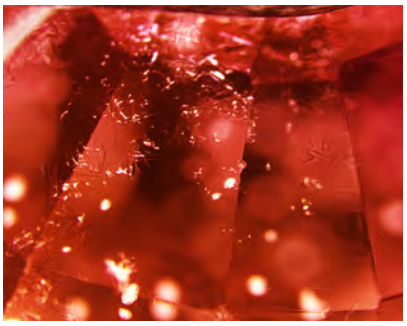

Figure 14. Synthetic overgrowth on an orange beryllium-diffused sapphire. Field of view 1.60 mm.

analyses revealed that the red oval was a heated ruby of Burmese origin with moderate flux residues in fissures. The orange round was identified as a beryllium-diffused sapphire. Both stones had synthetic overgrowth around the girdles and/or cavities (figures 13 and 14) that could be confirmed by different reactions under cross-polarized light. We tested the overgrowths with laser ablation–inductively coupled plasma–mass spectrometry (LA-ICP-MS) with calibration using NIST 612 and 610 standards.

The chemical compositions of these synthetic overgrowths were different from those of corundum; they also varied between the samples. Sodium (9980 ppmw), calcium (40,100 ppmw), magnesium (84,400 ppmw), and silicon (23,400 ppmw) were extremely high in the overgrowth on the flux-heated ruby; beryllium (36,650 ppmw) was extremely high and silicon (909 ppmw) very high in the overgrowth on the beryllium-diffused sapphire (table 1). Boron was detected only in the overgrowth on ruby (59 ppmw). Aluminum was not quantified since it was used as an internal standard. However, the high aluminum signal indicated that the overgrowth contained corundum and/or alumina-related material.

Flux is used for artificial heat treatment of rubies, and there are many types of fluxes such as oxides, borates, silicates, molybdates, and fluorides, as well as various combinations of materials (J.L. Emmett, "Fluxes and the heat treatment of ruby and sapphire," Fall 1999 *G&G*, pp. 90–92). During flux-assisted heat treatment with or without diffusion, material from the surface of the corundum as well as the alumina crucible and inclusions will dissolve to some degree into the molten flux. On cooling, the flux becomes supersaturated in alumina and crystallizes out onto the nearest convenient surface, often on the stones themselves (J.L. Emmett et al., "Beryllium diffusion of ruby and sapphire," Summer 2003 *G&G*, pp. 84–135). Uncommon elements for corundum such as sodium, calcium, and silicon obtained from the overgrowth on heated ruby in high concentration indicate that the overgrowth was mainly derived from fluxes. These elements are comparatively insignificant for the overgrowth on beryllium-diffused sapphire. On the contrary, extraordinarily high beryllium in the overgrowth on Be-diffused sapphire indicates deposition of this additional element in the treatment. Other elements, such as magnesium and zirconium (detected at moderate to high levels), and metals such as nickel, copper, zinc, and lead (detected from both overgrowths at lower levels) may be from the inclusions or the flux.

LA-ICP-MS results (table 1) also indicate that the ruby could be misidentified as Be-diffused since the overgrowth contains a certain amount of beryllium, a possible by-product of the furnace. It is important for gemologists to check other elements such as magnesium, silicon, and calcium in order to confirm that LA-ICP-MS was performed on the overgrowth.

Yusuke Katsurada

TABLE 1. Elements in heated ruby and Be-diffused sapphire and their synthetic overgrowths detected by LA-ICP-MS (avg. concentration in ppmw[a]).

	Heated ruby		Be-diffused sapphire	
Element	Stone	Overgrowth	Stone	Overgrowth
Be	bdl[b]	5.00	8.86	36,650[c]
B	bdl	59.0	bdl	bdl
Na	bdl	9980	bdl	10.6
Mg	10.5	84,400	61.1	328
Si	bdl	23,400	bdl	909
K	bdl	1790	bdl	bdl
Ca	bdl	40,100	bdl	bdl
Ni	bdl	104	0.42	6.20
Cu	1.71	50.1	bdl	8.34
Zn	bdl	64.0	bdl	12.7
Zr	0.04	27.6	bdl	296
Pb	bdl	93.7	bdl	0.15

[a] *All detection limits are below 4 ppmw except for Si (heated ruby: 113.5 for stone, 104.1 for overgrowth; Be-diffused sapphire: 93.3 for stone, 80.0 for overgrowth) and Ca (heated ruby: 16.95 for stone, 15.79 for overgrowth; Be-diffused sapphire: 16.95 for stone, 15.79 for overgrowth).*
[b] *bdl: below detection limit*
[c] *These values were linearly extrapolated with pulse-analog linear dynamic range measurement of the instrument.*

Figure 15. This 1.76 ct synthetic diamond was submitted with a fake GIA inscription (partially redacted for privacy) of an actual GIA report number for a natural diamond.

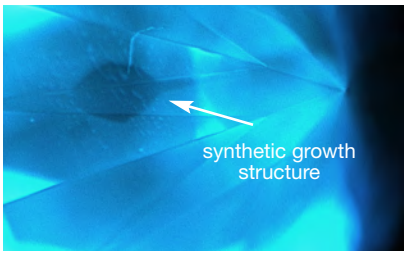

Figure 16. DiamondView imaging showed the synthetic growth structure and blue phosphorescence typical of HPHT-grown synthetic diamonds.

SYNTHETIC DIAMOND

Fraudulently Inscribed to Match Natural Diamond Report

Improvements in diamond growth technology and methods have led to a noticeable increase in colorless synthetic gem diamonds in recent years. Concerns in the diamond industry focus on laboratory-grown diamonds not being properly disclosed or even being sold as natural stones. Through careful examination and analysis, gemological laboratories can separate natural from synthetic diamonds. Occasionally, however, fraud is involved in attempting to conceal a gem's identity. The Carlsbad laboratory witnessed such an attempt.

On this occasion, a round brilliant cut (figure 15, left) was submitted for an updated diamond grading report. Its girdle was inscribed with an actual GIA report number issued in 2015 (figure 15, right). The older report was for a natural, untreated diamond and contained the following grading information: 1.74 ct, round brilliant cut, D color, Excellent cut grade, and VVS_1 clarity. Upon grading, the new submission was described as a 1.76 ct round brilliant cut with F color, Excellent cut grade, and VS_1 clarity. Moreover, our screening processes determined that the newly submitted sample needed additional testing to determine its origin. This examination revealed it to be an HPHT-grown synthetic diamond. Synthetic cuboctahedral growth structure and phosphorescence were clearly visible in DiamondView imaging (figure 16).

Aside from the observed discrepancies in weight (1.74 vs. 1.76 ct), color (D vs. F), and clarity (VVS_1 vs. VS_1), FTIR spectra clearly showed that these were not the same diamond. The natural diamond from the original report was type Ia with aggregated nitrogen impurities, while the new one was type IIb with boron impurities (figure 17). Careful examination of the report number inscribed on the synthetic diamond revealed a font different from the one used by GIA, proving that it was not an authentic inscription.

While most synthetic diamonds that come to the laboratory are properly disclosed, some are submitted out of concern that a stone presented as natural might be synthetic. Rarely do we encounter the type of blatant fraud described here. It is important for the industry and public to exercise caution, because these types of misleading practices do occur. We believe the submitting client noticed inconsistencies with the GIA report information and sent it to the lab for an updated report. If any doubt exists or some aspect of a diamond (such as an inscription) seems odd, the stone should be sent to a gemological laboratory for verification.

Christopher M. Breeding and Troy Ardon

Screening of Mounted Melee Using The GIA iD100

As previously reported in the *G&G* Lab Notes section (Fall 2016, p. 307), significant amounts of melee-size

Figure 17. FTIR absorption spectra revealed that the synthetic diamond was type IIb, whereas the fraudulently inscribed report number referred to a natural type Ia diamond. The spectra are offset for clarity.

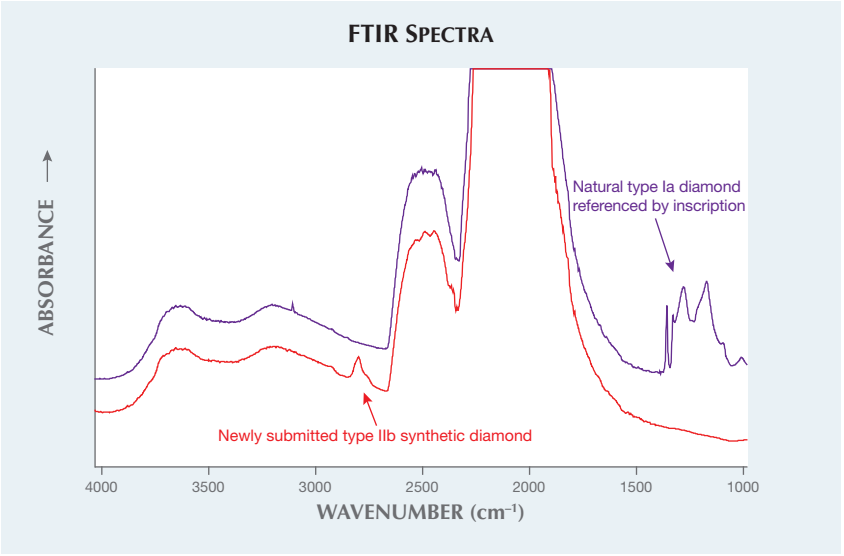

synthetic diamonds, both HPHT- and CVD-grown, are being manufactured for the jewelry industry. Over the past year, we have seen more instances of synthetics incorporated into finished jewelry pieces (e.g., Fall 2017 Lab Notes, p. 239).

Recently in GIA's New York laboratory, we examined a diamond ring with 100 colorless melee side stones, each about 0.5 mm in diameter (figure 18). Using the new GIA iD100 screening device, we were able to screen these melee. The device uses sophisticated spectroscopy technology to distinguish natural diamonds—either loose or mounted—from synthetics and simulants. The operator simply points the probe at a diamond, and the result is given within two seconds. Out of the 100 melee from this ring, one stone was referred by the GIA iD100 for further testing (figure 19).

Upon further examination, the stone was determined to be a type IIa diamond (no detectable nitrogen impurity). Examination in the De Beers DiamondView instrument revealed strong phosphorescence to short-wave UV radiation, typical for HPHT-grown synthetic diamonds (figure 20). Further examination using photoluminescence (PL) spectroscopy detected a very weak silicon impurity and a very high concentration of nickel, often a catalyst used to grow HPHT synthetic diamonds.

This ring offered an excellent example of how the GIA iD100 can quickly screen very small mounted diamonds and accurately detect any synthetics or even simulants.

Figure 18. A diamond ring with 100 melee side stones incorporated into the setting.

Figure 19. One stone, about 0.5 mm in diameter, was referred by the GIA iD100 for further testing. The inset photo shows a prototype of the iD100.

Paul Johnson and Stephanie Persaud

Flux-Grown Pink SYNTHETIC SAPPHIRE with Unusual Crystal Inclusions

The Carlsbad laboratory recently received a saturated pink cushion mixed cut, mounted in a ring, that measured 14.02 × 10.35 × 6.24 mm (figure 21). Standard gemological testing yielded a refractive index of 1.760–1.768 and a weak ruby spectrum using a handheld spectroscope, properties consistent with pink sapphire. The stone displayed a strong orange fluorescence under long-wave UV and an odd chalky orangy yellow fluorescence under short-wave UV. While orange fluorescence is not unusual in pink sapphires, the intensity and the chalky yellow reaction were suspicious.

Microscopic examination revealed a single hexagonal, dark reflective platelet (figure 22); numerous transparent, colorless tabular to rounded doubly refractive crystals (figure 23) that showed interference colors under crossed polarizers; and a small fingerprint composed of elongated tubules. Observation in immer-

Figure 20. The referred melee displayed strong phosphorescence to short-wave UV radiation, as is typical of HPHT-grown synthetic diamonds.

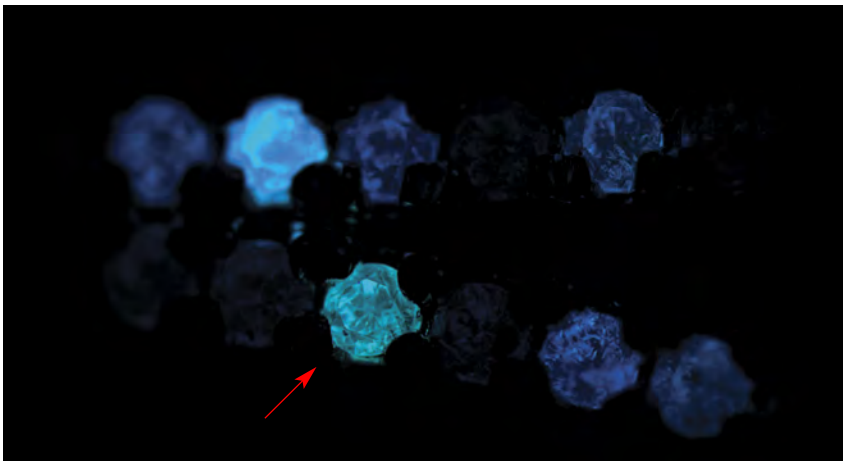

Figure 21. This pink stone proved to be a flux-grown synthetic sapphire with unusual crystal inclusions.

sion showed some weak, straight orange and pink zoning. This inclusion scene could easily be mistaken for natural as the transparent crystals bore a certain resemblance to zircon, a common inclusion in natural sapphires and particularly pink sapphires from Madagascar. The dark reflective platelet, which was presumably platinum, and odd fluorescence prompted further investigation.

The synthetic nature of the sapphire was confirmed using LA-ICP-MS. High amounts of Pt were detected, which would support a flux synthetic growth process. Small amounts of Fe and Be were present; Ga, Ti, and V were not detected. This

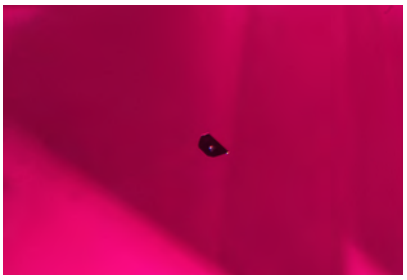

Figure 22. This dark reflective platinum platelet observed in the pink synthetic sapphire is a common inclusion in flux-grown synthetic corundum. Field of view 1.82 mm.

chemical profile also supports synthetic sapphire.

Transparent crystals of possible chrysoberyl ($BeAl_2O_4$) have been previously cited in flux-grown synthetic corundum (R.E. Kane, "The gemological properties of Chatham flux-grown synthetic orange sapphire and synthetic blue sapphire," Fall 1982 *G&G*, pp. 140–153). In that case, Chatham stated that heavy concentrations of beryllium were added to the original aluminum oxide formula, which would explain the presence of those crystals. In our pink sapphire, none of the crystals reached the surface, so we were unable to identify them with Raman spectroscopy. Small amounts of beryllium were detected, so chrysoberyl could be a possibility in this case as well.

Figure 23. The abundance of transparent crystals and crystal clusters could easily be mistaken for a natural inclusion scene in a pink sapphire from Madagascar. Field of view 1.79 mm.

The presence of these natural-looking crystals combined with the general lack of other inclusions for a stone of this size, particularly diagnostic flux fingerprints, could make correct identification very difficult for gemologists without access to advanced instrumentation. This is one case where advanced testing in a well-equipped gemological laboratory was necessary to make a conclusive identification.

Claire Ito

PHOTO CREDITS
Jian Xin (Jae) Liao—1; Paul Johnson—3, 5, and 20; Robison McMurtry—6, 7, 9, and 21; Jonathan Muyal—8; Nathan Renfro—10, 22, and 23; Sood Oil (Judy) Chia—11, 18, and 19; Emiko Yazawa—12; Yusuke Katsurada—13 and 14; Troy Ardon—15.

For More on Lab Notes

To watch video of the mobile inclusion in emerald (pp. 361–362), go to https://www.gia.edu/gems-gemology/fall-2017-labnotes-emerald-mobile-inclusion, or scan the QR code to the right.

LETTERS

NOTE ON CVD SYNTHETIC OVERGROWTH

I read with interest the Summer 2017 *G&G* Lab Note titled "CVD synthetic diamond overgrowth on a natural diamond" (pp. 237–239). The concluding paragraph states, "This synthetic overgrowth on a natural diamond with a Fancy color grade is the first GIA has seen." However, a Gem News entry published in the Summer 1991 *G&G* presented color photos of a synthetic bluish gray CVD diamond overgrowth over one rough and two faceted natural near-colorless type Ia diamonds (Koivula and Kammerling, 1991). This Gem News item was more recently reproduced in the *G&G In Review: Synthetic Diamonds* compilation book, published in 2005.

The treated gems were documented at the time by myself and other GIA researchers. A scientific article (Fritsch and Phelps, 1993) detailed the work first mentioned in the 1991 Gem News item. It already cautioned the jewelry industry about the availability of such a product and its possible misidentification. The highly doped boron film (approximately 220 ppm B, hence the dark color) was about 0.1 microns thick and deposited by the hot filament method. To everyone's surprise, the crystallographic orientation of the natural type Ia substrate had no noticeable influence on the quality of the type IIb CVD film. The film could be detected by abrasions on facet edges, infrared spectroscopy (absence of the boron acceptor center), and UV-visible spectroscopy (presence of the N3 center). Of course, no detailed low-temperature photoluminescence was done, as this became common practice on diamonds only around 1999, with the onset on HPHT-treated diamonds. Neither is there a clear influence of the type IIb layer on the infrared spectrum, in part due to its thinness and the difference in efficiency with today's infrared detectors.

The three samples were left with GIA Research. I would encourage the authors of the Lab Note to run a full characterization with more up-to-date methods. It is of interest that the stones were submitted to GIA as client stones and followed the normal procedure for blue diamonds at the time, yet this treatment went undetected.

This work predates by two years Yacobi et al. (1993), which the Summer 2017 Lab Note suggests was the first to report deposition of CVD synthetic diamonds on natural type Ia substrates, although not faceted, so less relevant to gemologists' concerns. (Yacobi's article, incidentally, was published in the same issue of *Diamond and Related Materials* as the Fritsch and Phelps article.) The recent Lab Note also states, "Deposition of a boron-doped CVD synthetic film of <10 microns on a natural gem-quality diamond was reported in 2005," whereas this had already been published almost 15 years prior, in 1991. Furthermore, in contrast with the 2005 article cited, spectroscopic data was presented in the 1993 article.

Emmanuel Fritsch
University of Nantes, CNRS, Team 6502
Institut des Materiaux Jean Rouxel (IMN), Nantes, France

References

Fritsch E., Phelps A. (1993) Type IIb diamond thin films deposited onto near-colorless natural gem diamonds. *Diamond and Related Materials*, Vol. 2, No. 2-4, pp. 70–74.

Koivula J.I., Kammerling R.C. (1991) Gem News: Bluish gray synthetic diamond thin films grown on faceted diamonds. *G&G*, Vol. 27, No. 2, pp. 118–119.

Yacobi B.G., Lebens J., Vahala K.J., Badzian A.R., Badzian T. (1993) Preferential incorporation of defects in monocrystalline diamond films. *Diamond and Related Materials*, Vol. 2, No. 2-4, pp. 92–99.

REPLY

We thank Prof. Fritsch for reading our Summer 2017 Lab Note and writing this letter to *Gems & Gemology*. In it we mentioned that this synthetic overgrowth diamond was the first GIA had seen, and several factors support this statement. It showed sharp boron peaks at 2455 and 2800 cm^{-1}, and nitrogen aggregates and platelet peaks in the 1000–1500 cm^{-1} region (see figure 1 at www.gia.edu/gems-gemology/fall-2017-letters-CVD-synthetic-overgrowth). Therefore, we classified it as mixed type Ia and IIb. In their 1993 *Diamond and Related Materials* article, Fritsch and Phelps coated natural, near-colorless type Ia diamonds by depositing boron-doped CVD film. They extrapolated the boron concentration of their coated diamonds using electrical conductivity rather than calculating it from the IR spectrum, which did not show any boron peaks. According to diamond type classification (Breeding and Shigley, 2009), the IR spectrum indicates a type Ia diamond, not a mixed type. The diamond we reported on in the last issue is the first CVD-coated mixed-type diamond detected at GIA using FTIR.

CVD-coated diamonds previously reported in *G&G* were not client diamonds (see Fritsch and Phelps, 1993; Eaton-Magaña, 2014). The CVD layer was deposited on natural diamonds for research purposes. In contrast, our diamond was submitted by a client, suggesting CVD-coated natural diamonds have already reached the market. The color has also been improved. Previous CVD-coated diamonds were dark bluish gray (Koivula and Kammerling, 1991; see figure 2 at www.gia.edu/gems-gemology/fall-2017-letters-CVD-synthetic-overgrowth) and an initially gray color that altered to Fancy Dark brownish yellowish gray after nine years of wear (Magaña, 2014; figure 2, center), whereas ours was graded as Fancy blue (figure 2, right). This was also the first undisclosed client-submitted CVD-coated diamond with blue color identified by GIA. The lack of disclosure and the Fancy blue color grade have significant consequences for the trade. Consequently, our note was translated to Chinese and Japanese on GIA's website.

The Lab Notes section is intended for new findings at GIA laboratories, especially among client-submitted stones. Unlike research papers, the entries are meant to be short. We try to choose only the most appropriate references. Fritsch and Phelps (1993) described the deposition method of the CVD layer and characterized the CVD-coated diamonds using spectroscopy and gemological methods. That same year, Yacobi et al. (1993) published a paper about growing CVD films on type Ia natural diamonds. They deposited the CVD film on the (001) and (111) planes at various temperatures. They discussed preferential incorporation of defects at different crystallographic planes using cathodoluminescence and Raman spectroscopy. Although Fritsch and Phelps (1993) is an important study, we felt that Yacobi et al. was a more comprehensive reference for our lab note.

Our team respects Prof. Fritsch's invaluable contributions to gemology, and we thank him for taking time to comment.

Kyaw Soe Moe
GIA, New York

References

Breeding C.M., Shigley J.E. (2009) The "type" classification system of diamonds and its importance in gemology. *G&G*, Vol. 45, No. 2, pp. 96–111.

Eaton-Magaña S. (2014) Lab Notes: Long-term durability of CVD synthetic film on natural diamond. *G&G*, Vol. 50, No. 2, p. 152.

Unusual Cloud in Diamond

GIA's laboratories issue clarity grades for many diamonds for the gem trade. So when we observe a diamond with clarity characteristics we have not encountered before, we generally consider those features to be rather rare and worth documenting for future reference.

Recently, just such a diamond was examined in the Carlsbad lab. It was a 0.62 ct round brilliant with very good polish and symmetry and a very light brown bodycolor. The diamond exhibited a faint light blue fluorescence to long-wave radiation and an inert reaction upon exposure to short-wave UV.

The gem's I_1 clarity grade resulted from a delicate cloud of cruciform dislocations (figure 1), forming numerous small interlinked cross-like patterns in the diamond host, which were visible face-up through the table facet. The shape and orientation of the overall cloud suggests that the cube face of the original diamond crystal was parallel to the table facet of the faceted diamond.

We regularly encounter cloud clarity features in diamonds, but this fascinating geometric network was a "first encounter" for us.

John I. Koivula
GIA, Carlsbad

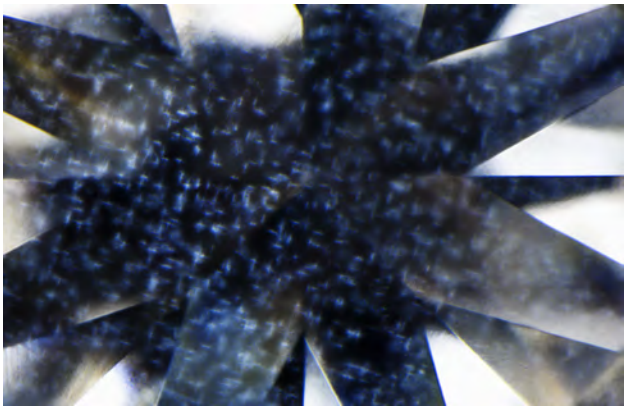

Figure 1. This delicate interlinked cross-like cloud pattern found in a 0.62 ct diamond has never been encountered in GIA's laboratories. Photomicrograph by Nathan Renfro; field of view 2.40 mm.

Hematite in Quartz: "A Rose by Any Other Name"

Careful exploration of the micro-world can often reveal extraordinary crystal formations, even in relatively inexpensive, somewhat ordinary jewelry. The silver pendant shown in figure 2, measuring 31.50 × 17.00 × 10.00 mm, was purchased by author CF in 1996 from a Brazilian dealer at the

Figure 2. A plain quartz silver pendant measuring 31.50 × 17.00 × 10.00 mm encapsulates extraordinary inclusions of complex hematite crystals. Photo by Conny Forsberg.

About the banner: Lattice-like exsolution products of hematite and ilmenite show iridescent colors with oblique fiber-optic lighting in an Australian orthoclase feldspar known in the trade as "rainbow lattice sunstone." Photomicrograph by Nathan Renfro; field of view 7.20 mm.
Editors' note: Interested contributors should contact Nathan Renfro at nrenfro@gia.edu and Jennifer-Lynn Archuleta at jennifer.archuleta@gia.edu for submission information.

Gems & Gemology, Vol. 53, No. 3, pp. 369–372.

© 2017 Gemological Institute of America

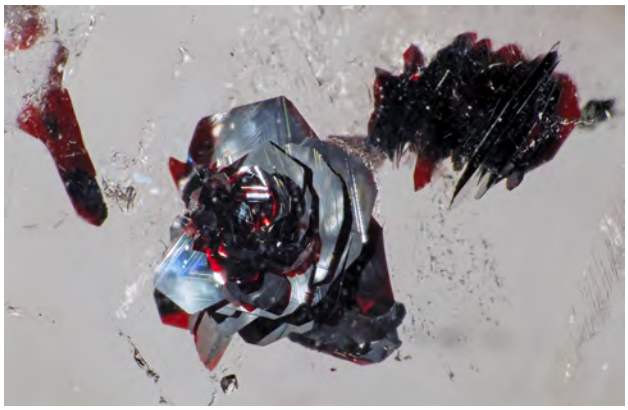

Figure 3. One of the quartz cabochon's perfect "rose" habit inclusions exhibits fine, well-crystallized thin platelets of hematite. Transmitted and oblique halogen fiber-optic lighting. Photomicrograph by Conny Forsberg; field of view 5.00 mm.

Pueblo Show in Tucson, Arizona. It stood out among many others for its aesthetic swarm of crystal inclusions (later identified by their color and morphology as hematite), while their host was confirmed to be quartz using standard gemological techniques, including refractive index and optical testing. Several of the included crystals exhibited a complex habit known to mineral collectors as a "hematite rose"—an aggregate of crystal platelets arranged very much like the blooms of its botanical namesake. One of these inclusions was oriented in such a way that it lent itself to easy observation and photomicrography; this is not always the case with jewelry pieces whose construction may obscure the internal view or make lighting the inclusions tricky. A halogen light source with dual fiber-optic wands was used to successfully illuminate the rose from an oblique angle and to bounce light off the microscope plate in order to provide transmitted lighting (figure 3).

While quartz is a silicate, hematite is an iron oxide; both crystalize in the trigonal system. The surfaces of the fine, well-crystallized platelets of hematite exhibit triangular growth steps revealing this mineral's underlying symmetry. These very thin plates reveal a deep red color in transmitted light. Quartz has a large thermal expansion coefficient, larger than that of hematite. Therefore, we would not expect cooling from the formation conditions to create a thin gap between the quartz and the hematite capable of producing thin-film interference colors, which are indeed absent here. Freely grown macro-specimens command hefty prices in the mineral-collecting world; however, an observant inclusionist may obtain one very frugally. This hematite crystal formation is as lovely as any rose and a fitting bloom for any gemologist's micro-world garden.

Conny Forsberg
Swedish Gem AB
Kisa, Sweden

Elise A. Skalwold and William A. Bassett
Ithaca, New York

Silvery Rutile "Tufts" in Quartz

Recently, author JG discovered a deposit of rock crystal quartz in El Dorado County in east-central California. To date, more than 1,000 quartz crystals have been recovered from a single pocket in this deposit. Almost 50 percent of those crystals contained interesting silvery gray tufts of the titanium dioxide mineral rutile (figure 4), which was identified using Raman spectroscopy. Rutile in quartz typically occurs as golden needles, but it can occasionally be found as reddish brown, green, or silvery gray needles.

While the cause of the star-like needle arrangement in these particular clusters is not known, it is possible that the gray rutile is overgrown on a core crystal of anatase, which is a polymorph of rutile and might influence the morphology of the cluster. Tufts of golden rutile with a similar morphology have been observed overgrown on blue core crystals of anatase by author NR, which may explain the morphology in this sample; however, it was not possible to confirm this. A similar occurrence of gray rutile overgrowth is known to occur in the material sold as "platinum quartz" from Currelo in Minas Gerais, Brazil, where it is overgrown on the other rutile polymorph, brookite (see E.J. Gübelin and J.I. Koivula, *Photoatlas of Inclusions in Gemstones*, Vol. 2, Opinio Verlag, Basel, Switzerland, 2005, p. 588).

While production volume of quartz with these silvery rutile inclusions remains uncertain, this deposit has already provided interesting and beautiful additions to the micro-world.

Nathan Renfro
GIA, Carlsbad

Jobadiah Giles
Risky Venture Minerals
Placerville, California

Figure 4. Quartz crystals containing stellate tufts of silvery gray rutile were recently discovered in east-central California. Photomicrograph by Nathan Renfro; field of view 9.48 mm.

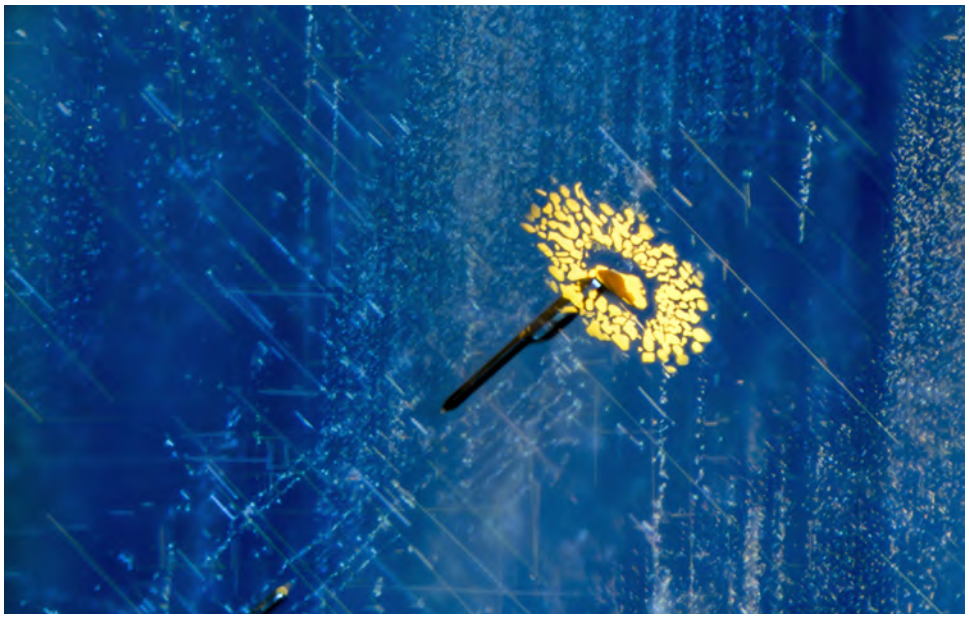

Figure 5. Reminiscent of a flower in a rainstorm, this inclusion scene has been dramatically enhanced using modified Rheinberg illumination to accentuate a growth blockage and thin-film rosette within a sapphire from Elahera, Sri Lanka. Photomicrograph by Jonathan Muyal; field of view 1.34 mm.

"Flower in the Rain" Inclusion in Sri Lankan Sapphire

The island of Sri Lanka is famous for gems but is also notable for its enormous biodiversity. It therefore seemed fitting that when these authors encountered a fascinating inclusion reminiscent of a beautiful flower within a Sri Lankan sapphire, it would embody these themes.

This 3.64 ct blue sapphire specimen from Elahera exhibited an interesting growth blockage resulting in an elongate tube capped by a rosette-like thin-film fluid inclusion. To further enhance the inclusion scene, Rheinberg illumination (Fall 2015 Micro-World, pp. 328–329) using blue and yellow filters provided additional contrast. This lighting technique transformed the inclusion scene into an easily imagined, vibrantly colored flower caught in a rainstorm, something one might encounter while visiting the tropical island nation (figure 5).

Growth blockages occur when a foreign mineral grain or particle interrupts the growth of a crystal (Spring 2010 Lab Notes, pp. 55–56). As the crystal continues to grow, an elongate void is typically produced, which may extend to the surface or be capped off, as seen in this sapphire. Even though a growth blockage is not diagnostic of Sri Lankan origin in sapphire, this inclusion scene is an appropriate symbolic representation of the "resplendent isle."

Jonathan Muyal and Nathan Renfro
GIA, Carlsbad

Growth Tube Cluster in Sapphire

Growth tubes are a typical inclusion in corundum and often seen during examination in the laboratory. While commonplace, a stunning cluster such as the one seen in figure 6 calls out to the photomicrographer. At the surface these tubes are cut through and some black debris has be-

Figure 6. Surface-reaching growth tubes within a sapphire exhibit unaltered yellowish staining, an indication that the stone has probably not been heated. Combined with other observations, this suggests a possible Madagascar origin. Photomicrograph by E. Billie Hughes; horizontal field of view 1.4 mm.

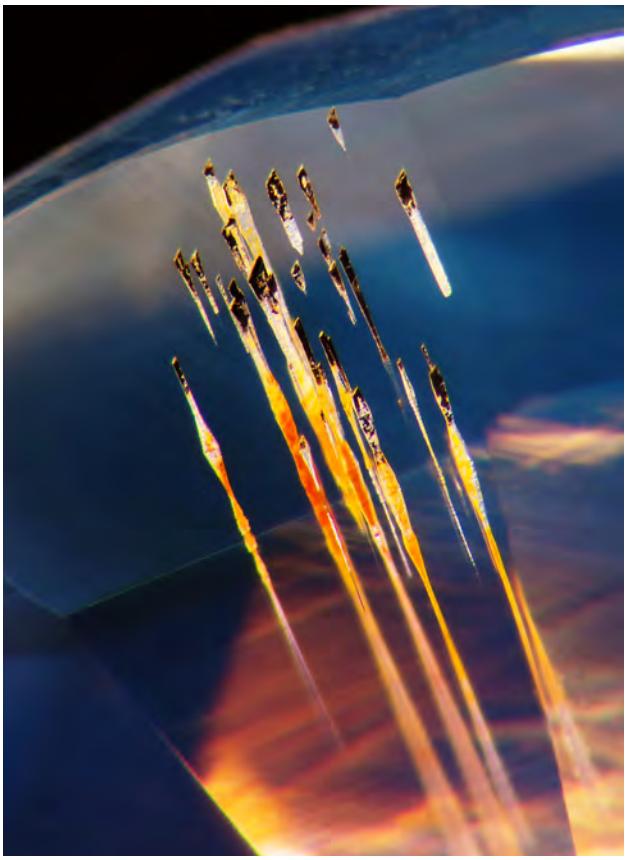

come lodged inside the ends, while deeper within the stone they still display a fiery glow, reminiscent of rockets launching into the sky.

Not only do these tubes spark the imagination, but they can actually tell us a lot about the identity of their sapphire host. The limonitic staining found deeper in the tubes is a yellowish orange, suggesting that they have not been altered by heat treatment. These stains often turn a darker reddish or brownish color in heat-treated stones (J.I. Koivula, "Useful visual clue indicating corundum heat treatment," Fall 2013 *G&G*, pp. 160–161).

Furthermore, we have observed in the past several months that these prominent growth tubes are a common feature in Madagascar sapphire. While the tubes can be found in corundum from other origins, they seem particularly common in the Madagascar material that has been entering the Bangkok market in greater numbers recently. When taken into account along with other features, they provide a clue to the origin of these sapphires. Thus, what initially appeared to be a mundane inclusion is both visually impressive and gemologically significant, as it provides hints to the origins and treatments of corundum.

E. Billie Hughes
Lotus Gemology Laboratory
Bangkok

Figure 7. This 247.02 ct bright yellow fluorite partial crystal, which measures 40.04 mm tall, hosts two large concretions of bone-white barite. Photo by Kevin Schumacher.

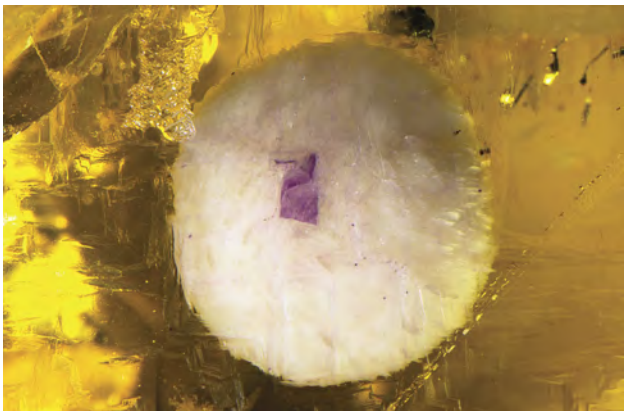

Figure 8. The largest of the two barite inclusions has a prominent purple spot on the top of its dome, which is easily seen against the white background provided by the inclusion. Photomicrograph by Nathan Renfro; field of view 13.71 mm.

Quarterly Crystal: Barite in Fluorite

Although gemologists deal primarily with fashioned gemstones, some crystal specimens are far too attractive as intact objects to be used as cutting rough. This is particularly true if they contain eye-visible inclusions like those seen in the 247.02 ct transparent yellow fluorite partial crystal shown in figure 7.

At 40.04 mm in its longest dimension, this specimen invites exploration of its inclusions, which were identified as barite using laser Raman microspectrometry. The larger of the two barites measures 7.0 mm in diameter and has a microscopically prominent rectangular purple spot on the apex of its dome (figure 8), which clearly stands out against the stark white background provided by the barite inclusion. Although the cause of the spot is unclear, the contrasting assemblage of colors adds to this specimen's value as an aesthetic collector piece.

John I. Koivula

G&G Gem News International

Contributing Editors
Emmanuel Fritsch, *University of Nantes, CNRS, Team 6502, Institut des Matériaux Jean Rouxel (IMN), Nantes, France* (fritsch@cnrs-imn.fr)
Gagan Choudhary, *Gem Testing Laboratory, Jaipur, India* (gagan@gjepcindia.com)
Christopher M. Breeding, *GIA, Carlsbad* (christopher.breeding@gia.edu)

COLORED STONES AND ORGANIC MATERIALS

Blue-green pyrope-spessartine garnet with high vanadium. A unique type of blue-green garnet has entered the market through New Era Gems (Grass Valley, California). The garnets reportedly come from a deposit near the border of Tanzania and Kenya. GIA's Carlsbad laboratory obtained a small parcel of blue-green rough material and two faceted stones (figure 1, top) for examination. Unlike traditional blue-green garnets that exhibit a color change from purplish or orange red in incandescent light to bluish or yellowish green in daylight, these essentially remained blue in the lighting conditions we tested (CIE standard illuminants D65, A, F10, and F9, and a cool LED light with a 7500K color temperature). They showed only a weak color change from violet or blue in incandescent light (figure 1, bottom) to green or blue-green in daylight (again, see figure 1, top). We chose two samples from the New Era parcel, one with a classic violet to blue-green color change (garnet 1) and one piece of this new material with a weak color change from blue to blue-green (garnet 2). These were polished into wafers and analyzed to understand their chemical composition and color behavior.

Standard gemological testing revealed a refractive index (RI) of 1.760 to 1.765 and a hydrostatic specific gravity (SG) of 3.83 to 3.88. Fluorescence was inert to long- and short-wave UV light. No pleochroism was seen with the dichroscope. Using a handheld spectroscope, we observed absorption lines in the blue and violet section and a very broad absorption band centered around 590 nm wavelength. These properties are consistent with garnet.

Laser ablation–inductively coupled plasma–mass spectrometry (LA-ICP-MS) composition analyses were performed using a Thermo Fisher iCAP Q ICP-MS coupled with a New Wave Research UP-213 laser ablation unit. USGS reference glasses GSD-1G and GSE-1G were used as external standards and ^{29}Si as the internal standard. The analyses were performed in the same region where the spectroscopic data was collected (table 1 at www.gia.edu/gems-gemology/fall-2017-gemnews-pyrope-spessartine-garnet). The garnets were predominantly composed of

Figure 1. Top: Twenty rough and two faceted garnets photographed under a light source with 6000K color temperature (a daylight-equivalent light simulator). Bottom: The same stones under a light source with 3100K color temperature (an incandescent light simulator). The 0.288 ct faceted stone measures 4.14 × 3.20 × 2.66 mm, while the 0.221 ct stone below it measures 4.01 × 3.09 × 2.10 mm. Photos by Kevin Schumacher.

Editors' note: Interested contributors should send information and illustrations to Stuart Overlin at soverlin@gia.edu or GIA, The Robert Mouawad Campus, 5345 Armada Drive, Carlsbad, CA 92008.

Gems & Gemology, Vol. 53, No. 3, pp. 373–388.

© 2017 Gemological Institute of America

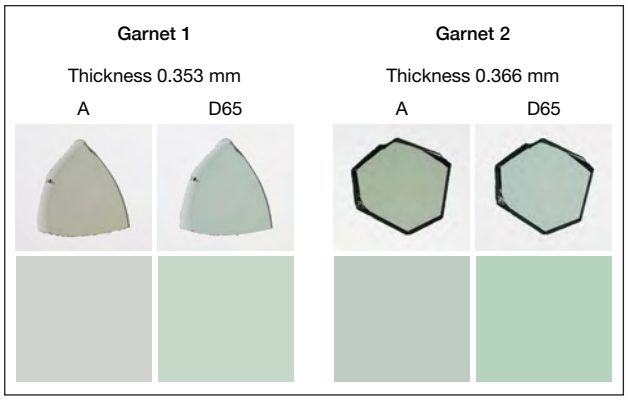

Figure 2. Top row: Photos of two garnets under incandescent light (A) and fluorescent light (daylight-equivalent light simulator D65). Bottom row: Calculated color panels under CIE A and CIE D65 illumination.

equal amounts of pyrope and spessartine. The main difference was the higher concentration of V_2O_3 in garnet 2 (2.3 wt.%) than in garnet 1 (1.6 wt.%). Based on the classification system from Stockton and Manson (Winter 1985 *G&G*, pp. 205–218), the material represented by these two garnets is pyrope-spessartine. Vanadium and manganese are known to be the main cause of color change in pyrope-spessartine, yet garnet 2 contained a much higher vanadium component than any of the color-change pyrope-spessartine ranges (0.13–1.65 wt.% V_2O_3) reported by Schmetzer et al. ("Color-change garnets from Madagascar: Variation of chemical, spectroscopic and colorimetric properties," *Journal of Gemmology*, Vol. 31, No. 5–8, 2009, pp. 258–259). To the authors' knowledge, gem-quality garnet with this chemical composition has never been reported.

UV-Vis-NIR spectra were collected with a Hitachi U-2910 spectrometer with a 1 nm spectral resolution at a scan speed of 400 nm/min. The spectra were reflection-corrected using a method previously described by the authors ("Vanadium- and chromium-bearing pink pyrope garnet: Characterization and quantitative colorimetric analysis," Winter 2015 *G&G*, pp. 348–369). The reflection-loss-corrected visible spectra were used to quantitatively calculate the material's color at a wide range of path lengths and under different lighting conditions. Calculated color panels of the two garnets under incandescent light (CIE A illumination) and daylight-equivalent lighting (CIE D65 illumination) are shown in figure 2. The two garnets were also photographed under incandescent light (equivalent to CIE A) and fluorescent light (equivalent to CIE D65) for comparison. The close match between our photos and the calculated color panels confirmed the accuracy of our calculation. Figure 3 shows the possible color exhibited by two representative garnets with different path lengths (defined by the stone's thickness) and the approximate corresponding carat weight of a well-proportioned round brilliant; for details of this calculation, see Sun et al. (2015). The high-vanadium garnet is bluer in incandescent light than the lower-vanadium garnet. Both become very dark at about 0.7 ct, which means the optimal color occurs in smaller sizes.

To understand why the garnets stayed essentially blue in the lighting conditions tested, we can examine the visible absorption spectra. The calculated reflection-loss-corrected absorption spectra of garnets 1 and 2 at 5 mm path length are shown in figure 4. V^{3+} produces the large absorption band centered at about 585 nm. This band strongly absorbs orange and yellow light and a smaller portion of the red part of the visible spectrum. At low concentrations of vanadium, this absorption band produces two transmission

Figure 3. The color panels of two garnets under CIE A and CIE D65 illumination are quantitatively reproduced. The garnets' colors are shown at different path lengths of light (defined by the thickness of the wafer) and carat weights. For each sample, the top and bottom rows represent the color under incandescent light (A) and daylight-equivalent light (D65), respectively.

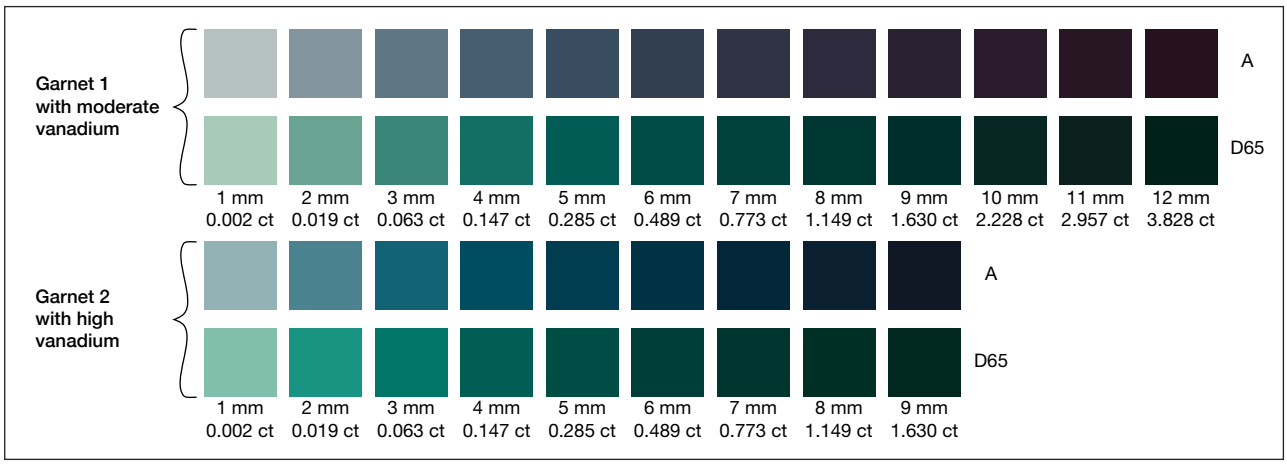

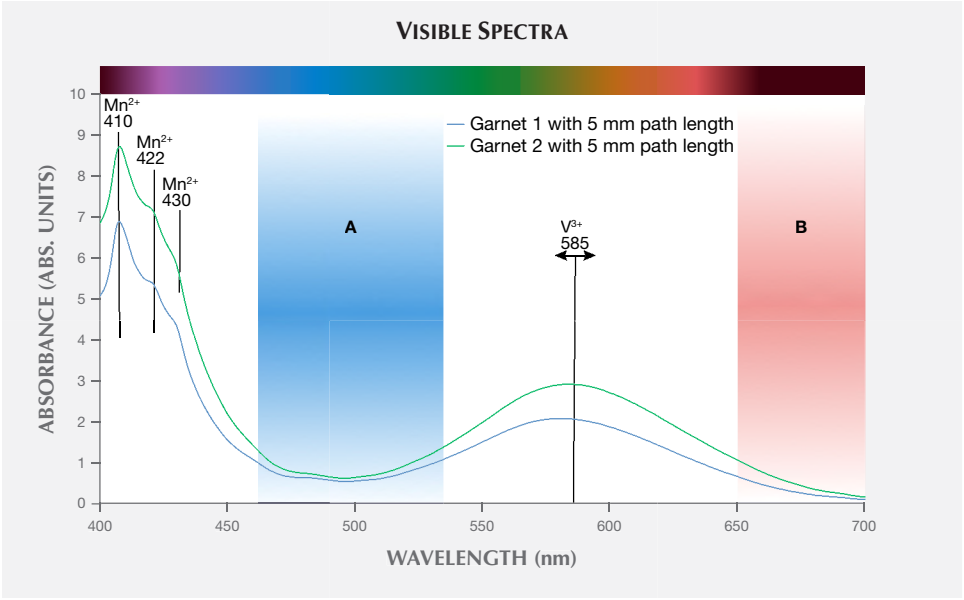

Figure 4. The calculated reflection-loss-corrected visible absorption spectra of garnets 1 and 2 with 5 mm path length; transmission window A is centered at 490 nm, while transmission window B is between 650 and 700 nm. Absorption bands at 410, 422, and 430 nm are caused by Mn^{2+}, and a wide absorption band between 550 and 650 nm is caused mainly by V^{3+}.

windows, one in the blue part of the spectrum (figure 4, window A) and one in the red (figure 4, window B). This is the cause of the color change in low-vanadium pyrope-spessartine, as incandescent illumination highlights the red transmission window and daylight illumination highlights the blue-green window. As the concentration of vanadium increases, the red transmission window is preferentially closed and the color in both incandescent and daylight illumination is determined solely by the blue-green transmission window A. The concentration of V^{3+} relative to other chromophores (Mn^{2+}, Fe^{2+}, and Cr^{3+}) is the fundamental reason why these higher-vanadium pyrope-spessartines remain blue under any lighting condition.

Ziyin Sun, Nathan D. Renfro, and Aaron C. Palke
GIA, Carlsbad

La Lechuga monstrance. The gold monstrance of the church of San Ignacio de Bogotá, with almost 1,490 Colombian emeralds, is one of the most remarkable examples of baroque artistry in devotional objects (figure 5). With its abundance of fine-color emeralds, the artifact was dubbed La Lechuga (Spanish for "lettuce"). It is now on a brief European tour until January 3, 2018.

In 1700, the first year of Philip V's reign, Spanish goldsmith José Galaz went to the territory of Nueva Granada to create a unique monstrance for the Jesuit church of San Ignacio de Bogotá. From 1700 to 1707, he used solid gold, enamel, and fine gem materials to create what became one of the most magnificent baroque monstrances ever produced. The approximately 80-cm-tall artifact is embellished with diamond, ruby, sapphire, amethyst, citrine, and baroque white natural pearl, along with the fine-quality Colombian emeralds. Further research might shed light on the provenance of these emeralds, which are possibly from the Muzo, Chivor, and Coscuez mines. Most have exquisite color and clarity, and the profusion of these gemstones in the circular aura makes it distinctively green. An interesting feature is the use of pearls in the gold lunette, the container where the host for

Figure 5. La Lechuga, a gold devotional artifact made for the church of San Ignacio de Bogotá, features nearly 1,490 Colombian emeralds. © Museo de Arte del Banco de la República.

the Eucharist is kept. Normally these lunettes have a crescent shape and are set with diamonds or no gems at all.

This monstrance was purchased by the Banco de la República de Colombia in 1985 and is now part of its Museo de Arte Miguel Urrutia collection. As one of Colombia's most important treasures, it almost never leaves the country. An exception was made in 2015 when it went to the Museo del Prado in Madrid, and in 2017 it has been on public display at the Museu Nacional de Arte Antiga in Lisbon (June 21–September 13) followed by an exhibition at the Louvre in Paris (until January 3, 2018). This tour offers a unique opportunity for visitors outside Colombia to experience this outstanding Iberian baroque monstrance and its important gemological content.

Rui Galopim de Carvalho
Portugal Gemas, Lisbon

The "Montana Queen" sapphire. In September 2016, while viewing a selection of large Montana sapphires mined by Potentate Mining at their new operation at Rock Creek, one stone stood out. It possessed a beautiful medium blue-green color and a hexagonal crystal form with a blue rim and golden center (figure 6). It weighed 31.98 ct (6.40 g) and appeared to be free of major internal defects. Sapphires this large make up less than 0.25% of Rock Creek's production, and they are typically fractured or otherwise included.

Most Rock Creek sapphires have frosted or etched surfaces, apparently as a result of partial resorption in the host rock. To assess the quality of this sapphire before cutting, a window was polished, allowing a view of the interior of the crystal; this removed just over one carat, as a surface crack was also ground away. The window revealed that the center gold spot was composed of golden rutile needles that could be cleared by heating. A mostly rehealed parting plane and a few crystal inclusions were also visible. We decided to heat the stone to dissolve the silk, hoping that the parting plane and internal inclusions would not fracture during the process. The heating, performed by Dale Siegford (The Sapphire Gallery, Philipsburg, Montana), dissolved all the silk and changed the rough's color to a deeper, more uniform blue (figure 7). Most importantly, none of the inclusions spread or formed larger fractures.

While size is always a cutting consideration, color is also a determining factor in the value of the finished gemstone. The pleochroism of sapphire crystals means that orientation is critical for the best presentation of color. This sapphire had a rich blue c-axis just slightly tinted with green, while the a-b axis was a medium shade of green. Fortunately, the crystal was shaped such that the best orientation for both color and size were the same—the table could be positioned directly on the c-axis. Our goal was to feature the stone's natural hexagonal shape, increasing yield and preserving the crystal's beauty. GemCad and GemRay were used to work through a series of designs, optimizing them for a combination of light return and scintillation. The intent was to use facets large enough to create broad flashes of color while concealing the minor inclusions. With a gem this rare there is no room for error, so the final design was test-cut on a smaller Rock Creek sapphire to validate the modeling.

Once we were satisfied with the result on the test stone, the cutting of the large gem began on the pavilion. Because the natural shape of the gem matched the final outline, only minor preforming was required; the rough gem weighed 30.84 ct when attached to the dop. There was a crack near one side of the gem, so it was dopped slightly off-center to ensure it would be removed in the cutting process. The gem was faceted in three steps: The facets were cut with a 600-grit sintered lap, followed by a pre-polish with 8,000-mesh diamond and an ultrafine polish using 100,000-mesh polycrystalline synthetic diamond. After completing the pavilion, the gem was transferred to a new dop and the process was repeated to cut the crown (figure 8).

The finished gem weighed 12.62 ct, for a yield of 39.5% from the original rough (figure 9). The authors are aware of only two larger faceted Montana sapphires, one with similar quality. Neither of those stones is blue—one is purple

Figure 6. The 31.98 ct (6.40 g) rough sapphire crystal as it was mined. Photo by Jeffrey R. Hapeman.

Figure 7. The rough sapphire after heating, with a window polished to view the interior. Photo by Jeffrey R. Hapeman.

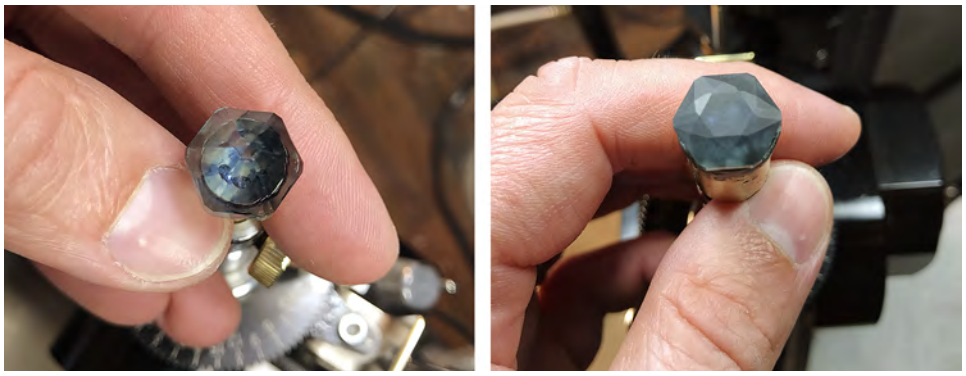

Figure 8. The sapphire during the cutting process. The polished pavilion is shown on the left and the rough-cut crown on the right. Photos by Jeffrey R. Hapeman.

and the other green—making this perhaps the largest faceted blue Montana sapphire, slightly larger than the famed 12.58 ct Big Sky sapphire. Due to its size, rarity, and beauty, this gem was named the "Montana Queen."

Jeffrey R. Hapeman
Earth's Treasury, Westtown, Pennsylvania
Keith M. Barron and Warren F. Boyd
Potentate Mining, Philipsburg, Montana

Update on Mozambique ruby mining and trading. Less than 10 years after discoveries inside the Niassa Reserve in 2008 and near Montepuez in 2009, rubies from northern Mozambique have taken a significant place in the trade. During the first few years, production came exclusively from unlicensed miners known as *garimpeiros*, who sold their production mainly to Thai, Sri Lankan, Tanzanian, and West African traders. The stones were smuggled to cutting and trading centers such as Thailand. The situation changed when Gemfields, which acquired mining licenses near Montepuez in 2011 and began operations in 2012, held its first rough ruby auction in Singapore in June 2014.

Since 2015, three factors have affected that dynamic, starting with an efficient low-temperature heat treatment technique developed in Sri Lanka and brought to Mozambique. As the treatment is very difficult to detect without lab instrumentation on faceted stones and even more so on rough, the challenge for dealers buying stones from garimpeiros was to avoid paying unheated ruby prices for stones that had been already heated. Many buyers purchased heated rough in Montepuez only to find out later in Thailand about their costly mistake. Within a few months, confidence in the stones from that network deteriorated and dealers found out that the only safe options for unheated rubies were to buy directly from Gemfields or to get reliable laboratory testing on any stones obtained elsewhere. The situation became difficult for those willing to take their chances buying illegally in Mozambique.

Figure 9. The finished 12.62 ct Montana Queen sapphire. Photo by Jeffrey R. Hapeman.

In early 2016, another significant change took place when the Mozambican government changed its policy on garimpeiros. Before 2016 the garimpeiros were, legally speaking, "informal" small-scale miners. The only legal issue was that they had no license. The police were only allowed to confiscate their mining equipment and question them before releasing them. But in 2016, mining for gemstones or gold without a license became a crime punishable by three years in jail. In February 2017 the government, which was facing major fiscal problems, changed tactics: Instead of taking legal action against garimpeiros, they would target buyers hiding in the towns. Several police operations were launched in Cabo Delgado, and many foreign buyers (mainly Tanzanian, Thai, Sri Lankan, and West African) were arrested, fined, and expelled. Rubies quickly became more scarce in the Thai markets. This probably explains why Gemfields had its most successful ruby auction ever in June 2017, recording more than US$54 million in sales.

Finally, as previously reported (W. Vertriest and V. Pardieu, "Update on gemstone mining in northern Mozambique," Winter 2016 *G&G*, pp. 404–409), two new mining companies, Mustang Resources and then Mozambican Ruby (formerly known as Metals of Africa), began operations near Napula village, north of the road linking Montepuez to Pemba in areas neighboring Gemfields. As these companies have not yet sold any production, their impact is still unknown.

In June 2017, the author visited northern Mozambique (figure 10) for the sixth consecutive year to collect reference samples. This time it was for Danat, the newly formed Bahrain Institute for Pearls & Gemstones. The team was composed of jewelry designer Erica Courtney; Dr. Cedric Si-

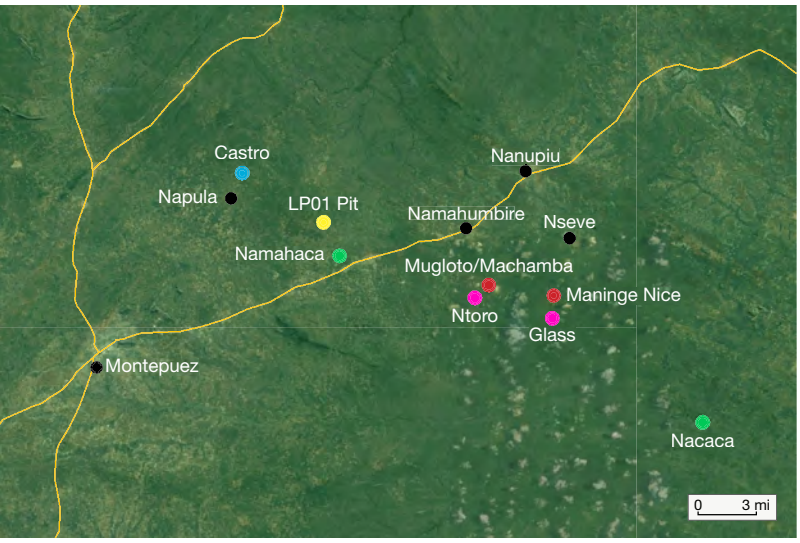

Figure 10. The main ruby mining areas of northern Mozambique. Those labeled in red are worked by Gemfields, and those in yellow by Mustang Resources. Green, pink, and blue areas are worked by garimpeiros*; the green areas show where they are allowed to mine. Pink and blue represent sites inside MRM and Mozambican Ruby, respectively.*

monet, a geologist with extensive experience in East African gem deposits; and a photographer and videographer.

Unlike previous years, we visited the area at an early stage of the dry season, which extends from June to November. The land was still green, and upon arriving we were struck by the lack of activity at the main garimpeiro villages on the road between Pemba and Montepuez. While in previous years we could see thousands of people and hundreds of shops at Nanupiu and Namahumbire, this time there were maybe a few hundred people in the streets and most of the shops were closed. It seemed that most of the garimpeiros had moved to other parts of the country.

Figure 11. An aerial view of MRM's new ruby washing plant, which uses dense media separation. Photo courtesy of Gemfields.

MRM (Montepuez Ruby Mining): Our visit to the MRM mine, owned by Gemfields and its local partner Mwiriti Limitada, took place during the record-breaking ruby auction in Singapore and a few days after Pallinghurst, Gemfields' main shareholder, attempted a takeover. We also saw representatives from the Chinese conglomerate Fosun, which was also looking to acquire Gemfields. The mine staff was thrilled by the results of the Singapore auction but uncertain about Gemfields' future. Afterward we learned that Pallinghurst was successful in the takeover. Gemfields was delisted from the London Stock Exchange on July 28, and a few days later Gemfields CEO Ian Harebottle announced his resignation. He was replaced by Sean Gilbertson.

Besides the excitement about the auction and the legitimate questions about the future of Gemfields, we observed some interesting changes at MRM. First, MRM continued to improve its mining and sorting capacity. Figure 11 shows a dense media separation (DMS) plant that became operational in December 2016, replacing the previous system of pulsating jigs. The results were said to be very encouraging, particularly regarding small material. Before, all material under 3 mm was rejected and stockpiled. With the new DMS plant, rubies under 3 mm can be collected very efficiently, and MRM's washing capacity has increased from 80 to about 150 tons per hour in ideal conditions. The sorting house scheduled to go next to the new DMS plant in 2017 will not be completed before summer 2018. Visiting the existing sorting house, we saw few improvements in rough processing efficiency. The author was able to once again select samples from recent production. These were mainly high-clarity, attractive rubies from the classic Mugloto/Machamba area, which has produced most of the stones auctioned by Gemfields since 2014.

Exploration continues, meanwhile, and mining is being planned for new areas east and west of the current pits at Mugloto/Machamba (producing secondary-type, iron-rich material with high clarity) or Maninge Nice (producing primary-type stones with moderate iron content and more inclusions and fractures). Glass, a secondary deposit south of Maninge Nice, was not bringing as much as expected, as it had been extensively worked by garimpeiros since 2009.

In summer 2017, the MRM mine employed 450 people. Including security and contractors, that number is more than 1,100 employees. Concrete houses have replaced the cargo containers once used as living quarters, and life there is now much more comfortable. Since the construction of the main camp, MRM has been able to focus on corporate social responsibility, and we could see significant results that have improved MRM's image in local communities. The company has built schools at Namahumbire and Nseve. We saw two chicken farms that appeared to be sustainable, and six farming associations created and supported by Gemfields. At Nseve, we visited a farming pilot program that could become very successful, as the area was fertile during Portuguese colonial times when the nearby reservoir was built. Agriculture disappeared after the civil war, which destroyed the local

communities and the economy. MRM is also financing a mobile health clinic, enabling government doctors to visit different villages each day to serve those with little access to health care. Finally, we could see that Gemfields was continuing to support conservation and community development in the Niassa Reserve with the "Niassa Lion" project.

Mustang Resources: In 2016, the author reported on the emergence of Mustang Resources, which acquired mining licenses in 2015. At the time they were focused on exploration and camp infrastructure. Mustang has been quite active, and the operation now employs about 130 people. A modern washing plant using rotary plants (figure 12) is in place. Jigs (the small "Bushman jig" version used for prospecting) and a small sorting house have been built. Mustang decided to concentrate on LP01, a promising area in the south of the concession where gem-rich gravels could be found at less than one meter depth. Operating at such shallow depth is inexpensive, as there is little overburden to be removed. The area had been discovered by garimpeiros (figure 13), and we saw mining from both Mustang and local villagers.

The stones are similar to those found in Glass or around Nacaca village (an area open for garimpeiros to the east of the Gemfields concession). This means that these are mainly secondary-type rubies that spent millions of years in gravels and show some abrasion. They have a fine pink to deep red color and are quite clean with rare fractures, but they tend to be smaller and their color is brighter than the production at Mugloto/Machamba, which has a higher iron content. We saw several fine clean rough stones up to 10 carats, but most of the production was under 1 carat.

We were informed that Mustang planned to have its first rough ruby auction at the end of November 2017 in Mauritius, as several tens of kilos had already been mined.

Figure 12. Mustang Resources' new washing plant consists of two rotary pans equipped with trammel screens and log washers. Its current capacity is about 600 tons per day. Photo by Vincent Pardieu.

Mozambican Ruby Lda.: While significant changes were visible in areas worked by Mustang and MRM, the same could not be said for Mozambican Ruby Lda. The project was clearly still in an early stage, with only a few employees and very basic equipment. The exploration program has nevertheless advanced considerably since last year, and more equipment is expected to arrive this year. The project is led by a small private company with a rather cautious approach. We visited the different pits mined by garimpeiros during the author's previous visit in 2016. The two pits at Castro were flooded and mainly being used by garimpeiros as a water reserve for washing the gravel they collected around the pit. The area seems to have great potential.

Our visit to the Montepuez area showed the evolution of ruby mining by MRM, Mustang, and Mozambican Ruby Lda., as well as by the garimpeiros. It now seems that the

Figure 13. A garimpeiro working near the LP01 pit inside Mustang Resources' concession near Napula village excavates the ruby-rich gravel under the topsoil. Photo by Vincent Pardieu.

legally operating mining companies are gaining the upper hand over the garimpeiros and the foreign buyers who smuggle stones to trading centers in Tanzania, Sri Lanka, and Thailand. It will be interesting to see what happens with Gemfields under Pallinghurst's full control and the impact of forthcoming production from Mustang.

Vincent Pardieu
VP Consulting SPC, Bahrain

Multi-color-zoned quartz from Brazil. Quartz very often crystallizes in zones during formation, when chemical or physical conditions change. An interesting example of strong zoning caused by variable iron content came recently from Bahia State in Brazil. No rough specimens were seen by the author, but several dozen flat cabochons up to about 4 cm long (figure 14) were available for study.

The quartz crystallized in five stages, each with a different type of iron. If there is any Fe in the original solution, it acts as a chromophore and produces citrine or amethyst; a higher Fe content will cause separate iron minerals to form. The oldest generation (1) is represented by parallel crystals of yellow citrine with small amethyst sectors, which can be described as ametrine. Their surface was covered by a thin quartz layer (2) with tiny goethite needles. The next generation (3) was a red layer, consistently about 3 mm thick, with fine agate-like zoning. The color was probably caused by very finely dispersed hematite, an identification based on typical color and microgranular texture. The next zone (4) was rich in pyrite, which formed fibers perpendicular to the older red layer, but pyrite can also form in this layer as tiny cubic crystals. After crystallization of the pyrite, the last pale purple amethyst layer (5) was filled with bundles of brown goethite needles up to about 3 mm, which also grew perpendicular to the original surface.

The inclusions in these attractive specimens can explain their complicated formation, with iron found in quartz structure (amethyst and citrine), in sulfide (pyrite), or in oxide (goethite and hematite).

Jaroslav Hyršl (hyrsl@hotmail.com)
Prague

Yellow, green, and blue sapphires reportedly from Antang and Gombe, Nigeria. GIA's Tokyo laboratory borrowed 19 sapphires (figure 15) from gem dealer Ambrose & Co. in Kofu, Japan. The samples consisted of eight blue, one bluish green, eight yellow, and one greenish yellow/blue bicolor sapphires, all faceted. They were reportedly from Antang and Gombe in northern Nigeria (figure 16). Mambilla, in the southeastern part of the country, is the only well-known Nigerian sapphire source (V. Pardieu et al., "Blue sapphires from the Mambilla Plateau, Taraba State, Nigeria," 2014, www.gia.edu/doc/Nigeria_Mambilla_Sapphire_US.pdf; Spring 2017 GNI, pp.134–135), and the two new sources are not well documented.

Sapphires from both Antang and Gombe are basalt related. The mines are located in a basement complex and

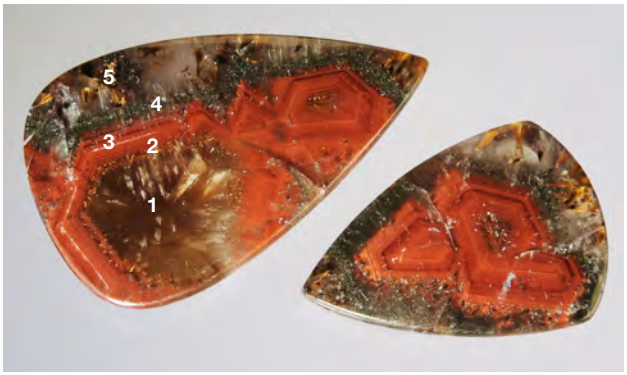

Figure 14. Cabochons of strongly zoned Brazilian quartz, measuring up to 4 cm long. The five described zones are numbered. Photo by Jaroslav Hyršl.

on Cretaceous/Tertiary sedimentary rocks near volcanic rocks. The sapphires are mined in alluvial deposits or unconsolidated sediments. According to the dealer, the blue sapphires were from Antang and the yellow sapphires and bicolor sapphire from Gombe. Brume Jeroh, the supplier in Nigeria, mentioned that Antang produces blue, green, yellow, and parti-color sapphires, while Gombe produces mainly yellow sapphires and a few blues. He also noted that stones from these sources may have been mixed together at the market in the city of Jos.

The samples' standard gemological properties are listed in table 1 at http://www.gia.edu/gems-gemology/fall-2017-gemnews-sapphires-nigeria. Refractive index and specific gravity values were all within the range of corundum. Representative inclusions observed in these sapphires are shown in figures 17 and 18. Quantitative analysis of trace elements was carried out with LA-ICP-MS, and the results are summarized in table 2 (http://www.gia.edu/gems-gemology/fall-2017-gemnews-sapphires-nigeria) and figure 19.

The yellow sapphires and the greenish yellow part of the bicolor sapphire showed a typically high Fe, and their Mg concentration is greater than Ti except for one sample (N08;

Figure 15. These sapphires (0.64–8.27 ct) are from Antang and Gombe, in northern Nigeria. Photo by Shunsuke Nagai.

Figure 16. Map of Nigerian sapphire sources. Sapphires from the new deposits at Antang and Gombe have potentially high quality.

again, see table 2 at http://www.gia.edu/gems-gemology/fall-2017-gemnews-sapphires-nigeria). As shown in figure 19, the high Fe (approximately 2000 ppma) and medium V (approximately 0.50–2.00 ppma) of all the yellow sapphires (N01 to N09) and the greenish yellow part of the bicolor sapphire (N10Y) showed the same trend as those of a bluish green sapphire (N11) and one blue sapphire (N12). The greenish yellow part of the bicolor sapphire (N10Y) matches other yellow sapphires in all elements, and the blue part of the bicolor (N10B) overlaps with N11 and N12. The titanium levels are significantly different between the two parts of N10. This matters, as the titanium is necessary for blue coloration in sapphire with iron. N11 and N12 show different trends from other blue sapphires (from N13 to N19) for V, Fe, and Ga. This suggests that these two samples originated from a different locality. Given that these two samples' trace element composition is close to that of the blue part of the bicolor sapphire (N10B) and different from the rest of the blue sapphires, we considered them to be from Gombe (again, see table 1). In addition, inclusions exhibited in figure 18 in N13–N19 were not seen in N11 and N12, and these two samples had similar features to each other, as shown in figure 17. Greenish blue and blue sapphires (N11 and N12) and the blue part of the bicolor sapphire (N10B) from Gombe show high Fe (approximately 2000 ppma) and medium V (approximately 1.50–2.00 ppma). Blue sapphires from Antang (from N13 to N19) show lower Fe (approximately 800–1500 ppma) and high V (approximately 4.50 ppma).

Although sapphires from these two new Nigerian sources are limited in quantity and color range, they are potentially high quality. The importance of the sources is

Figure 17. Inclusions in sapphires from Gombe: healed fissures with hazy edges (A), irregular particles and short needles (B), wavy graining (C), and flake-like particles (D). Photomicrographs in darkfield illumination (A–C) and diffused brightfield illumination (D) by Shunsuke Nagai. Fields of view 1.95 mm (A), 2.15 mm (B), 2.80 mm (C), and 2.80 mm (D).

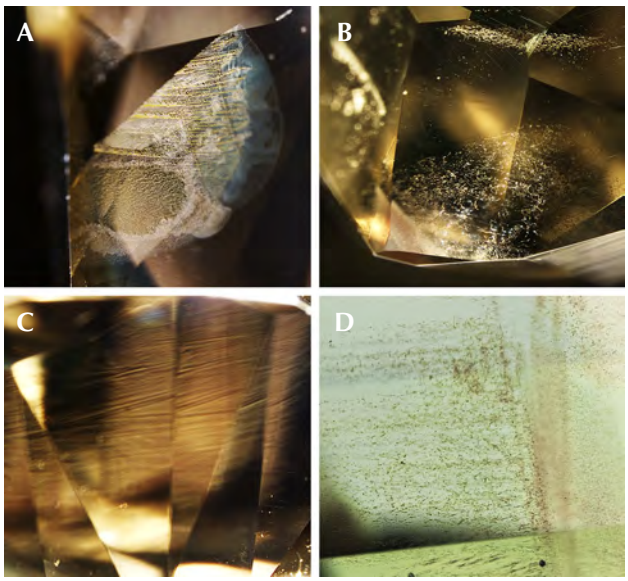

Figure 18. Inclusions in sapphires from Antang: zircon crystals (A), reflective thin films with hexagonal patterns (B), bands of minute particles and short needles (C), and angular banding and perpendicularly oriented particles (D). Photomicrographs in darkfield illumination by Yusuke Katsurada (A–C) and Shunsuke Nagai (D). Fields of view 2.80 mm (A), 1.00 mm (B), 4.00 mm (C), and 4.30 mm (D).

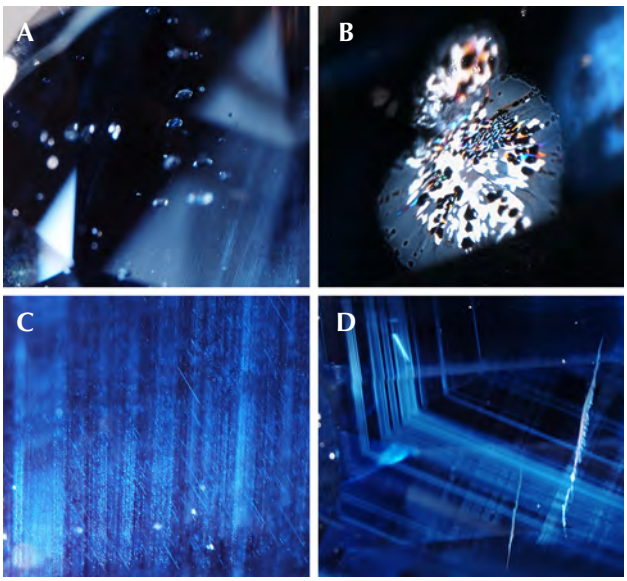

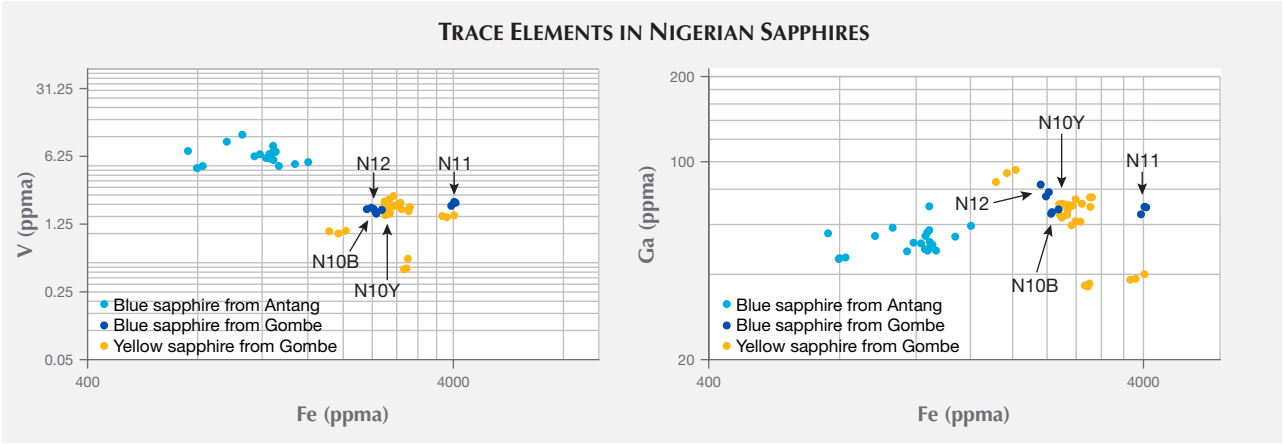

Figure 19. LA-ICP-MS quantitative analysis allowed the separation of blue sapphires from Antang and yellow sapphires in some trace elements (e.g., Fe vs. V and Fe vs. Ga). The two parts (N10Y and N10B) of the bicolor sapphire show a close trend. The bluish green sapphire (N11) and blue sapphire (N12) are considered to be from Gombe. Results are not averaged.

not yet known, and more field data and advanced testing data such as quantitative analyses of trace elements are needed. Despite the different trends in some trace elements between the localities, as this study revealed, they still overlap with trace elements of different magmatic origins including Mambilla (data not shown). Since characteristic inclusions are not always present in basalt-related sapphires and trace elements cannot always be separated, origin determination of these sapphires remains challenging. Interpretation of trace element data such as discriminant analyses and the building of a rich database are necessary.

Yusuke Katsurada
GIA, Tokyo

SYNTHETICS AND SIMULANTS

A melee-size CVD synthetic diamond in pearl and diamond jewelry. Since 2012, CVD synthetic diamonds have been tested and identified by NGTC labs in China, typically in sizes above 0.20 ct. Since 2015, a large number of melee-size colorless and near-colorless synthetic diamonds have been detected in daily screenings at NGTC labs. Melee-size HPHT synthetics are accurately screened and identified at NGTC labs using new devices, some of them developed by NGTC. Melee-size CVD synthetic diamonds were reported by GIA's Mumbai lab earlier this year (A. Krawitz, "GIA finds significant undisclosed synthetics," Diamonds.net, March 7, 2017).

In March 2017, NGTC's Beijing lab received 24 pieces of pearl and diamond jewelry (including the earrings seen in figure 20) from a domestic client, who claimed they were imported. Synthetic melee diamonds were identified in 14 of the 24 pieces. Most of the synthetic specimens were HPHT grown, but one was a melee-size CVD synthetic. The near-colorless CVD round brilliant circled in figure 21 was mounted in a pearl earring with about 200 natural melee diamonds. The estimated weight of this CVD melee is 0.01 ct. No obvious inclusions were found under 10× magnification.

Figure 20. A pair of pearl and diamond earrings set with about 200 natural melee diamonds and one CVD synthetic melee. Photo by Jun Su.

Figure 21. A CVD synthetic diamond (circled in red) was mounted in an earring along with very similar-looking natural melee diamonds. Photo by Shi Tang.

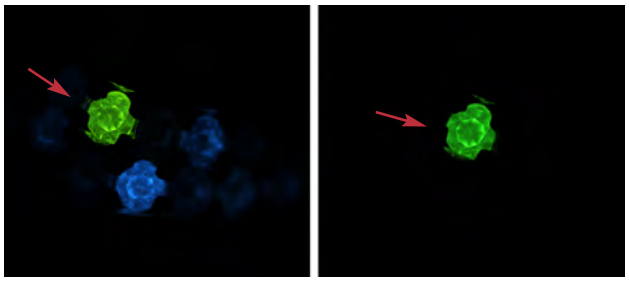

Figure 22. Left: The CVD-grown melee diamond (red arrow) shows green fluorescence in DiamondView imaging, while the natural melee below it exhibits blue fluorescence. Right: The DiamondView reveals the green phosphorescence of the synthetic melee, while the natural stone displays no phosphorescence. Images by Shi Tang.

Using NGTC's GV5000 rapid screening instrument, the UV luminescence of a group of diamonds can be observed at the same time. Unlike colorless to near-colorless HPHT synthetic melee, which normally displays strong phosphorescence, the CVD phosphorescence reaction tends to be weak or inert. The GV5000 provides broadband UV excitation, in which colorless to near-colorless HPHT synthetics display strong greenish blue phosphorescence for about 3–60 seconds. Colorless to near-colorless CVD synthetics normally emit weak phosphorescence that lasts less than 3 seconds, while natural diamonds very rarely show phosphorescence with medium to weak intensity for 1 to 2 seconds. Also, the fluorescence color under the GV5000 is mostly blue-white for natural diamonds, strong greenish blue for HPHT synthetics, and bluish green or green or orange to red for CVD synthetics (colorless to near-colorless). We noticed the green fluorescence and weak green phosphorescence of this melee and conducted further testing. The green fluorescence and phosphorescence were more pronounced in the DiamondView (figure 22), but the layered growth structure of CVD synthetics was still not seen due to the specimen's small size.

An absorption spectrum collected by micro-FTIR identified it as a type IIa synthetic diamond, with no N-related absorption. A weak 270 nm absorption band related to isolated nitrogen was detected in the UV-Vis spectrum. With 532 nm laser excitation at liquid nitrogen temperature, the PL spectrum showed strong SiV^- center double peaks at 736.6 and 736.9 nm (figure 23), consistent with CVD synthetic. A clear 978 nm emission also appeared in the PL spectrum with 785 nm laser excitation; the assignment of this emission is unknown. The green fluorescence was attributed to an H3 center, which means the specimen was HPHT-treated after growth.

This is the first time NGTC has identified a melee-size CVD synthetic diamond mounted alongside natural stones. This development is concerning, considering the challenge it would pose for gem laboratories. CVD synthetic screening requires more time and effort than HPHT synthetic screening, since the rapid methods of phosphorescence observation currently used would no longer be reliable. Therefore, new screening techniques and instruments are needed.

Shi Tang (tangs@ngtc.com.cn), Jun Su, Taijin Lu, Zhonghua Song, and Jie Ke
NGTC, Beijing

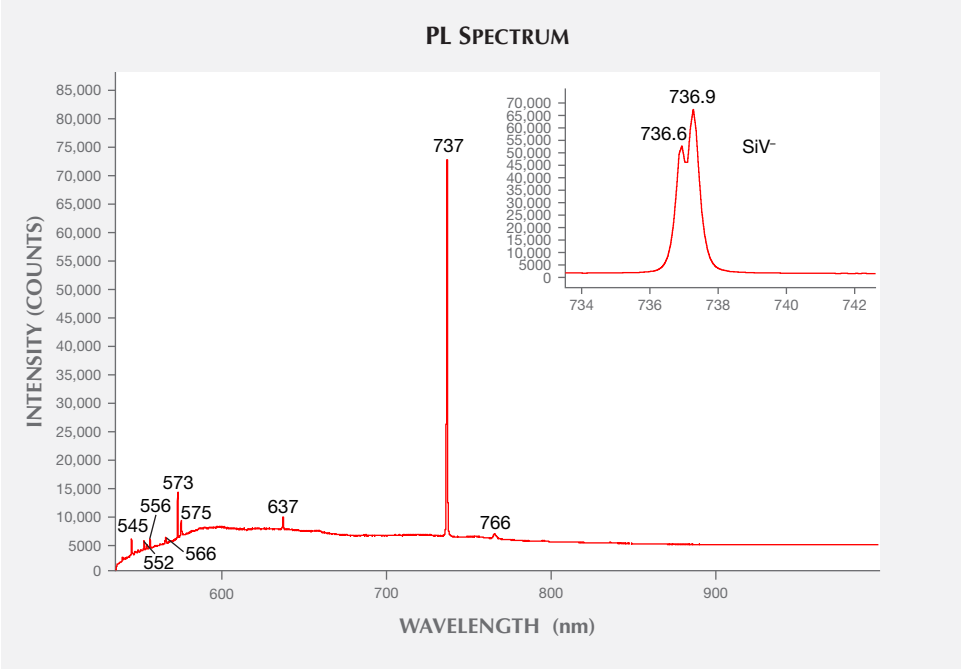

Figure 23. The melee-size CVD synthetic diamond shows strong SiV^- center emissions at 737 nm in the PL spectrum, as collected with a 532 nm laser.

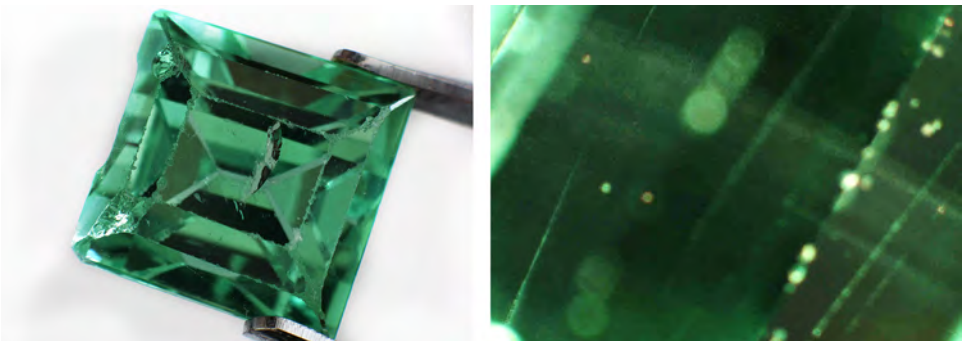

Figure 24. This 5.00 ct green synthetic sapphire showed clouds of bubbles along different directions (right, field of view 4.35 mm). Photos by Iurii Gaievskyi.

Unusual inclusions in green synthetic sapphire. A 5.00 ct green square step cut (figure 24, left) was submitted as a synthetic sapphire to the laboratory of the State Gemmological Center of Ukraine. Standard gemological testing gave an RI of 1.763–1.768, with a uniaxial negative optic sign and a birefringence of 0.005, as well as a hydrostatic SG of 3.94. The sample was inert to short- and long-wave UV radiation. Pleochroism was moderate green to yellowish green. Energy-dispersive X-ray fluorescence (EDXRF) spectroscopy showed only small amounts of Co (0.07 wt.% Co_3O_4 and CoO). Microscopic examination revealed abundant gas bubbles, including some along curved lines. From these observations we inferred that the Verneuil or Czochralski method was used to create this stone. These green synthetic sapphires are quite rare. There were also straight lines of bubbles in multiple directions (figure 24, right), which are extremely unusual in Verneuil- or Czochralski-grown synthetic sapphire.

Iurii Gaievskyi and Igor Iemelianov
State Gemmological Center of Ukraine, Kiev

TREATMENTS

Impregnated amazonite. A type of high-quality translucent blue amazonite feldspar (figure 25) has recently appeared in the jewelry market. Its vivid blue color and unusually high translucency are rarely seen in untreated mineral specimens and rough materials. A rough piece of this material and five beads with different quality grades were obtained for detailed examination at GIA's Carlsbad laboratory.

To induce the blue-green color in amazonite ($KAlSi_3O_8$), the potassium feldspar must contain structurally bound water in addition to lead, and then undergo irradiation (A.M. Hofmeister and G.R. Rossman, "A spectroscopic study of irradiation coloring of amazonite: structurally hydrous, Pb-bearing feldspar," *American Mineralogist*, Vol. 70, 1985, pp. 794–804).

FTIR spectroscopy revealed resin impregnation. A thin section cut from the middle of the rough (center of figure 26) was prepared to investigate the depth of impregnation and the origin of the vivid blue color. By performing FTIR in the middle of the section, we confirmed that the impregnation completely penetrated the material. Chemical analysis was obtained with a Thermo Fisher iCAP Q ICP-MS coupled with a New Wave Research UP-213 nm laser ablation unit. A line of 27 ablation spots crossed the whole section. Analysis revealed a microcline feldspar composition with a very minor albite component (figure 26). Pb concentration was irregularly distributed from one rim to the other, eliminating the possibility of Pb diffusion treatment (figure 26, violet data set). The concentration range of Pb was 11.7–44.6 ppma, or 120–432 ppmw. Albite portions contained higher Sr (red data set) and no Rb (blue data set) or Cs (green data set). In contrast, microcline portions contained higher Rb and Cs, and almost no Sr.

To test their chemical stability, the five beads were immersed in water, reagent alcohol, and then acetone for an hour apiece (figure 27, B–D). The quality of the beads increases gradually from left to right in figure 27. Neither water nor reagent alcohol affected the beads' appearance (figure 27, B–C). Many whitish fractures became evident on the surface of the smallest, third-largest, and largest beads after immersion in acetone for an hour (figure 27D). Their transparency diminished significantly, and they took on an unsightly mottled appearance. In contrast, the second-smallest and second-largest beads seemed largely unaffected. After 24

Figure 25. In this high-quality translucent amazonite bracelet, the average bead diameter is 12 mm. Photo by Kevin Schumacher.

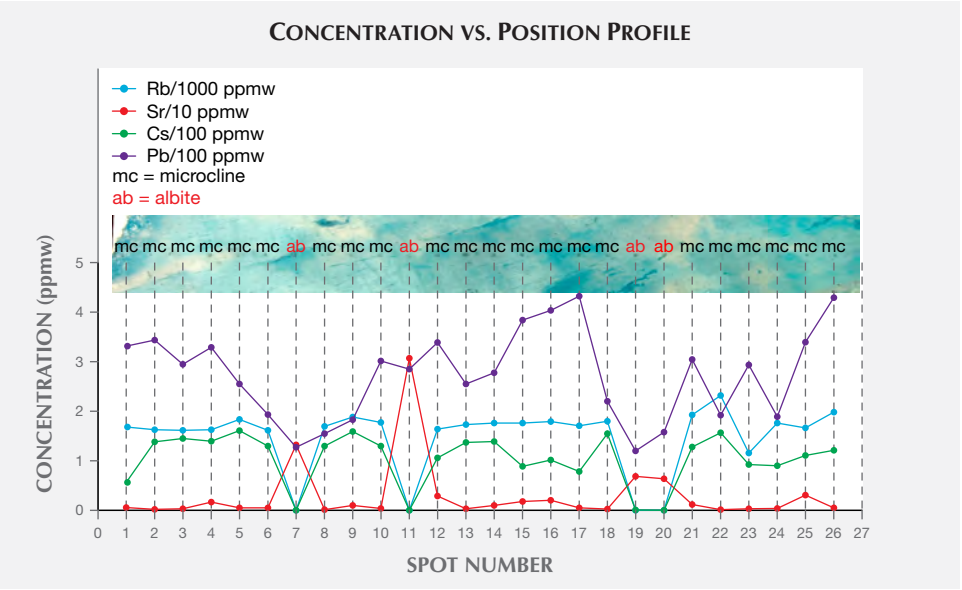

Figure 26. The amazonite's concentration vs. position profile revealed that it was mainly composed of microcline with minor albite. Spots laser-ablated from albite regions contain higher Sr and no Rb and Cs, while spots laser-ablated from microcline regions contain higher Rb and Cs and almost no Sr. The Pb concentration profile is irregularly distributed across the entire thin section (center image, field of view 19.27 mm). Photomicrograph by Jonathan Muyal.

hours of immersion in acetone, more whitish fractures became visible in the smallest, third-largest, and largest beads, revealing the true quality of the original material used for impregnation (figure 27E). Very minor whitish fractures were observed in the highest-quality bead (figure 27E, far right). During normal wear, consumers should avoid exposure to solvents that contain large portions of acetone, such as nail polish remover.

Ziyin Sun and Nathan D. Renfro

Figure 27. Amazonite beads without any post-treatment (A) and after immersion in water for an hour (B), reagent alcohol for an hour (C), acetone for an hour (D), and acetone for 24 hours (E). In all five rows, the bead quality increases gradually from left to right. Photos by Kevin Schumacher.

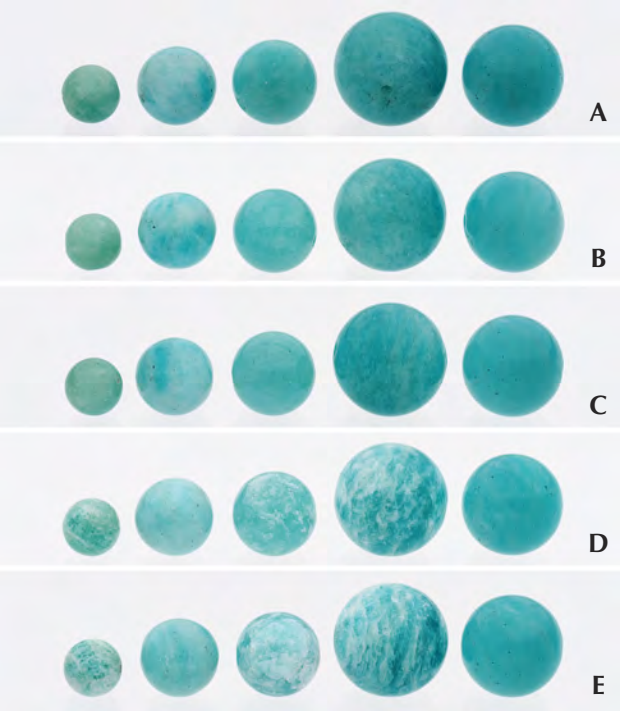

CONFERENCE REPORT

75th Swiss Gemmological Society Conference and European Gemmological Symposium. The 75th Swiss Gemmological Society (SGS) Conference and 6th European Gemmological Conference (EGC) were held together in Zermatt, Switzerland, June 30–July 1, 2017. Set at the Grand Hotel Zermatterhof, the conference featured 24 renowned speakers delivering a diverse, high-quality program.

Following the welcome address from SGS president **Hans Pfister**, the first presentation was from **Klemens Link** (Gübelin Gem Lab, Lucerne, Switzerland) on a new system for age determination of emeralds using LA-ICP-MS. This system provides useful geographic origin information for the gemstone's owner and high-quality data for scientific research. **Ulrich Henn** (German Gemmological Association, Idar-Oberstein) surveyed gems from central Namibia, starting with the discovery by German tin miners of tourmaline in Usakos in the early twentieth century. **Bernhard Berger** (Cartier, Paris) gave a 170-year history of Cartier, with special reference to the 1,800 pieces in the Cartier Collection. **Alan Hart** (Gem-A, London) delivered an illuminating talk on the Koh-i-Noor diamond from the British Crown Jewels, including its original cutting style prior to recutting in 1852.

Martin Rapaport (Rapaport, New York) was in typical energetic form for his keynote lecture on the state of the diamond industry, in which he highlighted the role of the gemologist. He suggested that gemologists create great value for the trade and should charge twice as much for their services, drawing applause. **Vincent Pardieu** (VP Consulting SPC,

Bahrain) presented on gemstones from East Africa. The challenge and opportunity for the future, he said, would be to balance gem discoveries and conservation, especially with new finds in and around Africa's national parks. **Thomas Hainschwang** (GGTL Laboratories, Balzers, Liechtenstein) spoke on GGTL's initiative to characterize treated diamonds. The aim is to create the most complete data set of natural-color versus treated-color diamonds. **Alan Hodgkinson** (Scottish Gemmological Association, Edinburgh) pondered the underappreciation of zircon, quoting Basil Anderson's description of them as "the most mysterious of gemstones." **Henry Hänni** (GemExpert GmbH, Basel, Switzerland) presented "sannan skarn," an ornamental gemstone from Pakistan that resembles maw-sit-sit and was introduced at the September 2016 Hong Kong show. **Guillaume Chautru** (Piaget, Geneva) spoke on the importance of gemological testing from a jewelry and watch manufacturer's point of view. **Michael Krzemnicki** (SSEF, Basel) detailed SSEF's inclusion research and new laser ablation–inductively coupled plasma–time of flight–mass spectrometry (LA-ICP-TOF-MS) capability. **Michael Hügi,** scientific committee chairman of SGS, presented the gems of Switzerland, especially the quartz that became works of art in the hands of European lapidaries from the 14th century onward. The guest of honor at the gala dinner, former Swiss president **Adolf Ogi**, gave an amusing talk on his career in politics.

The next morning, **Hanco Zwaan** (Netherlands Gemmological Laboratory, Leiden) discussed the characterization and formation of Sri Lankan metamorphic sapphires. **Andrey Katrusha** (New Diamond Technology, Russia) detailed the impressive results NDT has achieved in only three years of commercially producing large gem-quality synthetic diamonds. **Raquel Alonso-Perez** (Harvard Museum, Cambridge, Massachusetts) offered insights into the new emerald deposit in eastern Madagascar, based on her fieldwork there in September 2016. **Bruce Bridges** (Bridges Tsavorite, Kenya) looked back on 50 years of tsavorite with a video from the famous Scorpion mine and a moving tribute to his father, Campbell Bridges. **Wuyi Wang** (GIA, New York) updated the conference on synthetic gem-quality diamond and its identification, detailing GIA's research into this area. **Daniel Nyfeler** (Gübelin Gem Lab, Lucerne) addressed gemstone traceability and GGL's work to increase transparency in the colored stone supply chain.

Helen Molesworth (Gübelin Academy, Lucerne, Switzerland and Hong Kong) offered a historical perspective on the gem market using record auction prices and comparing values at different periods using a soldier's annual salary as a benchmark. Emeralds again came under the microscope in **Laurent Cartier's** (SSEF, Basel) talk detailing their history from ancient Egypt to modern Ethiopia. We were treated to the photography of **Jeff Scovil** (Phoenix, Arizona), who showed how he captures minerals, gems, and jewelry. **Joseph Taylor** (PT Cendana Indopearls, Indonesia) demonstrated how the Balinese philosophy of Tri Hita Karana is applied to his company's pearl farm in Indonesia. **Willy Bieri** (GRS, Meggen, Switzerland) spoke on the identification of the new sapphires being mined near Ambatondrazaka, Madagascar, and their differentiation from Kashmir sapphires. Thomas Hainschwang delivered a talk by **Franck Notari** (GGTL Laboratories, Geneva) on polycrystalline boehmite needles in corundum, and his proposal to rename these "Rose's channels" in homage to Gustav Rose, a nineteenth-century German mineralogist.

Figure 28. Differential interference contrast lighting reveals surface growth marks on Brazilian beryl. Photomicrograph by Jonathan Muyal; field of view 0.72 mm.

The next morning, following a trip on the famed Gornergrat Railway, a geological master class was held at an elevation of 3,100 meters. **Kurt Bucher** (University of Freiburg, Germany) detailed the geology of the Zermatt region.

The SGS 2018 Annual Meeting will take place May 7–8 in Lugano, Switzerland.

Edward Johnson
London

ANNOUNCEMENTS

Jonathan Muyal wins Royal Microscopical Society award. GIA Carlsbad staff gemologist and *G&G* contributor Jonathan Muyal took second place in the Light Microscopy–Physical Sciences division of the Royal Microscopical Society's biennial Scientific Imaging Competition. The award-winning image (figure 28) shows natural surface growth marks on Brazilian beryl. Mr. Muyal used differential interference contrast lighting to create the image.

James Shigley receives AGS Lifetime Achievement Award. Dr. James E. Shigley, GIA's distinguished research fellow, received the American Gem Society's Lifetime Achievement Award at the AGS Circle of Distinction dinner on July 25, 2017 in New York. Since joining GIA in 1982, Dr. Shigley has made countless contributions to the field. He has lectured extensively on gems and gem identification, authored or coauthored more than 60 *Gems & Gemology* articles, and edited the *G&G In Review* book series.